

UNIVERSIDAD DE CANTABRIA

PROGRAMA DE DOCTORADO INTERUNIVERSITARIO EN TECNOLOGÍAS DE LA
INFORMACIÓN Y COMUNICACIONES EN REDES MÓVILES (TICRM) / MOBILE
NETWORK INFORMATION AND COMMUNICATION TECHNOLOGIES (MNICT)



TESIS DOCTORAL

Propuesta de topologías de antena para sistemas de
comunicaciones 5G

PhD THESIS

A proposal of antenna topologies for 5G communication systems

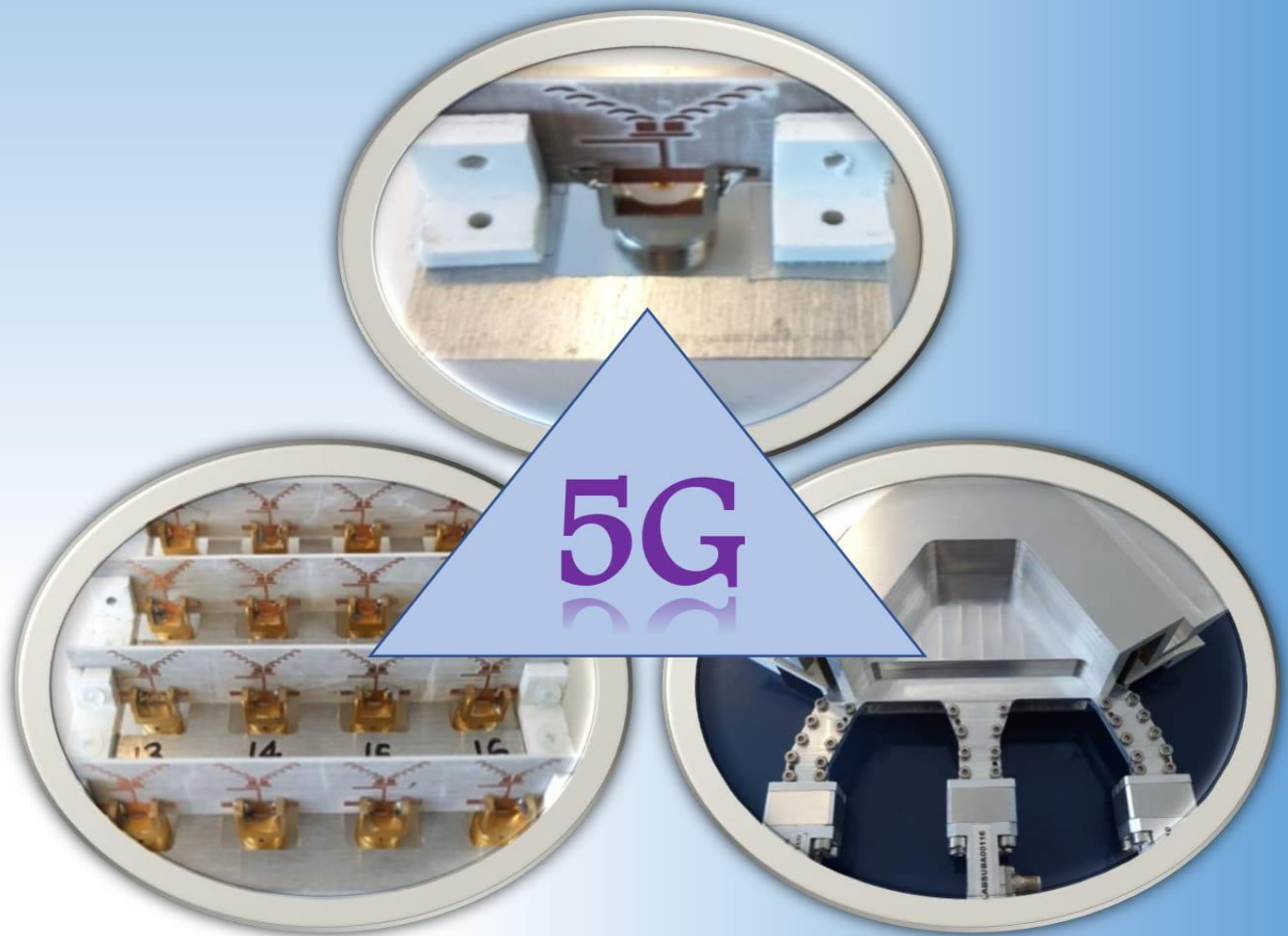
Realizada por: Vedaprabhu Basavarajappa

Dirigida por: José Basterrechea Verdeja

Escuela de Doctorado de la Universidad de Cantabria
Santander 2018

A Proposal of Antenna Topologies for 5G Communication Systems

- A Doctoral Thesis by Vedaprabhu Basavarajappa with supervision of Prof. Jose Basterrechea, carried out at the University of Cantabria and TTI Norte.



*To my wife Yashu,
my parents Gowramma and Basavarajappa,
my sister Chithprabha and brother Ambarish.*

Acknowledgment

At the outset, I would like to express my sincerest thanks to my Thesis Director Prof. Jose Basterrechea of the University of Cantabria for providing me with his valuable guidance and support during the PhD, both technically and otherwise. I can never forget the long interesting discussions filled with intellectual rewards that I have had with him. His intellectual fervour towards antennas will always inspire me.

My special thanks to H2020 Marie Curie 5Gwireless project and the project coordinator Prof. Marco Di Renzo for his constant support and encouragement throughout the project. I would also like to thank Prof. Cheng Xiang Wang for hosting me as a Visiting Scholar for four months at Heriot Watt University.

I would like to thank profusely Ms. Beatriz Bedia Exposito for her support and guidance at TTI in relation to the implementation aspects. Her sustained patience and encouragement kept me in good stead during the project. My sincerest thanks to Ms. Ana Ruiz, Head of Antenna Department, TTI for facilitating a proper channel for me whilst considering the formalities of carrying out a PhD at the University while being employed at TTI. She also introduced me to several aspects of antennas especially pertaining to antenna measurements. Special thanks to Dr. Ignacio Montesinos for the very many technical discussions on varied topics of antennas. Many thanks to Dr. Lorena Cabria who took ample time out to review my papers and always provided me with her timely comments and feedback. She also guided me towards various aspects of the PhD including on publishing. I would also like to thank Mr. Alberto Pellon for introducing me to new concepts and technologies in antenna design. TTI as a company is production driven, hence, a special mention to Mr. Borja Santander, Production Head, TTI for his help in manufacturing the antenna prototypes in a timely and efficient manner. His openness to suggestions and willingness to adapt the manufacturing accordingly in case of a later change helped me tremendously. Most importantly, I would like to offer my sincerest thanks to Juan Becerro, CEO, TTI for his vision and support throughout.

5Gwireless ITN gave me the opportunity to travel and visit different parts and cities of Europe. Thanks to my fellow ESRs in 5Gwireless - Carlos, Panos, Zahid, Giovanni, Alexis ... - my life has been greatly influenced by their varied outlooks and philosophies towards technology and life in general.

I cannot forget the good times I had in Spain with David, Alexia, Maialen and Carlos. I sincerely thank them for making my stay here filled with rich experiences.

My special thanks to my former advisors Prof. L. Basavaraj, Prof. K. J. Vinoy, Dr. Massimiliano Simeoni, Prof. Alexander Yarovoy, Dr. Peter Knott, Dr. Daniel O' Hagan and Prof. Vincent Fusco. It is by building on the focused guidance that they imparted to me during those times that I have been able to hone my skills and apply them now. I will always be deeply indebted to them.

Finally, I would like to thank my wife, my parents and my family for their constant support and encouragement during the PhD.

Due to space constraints, though it is not possible to mention everyone to whose help I am indebted, I would like to thank profusely everyone who has contributed and helped me in one way or the other in this endeavour.

Abstract

Methodologies for meeting the requirements of 5G by a structured and simplified design of antennas are proposed in this thesis for frequencies centred at 14 GHz, 28 GHz and 31 GHz.

Using a unique method for the refractive index retrieval, employed over S parameters, a special arrangement of parasitics was used to design and realize a directional, low-profile quasi-optic end fire antenna element with a gain around 5.5 dBi with a bandwidth of 1.5 GHz around 14 GHz. Experimental validation of the antenna element asserted its suitability for use in the 4x4 sub-array for Massive MIMO antenna array.

The 4x4 subarray antenna was designed with an interelement spacing of 0.8λ and was solved for individual element patterns using a full wave solver before applying postprocessing on it. The measured active reflection coefficient over a selected element is distributed over the range 13.5 GHz to 14.5 GHz with an $S_{nn} < -15$ dB. The mutual coupling between the ports for the best case is -31 dB and for the worst case is -25 dB. The 4x4 subarray employs two phasing networks that were designed to generate the two-phase states of 0° and 180° required for the beamswitching. The proposed multiple beamswitching scheme was applied on the antenna array and there was a good agreement between the simulated and measured antenna pattern for the different beamstates. For the generation of the boresight pattern a Co-polar gain varying around 18 dBi centred around 14 GHz was measured. The Cross-polar discrimination is around 20 dB around 14 GHz. For the generation of four beams a Co-polar gain of around 8 dBi at each beam and a Cross-polar discrimination varying from 10 to 20 dB is seen over the frequency band 13 to 15 GHz. Measurements made on other beamstates along other directions also agreed well with the simulations.

A novel two-phase state multibeam switching scheme proposed and applied over the designed 4x4 sub-array enables realization of multibeam along predefined directions spread over five selected validated beam states, though other beamstates can be obtained through the switching scheme. The scheme significantly reduces beamswitching latency generally associated with switching networks owing to the only-two-phase state proposition and that the switching is between multiple simultaneous beams rather than between single beams. This multibeam simultaneous beam footprint drastically reduces the switching time required for beam transition in conventional switching networks that need to hop between single beams.

Spatial modulation is a way of realizing Single RF MIMO. Spatial modulation harnesses pattern diversity to transmit implicit information over antenna patterns, where the implicitness comes from the selection of the antenna index to transmit the pattern. This requires the generation of beampatterns with low correlation coefficients (< 0.4) or ones that are orthogonal or non-overlapping to each other. A reconfigurable antenna beamswitching configuration that rotates a paired split beam over the azimuth for the range $\{0^\circ < \phi < 360^\circ\}$ in steps of 45° can be implemented on the subarray of a Massive MIMO array. The sub array can be 3x3 or 4x4 depending on the number of antennas in the Massive MIMO array. Recent interest in Massive MIMO antennas has been on 64 and 128 antennas, therefore it follows to have a subarray of 4x4 to act as the subarray beamswitching building block of the 64-antenna array.

The proposed beamswitching scheme employs electronic phase tethering that locks antenna elements or groups of antenna elements so that a control over the beam is attained which can

be mapped onto simple geometric relations. Such a switching scheme was applied over the 4x4 array and paired split beam patterns spread over the azimuth in time in steps of 45° were measured. A good agreement between the simulated and measured results was observed. A gain of around 8 dBi and an XPD of more than 10 dB is seen over these patterns between 13.5 GHz to 14.5 GHz. These patterns share the same phase centre which introduces an additional degree of normalization over the varied paired split beams formed when employed as a reconfigurable antenna array for spatial modulation purposes. The beamswitching scheme proposed incorporates pattern reconfigurability that introduces dual functionality into the array: Use in large scale arrays such as Single RF MIMO and the use in Spatial Modulation to transmit implicit information through antenna index.

For application in small cell scenarios at Millimeter Wave band, an all-metal multibeam waveguide lens antenna is proposed that projects multiple high directional beams of the order of 15 dBi over two bands centred at frequency of 28 GHz and 31 GHz. Experimental validation of the antenna confirms the phase extraction and compensation method proposed for simplifying the design process. The designed beam angles directed towards pointed three beam distributions over a 120° sector of a small cell can be used in millimeter wave based 5G LMDS small cell scenarios. These antennas are conceptualized, designed and tested with due considerations to current 5G requirements and therefore are 5G-ready. The thesis presents a detailed treatise on these antennas.

Resumen

En esta Tesis Doctoral se proponen nuevas topologías de antena para comunicaciones 5G orientadas a su empleo en sistemas Massive MIMO, sistemas Single RF MIMO y sistemas de comunicaciones en banda Milimétrica. Su conceptualización y diseño se ha realizado tras una revisión exhaustiva del estado del arte en antenas para 5G. Fruto de esta revisión, se decidió investigar en tres líneas fundamentales: el empleo de elementos radiantes direccionales para agrupaciones multihaz para Massive MIMO, elementos radiantes con diagrama reconfigurable para su empleo en sistemas Single RF con Modulación Espacial y una solución basada en el concepto de lente para el caso multihaz en ondas milimétricas. A lo largo de esta Tesis Doctoral se realiza una presentación detallada del diseño conceptual, el diseño específico y la fabricación y validación experimental de cada uno de los tres diseños de antena desarrollados, así como del elemento radiante básico utilizado para implementar las agrupaciones de los dos primeros diseños.

En los siguientes párrafos, se resumen las características fundamentales relacionadas con cada uno de estos diseños.

A) Elemento radiante EndFire Cuasi-Óptico

Se propone un nuevo elemento radiante de tipo endfire inspirado en los principios de las fibras ópticas. La disposición específica de elementos parásitos, basada en la modificación del índice de refracción, provoca una mejora de ganancia así como una respuesta en frecuencia de potencial banda ancha cuyas características no han sido exploradas debido al interés específico en la banda de 14 GHz.

La antena propuesta presenta una configuración de parásitos subresonantes inspirada en las fibras ópticas de perfil de índice gradual, de forma que facilita la concentración del campo generado por el dipolo excitador en la dirección endfire. Con la ayuda de un simulador electromagnético, tras un proceso de optimización geométrica, se ha obtenido un diseño operativo en la banda de 14 GHz con una ganancia teórica en torno a 6 dBi y un ancho de banda de 1.5 GHz. Dado que el elemento se ideó para su integración en una agrupación, se ha considerado importante incluir en el análisis una estructura de soporte similar a la que se empleará posteriormente.

Se ha construido un prototipo que, ha sido validado experimentalmente mediante medidas en reflexión y medidas de cortes del diagrama y ganancia en cámara anecoica. Las características de reflexión confirman el ancho de banda de 1.5 GHz en torno a la frecuencia de diseño. Las medidas de los cortes del diagrama han confirmado el carácter direccional del elemento obtenido de las simulaciones. Además, han confirmado la existencia de una desviación del máximo de radiación del elemento de unos 20° respecto a la dirección endfire, causada por la carga asimétrica de los brazos del dipolo con los parásitos, que desde el punto de vista de su empleo en los esquemas de conmutación de haces que se utilizarán posteriormente tiene un efecto despreciable. Las medidas de ganancia proporcionaron un valor en torno a 5.5 dBi en la banda de interés.

Queda abierta la posibilidad de mejorar la respuesta de este elemento para otras aplicaciones mediante la corrección de la desviación de 20° de su máximo de radiación, mejorando la técnica presentada en el capítulo 3 con carga asimétrica de los brazos del

dipolo. También puede resultar de interés mejorar la ganancia del elemento recurriendo a otras configuraciones novedosas de parásitos inspirados en la técnica de cambio de índice de refracción propuesta.

Por otra parte, actuaciones sobre el elemento radiante que permitan la reducción de su perfil, incrementar su ancho de banda o generar polarización dual son aspectos de investigación que quedan abiertos para el futuro.

B) Agrupación para Massive MIMO

El elemento radiante endfire cuasi-óptico diseñado se ha empleado como elemento radiante en el diseño de una agrupación 4x4 que se utilizaría como base de sistema MIMO 8x8. La agrupación ha sido caracterizada teóricamente con la ayuda de un simulador de onda completa. Se determinó un espaciado óptimo entre elementos de 0.8λ que proporciona un aislamiento entre puertos mejor de 25 dB. Para generar los múltiples haces requeridos para Massive MIMO, se ha propuesto un sistema de excitación basado exclusivamente en dos estados de fase (0° , 180°) que da lugar a diferentes configuraciones simétricas de haces aprovechando la respuesta ante las excitaciones impares de la distribución de elementos.

Para la validación de la propuesta, se ha construido y medido un prototipo del diseño. Este prototipo se ha caracterizado experimentalmente y contrastado con los resultados del diseño teórico, tanto en términos de reflexión y acoplos mutuos entre puertos, como en términos de respuesta en radiación en cámara anecoica.

La respuesta en reflexión en los puertos de la antena proporciona un ancho a 10 dB que cubre sobradamente la banda de interés y los parámetros de acoplo mutuo están incluso en el peor caso por debajo de -23 dB, mostrándose por debajo de -30 en la mayor parte de los casos.

Para la caracterización experimental en cámara anecoica, se han diseñado dos circuitos de alimentación de tipo corporativo que permiten generar los dos estados de fase necesarios para excitar los puertos en las cinco configuraciones consideradas mediante la conexión mediante cables de sus salidas con los puertos de los distintos elementos radiantes. En todos los casos considerados, el contraste de los resultados teóricos con los experimentales ha resultado muy satisfactorio: se han obtenido las direcciones de apuntamiento de haces y las ganancias con niveles de polarización cruzada inferiores a 10 dB en el peor caso.

En definitiva, puede considerarse el esquema de excitación multihaz propuesto ha sido validado experimentalmente en cinco de sus posibles estados de excitación.

Quedan abiertas algunas líneas de trabajo futuras entre las que podrían citarse: la utilización de desfases programables de tres estados (0° , 180° , open) en cada uno de los puertos o de acopladores híbridos de 180° con conmutadores para seleccionar entre puertos las excitaciones, así como la investigación sobre otras posibles orientaciones de los haces utilizando como bloque básico el mecanismo de excitación impar propuesto en combinación con otras configuraciones de fase estructuradas.

C) Agrupación con diagrama reconfigurable para Modulación Espacial

El subarray 4x4 para Masive MIMO puede encontrar su aplicación en sistemas con Modulación Espacial cuando se combina con el novedoso esquema de conmutación de haces en acimut desarrollado. Éste utiliza una unidad básica radiante constituida por el elemento central de una agrupación 3x3 y otro de los que le rodean con excitación antisimétrica cuya rotación en sentido de las agujas del reloj permite obtener una total de ocho diagramas espacialmente diferenciados que comparten el mismo centro de fase. El correcto funcionamiento de este esquema de conmutación se ha validado mediante simulaciones realizadas con ayuda del simulador de onda completa.

Para su integración en sistemas Massive MIMO con 64,128 o 256 elementos radiantes, el esquema de conmutación propuesto inicialmente con 3x3 elementos, se adaptaba mejor mediante la división de la agrupación en subagrupaciones de 4x4 elementos, sobre los que la utilización de bloques de 2x2 elementos enfrentados y excitados de forma antisimétrica, permite también la obtención de ocho diagramas espacialmente diferenciados que comparten centro de fase. Este mapeado escalable y flexible del esquema de reconfiguración de diagrama propuesto, resulta idóneo para su utilización en escenarios de Single/Few/Reduced RF MIMO, en especial para su empleo en Modulación Espacial que implica la transmisión implícita del índice identificador de la antena.

El funcionamiento del esquema se ha validado experimentalmente utilizando el prototipo desarrollado para validar la propuesta para Massive MIMO. En concreto se han comparado los resultados teóricos y experimentales para los cortes del diagrama en cinco de las ocho configuraciones resultantes con buenos resultados. Las medidas de ganancia y discriminación crosspolar han proporcionado valores de 8 dBi y superiores a 10 dB, respectivamente, en todos los casos.

Posibles extensiones del esquema propuesto pueden orientarse a la introducción de una cuarta dimensión adicional de indexado de la subagrupación al diagrama de constelación de Modulación Espacial, lo que impactaría directamente sobre la demodulación en los receptores. Otro campo emergente muy reciente en el que podrían explorarse las características del diagrama reconfigurable del esquema de excitación propuesto es el de Index Modulation.

D) Antena Multihaz de Lente para ondas milimétricas

Se propone una antena multihaz muy direccional basada en una lente implementada en guía de placas paralelas orientada a compensar las elevadas pérdidas de propagación en la banda de milimétricas. En el Capítulo 6, se presenta el diseño y la validación experimental de la misma. El diseño es el resultado de un proceso de co-diseño de cuatro diseños dependientes integrados para trabajar de forma unificada. La antena se ha diseñado para operación en banda dual a 28 y 31 GHz con anchos de banda de 1 GHz, lo que la convierte en una potencial candidata para su empleo en sistemas LMDS en bandas milimétricas para 5G.

El diseño se ha realizado para conseguir 3 haces directivos desviados 60° entre sí (+60°, 0°, -60°), lo que permitiría su empleo en pequeñas celdas 5G LMDS en banda milimétrica que requieran una proyección angular de 120° en cada sector de la celda. Otra aplicación

potencial de la antena se puede buscar en el ámbito de los radares de vigilancia en forma de agrupación circular de 3 sectores de 120° .

La principal novedad del diseño propuesto con respecto a los que se pueden encontrar para este tipo de estructuras en la literatura radica en el empleo del primer modo TE de la guía de placas paralelas, en lugar del modo fundamental de la misma de tipo TEM. Esto da lugar a una antena que presenta polarización lineal ortogonal a los diseños convencionales.

Otro aspecto a resaltar del diseño es su simplicidad conceptual que implica ciertas restricciones en cuanto a las prestaciones que es posible obtener de la antena. El empleo de un simulador de onda completa en la etapa de diseño implica un elevado coste computacional

El diseño, que ha tenido en cuenta las restricciones impuestas por el proceso de fabricación utilizado, se ha implementado en un prototipo que ha sido caracterizado experimentalmente. Los resultados obtenidos de las medidas de parámetros S, ganancia y cortes del diagrama asociado a cada puerto de excitación se han comparado con los proporcionados por las simulaciones realizadas durante el proceso de diseño con un elevado grado de concordancia entre los mismos.

La metodología de diseño propuesta permitiría la realización de diseños alternativos con diferente separación angular de los haces e incluso con un mayor número de haces con menor separación angular, con las limitaciones geométricas impuestas por los alimentadores utilizados, consistentes en bocinas rectangulares Plano E, y por sus acoplos mutuos.

En el futuro, podría mejorarse significativamente la técnica de compensación de fase utilizada para desarrollar una técnica de diseño y optimización estructurada tanto para la altura como para la geometría de la lente en PPW que permita dar cuenta de los efectos no considerados en el modelo. Probablemente, la mejor opción sería recurrir a una técnica de trazado de caminos. Con ello solamente sería preciso recurrir al simulador de onda completa para validar el esquema de diseño y optimización basado en trazado de caminos.

En resumen, en la Tesis se presenta el diseño e implementación de antenas para tres escenarios 5G de Massive MIMO, Single RF MIMO y Ondas Milimétricas, respectivamente, poniendo el énfasis en los aspectos teóricos y la caracterización experimental de cada una de ellas

Table of Contents

Acknowledgment.....	i
Abstract.....	iii
Resumen	v
List of acronyms	xiii
List of Figures.....	xv
List of Tables.....	xxi
Chapter 1	1
Introduction	1
1.1 Evolution of the G networks	1
1.2 Need for 5G antennas.....	3
1.3 Requirements on 5G antennas.....	3
1.4 Problem description and challenges towards the realization	4
1.5 Outline of the chapters	5
1.6 List of original contributions.....	5
1.7 References	7
Chapter 2	9
5G requirements and State-of-Art	9
2.1 Introduction	9
2.2 Massive MIMO	10
2.2.1 Key Aspects of Massive-MIMO	11
2.2.2 Massive MIMO demonstrators.....	11
Argos	12
Lund LuMaMi	12
Samsung	13
2.2.3 Other multibeam antenna designs	14
2.3 Single-RF MIMO Antennas.....	15
2.3.1 Parasitic Antenna Array	17
2.4 Millimeter wave antennas	19
2.4.1 Key aspects and Challenges at mmWave beamforming	20
2.4.2 Antenna designs for mmWave band	22
2.5 Conclusion.....	29
2.6 References	31
Chapter 3	35

Quasi-optics endfire antenna element.....	35
3.1 Introduction.....	35
3.2 Antenna Element Design Principle.....	36
3.2.1 Driver dipoles:.....	36
3.2.2 The printed reflector.....	37
3.2.3 The parasitics.....	40
3.2.4 Effect of antenna back plate	44
3.3 Antenna characteristics	45
3.3.1 Possible alternate realization of the antenna	49
3.4 Conclusion.....	51
3.5 References	52
Chapter 4	53
Massive MIMO antenna array	53
4.1 Introduction	53
4.2 Antenna Array Design and Beamswitching Concept.....	54
4.2.1 Fundamental beam unit	54
4.2.2 Antenna Array design.....	56
4.2.3 Phase shifting feed network design.....	58
4.3 Antenna Array Measurements and Discussion.....	65
4.4 Conclusion.....	77
4.5 References	78
Chapter 5	79
Spatial modulation aided Single- RF MIMO	79
5.1 Introduction	79
5.2. Single RF MIMO Technologies	81
5.2.1 ESPAR (Electronically scanned parasitic antenna array)	81
5.2.2 Beam-space MIMO	84
5.2.3 Spatial Modulation	88
5.3 Single RF MIMO Antenna array concept	90
5.3.1 Antenna description.....	90
5.3.2 Antenna scheme of excitation.....	90
5.3.3 Switching scheme, excitation matrices and rotational beams	91
5.3.4 Full wave simulator calculated 3D Correlation Coefficient.....	94
5.4 Single RF MIMO antenna array measurement and discussion	95
5.4.2 Pattern and gain measurements	98

5.5 Conclusion	104
5.6 References	105
Chapter 6	107
Millimeter wave antenna	107
6.1 Introduction	107
6.2 Design principle	109
6.3 Antenna Design.....	117
6.3.1 Design of the parallel plate waveguide	118
6.3.2 Design of the feeding horns	119
6.3.3 Design of the ridge-based lens	119
6.3.4 Design of the flared radiating aperture.....	120
6.4 Measurement and Discussion	120
6.4.1 S parameter measurement	125
6.4.2 Port -to- Port isolation measurement.....	126
6.4.3 Radiation Pattern stability over the designed dual wideband validated by simulations	126
6.4.4 Pattern and gain measurement	133
6.5 Conclusions	138
6.6 References	139
Chapter 7	141
Conclusion	141

List of acronyms

3GPP: Third Generation Partnership Project
5G: Fifth generation
5GPPP: 5G public private partnership
AAS: Active Antenna System
AD: Amplitude Detector
ADC: Analog to Digital Converter
AMPS: Advanced Mobile Phone System
ASE: Area Spectral Efficiency
ASP: Arc Shaped Parasitics
AUT: Antenna Under Test
BE: Bandwidth Efficiency
BPSK: Binary Phase Shift Keying
BS: Base Station
CAD: Computer Aided Design
CATIA: Computer Aided Three-Dimensional Interactive Application
CDMA: Code Division Multiple Access
CMOS: Complementary Metal Oxide Semiconductors
CNC: Computer Numerical Control
CP: Cyclic Prefix
CPE: Customer Premises Equipment
CPS: Co-Planar Strip line
CPW: Co-Planar Waveguide
CSI: Channel State Information
CST: Computer Simulation Technology
DAC: Digital to Analog Converter
DC: Direct Current
DL: Downlink
EDGE: Enhanced Data Rates for GSM Evolution
EE: Energy Efficiency
EM: Electro Magnetic
EMC: Electromagnetic Compatibility
EMI: Electromagnetic Interference
ESPAR: Electronically Scanned Parasitic Antenna Arrays
ETSI: European Telecommunications Standards Institute
F/B: Front-to-Back Ratio
FM: Frequency Modulation
FPGA: Field Programmable Gate Array
FSK: Frequency Shift Keying
Gbps: Giga bits per second
GHz: Giga Hertz
GPRS: General Packet Radio Service
GSM: Global System for Mobile Communications
HFSS: High Frequency Structure Simulator
HSPA: High Speed Packet Access
IoT: Internet of Things
IP: Internet Protocol
ISO: International Organization for Standardization
KPI: Key Performance Indicators
LMDS: Local Multipoint Distribution System

LNA: Low Noise Amplifier
LoS/LOS: Line of Sight
LPKF: Leiterplatten Kopier Fräsen (Circuit board copy milling)
LS MIMO: Large Scale MIMO
LTE: Long Term Evolution
LuMaMi: Lund Massive MIMO
MIMO: Multiple Input Multiple Output
MIPP: Mirror Image Pattern Pair
MMS: Multi Media Messages
MS: Mobile Station
MUBF: Multi-user beamforming
NLOS: Non-Line of Sight
NMT: Nordic Mobile Telephony
NR: New Radio
NTT: Nippon Telegraph and Telephone
O2I: Outdoor to Indoor
OFDM: Orthogonal Frequency Division Multiplexing
OSTBC: Orthogonal Space Time Block Coding
OTA: Over-the-Air
PCB: Printed Circuit Board
PIN: p-type intrinsic n-type
PPW: Parallel Plate Waveguide
PSK: Phase Shift Keying
PVC: Poly-Vinyl Chloride
QLC: Quasi-Lumped Couplers
QoS: Quality of Service
RPG: Role Playing Games
SCS: Subcarrier Spacing
SDR: Software Defined Radio
SE: Spectral Efficiency
SIC: Self Interference Cancellation
SIW: Substrate Integrated Waveguide
SLL: Side Lobe Level
SMA: Sub Miniature Version - A
SPA: Switched Parasitic Antenna array
SPMT: Single Pole Multiple Throw
SPTT: Single Pole Three Throw
TACS: Total Access Communication System
TDD: Time Division Duplexing
TDM: Time Division Multiplexing
TE: Transverse Electric
TEM: Transverse Electric Magnetic
UE: User Equipment
UMTS: Universal Mobile Telecommunication Systems
VNA: Vector Network Analyzer
VNI: Visual Networking Index
WR: Waveguide Rectangular
XP: Cross Polar
XPD: Cross Polar Discrimination
ZFB: Zero Forcing Beamforming

List of Figures

<i>Figure 2.1 5G key performance indicators (Source: ITU-R WP5D, 2015)</i>	<i>10</i>
<i>Figure 2.2 Argos Antenna Front End [7]</i>	<i>12</i>
<i>Figure 2.3 Lund LuMaMi Antenna Front End [8]</i>	<i>13</i>
<i>Figure 2.4 Samsung Antenna Front End [9]</i>	<i>13</i>
<i>Figure 2.5 Time Division Multiplexing in MIMO Receivers [14]</i>	<i>16</i>
<i>Figure 2.6 Code Division Multiplexing [14]</i>	<i>16</i>
<i>Figure 2.7 Antenna Selection Technique [14]</i>	<i>16</i>
<i>Figure 2.8 Single RF Chain MIMO Using Low Power CMOS Switches [15]</i>	<i>18</i>
<i>Figure 2.9 Integrated Radiator for Single-RF MIMO [16]</i>	<i>18</i>
<i>Figure 2.10 Switched Parasitic Array at 2.6 GHz [17]</i>	<i>19</i>
<i>Figure 2.11 Typical hybrid beamforming transmit architecture for a full array [24] ..</i>	<i>21</i>
<i>Figure 2.12. Tilted combined beam antenna [30]</i>	<i>23</i>
<i>Figure 2.13 Turning torso antenna [31]</i>	<i>23</i>
<i>Figure 2.14 Improved XPD antenna [32]</i>	<i>24</i>
<i>Figure 2.15 Double dipole antenna at 122 GHz with return loss [33]</i>	<i>24</i>
<i>Figure 2.16 SIW antenna array [34]</i>	<i>25</i>
<i>Figure 2.17 Inkjet printed multilayer Yagi Uda antenna (a) 3 director elements (b) 5 director elements (c) microstrip to slot line transition (d) slightly bent substrate antenna [35]</i>	<i>25</i>
<i>Figure 2.18 Geometry of the aperture coupled magnetic electric dipole antenna and the fabricated prototype [36]</i>	<i>26</i>
<i>Figure 2.19 3D configuration of the Ka band CP array and fabricated prototype [37] ..</i>	<i>27</i>
<i>Figure 2.20 Planar prototype and the convex prototype of the conformal array [38] ..</i>	<i>27</i>
<i>Figure 2.21 Model and fabricated prototype of the planar aperture antenna [39]</i>	<i>27</i>
<i>Figure 2.22. SIW arrays: SIW fed slot array 0 and SIW fed chain array [41]</i>	<i>29</i>
<i>Figure 3.1 Front view of the dipole printed on the substrate</i>	<i>36</i>
<i>Figure 3.2 Back view of the dipole on the substrate</i>	<i>37</i>
<i>Figure 3.3 Variation of frequency response with dipole arm length</i>	<i>37</i>
<i>Figure 3.4 Printed reflector profile</i>	<i>38</i>
<i>Figure 3.5 Effect of the variation of ref_x on return loss frequency response</i>	<i>38</i>
<i>Figure 3.6 Effect of the variation of tx (transition width) on cross polar level for Φ_{i0} plane</i>	<i>38</i>
<i>Figure 3.7 Effect of the variation of tx (transition width) on cross polar level for Φ_{i90} plane</i>	<i>39</i>
<i>Figure 3.8 Effect of the variation of tz (transition length) on cross polar level for Φ_{i0} plane</i>	<i>39</i>
<i>Figure 3.9 Effect of the variation of tz (transition length) on cross polar level for Φ_{i90} plane</i>	<i>39</i>
<i>Figure 3.10 Surface current distribution on the reflector at phase 0°, 90° and 180° at 14 GHz</i>	<i>39</i>
<i>Figure 3.11 Rectangle shaped parasitic and the two square parasitics coupling onto the dipole.</i>	<i>40</i>
<i>Figure 3.12 A single unit cell of the arc shaped parasitic</i>	<i>42</i>
<i>Figure 3.13 Illustration depicting the way of refractive index retrieval</i>	<i>43</i>

<i>Figure 3.14 Real part of the refractive index of the unit cell parasitic arc shaped resonators from centre towards edges.....</i>	<i>43</i>
<i>Figure 3.15 Gradient depiction of the gradient variation of the refractive index</i>	<i>43</i>
<i>Figure 3.16 (a) Antenna without back plate (b) with holed back plate</i>	<i>44</i>
<i>Figure 3.17 3D Co-Polar radiation pattern of the antenna (a) Without back plate (b) With back plate</i>	<i>44</i>
<i>Figure 3.18 3D Cross-Polar radiation pattern of the antenna (a) Without back plate (b) With back plate</i>	<i>45</i>
<i>Figure 3.19 Cross polar discrimination (XPD) comparison for cases of without and with back plate.....</i>	<i>45</i>
<i>Figure 3.20 Low profile, high gain Quasi-Yagi antenna element dimensions.</i>	<i>46</i>
<i>Figure 3.21 Simulated and measured return loss behaviour of the antenna element operating from 13.5 GHz to 15 GHz for 10 dB return loss.</i>	<i>46</i>
<i>Figure 3.22 Surface current distribution at 14 GHz.</i>	<i>47</i>
<i>Figure 3.23 Comparison of simulated and measured elevation cut (a) simulation curve is without anechoic chamber backplate (b) Simulation curve is with anechoic chamber backplate.....</i>	<i>47</i>
<i>Figure 3.24 Comparison of simulated and measured azimuth cut (a) simulation curve is without anechoic chamber backplate (b) Simulation curve is with anechoic chamber backplate.....</i>	<i>48</i>
<i>Figure 3.25 Fabricated prototype with size of a square cm and the supporting structure.</i>	<i>48</i>
<i>Figure 3.26 Anechoic chamber support</i>	<i>48</i>
<i>Figure 3.27 Simulated and measured gain plot vs frequency</i>	<i>49</i>
<i>Figure 3.28 (a). Front view (b). Back view</i>	<i>50</i>
<i>Figure 3.29 Vector surface currents at 14 GHz.....</i>	<i>50</i>
<i>Figure 3.30 Surface currents at 14 GHz</i>	<i>50</i>
<i>Figure 3.31 Radiation pattern plot at Phi 0 and Phi 90 plane.....</i>	<i>51</i>
<i>Figure 4.1 Building block of the multi-beam scheme</i>	<i>55</i>
<i>Figure 4.2 Inter element spacing dependent phasing-enforced, beam pointing for two element array.</i>	<i>56</i>
<i>Figure 4.3 Simulation model of the 4x4 array with supporting structure.</i>	<i>57</i>
<i>Figure 4.4 Simulated return loss (S_{nn}) of the 4x4 array antenna.</i>	<i>57</i>
<i>Figure 4.5 Port to port isolation with respect to port 1.</i>	<i>58</i>
<i>Figure 4.6 Simulated radiation efficiency over the 16 ports.</i>	<i>58</i>
<i>Figure 4.7 Line impedance distribution along the $0^\circ/180^\circ$ phasing network.</i>	<i>59</i>
<i>Figure 4.8 (a) Top view of the all 0° phase network (b) Top view of the 0° and 180° phase network (c) Back view of the 0° and 180° phase network.</i>	<i>60</i>
<i>Figure 4.9 Phase response of the dual phasing network of 0° and 180°.</i>	<i>61</i>
<i>Figure 4.10 180°-degree hybrid-based phasing network</i>	<i>61</i>
<i>Figure 4.11 Fabricated 4x4 array (a) Front view (b) Back view.</i>	<i>65</i>
<i>Figure 4.12 Measured S parameters compared with active S parameter with respect to port 6.</i>	<i>66</i>
<i>Figure 4.13 Measured Mutual coupling between ports 1 and 5 which is shown to represent the worst case.</i>	<i>67</i>

Figure 4.14 Measured Mutual coupling between ports 6 and 11 which is shown to represent the best case.....	67
Figure 4.15. Fabricated phasing network (a) Equal phase (b) $0^\circ/180^\circ$ phase	68
Figure 4.16 Simulated (a) Frequency response of the magnitude of S_{ij} of the 0° phasing network (b) Phase of S_{ij} of the 0° phasing network (c) Frequency response of the magnitude of S_{ij} of the $0^\circ/180^\circ$ phasing network (d) Phase for the $0^\circ/180^\circ$ phasing network	69
Figure 4.17 Fabricated antenna array with phasing network.	70
Figure 4.18 Pattern measurement of the 4x4 antenna array in anechoic chamber.	71
Figure 4.19 Simulated vs measured pattern state A.	72
Figure 4.20 Measured gain vs frequency pattern state A.....	72
Figure 4.21 Simulated vs measured pattern state B.	73
Figure 4.22 Measured gain vs frequency pattern state B.....	73
Figure 4.23 Simulated vs measured pattern state C.....	74
Figure 4.24 Measured gain vs frequency pattern state C.	74
Figure 4.25 Simulated vs measured pattern state D.	75
Figure 4.26 Measured gain vs frequency pattern state D.	75
Figure 4.27 Simulated vs measured pattern state E.....	76
Figure 4.28 Measured gain vs frequency pattern state E.....	76
 Figure 5.1 Technologies to realize Single/few/reduced-RF MIMO	79
Figure 5.2 Indoor twin beam antenna for non-boresight multi-user azimuthal coverage	80
Figure 5.3 Illustration of ESPAR antenna with 7 elements on an infinite ground plane.....	82
Figure 5.4 Seven element ESPAR antenna equipped with adaptive beamforming algorithm [8]	83
Figure 5.5 The ESPAR setup depicted for mobile computing application [9].....	83
Figure 5.6 The beam-switched planar parasitic antenna array [10]	84
Figure 5.7 Classical MIMO	85
Figure 5.8 Beamspace MIMO [12]	86
Figure 5.9 Switched parasitic antenna array [12].....	86
Figure 5.10 Switched parasitic antenna array and the control circuitry setup [13]	87
Figure 5. 11 Planar printed three element SPA for mobile applications [1].....	87
Figure 5. 12 Transmit MIMO techniques [14].....	88
Figure 5.13 Spatial modulation three-dimensional encoding 3D constellation [14]	89
Figure 5.14 Reconfigurable antenna geometry.....	90
Figure 5.15 Antenna pairs for the orientation of the sequential rotational far field	91
Figure 5.16 Antenna array excitation matrices (Amp: Amplitude; Ph: Phase; 0: Port not excited)	92
Figure 5.17 Rotational pattern beams.....	93
Figure 5.18 9x9 array with single RF MIMO scheme built on 3x3 subarray.....	95
Figure 5.19 Fabricated antenna array.....	96
Figure 5.20 Excitation matrices of the five states	96
Figure 5.21 Pictorial depiction of the attainable rotate beam patterns.....	97
Figure 5.22 Antenna measurement setup in anechoic chamber.....	98
Figure 5.23 Rotate 1 pattern	99

<i>Figure 5.24 Measured Gain vs frequency for rotate 1</i>	99
<i>Figure 5.25 Rotate 2 pattern</i>	100
<i>Figure 5.26 Measured Gain vs frequency for rotate 2</i>	100
<i>Figure 5.27 Rotate 3 pattern</i>	101
<i>Figure 5.28 Measured Gain vs frequency for rotate 3</i>	101
<i>Figure 5.29 Rotate 4 pattern</i>	102
<i>Figure 5.30 Measured Gain vs frequency for rotate 4</i>	102
<i>Figure 5.31 Rotate 5 pattern</i>	103
<i>Figure 5.32 Measured Gain vs frequency for rotate 5</i>	103
<i>Figure 6. 1 Transversal section of the waveguide lens antenna</i>	110
<i>Figure 6.2 Depiction of the wavefront transformation</i>	111
<i>Figure 6.3 Cylindrical phase distribution without the ridge lens at 28 GHz</i>	112
<i>Figure 6.4 Cylindrical to planar phase distribution due to the ridge lens at 28 GHz</i> .	113
<i>Figure 6.5 Comparison of the obtained pattern directionality and beamwidth for the case</i>	113
<i>Figure 6.6 Phase distribution along the central YZ plane at 28 GHz</i>	114
<i>Figure 6.7 (a) Initial design with sharp corners on the lens and (b) final design with chamfered corners showing the phase distribution on the central plane when port 1 is excited at 28 GHz</i>	115
<i>Figure 6.8 (a) Initial design with sharp corners on the lens and (b) final design with chamfered corners showing the phase distribution on the central plane when port 2 is excited at 28 GHz</i> .	116
<i>Figure 6.9 (a) Initial design with sharp corners on the lens and (b) final design with chamfered corners showing the phase distribution on the central plane when port 3 is excited at 28 GHz</i> .	117
<i>Figure 6.10 3D perspective view of the dual band multi-beam antenna</i>	118
<i>Figure 6.11 Top exploded view of the antenna</i>	121
<i>Figure 6.12 Bottom exploded view of the antenna</i>	122
<i>Figure 6.13 Model of the assembled antenna</i>	122
<i>Figure 6.14 WR28 to custom horn aperture transitions for the three ports</i>	123
<i>Figure 6.15 (a) Front view of the fabricated prototype (b) Side view of the fabricated prototype (c)Top view of the millimeter wave antenna prototype</i>	124
<i>Figure 6.16 Simulated vs measured return loss at port 1</i>	125
<i>Figure 6.17 Simulated vs measured return loss at port 2</i>	125
<i>Figure 6.18 Simulated vs measured return loss at port 3</i>	126
<i>Figure 6.19 Port-to-Port isolation</i>	126
<i>Figure 6.20 Normalized directivity pattern vs frequency around 28 GHz for Phi0 plane at port1</i>	127
<i>Figure 6.21 Normalized directivity pattern vs frequency around 28 GHz for Phi0 plane at port2</i>	127
<i>Figure 6.22 Normalized directivity pattern vs frequency around 28 GHz for Phi0 plane at port3</i>	128
<i>Figure 6.23 Normalized directivity pattern vs frequency around 28 GHz for Phi90 plane at port1</i>	128

<i>Figure 6.24 Normalized directivity pattern vs frequency around 28 GHz for $\theta=+63^\circ$ plane at port2</i>	<i>129</i>
<i>Figure 6.25 Normalized directivity pattern vs frequency around 28 GHz for $\theta=-63^\circ$ plane at port3</i>	<i>129</i>
<i>Figure 6.26 Normalized directivity pattern vs frequency around 31 GHz for Φ_0 plane at port1</i>	<i>130</i>
<i>Figure 6.27 Normalized directivity pattern vs frequency around 31 GHz for Φ_0 plane at port2</i>	<i>130</i>
<i>Figure 6.28 Normalized directivity pattern vs frequency around 31 GHz for Φ_0 plane at port3</i>	<i>131</i>
<i>Figure 6.29 Normalized directivity pattern vs frequency around 31 GHz for Φ_{90} plane at port1</i>	<i>131</i>
<i>Figure 6.30 Normalized directivity pattern vs frequency around 31 GHz for $\theta=+63^\circ$ plane at port2</i>	<i>132</i>
<i>Figure 6.31 Normalized directivity pattern vs frequency around 31 GHz for $\theta=-63^\circ$ plane at port3</i>	<i>132</i>
<i>Figure 6.32 Antenna measurement setup in the anechoic chamber.....</i>	<i>134</i>
<i>Figure 6.33 Simulated vs measured pattern at port 1 for 28 GHz.....</i>	<i>135</i>
<i>Figure 6.34 Simulated vs measured pattern at port 2 for 28 GHz.....</i>	<i>135</i>
<i>Figure 6.35 Simulated vs measured pattern at port 3 for 28 GHz.....</i>	<i>135</i>
<i>Figure 6.36 Simulated vs measured pattern at port 1 for 31 GHz.....</i>	<i>136</i>
<i>Figure 6.37 Simulated vs measured pattern at port 2 for 31 GHz.....</i>	<i>136</i>
<i>Figure 6.38 Simulated vs measured pattern at port 3 for 31 GHz.....</i>	<i>136</i>
<i>Figure 6.39 Measured Gain and XPD vs frequency at port 1.....</i>	<i>137</i>
<i>Figure 6.40 Measured Gain and XPD vs frequency at port 2.....</i>	<i>137</i>
<i>Figure 6.41 Measured Gain and XPD vs frequency at port 3.....</i>	<i>137</i>

List of Tables

<i>Table 1.1 Comparison of antenna features before 5G and in 5G.</i>	<i>3</i>
<i>Table 2.1 Comparison of Massive MIMO Setups.....</i>	<i>14</i>
<i>Table 2.2 Comparison of different antenna types based on gain, polarization and bandwidth</i>	<i>28</i>
<i>Table 4.1 Demonstration of the two-phase vector alignment Beamswitching scheme. .</i>	<i>63</i>
<i>Table 4.2 Pattern steering excitation. $K = \text{amp1}$, phase 0; $-K = \text{amp1}$, phase 180; '0' implies no port excitation</i>	<i>64</i>
<i>Table 4.3 Measured mutual coupling between ports of the antenna array at 14 GHz. .</i>	<i>66</i>
<i>Table 5.1 Phasing scheme of the 3x3 antenna</i>	<i>91</i>
<i>Table 6.1 Simulated vs measured beam gains at the three ports over the dual band ..</i>	<i>134</i>

Chapter 1

Introduction

The increased contemporary interest in Telecommunications and advanced Telecommunication equipment in the recent years is evident in the widespread proliferation of mobile devices made live, operational and interactive by the ubiquitous internet. The 2017 CISCO Visual Networking Index (VNI) [1] makes a forecast of the upcoming requirements up to 2021 in terms of the amount of the data to be handled. To set the stage on the requirements, in terms of cellular traffic at the time of writing of the thesis, a brief description of the present and forecasted traffic is as follows: Since there has been a gradual transition to more of visual information exchange, globally, Internet Protocol (IP) video traffic has increased by 73 percent since 2016 and it will be 82 percent of all consumer Internet traffic by 2021. Virtual reality and augmented reality traffic is expected to increase 20-fold between 2016 and 2021. Live internet video will grow 15-fold from 2016 to 2021. With respect to mobile data traffic, globally there will be an increase of sevenfold between 2016 and 2021. Global mobile data traffic will grow twice as fast as fixed IP traffic from 2016 to 2021, which implies - mobility and reconfigurability will be a key consideration in these networks. Most importantly, in 2016, wired devices accounted for the majority of IP traffic at 51 percent, but by 2021, wired devices will account for only 37 percent of IP traffic, while Wi-Fi and mobile devices will account for 63 percent of IP traffic. This clearly highlights the gradual transition to Over-the-Air (OTA) devices and communications soon, that offer the luxury of mobility and comfort while using the internet.

1.1 Evolution of the G networks

With the above scenario of the current requirements and forecast on the traffic, it is worthwhile to have a brief digression to the evolution of the generation of the ‘G’ mobile networks with a focus on the corresponding antenna interfaces for 1G, 2G, 3G, 4G before presenting 5G in detail.

1G: Though the first successful demonstration of wireless link was made in 1897 by Guglielmo Marconi, it was not until the 1980s that a widespread mobile wireless telephone network was deployed. The first generation of wireless telephone technology was original, voice only-1G introduced back in 1981 by Nordic Mobile Telephony (NMT) primarily in the Nordic countries. Another standard namely the Advanced Mobile Phone System (AMPS) was an analog mobile phone system developed by Bell Labs and was originally introduced in 1983 in North America. AMPS cellular service operated in the 850 MHz cellular band. Wireless phones were used for voice only. The base station antenna tower covered a cell radius of 2-20 Km with the required cell site transmitter power at 100W. The mobile side receiver handled power around 3 W. For voice, Frequency Modulation (FM) was used and for control signalling, Frequency Shift Keying (FSK) was used. The total achievable bit rate was 10 kbps. The other first-generation systems were the Total Access Communication System (TACS) in UK, Nippon Telegraph and Telephone (NTT) in Japan, NMT450 and NMT900 in Nordic countries and C450 in Germany. With all these initial merits, the 1G system had drawbacks pertaining to poor battery, large power consumption, poor voice quality, large devices with little or no portability, no security

and frequent call drops- which of course, largely inspired and drove the development towards 2G systems. The antenna technology used at the cell tower (current base station eNodeB) were mainly omnidirectional and vertically polarized. The receiver end employed thin-rod based extendable monopole antennas.

2G: The second generation began in 1991 in Finland with the introduction of digital radio signals for voice transmission as opposed to the analog in the 1G, which was the primary difference between 1G and 2G. This shift to digital was based on the European Global System for Mobile Communications (GSM). The other difference from 1G was that the 2G system supported data in terms of SMS text, pictures and multimedia messages (MMS). The speed offered by General Packet Radio Service (GPRS) in 2G is a theoretical maximum transfer speed of 50 Kbit/s (40 Kbit/s in practice) and with (Enhanced Data Rates for GSM Evolution) EDGE, there is a theoretical maximum transfer speed of 1 Mbit/s (500 Kbit/s in practice). 2G is operational in most countries presently although majority have planned to decommission it by 2020. The antenna technologies used in 2G bases stations employ dual polarization MIMO with remote electrical down tilt, and in some cases dual band capacity improvement. The operational frequencies are generally over a quad band 850/900/1900/2100 MHz at the base station and the receiver antenna in the phone receiver generally employs 1x2 MIMO diversity with moderate omni-directional pattern gains for the antennas. Despite these advantages and improvements, the speed and fast handling, data intensive applications such as video were among the few drawbacks seen in 2G. This led to the next generation of 3G.

3G: The third generation was introduced in 2000 with the primary difference with 2G being the speed. The speed was increased from 500 Kbps to 2 Mbps. The latest HSPA+ can provide downlink speeds of up to 168 Mbps and an uplink speed of 22 Mbps. This heralded the era of Smart phones and low buffering, fast communications, video, 3D and Online Multi-user Role-Playing Games (RPGs) with moderate latency, live TV streaming became possible. The Universal Mobile Telecommunication Systems (UMTS) and Code Division Multiple Access (CDMA2000) are considered the major standards of 3G. The frequencies used in 3G involve multiple bands (usually three) between 1.8 GHz to 2.2 GHz. At the base station side, the antenna technology upgraded to integrated active antennas and an increase the number of antenna elements with either/all of the horizontal/vertical/slant polarization. The receiver/mobile antenna design improved and focused on providing smaller form factor, better device integration, including the chassis and hand effects in the design and taking into consideration the Electromagnetic Interference/ Electromagnetic Compatibility (EMI/EMC) effects.

4G: Long term evolution (LTE) is commonly referred to as Advanced 4G or 4G LTE. The first LTE deployment was made in Oslo and Stockholm in 2009. 4G marked the complete migration to packet switched networks from circuit switched networks. These packets switched networks provide gigabits access. LTE or 4G antennas operate over the band 700-900 MHz band and/or 1700-2800 MHz band either in multiband/wideband configurations. Recently the focus is shifting towards narrow beam antennas at the base station that helps in sectorization with minimal inter cell interference. Other LTE base station antennas include phased arrays, beam-switched antenna and adaptive beamforming antennas. At the receiver side 2x2 and 1x4 MIMO antennas are being used to employ pattern diversity as in IEEE 802.11n. IP telephony, mobile web access, High definition mobile TV and video conferencing are some of the features 4G focuses on delivering. With such features provided by 4G, the distinction with 5G is in the marked increase of Quality of Service (QoS) offered by 5G in terms of the dimensions of data

speed, latency, spectral efficiency and energy efficiency. Therefore, there is a shift towards 5G. 5G being deployed with early test-bed trials recently, a coexistence between 4G and 5G is seen now.

1.2 Need for 5G antennas

The design of air interfaces is predominantly dependent on the antenna design. 5G, owing to the stringent requirements, as detailed in the discussed traffic predictions of CISCO in the beginning of the chapter, requires largely a complete re-architecting of the devices to be deployed (barring the cases where a non-standalone deployment is made on existing 4G architectures). Therefore, this necessitates the design, conceptualization and validation of next generation antennas that exhibit features mostly non-existent in the previous generations. Moreover, the antennas need to simultaneously cater to the needs set by the upcoming transceiver technologies in 5G like the Massive MIMO, Single/Few RF/Reduced RF MIMO or the weathered but timely millimeter wave. The design of antennas to each of these technologies varies from their predecessor technologies (1G-4G) mainly over 10 different dimensions – to the best of author's knowledge. This is highlighted in the Table 1.1 below as a comparison with previous 1G - 4G antenna designs.

Base station Antenna Feature	4G and before	5G
Frequency of operation	0.8, 0.9, 1.8, 2.1 and 2.6 GHz and wideband 1.7-2.7 GHz	TV Whitespace, 3.5 GHz, > 10 GHz wideband
Beam pattern	Sectoral and omni-directional	Highly Directional
Number of beams	Single or Dual	Multiple beam desired
Reconfigurability	Generally, no reconfigurability	Integral part
Type of Cell deployment	Macro cells	Small, Pico, Femto cell
Gain of antennas	Moderate gain (10-12 dBi)	High gain exceeding 20 dBi
Form factor	Generally large	Small for millimeter wave
Power handling capability	Moderate	High (Massive MIMO)
Scanning plane	Generally, Azimuth scan	Azimuth and elevation scan
Tilt plane	Elevation tilt	Becomes largely redundant

Table 1.1 Comparison of antenna features before 5G and in 5G.

1.3 Requirements on 5G antennas

With these features of 5G antennas introduced, it follows to understand the requirements set by the standardization bodies ETSI and 3GPP on the 5G antennas. The requirements have two dimensions: One for the base station antenna technology and the other for the receiver/mobile.

1.3.1 Base station beam patterns: Referring to the recent [2] , though traditional single beam antennas may have clear definitions of features such as Front to Back(F/B) ratio and Side lobe Level (SLL) , in case of Active Antenna Systems (AAS) or Simultaneous Multibeam systems it is not possible to distinguish between wanted and unwanted radiations as the AAS involves continuous reconfiguration of pattern which in-turn depends on features such as beamforming algorithm used, tapering applied among a few things. Nevertheless, a declaration has been made to assess Base Station (BS) based on the in-cell and out-of-cell radiation characteristics. More details can be found in Section 9.9 of [2].

1.3.2 Receiver beam patterns: Referring to [3], the Customer premises equipment (CPE) antenna element should have a gain of 5 dBi, 90° HPBW in Azimuth and elevation and a $\lambda/2$ inter-element spacing. An additional 3dBi gain is added for two polarization directions.

1.3.3 Beamswitching time: It is necessary that the Base station steer the beam in time so that there is no detrimental impact on the Downlink (DL). To attain this, section 9.10 of [2] requires the switching time to be at least less than the cyclic prefix (CP) length. The CP length decreases with increase in Sub-Carrier Spacing (SCS) of Orthogonal Frequency Division Multiplexing (OFDM).

1.4 Problem description and challenges towards the realization

In the above Table 1.1, the entries, under the 5G antenna features simultaneously highlight the problems and challenges in realizing these features. For example, the necessity to cast multiple simultaneous beams brings with it challenges associated with maintaining uniform directivity over all the beams, maintaining required XPD over multiple beams, projecting onto pre-defined angles, the switching speed - to name a few. In the same way, as discussed in detail in the chapters of the thesis, the other features also exhibit challenges of the same or higher nature towards their realization.

The problem mainly addressed in the thesis is the design of antennas for the three 5G technologies namely Massive MIMO, Single RF MIMO and Millimeter wave. Each of these technologies has its own merits in bringing 5G to fruition.

Massive MIMO proposes to have massive number of multiple antennas to achieve better throughput and spectral efficiency. This implies the need for a custom-made antenna design that can cast multiple beams to multiple users thereby enhancing spectral efficiency and per user throughput.

The Single RF MIMO technology proposes to reduce the amount of RF power fed into the antenna by reducing the number of RF chains. This requirement necessitates the design of antenna system that can provide multi-antenna, multi-beam functionality but with reduced or Single RF chains. One of the Single RF MIMO technologies namely Spatial modulation, requires the use of antenna-index based pattern reconfigurable antenna system. To obtain pattern reconfigurability over the same phase center is a striking challenge and it can be used for transmission over time schemes (TDD).

The Millimeter wave antenna needs the design of an antenna with a high directivity to combat the high path loss at Millimeter Wave frequencies (> 10 GHz). So, one of the main problem addressed is to introduce a technique into the millimeter wave antenna that can enhance its

directivity. Also, Millimeter wave propagation can benefit from the use of multiple beams and the rich scattering environment information that arises from use of multiple beams. Therefore, the problems mainly addressed in millimeter wave antenna design were attaining high directivity and directional multiple beams.

1.5 Outline of the chapters

The thesis is organized into seven chapters, the first chapter introduces and sets the stage, discusses the need and requirements for 5G antennas along-with the problem description and challenges towards the realization. Chapter 2 addresses the 5G requirements in more detail and presents a detailed survey of the state-of-the-art. Chapter 3 presents the concept, design and experimental validation of the quasi-optic endfire antenna element. Chapter 4 presents a novel two vector beamswitching scheme applied on the designed and fabricated 4x4 Massive MIMO sub-array. The experimental validation of the array is also presented in the chapter. Chapter 5 presents a reconfigurable Single RF MIMO antenna array for use in Spatial modulation along with the experimental validation of the concept. Chapter 6 presents a Millimeter wave multibeam antenna using waveguide lens for dual band operation centered at 28 GHz and 31 GHz with a bandwidth of 1 GHz each. A prototype has been built and the concept has been experimentally validated. Chapter 7 concludes, highlighting the implications of the work carried out and the potential future extensions.

1.6 List of original contributions

Chapter 2:

A broad exhaustive, unique survey of the previous and existing works related to Massive MIMO, Single RF MIMO and Millimeter Wave is performed. The ideas in chapter 3, 4, 5 and 6 are based and built upon this exhaustive survey platform developed.

Chapter 3:

A novel quasi-optic based antenna element operational at 14 GHz is developed. A unique gradient refractive index-based location of the parasitics is proposed to enhance directivity.

Chapter 4:

- ❖ A novel two vector state beamswitching scheme is proposed.
- ❖ A methodology to achieve multibeam operation using a uniquely defined basic building block is presented giving scope for the easy adaption of the proposed theory to different multibeam scenarios.
- ❖ A 14 GHz 4x4 antenna array was designed, fabricated and experimentally validated.

Chapter 5:

- ❖ A new first-of-its-kind pattern reconfigurable antenna at 14 GHz was developed, for use in modulation schemes such as spatial modulation that harness antenna index information.
- ❖ A method to extend the 4x4 subarray index as additional implicit information when used in larger arrays was proposed. This is only made possible because of the unique reconfiguring scheme proposed in Chapter 5.

Introduction

- ❖ The proposed pattern switching scheme has been experimentally validated.

Chapter 6:

- ❖ A new all-metal Multi-Beam Millimeter Wave antenna with ridge-based lens built over a parallel plate waveguide is proposed. The main contribution over the already existing literature in this area is the proposition of a methodology towards designing the lens using selective, informed full wave simulations by phase extraction and compensation - that reduces the design time.
- ❖ The prototype has been experimentally validated at 28 GHz and 31 GHz considering the challenges associated with multi-beam measurements at these frequencies.

1.7 References

- [1] 2017 CISCO Visual Networking Index (VNI), Document ID:1465272001663118. [Weblink](#)
- [2] 3GPP Specification series, “General aspects for Base Station (BS) Radio Frequency (RF) for NR.” [Weblink](#)
- [3] 3GPP Specification series, “General aspects for User Equipment (UE) Radio Frequency (RF) for NR.” [Weblink](#)

Chapter 2

5G requirements and State-of-Art

2.1 Introduction

Over the recent years there has been an increasing demand for cellular traffic in terms of not only voice but also high definition data that is to be served with little redundancy. The present 4G and LTE based networks require re-architecting of current cellular principles to make 5G a reality. According to the 5G public private partnership (5GPPP) recently formed by the EU, 5G networks need to provide 1000 times higher capacity with a close to 90% reduction in energy consumption.

There has been focus on achieving high data rates through advanced cellular technologies. An array of key parameters has been identified and these parameters are being used to guide the path forward. These parameters include but are not limited to peak data rate, cell edge data rate, cell spectral efficiency, mobility, cost efficiency, simultaneous connections and latency with the focus on Spectral and Energy efficiency. Figure 2.1 depicts this requirement in comparison to currently offered services in terms of eight performance metrics often referred to as key performance indicators (KPIs). The peak data rate is targeted at 20 Gbps from the current 1 Gbps. The spectral efficiency is aimed to be tripled, with mobility catering to velocity of 500 km/h from the currently supported 350 km/h. The latency of the system will be targeted at 1ms from the current 10ms. As can be seen several folds of increase on each of the performance metrics is expected. Along the way to attain these metrics 5G technologies should focus on attaining higher sum capacity i.e support multiple users in the same cell. This can be attained by having a larger bandwidth, more number of channels (Massive MIMO, Cooperative Massive MIMO), better power efficiency, minimized interference, improved spectral and energy efficiencies. Incorporating pico and femto cells, densifying the cells by ultra-dense cellular networks are ways to increase substantially the spectral efficiency and the sum capacity of the cellular network.

Current cellular networks, based on the postulate that transmission technologies rely on a small number of all-active antenna elements, are at the point of failure in delivering the requested spectral efficiency and energy efficiency. Under this postulate the spectral efficiency increase is only marginal. Also, since most of these antennas are active, the marginal spectral efficiency gain is decreased further owing to increase of total internal power dissipation which in turn is proportional to the number of active antenna elements. Thus, this postulate cannot be used to guide the design of 5G. Therefore, to overcome this drawback a recently proposed transmission technology namely the Large Scale Massive Multiple Input Multiple Output (MIMO) made of hundreds of low power antenna elements is one among the three technologies focused upon in the thesis. The other two being Single RF MIMO and millimeter wave communication. Single RF MIMO technology focuses on having antenna architectures that reduce the number of RF chains that are fed into the array thereby minimizing the power consumption. Millimeter wave technology opens a complete wideband of spectrum in the millimeter wave frequencies that

enhances the bandwidth that can be tapped to largely enhance the amount of achievable data rate.

One technological challenge in this respect is to make efficient use of space while retaining enhanced transmission by deploying custom made 3D large scale antenna arrays. A review of the current state in the Massive MIMO reveals, that the very few experimental results available on Massive MIMO's performance are based on virtual single or bi-dimensional large-scale antennas. To pack hundreds of antennas in small space, custom made 3D antenna designs would be required. In this context, the capability to have multi directional selective, simultaneous beam steering is necessary. Therefore, the major motivation was to have 3D large scale antenna-arrays designed and manufactured whose conceptual and experimental validation is discussed in the thesis.

Attention is also paid along this Thesis to the other two antenna technologies namely the single RF MIMO and the millimeter wave that are being considered at this moment on the 5G arena.

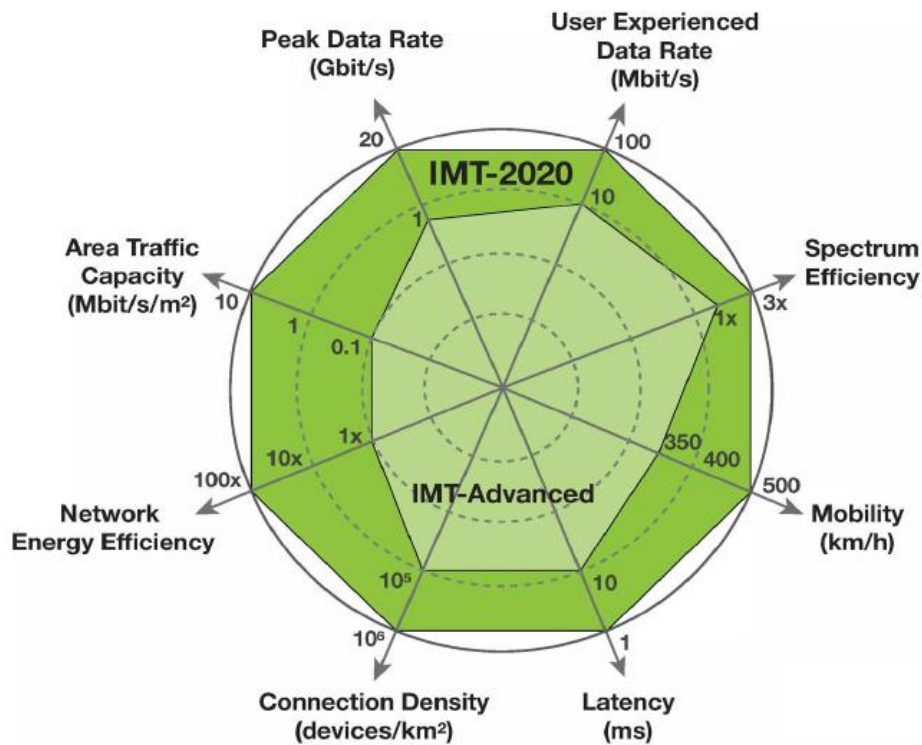


Figure 2.1 5G key performance indicators (Source: ITU-R WP5D, 2015)

2.2 Massive MIMO

The Massive MIMO system equipped with multiple antenna technology is one of the most promising technologies to achieve these performance metrics. It primarily focuses on improving the spectral efficiency by use of a large number of antennas. To meet the exploding cellular traffic requirements, the solution is to have large scale MIMO to increase data throughput and range while transmitting with no additional power and bandwidth. The control parameters like bandwidth efficiency (BE), spectral efficiency (SE) and energy efficiency (EE) majorly guide the design of the system. Certain phenomenon like pilot contamination majorly

constrain the performance due to pilot reuse in multicell, however the use of excessive degrees of freedom offered by large scale MIMO (LS MIMO) is an added advantage. The Massive MIMO antenna system requires several antennas operating in tandem in an array equipped with beamforming and null steering. The traditional antenna array has the down tilt fixed and have beam control in the horizontal direction and almost no control over the beam in the vertical direction. An approach to this problem is to have 3D antenna arrays like rectangular, spherical and cylindrical configurations that can provide both horizontal and vertical beam control. When the antennas are arranged in an array, other factors like the mutual coupling between the antenna elements, array blinding effects, correlation and cross polarization when deployed as an antenna array are to be considered. Since these factors are majorly interdependent the solution reached is often a trade-off between several factors. A few of the most important key aspects of Massive MIMO are discussed next.

2.2.1 Key Aspects of Massive-MIMO

Interference: The inherent presence of interference in communication systems has always been a key factor in deciding the performance and design of these systems. To have a power efficient and low complexity design, [1] propose an interference driven antenna selection scheme that selects a subset of antennas that operate on the principle of constructively selecting those antenna elements that add up in phase and thus maximize the constructive interference in the used PSK modulation scheme. They also present a closed form expression that captures the power benefits of the scheme.

Spatial Modulation: In [2], the concept of spatial modulation, which involves obtaining the same data rates as open loop MIMO for MIMO with selected antenna subsets is discussed. It is possible to obtain the same data rate, as the information in spatial modulation is transmitted on the antenna index as well. [2] also derives an upper bound for the capacity of spatial modulation.

Energy and Spectral Efficiency: The energy and spectral efficiency of a Massive MIMO are key considerations to gauge its performance in each scenario. In [3], a performance analysis is done on the impact of increased number of antennas in a fixed physical space on the energy efficiency. It has been found that the energy efficiency does not increase monotonically with increased number of antennas. The closely packed antennas increase the mutual coupling which in turn decreases the energy efficiency.

Number of antennas: The influence of number of antennas on the energy efficiency brings naturally the next question- how many antennas do we need in massive MIMO? [4] and [5] address this question. [4] considers multi cell massive MIMO and proposes that having the same number of antennas in the base stations of a multi cell has no loss in energy efficiency due to the flatness of the energy function. [5] derives how many antennas are needed per user terminal to achieve the percentage performance.

Area Spectral and Energy Efficiency: The calculations of area spectral efficiency and area energy efficiency devised in [6] provide a way to obtain the number of antennas, number of users and the number of symbols over which the channel remains same.

2.2.2 Massive MIMO demonstrators

Recently a few antenna array configurations to operate as massive MIMO have been devised. Mainly Argos [7], NI/Lund [8] and Samsung [9] have proposed massive MIMO arrays. A

comparison of these massive MIMO designs with their features, description, advantages and possible improvements is discussed next and a table is provided for a comparison.

Argos

To realize massive MIMO, large number of antennas are deployed at the base station. However, this increase in number of antennas implies that the baseband processing block, the channel estimation, transmission synchronization and channel calibration need to be scaled up too which can be challenging. To address this ARGOS employs Multi-user beamforming (MUBF). It demonstrates a platform with 64 antennas and Zero forcing beamforming (ZFB) and conjugate beamforming, latter is computationally less intensive and therefore achieves a lower spectral capacity compared to ZFB. In Argos, to realize MUBF linear precoding was used as other methods were seen to be practically infeasible [7]. In effect MUBF improves spectral capacity by spatial multiplexing, achieves cost effective and energy efficient solution by using substantial number of antennas to achieve a large directional gain and allows battery constrained terminals to use low power and still have high spectral capacity. It was found by experimental studies that MUBF can scale up with number of antennas aided by the new methods of calculating beamforming weights and channel estimation. The Argos antenna front end is shown in Figure 2.2.



Figure 2.2 Argos Antenna Front End [7]

Lund LuMaMi

With regards to antenna design, the LuMaMi [8] consists of a T shaped array made of $\lambda/2$ dual polarized shorted patch elements. The feed placement and element size vary from the center of the array to the edges to compensate for the array effects that influence individual elements differently. Apart from the high throughput baseband processing and low latency architecture, the LuMaMi provides flexibility of extension of number of antennas, the antenna front end is shown in Figure 2.3.



Figure 2.3 Lund LuMaMi Antenna Front End [8]

Samsung

Pertaining to achieving 5G requirements using mmWave communication, in [9] the authors show that the key parameters to characterize propagation characteristics like the path loss exponent can be made comparable to the cellular band if the Tx and Rx antennas are used to produce high beamforming gains. Appropriate beamforming is necessary to overcome the unfavorable path loss, and this can be performed either in a Digital or Analogue way. Both have their individual pros and cons - digital has a better performance at increased complexity and cost while analogue is simple but generally less flexible. In [9] the authors propose a hybrid digital analogue beamforming to retain both the pros leading to high beamforming gains. An 8x4 uniform planar array was used with sub arraying to reduce hardware complexity as shown in Figure 2.4. Lately the research focus has mainly been on achieving high data rates even in high mobility scenarios.

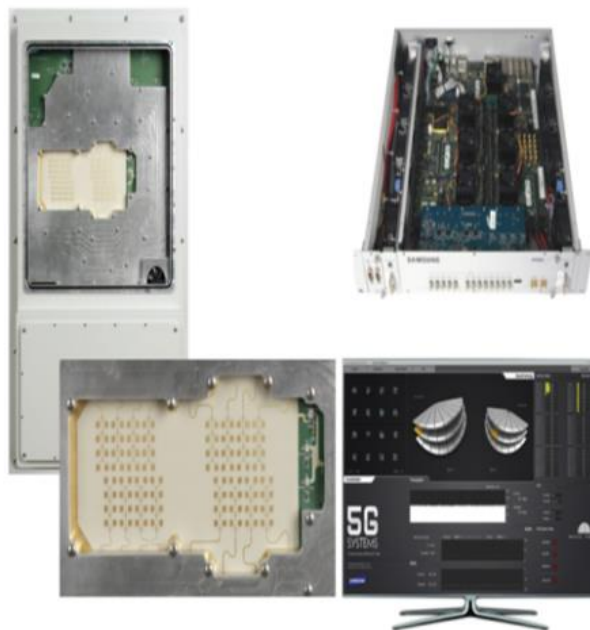


Figure 2.4 Samsung Antenna Front End [9]

It can be clearly seen from the above three massive MIMO architectures that they focus on beamforming to achieve high gains and use arrays with sub arrays or customized elements towards the edges to alleviate array effects. Hybrid analogue and digital beamforming is seen to be the way forward. The table below gives a quick comparison of these massive MIMO antennas:

Group	Band	Hardware	N° of Base Station Antennas
Lund/NI	2.6 GHz	RUSK Channel Sounder	128 (Cylindrical)
Argos	2.4 GHz	WARP	64 (Planar)
Samsung	1-28 GHz	-	64(Planar)

Table 2.1 Comparison of Massive MIMO Setups

2.2.3 Other multibeam antenna designs

Other related multibeam antenna designs proposals that can be used for Massive MIMO are presented on this section. A comparison with the proposed 4x4 antenna array is discussed in detail in chapter 4.

For example, paper [10], presents a way to attain multi-beam radiation using a 3x3 antenna array of probe fed patch antennas. The probe fed patch antennas are coupled to each other using four microstrip lines that act as substitute for feeding network. Up to nine beams can be obtained with a gain of 9 dBi to 10.4 dBi. The scanning range in the vertical direction is $\pm 24^\circ$ and in the horizontal it is $\pm 45^\circ$. The antenna array operates around 12 GHz. In contrast to the above paper, which uses beam steering without a feeding network, the proposed antenna array in the thesis uses a beamswitching scheme with a two-vector state phase feeding network. Multiple simultaneous beams of up to four at a time can be obtained using the proposed feeding scheme.

On the other hand, [11] introduces a way to beam-switch along the azimuthal plane along 360° without the use of conventional butler matrices, phase feeding networks, or ESPAR based strategies. The concept introduced in the paper revolves around Quasi-lumped couplers (QLCs) which are a pair of parallel transmission lines separated by two tunable varactors giving rise to a four-port network. The ratio of the power between the input port and the output port of each QLC can be controlled by varying the capacitance of the varactor. A circular cascaded network of the QLCs are used to attain both a round-robin way to circulate power to attain operations in both single and multi-mode. The output port of each of these QLCs are connected to a Yagi antenna. The power that is fed to the Yagi antennas can be cycled through the network in a multi-beam mode, which requires the use of a rat race coupler to act as the power recycling unit. However, to switch between multiple elements along the circle would mean the design of multiple, multi layered reconfigurable rat race couplers which is a limitation of this proposal. The operating range of the antenna is decided by the QLC configuration and in the proposed design it is set at 1 GHz. The scalability of the design to higher frequencies would necessitate the consideration of appropriate substrate material considerations and tangent losses, which in turn would limit the efficiencies. In comparison to the above paper, the proposed beamswitching scheme in the thesis operates in the radiating half-plane rather than in the azimuth 360° plane. It also operates at a frequency of 14 GHz as compared to 1 GHz in the QLC design and will not need multi-layered rat race couplers for multi-mode beam switching operation.

The impact of mutual coupling and edge effects on the gain variation along large arrays is investigated in [12] where two arrays made of dipoles and patch elements are compared. It is proposed that due to the omni-directional pattern of the dipoles the gain variation is more due to the increased mutual coupling between the elements and an increased observed deviation is seen in the embedded element gain. On the contrary in the directional patch elements the coupling is much lower. The arrays are composed of 32 elements each and their performance is evaluated for edge effects in a finite configuration. In comparison to the proposed antenna structure in the thesis, paper [12] states that in case of the directional patch array there is a lower gain variation between elements at angles closer to the direction normal to array; similar observations have been made and verified experimentally in the proposed 4x4 antenna array. The gain along the boresight is similar with no much variation. Although along other directions which are oblique to the normal direction there is a drop in the gain. The paper also concludes that more directive patch elements are a better choice for Massive MIMO.

Furthermore, [13] proposes a way to switch between five beams and tilt each of the beams in the plane perpendicular to the comb line feed. The antenna has been designed for operation around 76.5 GHz whose operation and design principle used should be scalable to sub-6 GHz frequencies. Five parallel comb line feed networks consisting of 3 lines each are fed by a 3-way power divider using RF switch. There are five such RF switches each connecting a triplet of comb lines. The phasing provided to the comb lines is controlled by changing the length of the transmission lines between the feeding point and the radiating element. The antenna provides tilt in the elevation plane. Since it uses selective beam switching in contrast to beam forming, whole aperture is not used effectively. In comparison to the paper [13], the proposed 4x4 antenna array in the thesis provides beam tilts using a two-vector state beam switching scheme and operates at 14 GHz. The required phasing is provided by the transmission line feeding network.

2.3 Single-RF MIMO Antennas

To meet the demand of the growing mobile data traffic, architectures such as the massive MIMO antenna arrays discussed above are suitable candidates. These arrays inherently have a large number of antennas and therefore would require multiple RF chains to interface them to and from the wireless channel. This would add to the cost and complexity of realizing RF chains. Therefore, an alternative to this is the use of single RF chain MIMO that uses a single RF chain and still interfaces between the multiple antennas. It can operate through techniques like the time division multiplexing, code division multiplexing, antenna selection or the recent parasitic antenna method for single RF.

The Time Division Multiplexing in MIMO receivers uses a single receiver, an RF switch and signals from multiple antennas are selected, captured and processed in the digital signal processor separately. The switching speed and careful alignment of data are matters of concern with regards to the RF switch [14]. The RF switch selects the antenna signal over every symbol time interval of the modulated signal. The single front end RF receiver using the TDM technique can be realized as a single RF architecture by time multiplexing the antenna signals using SPMT (single pole multiple throw) switch. This architecture uses the same number of antennas as the conventional topology however instead of having multiple RF chains a single RF chain achieves the requirement by using a SPMT switch and time multiplexing. This reduces

the number of RF chains from N to 1 and significantly reduces the cost and RF design mismatch. Figure 2.5 shows a general block diagram of this architecture.

In code division multiplexing signals of each antenna must be multiplied by orthogonal codes and then added together. A single RF front end then down converts these summed RF signals to baseband. In the baseband sections the signals are multiplied by the orthogonal codes, integrated and demultiplexed. This is shown in Figure 2.6

In Antenna selection method, a few of the antennas of the all available antennas are selected and the system uses fewer RF chains than the number of transmitters or receivers. The received Signal to Noise ratio must be known a priori in this technique. The architecture is shown in Figure 2.7.

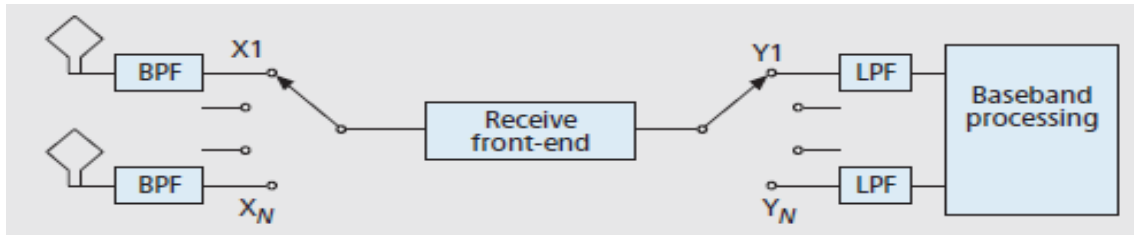


Figure 2.5 Time Division Multiplexing in MIMO Receivers [14]

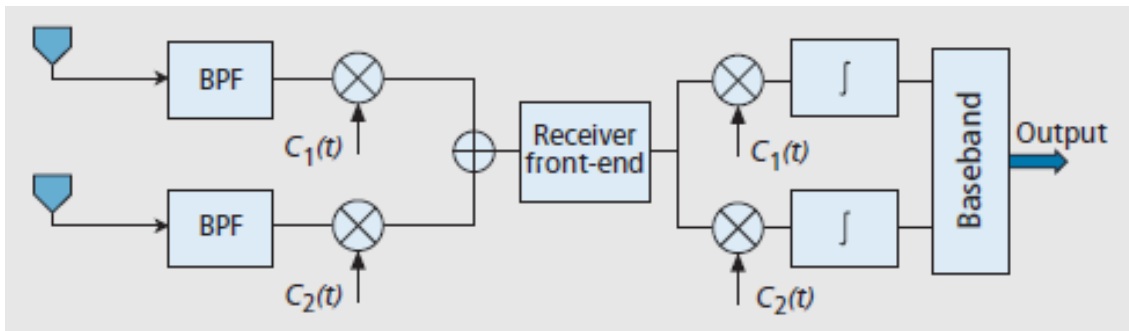


Figure 2.6 Code Division Multiplexing [14]

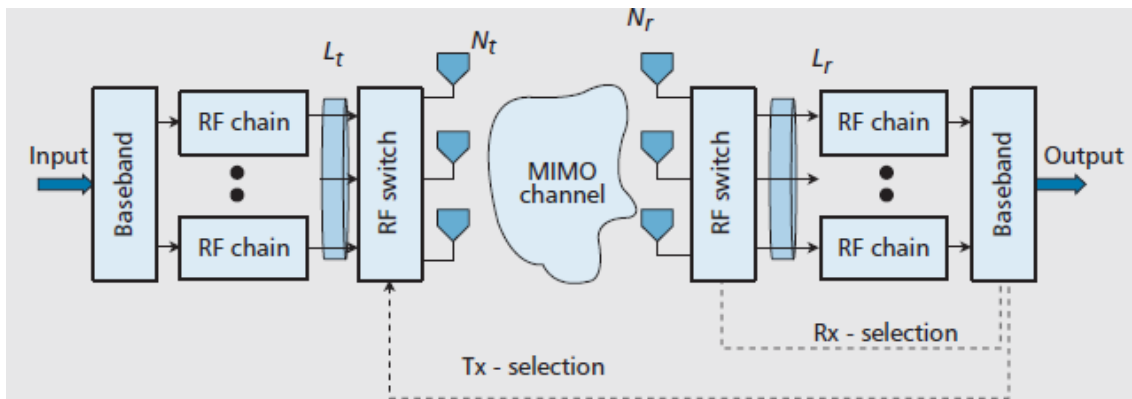


Figure 2.7 Antenna Selection Technique [14]

2.3.1 Parasitic Antenna Array

MIMO systems with multiple antenna elements on transmit and receive sides have been a topic of very active research in the recent years. Despite this significant research MIMO systems have not proliferated or incorporated to an appreciable extent in mobile handsets, base station antennas or sensor nodes. Much of this can be attributed to physical size, power constraints and cost. To transmit multiple data streams by multiplexing as required by MIMO concept, the individual antenna elements should be sufficiently spaced from each other and well de-correlated. Owing to the small size of the radio terminal or the base station footprint the number of antennas that can be de-correlated from each other also reduces and thus the physical size of the terminal becomes a key deciding factor in MIMO operation. Also, there is the glaring need of each antenna to be fed by its own RF chain which increases the cost, the required baseband processing and the RF circuitry as well. This also increases the power dissipation in the unit. The requirement of each antenna to be linked to an RF chain can be waived off by incorporating a new type of antenna technology namely the parasitic antenna array. In the conventional MIMO and array processing the RF signals and their baseband counterparts undergo intelligent processing at the digital signal processor in the baseband domain. In parasitic antenna array technology advanced mixed digital analogue techniques are used taking advantage of the mutual coupling mechanism which elsewhere is generally not desired. The active excitation induced on some elements causes mutual coupling to take place between the passive elements and causes them to radiate and depending on the ways of excitation this radiation can be controlled. This allows for spatial multiplexing and a performance comparable to that of conventional MIMO when having a few or a single RF chain.

Among the few antenna designs using the parasitic antenna array methodology for single RF purposes, four different methodologies have been selected and discussed here to set the tone for design of Single RF antennas based on this technology. They are compared against the proposed single RF MIMO antenna array to be discussed in detail in chapter 5.

A design for single RF chain MIMO using low power CMOS switches is proposed in [15]. The important implementation in this design is the use of discrete switch which simplifies the design and implementation of DC bias circuitries and reconfigurable loads. It provides a compact antenna structure optimized for multiplexing multiple signals. The over the air experiments for multiplexing two BPSK signals at 2.45 GHz are performed to confirm the effectiveness of the antenna. Figure 2.8 shows the antenna setup. The here proposed 3x3 Single RF MIMO array offers beam control and switching along the azimuth 360° whereas the design in [15] is validated for operation as a single arm of ESPAR (Electronically scanned parasitic antenna array).

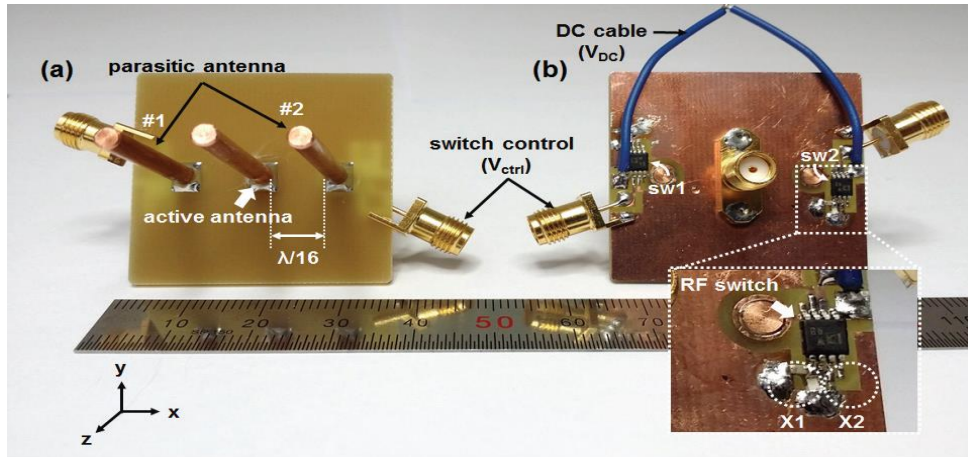


Figure 2.8 Single RF Chain MIMO Using Low Power CMOS Switches [15]

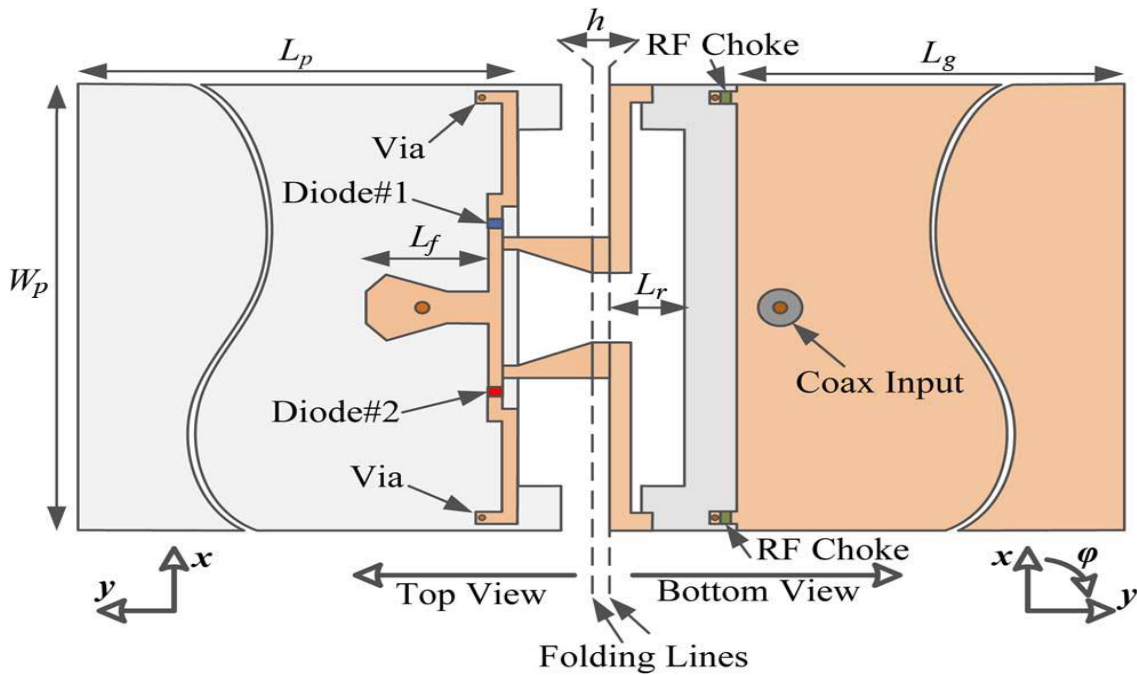


Figure 2.9 Integrated Radiator for Single-RF MIMO [16]

One of the earliest designs to realize Single RF MIMO is shown in [16]. Integration to small wireless devices being a matter of concern owing to the miniaturization of devices these days, [16] propose a novel antenna made of integrated radiator rather than physically separated dipoles. It simplifies the DC bias circuitry for BPSK modulated signals and does not require any external reconfigurable matching circuits. A prototype achieving single RF chain multiplexing at fixed frequency is designed and validated by measurements. The antenna is shown in Figure 2.9. Mirrored image pattern pairs are obtained using a PIN diode controlled Single RF switching to realize orthogonal basis functions onto which complex vector radiation patterns are mapped. The scheme proposes a board integrated way to switch between patterns. The antenna operates in the 1.9 to 2.2 GHz frequency range and its design is focused towards the mobile device. The here proposed Single RF MIMO antenna array operates around 14 GHz and is intended for integration in the base station side. The switching in the proposed design is

attained using a switchable feeding network. The mirrored image pattern pair (MIPP) are obtained using a 2-vector phase excitation scheme.

In yet another venture [17], a spatial multiplexing with a single radio with proof of concept and experiments is demonstrated. The concept of transmitting multiple signals using one RF chain and a compact switched parasitic array is validated. The experiments were conducted at 2.6 GHz in an indoor environment using a prototype made of printed dipole of which the centre one is active and coupled to two other passive ones as in the Figure 2.10. The approach here varies from that in [17] in being a printed configuration.

Finally, [18] proposes a reconfigurable antenna for spatial modulation purposes. The antenna design consists of a meander line radiating element which is surrounded by two L shaped resonators connected to PIN diode switches. By controlling the way in which the switches are toggled, several radiation patterns are generated to aid in spatial modulation. The antenna operates around 2-3 GHz. The proposed Single RF MIMO antenna array in this Thesis uses phase aided switching and does not harness the use of reflectors along specified switching directions as in [18] where the L shaped resonators alternately act as director and reflector.

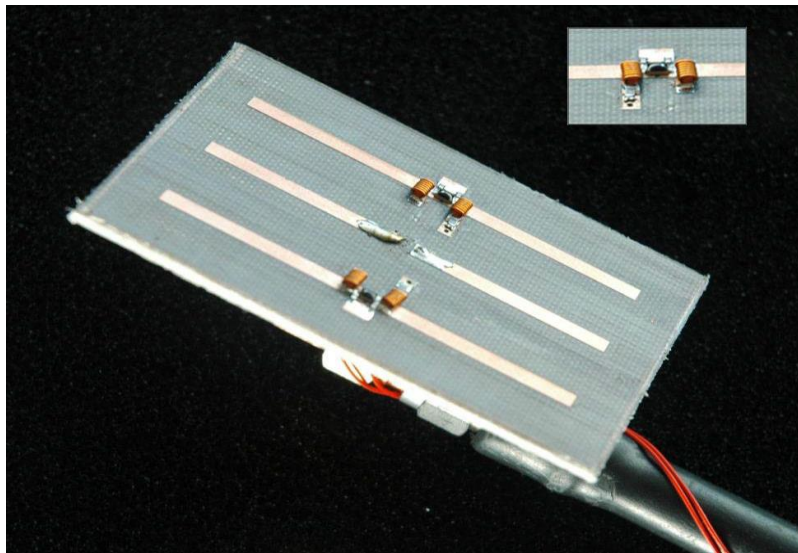


Figure 2.10 Switched Parasitic Array at 2.6 GHz [17]

2.4 Millimeter wave antennas

The recent increase in cellular traffic at the microwave frequency band has shifted the focus towards the underutilized wide millimeter wave spectrum. Current cellular networks based on the postulate that high frequencies are unfavourable to cellular communications cannot keep pace with the mobile data explosion by maintaining the required spectral and energy efficiency. Cellular communications occur at microwave frequencies (below 6GHz). The postulate that higher frequencies (greater than 6 GHz) introduce a larger attenuation unfavourable to cellular communications cannot be relied upon. But at microwave frequencies the channel bandwidth is limited and since the area spectral efficiency (ASE in bits/Hz/m²) linearly increases (best-case) with bandwidth, the ASE would be limited; the spectral efficiency is as well bounded by the transmit power. 5G therefore cannot be designed on this postulate. Recently in 2013,

experimental results showed that high frequencies are not that harmful for cellular communication. Experiments further showed that mmWave transmission can offer an increased SE compared to lower frequency transmission. One of the challenges addressed in the thesis is to overcome unfavourable mmWave propagation by high gain beamforming antennas design. MmWave systems need to employ directional beamforming with very large antenna arrays at both transmitter and receiver to realize sufficient link margin to overcome the high path loss at high frequencies.

At conventional microwave frequencies, the design of the antennas and of the beamformer is decoupled to exploit the flexibility of full digital beamforming. This is no longer possible at mmWave as full digital signal processing is too expensive and leads to high power dissipations. A brief review of the mmWave beamforming and beamforming techniques in general and the state-of-the-art are discussed in next subsections.

2.4.1 Key aspects and Challenges at mmWave beamforming

Hybrid beamforming multiuser scenario with common scatterers: mmWave signals owing to their smaller wavelength allow a large number of antennas to be packed into a small size antenna aperture. In conventional digital beamforming each of these antennas are connected to RF chain before digital beamforming is performed, however this is not practical at mmWave frequency considering the large number of antennas involved. Therefore, hybrid beamforming is performed which reduces the number of RF chains. Generally, the algorithms to date which compute the hybrid beamforming matrix and the analog beamforming matrix do so by assuming mmWave multipath channel model, where propagation paths corresponding to different users have independent angles of arrival at the base station [19]. However, channel measurements for mmWave frequency band show that rough surface/diffuse scattering exists in mmWave, and its diffuse range increases as the wavelength shrinks [20]. This gives rise to common scatterers with similar propagation paths and angle of arrival, which may add severely to the inter user interference. This is an important challenge that needs to be addressed.

Codebook and non-code book beamforming: Existing dominant analog beamforming schemes can be generally divided into two categories, i.e., the non-codebook beamforming and the codebook-based beamforming. Though non-codebook beamforming offers excellent low complexity designs, they require perfect channel state information (CSI) to be acquired by the Base station (BS) which can be challenging given the limited number of RF chains [21]. The codebook-based beamforming on the other hand has an increased complexity overhead due to search complexity. Higher number of iterations between the BS and the mobile station (MS) leads to greater practical system overhead.

Low rank of the channel matrix: Generally, in mmWave communications, the rank of the MIMO channel matrix tends to be low, due to the presence of a strong LoS component [22]. The spatial arrangement of antennas needs to be specifically adjusted to increase the rank of the channel matrix [22]. This is often a challenge. To address this recently spacing between analog beamformers were optimized to maximize the channel matrix rank in a mmWave MIMO environment using a technique called Generalized Spatial Modulation [23].

Range and directional communication: The smaller wavelength of mmWave signals proportionally enables greater antenna gain for the same physical aperture size of the antenna

[24]. And therefore, the higher frequencies of mmWave signals do not decrease the free space propagation loss if the antenna area remains fixed and proper beam forming is performed. The gain obtained in the phased array scenario for an array of N antennas is given by [24]

$$\text{Gain(array)} = \text{Gain (single antenna)} + 10\log_{10}(N) \text{ dB}$$

Obtaining high directional beamforming gains can completely compensate for and further reduce the increase in the path loss with frequency. This however poses a challenge in the design of synchronization and broadcast signals used in initial cell search. These signals need to be scanned over a range of angles and this spatial searching, owing to highly directional beam, results in delay in BS detection in handovers.

Shadowing: mmWave signals are very prone to shadowing. Materials such as brick, human body can attenuate signals by 40-80 dB [24]. A correct assessment of the shadowing environment and accounting for the attenuation loss by increasing the beamforming gains offers significant challenge in realizing beamforming networks.

Rapid channel fluctuations: For a given mobile velocity, channel coherence time is very small in the mmWave range. The Doppler spread at 60 km/hr at 60 GHz is over 3 kHz [25] and hence the channel will change in the order of hundreds of microseconds. To keep in pace with this it is indeed challenging to design low latency beamforming networks than can accommodate the rapidly fluctuating channel state.

Fully Digital vs Mixed Digital/Analogue Solutions: Fully digital beamforming methods require one RF chain per antenna. The hybrid/mixed digital/analogue solution divides signal processing into digital and analogue domains to support multi stream and multi user. A hybrid transmit full array beamformer is shown in Figure 2.11. The hybrid beamforming consists of fewer number of RF chains with digital processing in the baseband or RF domain followed by analogue processing to obtain antenna beamforming gains [24]. The challenges in hybrid/mixed beamforming when compared to fully digital are listed below:

- **Number of RF chains and analogue phase shifters:** This needs to be arrived at optimally considering the multiplexed and antenna elements. The performance of the fully digital beamforming is targeted keeping in view the hardware cost and power constraints.

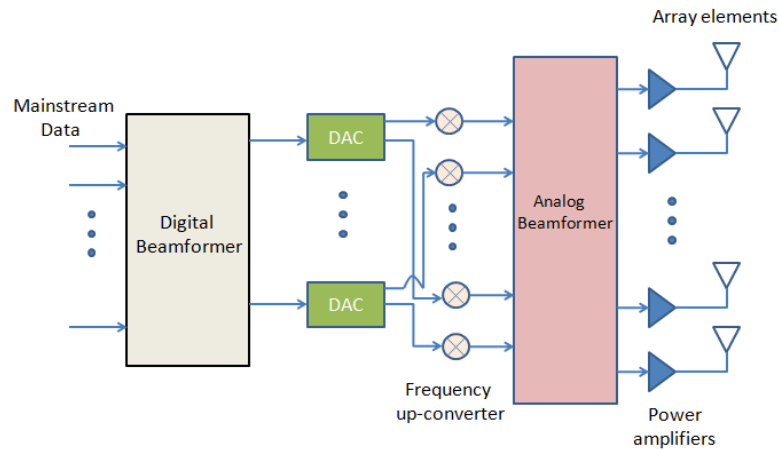


Figure 2.11 Typical hybrid beamforming transmit architecture for a full array [24]

- **Channel estimation:** Channel estimation is a key factor in any type of beamforming or massive MIMO related processing. The limited number of RF chains as compared to the number of antenna elements in hybrid beamforming presents a bottle neck in channel estimation. Thus, channel estimation in hybrid beamforming is an optimization problem that identifies optimal RF transmit receive pairs to maximize mutual data.
- **Beam training and feedback:** Reference signal sequences designed for joint baseband and RF beamforming to reduce the feedback and training overhead can yield low complexity power efficient implementations.

To summarize, millimetre wave spectrum comes inherently with a large bandwidth and its LOS propagation limitation can be overcome by high gain beamforming. A recent study has shown the mmWave communication to be useful for cellular communications practically [25]. Advanced methods of mmWave beamforming that employ both the advantages of analogue and digital beamforming together called hybrid beamforming are being used recently [24]. The papers [26] and [27] provide a broad overview and survey of the large scale MIMO systems and [24] considers a detailed review of mmWave beamforming to date. It identifies the main drawbacks of mmWave like increased path loss and discusses about high gain beamforming techniques to overcome this. The diverse ways of beamforming like digital, analogue or their hybrid are discussed along with the emerging trends in mmWave beamforming. To perform hybrid beamforming, analogue phase shifters are generally used. An interesting proposition is to change to switches that consume less power and have a low [29].

2.4.2 Antenna designs for mmWave band

Antenna designs have been proposed recently keeping the mmWave band in consideration. A selection of these antennas is presented, and their architectures discussed in brief in next paragraphs.

One such antenna design [29] is the tilted combined beam antenna that provides a tilted radiation in the elevation plane operating around the 28 GHz band, as shown Figure 2.12. Instead of using array to provide the elevation angle tilt, two radiating elements are used to produce the tilted beam. One is a group of microstrip patches and the other is a waveguide aperture. A relatively high antenna gain of 7.4 dBi even with wide beam spreading across the azimuthal plane can be obtained. The tilted beam is obtained without using antenna arrays or active RF components. Of the two radiating elements one is for a wide beamwidth on the azimuthal plane and the other is for strong radiation in the elevation plane. To obtain a high gain beam in the desired tilted direction the spacing between the two radiators is optimized. This antenna design is of interest in multilayer sectoring methodology which is a new way of sectoring cell site based on radius.

Dual slant polarization is of key importance in massive MIMO antenna arrays owing to the ease with which the polarized components can be resolved at the receiver. [31] proposed a design termed the turning torso antenna shown in Figure 2.13, which uses three orthogonal hexagonal stacked rings operating at 3.7 GHz. The arrangement allows 18 beams along the entire 360° range with a gain of 16.6 dBi.

Another dual polarized base station antenna element [31] is shown in Figure 2.14 which uses four parasitic elements placed in a square contour to increase the cross polar discrimination (XPD). The principle of wide beamwidth and high XPD was investigated.

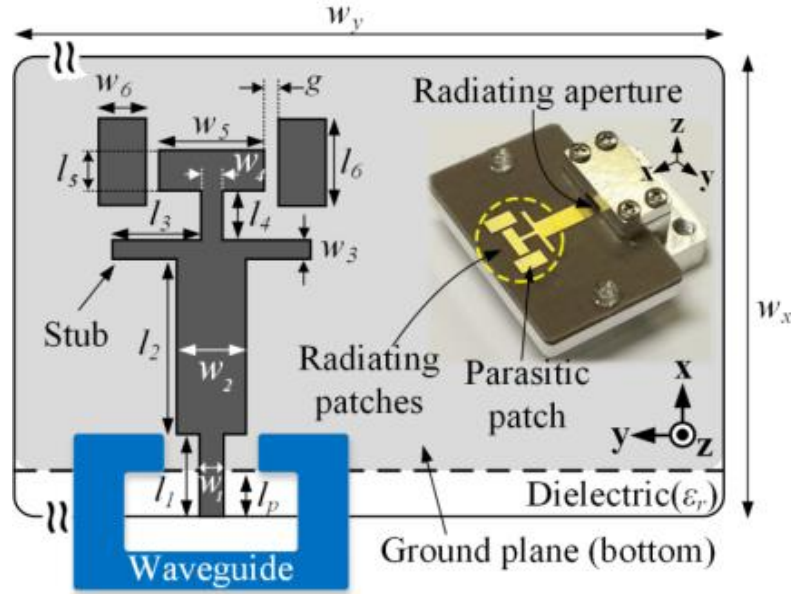


Figure 2.12. Tilted combined beam antenna [30]

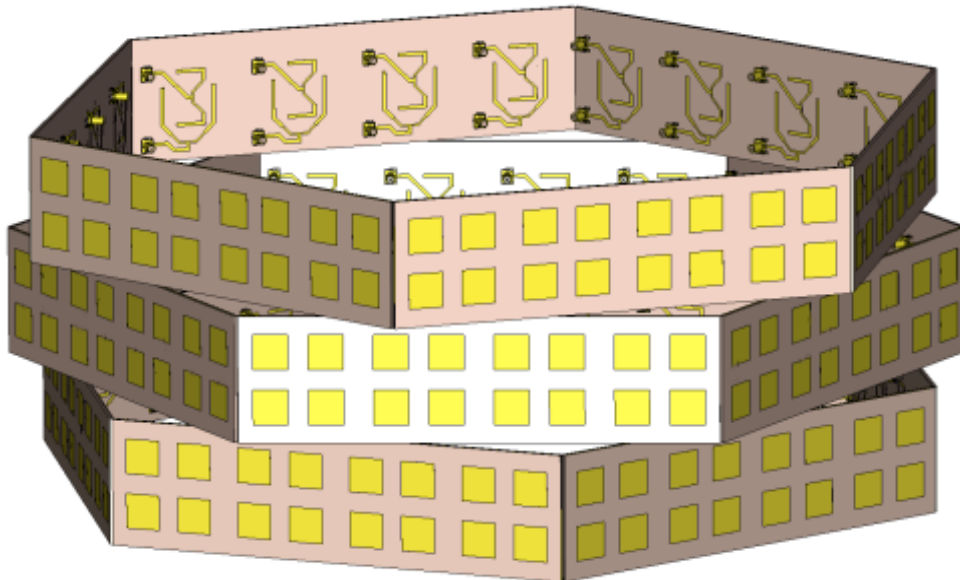


Figure 2.13 Turning torso antenna [31]

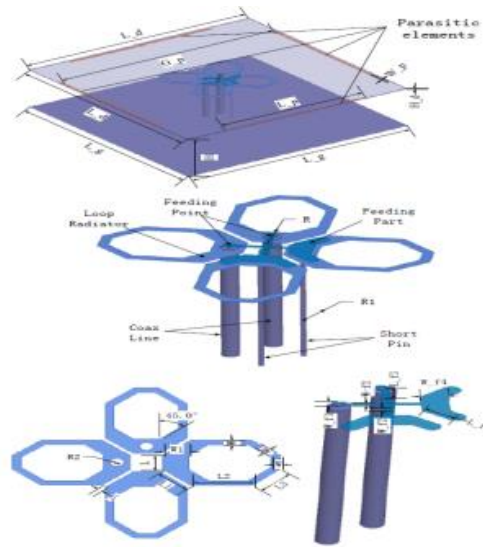


Figure 2.14 Improved XPD antenna [32]

Another antenna design as described in [33] and shown in Figure 2.15 is a two-folded dipole fed in phase with a CPW transmission line with four parasitic patches surrounding it to enhance directivity and minimize surface waves. It operates at 122 GHz with a gain of 11 dBi.

A work that focuses on substrate integrated waveguide technology (SIW) is shown in Figure 2.16. SIW is relatively easy to integrate and compact. It also provides a low loss feeding network to the antenna. The antenna in [34] operates in the 76-86 GHz E-band with antenna design made of SIW technology. It has a high gain of up to 15 dBi and wide beamwidth of 25 degrees in E plane and 30 degrees in H plane. It uses the mainstream PCB process and has four metal layers and three substrate dielectric layers. It is a low cost steerable E band antenna with a SIW feed network made of H and T junctions to feed the antenna element.

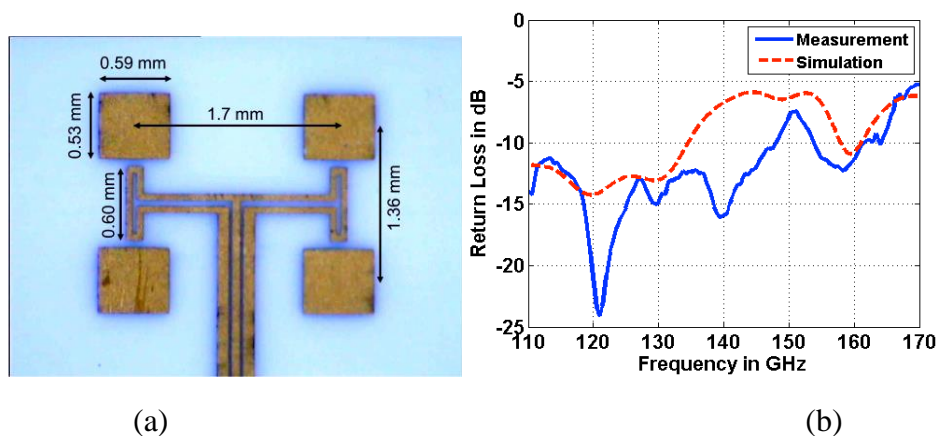


Figure 2.15 Double dipole antenna at 122 GHz with return loss [33]

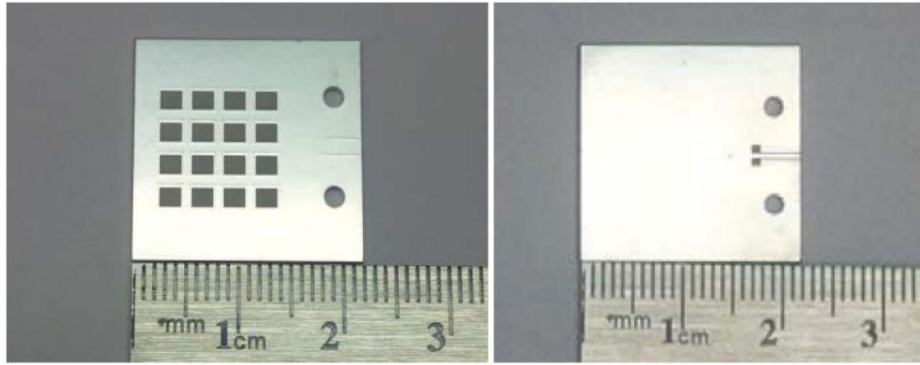


Figure 2.16 SIW antenna array [34]

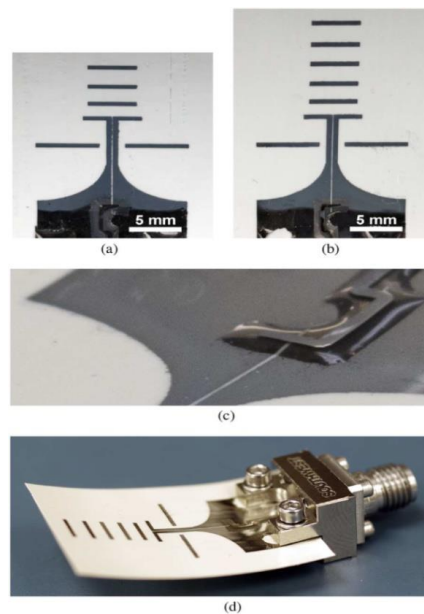


Figure 2.17 Inkjet printed multilayer Yagi Uda antenna (a) 3 director elements (b) 5 director elements (c) microstrip to slot line transition (d) slightly bent substrate antenna [35]

The antenna design for the large-scale MIMO needs to be scalable. The cost of fabrication and deployment at mmWave frequencies limits this from being feasible, especially when designing 3D antennas. A recent fabrication technique that has been gaining momentum owing to its low cost, scalability and environment friendliness is inkjet printing. [35] has proposed a Yagi-Uda antenna with gain of 8 dBi in the 24.5 GHz frequency range using inkjet printing methodology shown in Figure 2.17. It further demonstrates the technology's potential for integration with on-chip and on-package fabrication schemes. It also shows a good RF integrity of both the metallic and dielectric ink materials within the inkjet printing process. Multi-layer material deposition is used to realize the 3D antenna structure including realization of the dielectric substrate to support the microstrip to slot line transition. One major advantage of this technology is the ease of post process deposition of antennas onto any rigid or flexible active/passive circuit topology. It can be seen this brings in an extra degree of freedom - blending into the pre-existing design.

Recently mmWave communication antennas have been designed using the patch or the slot. These designs have narrow impedance bandwidth and radiation pattern bandwidth. To enhance

this, design with SIW and dual polarization incorporated in it is proposed in [36] and shown in Figure 2.18. An aperture coupled magneto electric dipole is presented that is designed over three layers of substrate, with a four-element patch antenna built on the top layer aided by a cross slot to enhance impedance matching. This structure is further controlled by a beamforming network made of a 90° coupler. The beamforming network allows steering the beam along 2D and can be extended to a beamswitching network by incorporating switches. The use of magneto electric dipole concept reduces the back-lobes and ensures a good front-to-back ratio of 20 dB. The antenna and the array operate at 60 GHz and several other contemporary similar design techniques employ slots, patches, dipoles and cavity to realize multibeam along 1D and 2D. The 1D multibeam is along the azimuthal or elevation plane like fan beams with narrow beamwidths cast simultaneously along the azimuthal plane, while not covering the other dimension. The 2D multibeam jointly covers azimuthal and elevation dimensions. These techniques mostly operate in the linear polarization and have an impedance bandwidth ranging from 12-19%. The design has an impedance bandwidth of 22%.

Circular polarization has been generally treated next to dual polarization in cellular communications, however it is used in anti-multipath interference and good polarization matching. A wideband, high efficiency, circular polarized planar array antenna operating at Ka band is presented in [37] and its exploded view is shown in Figure 2.19. The radiating element is a cross slot with four parasitic patches. The aperture coupling technique is used by the array and is fabricated using PCB. A gain of 18 dBiC in the frequency band of 26-30 GHz is obtained.

While mmWave beamforming is majorly concerned with high gain beamforming to improve data rates, beamswitching employed at pico or femto cell sites to switch the beam along different UEs would be an added advantage. Millimeter wave beamswitching has been presented in [37] using a conformal antenna array. It consists of 3 antenna arrays of 16 patch elements in each array operating at 61 GHz. A single pole three throw (SPTT) switch controls the beam switching. The fabricated antenna array is shown in Figure 2.20.

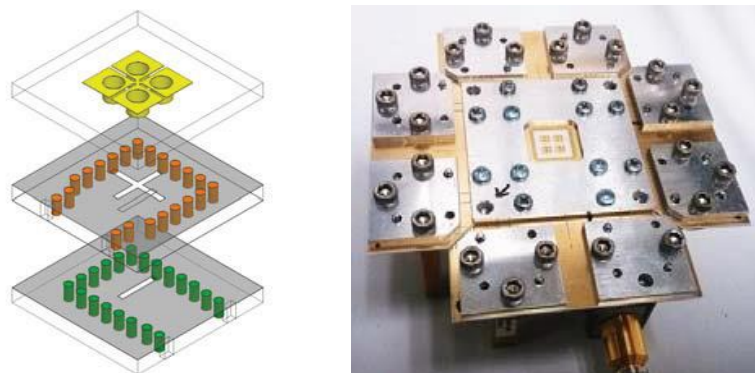


Figure 2.18 Geometry of the aperture coupled magnetic electric dipole antenna and the fabricated prototype [36]

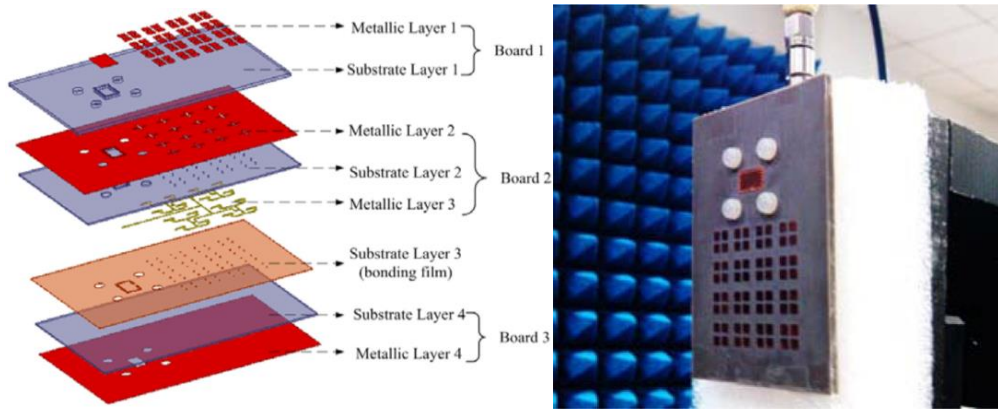


Figure 2.19 3D configuration of the Ka band CP array and fabricated prototype [37]

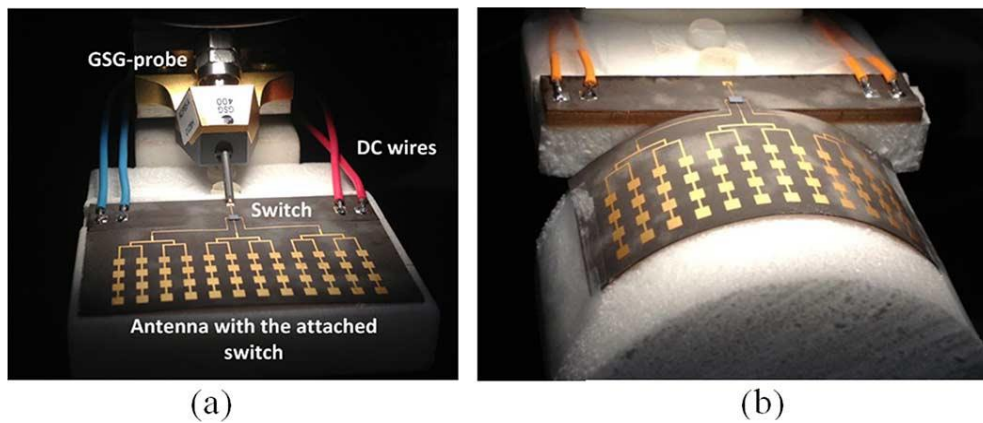


Figure 2.20 Planar prototype and the convex prototype of the conformal array [38]

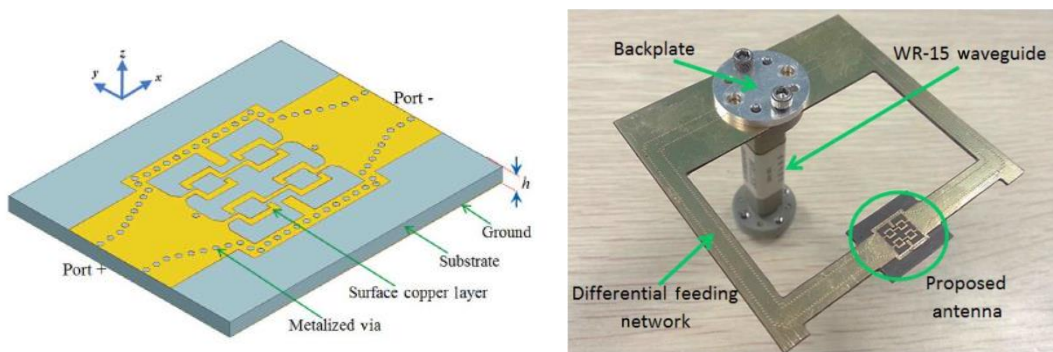


Figure 2.21 Model and fabricated prototype of the planar aperture antenna [39]

A design that uses differential feeding to obtain high gain circular polarization at mmWave frequency is proposed in [38]. It has a wide bandwidth and can be fabricated using PCB process that makes the antenna easy to integrate to differential circuits. The antenna consists of open cavity made of metalized vias which encloses loop like strip fed differentially [38] and is shown in Figure 2.21. The aperture's E field together with the travelling wave current give rise to the circular polarization. The antenna operates at 60 GHz and achieves 3 dB AR (Axial Ratio) of 16.7% while providing a peak gain of 14.6 dBi. The antenna is low cost and has a low profile as it can be realized on a single layer laminate and is fabricated using standard planar circuit

technology. The differential feeding scheme of the antenna further eliminates the use of baluns as these can be integrated into the differential mmWave circuits directly and effectively.

A comparison of the antennas discussed above is shown in Table 2.2. It can be deduced from the table that for the millimeter wave band the antenna gains vary around 15-20 dBi with the percentage impedance bandwidth being the highest for the XPD enhanced antenna. Linear, Dual and Circular polarization configurations have been realized.

Considering the cellular communication link, antennas need to be designed for backhaul link and access point to UE link. High gain and directive beam and quasi optical systems are needed. SIW fed slot array [39], SIW fed chain array [40] are two examples shown in Figure 2.22 to obtain high gain narrow beams. The SIW fed slot array has a peak measured gain of 33.1 dBi at 61.5 GHz with an efficiency of 56.8% while the SIW fed chain array has a radiation efficiency of 74%.

For the access point to UEs, beamswitching or beamsteering antennas are required owing to the mobility of UEs. Other than the SIW arrays used for the backhaul link, the 60 GHz beam switched receiver that is presented in [41] uses GaAs switches on a liquid crystal polymer substrate; the active peak gain is 27.5 dBi. Beam switched antennas have also been realized using Rotman lens [42] and integrated reflector systems [43].

Antenna type	Frequency Band	Gain (dBi)	Polarization	Impedance Bandwidth
Tilted combine beam antenna	27.2 GHz - 28.7 GHz	7.4 dBi	Linear	5.4%
Hexagonal stacked ring	3.64GHz-3.8 GHz	16.6 dBi	Dual	3.6%
Improved XPD antenna	1.7-2.7 GHz*	8.9 dBi	Dual	45%
Inkjet printed multilayer Yagi Uda antenna	21-27 GHz	8 dBi	Linear	25%
Aperture coupled magneto electric dipole	53.4-71.8 GHz	12.5dBi	Dual	29.3%
Ka band array	26.4-30.3 GHz	17.4dBic	Circular	13.7%
Conformal array	57-63 GHz	18.8 dBi	Linear	10%
Differentially fed planar aperture antenna	57-66 GHz	14.6 dBi	Circular	16.1%

Table 2.2 Comparison of different antenna types based on gain, polarization and bandwidth

**Antenna operating in microwave band shown as it offers a technique to better cross polarization discrimination that could hold as well in mmWave band*

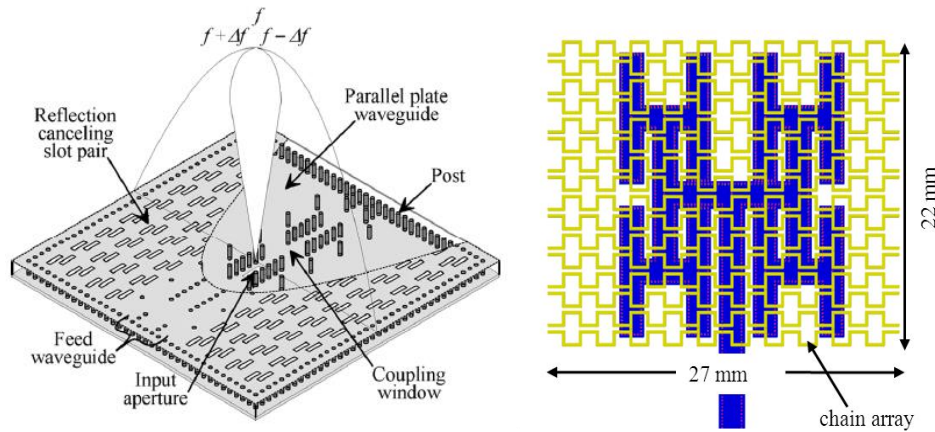


Figure 2.22. SIW arrays: SIW fed slot array and SIW fed chain array [41]

2.5 Conclusion

The state-of-the-art survey on three Massive MIMO, Single RF MIMO and millimeter wave antenna implementations discussed, provide valuable insight into the way forward in designing of these antennas. In the design of large scale MIMO systems the major concerns would be majorly the size, power consumption and cost. With the advent of new advanced manufacturing techniques, and specialized hardware both in the analogue and digital domains, the cost and power consumption could be significantly lowered. The Argos group state that the antenna array operation was only limited by the number of modules available and can be significantly scaled up with similar performance with more number of antennas. The size of the antenna array can be brought down by operating in the millimeter wave band to attain high gain beams through antenna arrays that occupy the same physical aperture as a microwave antenna array. This exemplifies the concept of reduced size antennas with the same physical aperture area used to provide high gains as in the millimeter wave related work discussed earlier. The baseband processing can be moved to the software defined radio (SDR)'s FPGAs so that full real time processing can be done efficiently reducing the latency. An identification of the key parameters to be considered in Massive MIMO paves the way to quantify the massive MIMO antenna array design process.

Reduction in power consumption can be achieved by reduction in number of RF chains using Single RF MIMO antennas designed to transmit orthogonal patterns using mirror image pattern pairs. Of the different methodologies discussed for realizing single RF chain MIMO, the one with an increased matter of interest keeping antenna design in view is the parasitic antenna array methodology. This could be used to develop antennas for beam space MIMO. Once a working prototype at the known orders of modulation is performed, systems supporting higher modulation, or a greater number of multiplexing streams could be focused upon.

The review reveals that mmWave band is promising for high data rate communications when antennas designed for mmWave band are used in conjunction with high gain analogue and digital beamforming. The antenna design at these frequencies is guided mainly by alleviating the array effects in large scale array antennas by employing customized elements towards the edges of the array. For antenna design, parameters like the polarization ports isolation, gain, possibly dual slant polarization, feed network, or possibility of attaining super directivity by packing the antenna elements close, are some of the design considerations. Antenna array

configurations in 3D like the cylindrical or spherical or lens-based antennas have potential to offer 360-degree beamforming which is ideal in a small cell or pico-cell environment. Multilayer and 120° sectoring are key areas to better 5G deployments. Multilayer sectoring uses different elevation angles at the base station to cast different concentric beams, centred around the base station, while maintaining the same azimuthal beamwidth.

A synergy between the three areas of Massive MIMO, Single RF MIMO and millimeter wave beamforming will allow the realization of 5G performance metrics.

2.6 References

- [1] P. Amadori, C. Masouros, "Interference Driven Antenna Selection for Massive Multi-User MIMO," in *IEEE Trans. On Vehicular Technology*, vol. 65, no. 8, pp. 5944-5958, Aug. 2016.
- [2] D. A. Basnayaka, M. Di Renzo, H. Haas, "Massive But Few Active MIMO," in *IEEE Trans. On Vehicular Technology*, vol. 65, no. 9, pp. 6861-6877, Sep. 2016.
- [3] S. Biswas, C. Masouros, T. Ratnarajah, "Performance Analysis of Large Multi-User MIMO Systems with Space-Constrained 2D Antenna Arrays," in *IEEE Transactions on Wireless Communications*, vol. 15, no. 5, pp. 3492-3505, May 2016.
- [4] H. Yang, T. L. Marzetta, "Energy Efficient Design of Massive MIMO: How Many Antennas?" in *IEEE 81st Vehicular Technology Conference (VTC Spring)*, pp. (1-5), 11-14 May 2015.
- [5] J. Hoydis, S. ten Brink, M. Debbah, "Massive MIMO: How many antennas do we need?" in *Proc. 2011 49th Annual Allerton Conference on Communication, Control, and Computing*, pp. 545-550, Monticello, IL (USA), 28-30 Sept. 2011.
- [6] Y. Xin, D. Wang, J. Li, H. Zhu, J. Wang and X. You, "Area Spectral Efficiency and Area Energy Efficiency of Massive MIMO Cellular Systems," in *IEEE Transactions on Vehicular Technology*, vol. 65, no. 5, pp. 3243-3254, May 2016.
- [7] C. Shepard, H. Yu, N. Anand, E. Li, T. L. Marzetta, R. Yang, L. Zhong. "Argos: Practical Many-Antenna Base Stations," in *Proc. ACM Int. Conf. Mobile Computing and Networking (MobiCom)*, Aug. 2012.
- [8] J. Vieira, S. Malkowsky, K. Nieman, Z. Miers, N. Kundargi, L. Liu, I. Wong, V. Owall, O. Edfors, F. Tufvesson, "A flexible 100-antenna testbed for Massive MIMO," in *Globecom Workshops*, 2014, vol., no., pp.287-293, 8-12 Dec. 2014.
- [9] W. Roh, J.-Y. Seol, J. Park, B. Lee, J. Lee, Y. Kim, J. Cho, K. Cheun, F. Aryanfar, "Millimeter-wave beamforming as an enabling technology for 5G cellular communications: theoretical feasibility and prototype results," in *Communications Magazine, IEEE*, vol.52, no.2, pp.106-113, Feb. 2014.
- [10] D. Guan, Y. Zhang, Z. Qian, Y. Li, M. Asaadi and C. Ding, "A Novel 2-D Multibeam Antenna Without Beamforming Network," in *IEEE Transactions on Antennas and Propagation*, vol. 64, no. 7, pp. 3177-3180, July 2016.
- [11] P. Y. Wang et al., "Beam Switching Antenna Based on a Reconfigurable Cascaded Feeding Network," in *IEEE Transactions on Antennas and Propagation*, vol. 66, no. 2, pp. 627-635, Feb. 2018.
- [12] C. M. Chen, V. Volski, L. Van der Perre, G. A. E. Vandenbosch and S. Pollin, "Finite Large Antenna Arrays for Massive MIMO: Characterization and System Impact," in *IEEE Transactions on Antennas and Propagation*, vol. 65, no. 12, pp. 6712-6720, Dec. 2017.

- [13] H. Tanabe, K. Sakakibara and N. Kikuma, "Multibeam-switching millimeter-wave antenna using beam-tilting design in perpendicular plane to feed line of microstrip comb-line antenna," 2017 IEEE MTT-S International Conference on Microwaves for Intelligent Mobility (ICMIM), pp. 139-142, Nagoya, 2017.
- [14] A. Mohammadi and F. M. Ghannouchi, "Single RF front-end MIMO transceivers," in *IEEE Communications Magazine*, vol. 49, no. 12, pp. 104-109, Dec. 2011.
- [15] Y. K. Cho, J. N. Lee, Y. H. Lee, G. Jo, J. Oh and B. H. Park, " $\lambda/16$ spaced single RF chain MIMO antenna using low-power CMOS switches," in *Proc. 2015 European Microwave Conference (EuMC)*, pp. 726-729, Paris, 2015.
- [16] M. Yousefibeiki and J. Perruisseau-Carrier, "Towards Compact and Frequency-Tunable Antenna Solutions for MIMO Transmission with a Single RF Chain," in *IEEE Transactions on Antennas and Propagation*, vol. 62, no. 3, pp. 1065-1073, March 2014.
- [17] O. N. Alrabadi et al., "Spatial Multiplexing with a Single Radio: Proof-of-Concept Experiments in an Indoor Environment with a 2.6-GHz Prototype," in *IEEE Communications Letters*, vol. 15, no. 2, pp. 178-180, February 2011.
- [18] A. Ourir, K. Rachedi, D. T. Phan-Huy, C. Leray and J. de Rosny, "Compact reconfigurable antenna with radiation pattern diversity for spatial modulation," in *Proc. 2017 11th European Conference on Antennas and Propagation (EUCAP)*, pp. 3038-3043, Paris, 2017.
- [19] J. Li, L. Xiao, X. Xu, and S. Zhou, "Robust and Low Complexity Hybrid Beamforming for Uplink Multiuser MmWave MIMO Systems", in *IEEE Communications Letters*, 2016.
- [20] T. S. Rappaport, G. R. Mac Cartney, M. K. Samimi, and S. Sun, "Wideband millimeter-wave propagation measurements and channel models for future wireless communication system design," *IEEE Trans. Commun.*, vol. 63, no. 9, pp. 3029-3056, Sep. 2015.
- [21] X. Gao, L. Dai, C. Yuen, and Z. Wang, "Turbo-Like Beamforming Based on Tabu Search Algorithm for Millimeter-Wave Massive MIMO Systems", in *IEEE Transactions on Vehicular Technology*, vol. 65, no. 7, pp. 5731-5737, July 2016.
- [22] F. Bøhagen, P. Orten, and G. E. Øien, "Design of optimal high rank line-of-sight MIMO channels," *IEEE Transactions on Wireless Communications*, vol. 6, no. 4, pp. 1420-1424, Apr. 2007.
- [23] N. Ishikawa, R. Rajashekar, S. Sugiura, and L. Hanzo, "Generalized Spatial Modulation Based Reduced-RF-Chain Millimeter-Wave Communications," in *IEEE Transactions on Vehicular Technology*, vol. 66, no. 1, pp. 879-893, Jan. 2016.
- [24] S. Kutty and D. Sen, "Beamforming for Millimeter Wave Communications: An Inclusive Survey," in *IEEE Communications Surveys & Tutorials*, vol. 18, no. 2, pp. 949-973, Second quarter 2016.

- [25] S. Rangan, T. S. Rappaport and E. Erkip, "Millimeter-Wave Cellular Wireless Networks: Potentials and Challenges," in *Proceedings of the IEEE*, vol. 102, no. 3, pp. 366-385, March 2014.
- [26] Y. Kim *et al.*, "Feasibility of Mobile Cellular Communications at Millimeter Wave Frequency," in *IEEE Journal of Selected Topics in Signal Processing*, vol. 10, no. 3, pp. 589-599, April 2016.
- [27] K. Zheng, L. Zhao, J. Mei, B. Shao, W. Xiang and L. Hanzo, "Survey of Large-Scale MIMO Systems," in *IEEE Communications Surveys & Tutorials*, vol. 17, no. 3, pp. 1738-1760, third quarter 2015.
- [28] L. Lu, G.Y. Li, A.L. Swindlehurst, A. Ashikhmin, and R. Zhang, "An Overview of Massive MIMO: Benefits and Challenges", *IEEE Journal of Selected Topics in Signal Processing*, vol. 8, no. 5, pp. 742-758, 2014.
- [29] R. Méndez-Rial, C. Rusu, N. González-Prelcic, A. Alkhateeb and R. W. Heath, "Hybrid MIMO Architectures for Millimeter Wave Communications: Phase Shifters or Switches?" in *IEEE Access*, vol. 4, pp. 247-267, 2016.
- [30] J. Park, J. Ko, H. Kwon, B. Kang, B. Park and D. Kim, "A Tilted Combined Beam Antenna for 5G Communications Using a 28-GHz Band," in *IEEE Antennas and Wireless Propagation Letters*, vol. 15, pp. 1685-1688, 2016.
- [31] R. Ma, Y. Gao, C. Parini and L. Cuthbert, "Dual-polarized turning torso antenna array for massive MIMO systems," *2015 9th European Conference on Antennas and Propagation (EuCAP)*, Lisbon, 2015, pp. 1-2.
- [32] Y. Luo, Q. Chu and D. Wen, "A Plus/Minus 45 Degree Dual-Polarized Base-Station Antenna with Enhanced Cross-Polarization Discrimination via Addition of Four Parasitic Elements Placed in a Square Contour," in *IEEE Transactions on Antennas and Propagation*, vol. 64, no. 4, pp. 1514-1519, April 2016.
- [33] S. Beer and T. Zwick, "122 GHz antenna-integration in a plastic package based on a flip chip interconnect," *2011 IEEE MTT-S International Microwave Workshop Series on Millimeter Wave Integration Technologies*, Sitges, 2011, pp. 37-40.
- [34] V. Miraftab, Wenyao Zhai and M. Repeta, "A wideband low-cost E-band SIW antenna array for high capacity mmWave radio," *2015 IEEE MTT-S International Microwave Symposium*, Phoenix, AZ, 2015, pp. 1-3.
- [35] B. K. Tehrani, B. S. Cook and M. M. Tentzeris, "Inkjet Printing of Multilayer Millimeter-Wave Yagi-Uda Antennas on Flexible Substrates," in *IEEE Antennas and Wireless Propagation Letters*, vol. 15, pp. 143-146, 2016.
- [36] Y. Li and K. Luk, "60-GHz Dual-Polarized Two-Dimensional Switch-Beam Wideband Antenna Array of Aperture-Coupled Magneto-Electric Dipoles," in *IEEE Transactions on Antennas and Propagation*, vol. 64, no. 2, pp. 554-563, Feb. 2016.

- [37] J. Wu, Y. J. Cheng and Y. Fan, "Millimeter-Wave Wideband High-Efficiency Circularly Polarized Planar Array Antenna," in *IEEE Transactions on Antennas and Propagation*, vol. 64, no. 2, pp. 535-542, Feb. 2016.
- [38] V. Semkin *et al.*, "Beam Switching Conformal Antenna Array for mm-Wave Communications," in *IEEE Antennas and Wireless Propagation Letters*, vol. 15, pp. 28-31, 2016.
- [39] D. J. Bisharat, S. Liao and Q. Xue, "High Gain and Low Cost Differentially Fed Circularly Polarized Planar Aperture Antenna for Broadband Millimeter-Wave Applications," in *IEEE Transactions on Antennas and Propagation*, vol. 64, no. 1, pp. 33-42, Jan. 2016.
- [40] K. Hashimoto, J. Hirokawa and M. Ando, "A Post-Wall Waveguide Center-Fed Parallel Plate Slot Array Antenna in the Millimeter-Wave Band," in *IEEE Transactions on Antennas and Propagation*, vol. 58, no. 11, pp. 3532-3538, Nov. 2010.
- [41] A. Lamminen and J. Säily, "High gain 60 GHz LTCC chain antenna array with substrate integrated waveguide feed network," *2012 6th European Conference on Antennas and Propagation (EUCAP)*, Prague, 2012, pp. 2569-2573.
- [42] C. E. Patterson, W. T. Khan, G. E. Ponchak, G. S. May and J. Papapolymerou, "A 60-GHz Active Receiving Switched-Beam Antenna Array with Integrated Butler Matrix and GaAs Amplifiers," in *IEEE Transactions on Microwave Theory and Techniques*, vol. 60, no. 11, pp. 3599-3607, Nov. 2012.
- [43] J. Schoebel *et al.*, "Design considerations and technology assessment of phased-array antenna systems with RF MEMS for automotive radar applications," in *IEEE Transactions on Microwave Theory and Techniques*, vol. 53, no. 6, pp. 1968-1975, June 2005.
- [44] Y. J. Cheng, W. Hong and K. Wu, "Millimeter-Wave Substrate Integrated Waveguide Multibeam Antenna Based on the Parabolic Reflector Principle," in *IEEE Transactions on Antennas and Propagation*, vol. 56, no. 9, pp. 3055-3058, Sept. 2008.

Chapter 3

Quasi-optics endfire antenna element

3.1 Introduction

Scenarios of high data rate transmission of several Gbps require the use of larger bandwidth and high directivity beams. The larger bandwidth is attained by shifting to a higher millimeter wave frequency and to obtain such a high directivity beam, antennas, need to be designed to focus the far-field with high F/B ratio. When employed in an array such an antenna further enhances the directivity gain offered due to the array. Recently there has been an increasing interest in the 14-15 GHz band [1]-[3]. A printed antenna configuration is promising owing to the simplicity of manufacturing, scalability and the cost. The conventional patch and printed dipole antennas generally have an omnidirectional low directivity pattern. Among the techniques used to enhance this directivity, the use of parasitic elements coupled to the patch is appealing. In agreement with this, an endfire antenna element based on quasi-yagi and fibre-optics principle is proposed in this chapter. The designed antenna element has its gain and directivity mainly enhanced by a unique arrangement of parasitics around the driving sources drawing largely from reconfiguring the refractive index; following the fibre-optics principle.

An endfire beam typically has a higher directivity in comparison to the boresight beam. Endfire antenna topologies such as the helical antenna, antipodal Vivaldi antenna and the Yagi-Uda antenna have been used in applications such as ultra-wideband, phased array, radars and microwave imaging. Printed endfire antenna elements have been used for high gain applications. These are generally fed by a half wavelength resonant driver and the coupling between the driver and the director is set to maximize the gain. The compactness of resonant type antennas and the broad bandwidth characteristics were both simultaneously achieved in a single Yagi antenna [4] where a microstrip to CPS transition balun used adds to the profile length. With the compactness and broad bandwidth addressed by antennas in [4] and [5], papers [6] and [7] focus on improving the antenna gain using techniques of a microstrip fed inset patch as the driver, with parasitic patches added as directors to enhance the gain. The dipole feeding point in this antenna design is based upon [8], where the antenna operates in the 2-4 GHz band with a gain around 5 dBi over the band. Since Yagi-Uda antennas or the endfire antennas in general are protrude-out-of-wall configurations, it adds immensely if this dimension of profile length could be minimized while retaining the gain characteristics. The novelty of the antenna that is presented in this chapter is three-fold: It offers the characteristics of [4-7], proposes a feeding structure to minimize the profile length and adds around 3 dBi to the gain of a basic Yagi antenna by incorporating a specific novel arrangement of arc shaped parasitics in front of the driver dipole. This launches the surface waves in a better way and aids in their transformation into directional far-field components.

This chapter introduces a 6 dBi endfire antenna element operating with a bandwidth of 1.5 GHz around 14 GHz. The driving function to attain this gain is the shape and the fashion in which

the directors are arranged: inspired from fibre optics operational principle. A prototype of the low-profile antenna element which measures a square cm across has been fabricated and experimentally validated. This antenna element can find potential application in antenna arrays where multiple highly directional beams are required such as Multi-user Massive MIMO for 5G communications.

The chapter is organized as follows: The antenna element design principle is introduced first, followed by the design procedure, the antenna fabrication and experimental validation of the fabricated antenna element.

3.2 Antenna Element Design Principle

The design philosophy adapted rests on the use and integration of three basic elements that form the antenna design: the driver dipoles, the printed reflector and the parasitics. The antenna was brought into operation over an evolved sequential design following first principles. In the following, the design of each of this is discussed.

3.2.1 Driver dipoles:

The substrate chosen has a dielectric constant $\epsilon_r = 3.55$ and $\tan \delta = 0.0027$ and has a thickness of 0.508 mm. The substrate area was so chosen to mitigate the surface waves and the fringing edge effects to a considerable extent by maintaining a peripheral distance between the structure to the boundaries greater than a quarter wavelength. The substrate area was thus set to 12 mm x 11 mm. A $\lambda/2$ printed dipole centred at the chosen frequency of 14 GHz was designed. The arms of the dipole were chosen to be printed on the opposite sides of the substrate to act as a self-balancing structure. The Figure 3.1 shows the front view of the design of an arm of the dipole on the substrate and the Figure 3.2 shows the back view of the other arm. Initially, the length of each arm was selected as $\lambda_0/4$ at 14 GHz, equal to 5.35 mm. The length of arm was later fine-tuned through full wave simulations to 3.9 mm to have the band centred at 14 GHz. A parametric variation of the arm length and its effect on return loss is shown in Figure 3.3. For this parametric variation other parameters such as the transition length and width, the reflector length and width are kept constant and only the arm length is varied in steps of 0.25 mm, displaying the tuning behaviour over the 12 GHz to 18 GHz range for an arm length variation from 3 mm to 5.25 mm. This tuning behaviour demonstrates the potential of the antenna to be reconfigured in frequency.

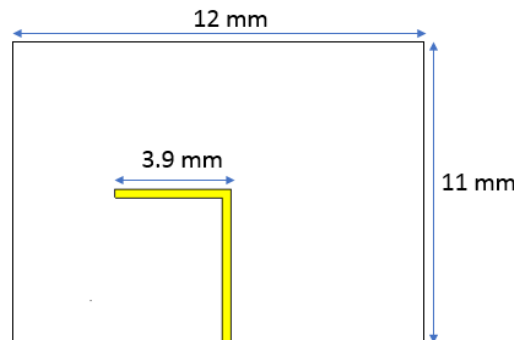


Figure 3.1 Front view of the dipole printed on the substrate

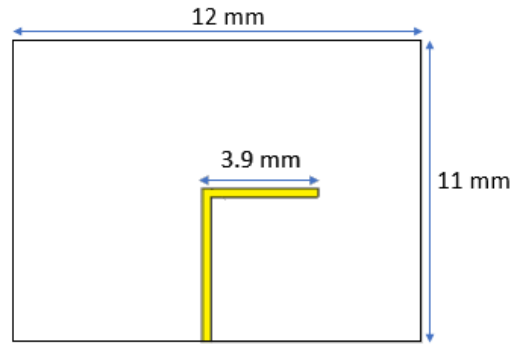


Figure 3.2 Back view of the dipole on the substrate

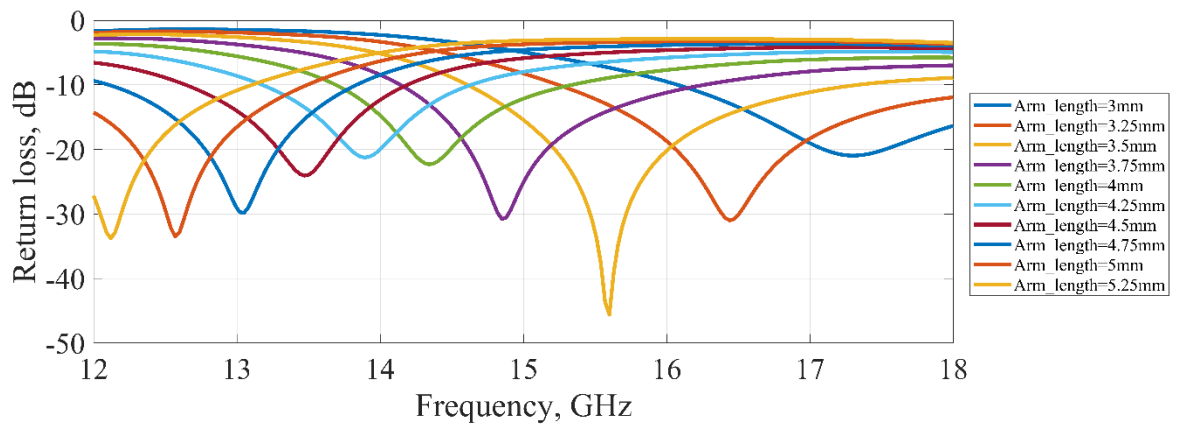


Figure 3.3 Variation of frequency response with dipole arm length

3.2.2 The printed reflector

The antenna design requires a printed reflector to enhance the directivity and the Front-to-back ratio. The design of the printed reflector is performed to use the reflector both as a ground and as a supporting structure to the SMA feeder connector. This requirement makes the reflector a stepped design with the length of the section facing the SMA near to $\lambda_0/4$ at 14 GHz and equal to 5.5 mm. The actual reflector length is $\lambda_0/2$ at 14 GHz equal to 10.7 mm. The final printed reflector, which is printed on the face opposite to the side where the SMA pin connects, is shown in Figure 3.4 with its optimized dimensions.

A parametric study was performed over the transition width (tx), length (tz) and the reflector length (ref_x). As shown in Figure 3.5, the reflector length variation (ref_x) does not affect the frequency behaviour excessively. This strengthens the dependence of the frequency behaviour of the antenna mainly on the arm length as shown in Figure 3.3 with the reflector aiding in enhancing the front-to-back ratio. A redesign of the reflector is needed for each tuning frequency. It was observed that the transition dimensions affect the amount of realizable cross polar levels. A parametric study of this dependence was performed by varying the transition length (tz) and transition width (tx) vs the observable cross polar levels at Phi0 and Phi90 principal cut planes and results are shown in Figures 3.6-3.9. It was seen that the effect of varying the transition width (tx) is not as pronounced as the effect of varying the transition length (tz). Variation of tz controls the observable cross polar levels. As seen from Figure 3.9, a substantial increase in the cross polar levels is seen for variation over tz around the boresight.

The length before the transition step is a crucial factor that controls the cross polar levels of the antenna and therefore has been deduced to be equal to 1.66 mm both by considering the surface current distribution as shown in Figure 3.10 and the cross polar levels of the pattern. Here the surface current distribution is stronger on the dipole arms for the depicted cases of absolute surface current phase of 0,90 and 180 degrees, showing the reflector performs the field enhancement through reflection. The full wave solver calculated values of the cross polar levels after the full design of the antenna helps also in deciding the transition step length of $t_z=1.66$ mm and plays a critical role in the design.

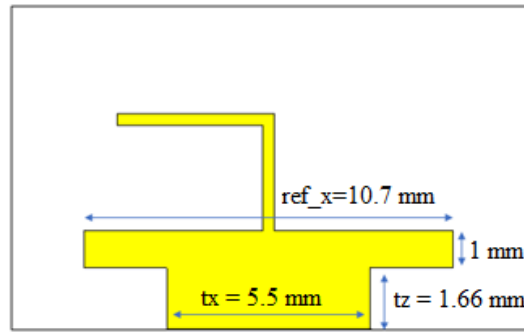


Figure 3.4 Printed reflector profile

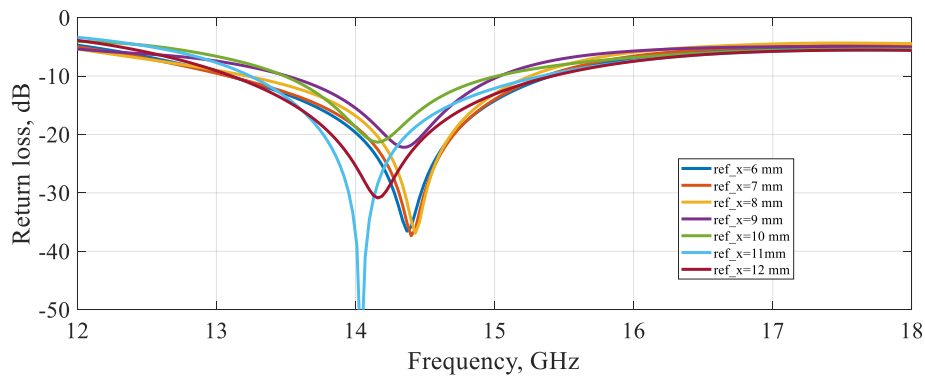


Figure 3.5 Effect of the variation of ref_x on return loss frequency response

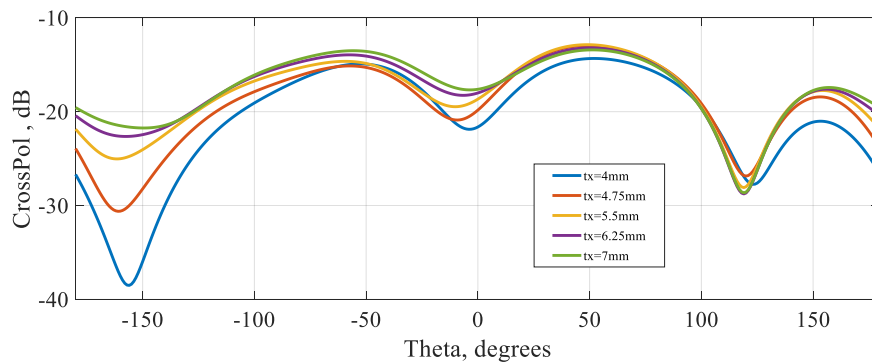


Figure 3.6 Effect of the variation of tx (transition width) on cross polar level for Φ_0 plane

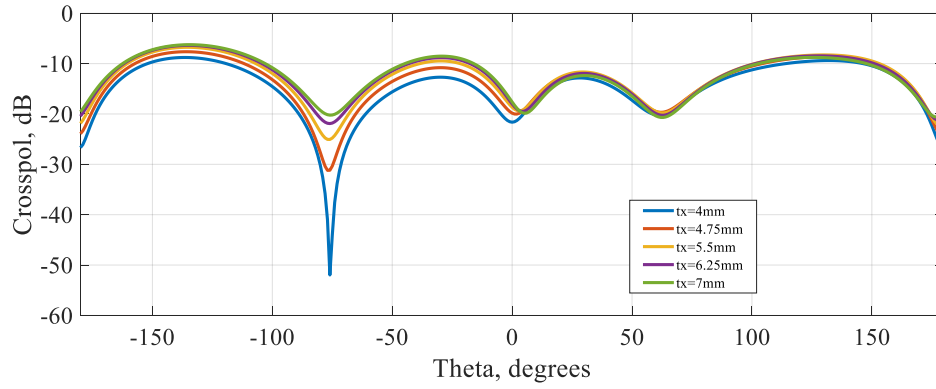


Figure 3.7 Effect of the variation of tx (transition width) on cross polar level for Phi90 plane

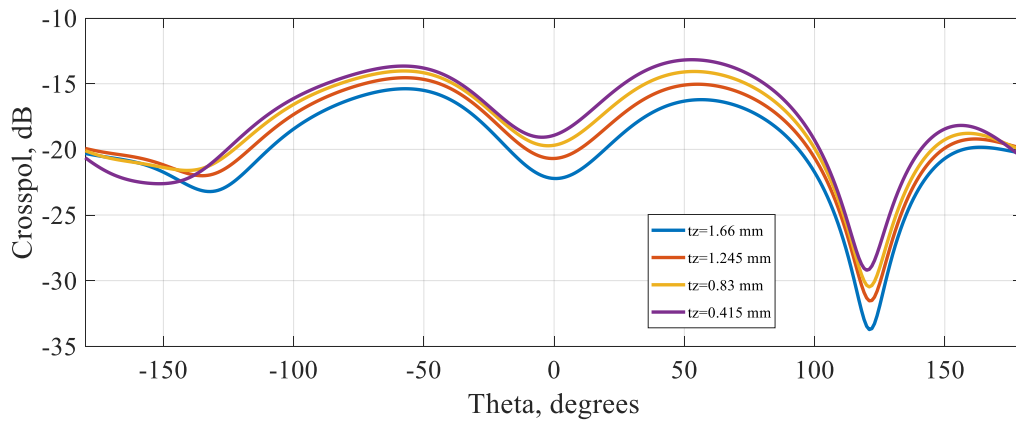


Figure 3.8 Effect of the variation of tz (transition length) on cross polar level for Phi0 plane

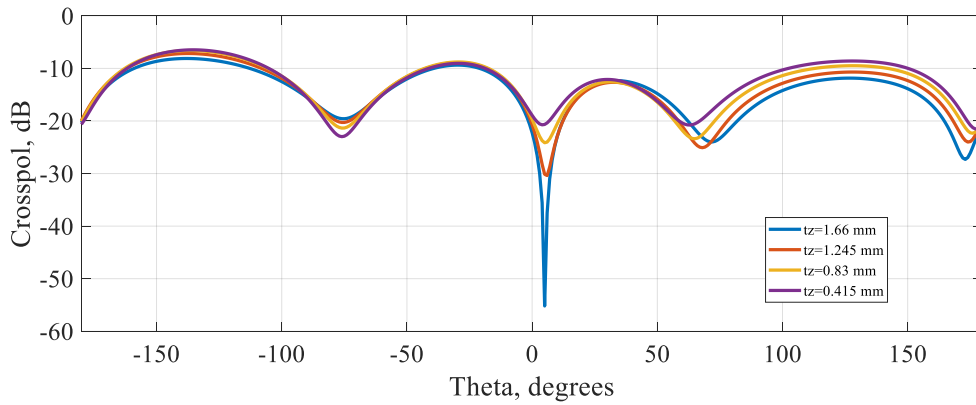


Figure 3.9 Effect of the variation of tz (transition length) on cross polar level for Phi90 plane

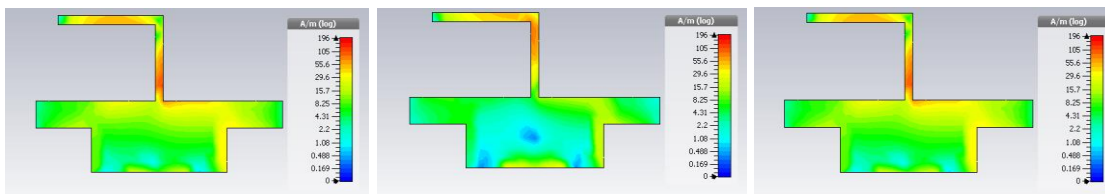


Figure 3.10 Surface current distribution on the reflector at phase 0°, 90° and 180° at 14 GHz.

3.2.3 The parasitics

In Figure 3.10 the surface current distribution shows the currents strongly distributed on the dipole arms. It is intended to couple the electric field due to this onto the parasitics in a constructive way to enhance the far field gain. To achieve this a systematic distribution of parasitics is proposed. The first parasitic that couples the dipole arm field is a rectangle shaped parasitic as shown in Figure 3.11. The electric field coupled onto this rectangle shaped parasitic is distributed along two oblique directions, using two symmetrically placed square parasitic elements, whose dimensions are $0.05\lambda \times 0.05\lambda$ that translates to $1\text{mm} \times 1\text{mm}$; each suitably spaced from each other to enhance coupling, while equally distributing the electric field along two symmetric oblique directions. Figure 3.11 shows the rectangle shaped parasitic and the two square parasitics coupling onto the dipole. The capacitive coupling gap between them was set to maximize the coupling.

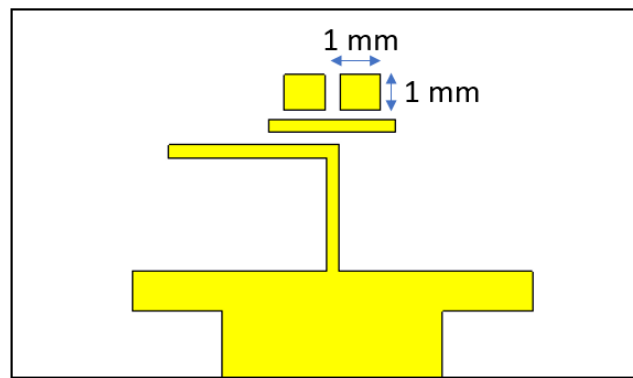


Figure 3.11 Rectangle shaped parasitic and the two square parasitics coupling onto the dipole.

In the following, the design of the arc shaped parasitics is discussed. The shape of the parasitics to channel the electric field obliquely was chosen as an arc to maximize the coupling by maximizing the amount of exposed surface area that couples onto the next parasitic. The fibre optics principle was used to position the parasitics along the antenna plane in front of the square resonators. The design derives its inspiration from a graded index fibre optic cable that operates on converting the substrate into a graded refractive index material whose real refractive index is maximum at the centre and decreases towards the edges. This is achieved by the methodical placement of the arc shaped parasitics in front of the driver dipoles over the antenna plane. The procedure to arrive at this is discussed next.

The dielectric substrate used in the antenna can be considered a homogeneous slab for the frequencies under consideration. The refractive index is the reconfigurable parameter that is used to direct the mechanism of radiation. Then according to [9], the general procedure for the retrieval of the material parameters, in this case the real part of the refractive index is as follows: The arc shaped parasitics are placed in such a way to focus the electric field towards the boresight axis. A one-dimensional transfer matrix T relates the fields on one side of a slab to the other. For a homogeneous 1D slab, it takes the form:

$$T = \begin{pmatrix} \cos(nkd) & -\frac{z}{k} \sin(nkd) \\ \frac{k}{z} \sin(nkd) & \cos(nkd) \end{pmatrix} \quad \dots (3.1)$$

where n is the refractive index, z is the wave impedance, k the wave number and d the thickness of the slab. A scattering matrix relates the impinging field amplitude to the outgoing field amplitude. The elements of the S matrix can be related to the elements of the T matrix as in [10]:

$$\begin{aligned} S_{21} &= \frac{2}{T_{11} + T_{22} + \left(ikT_{12} + \frac{T_{21}}{ik} \right)}, \\ S_{11} &= \frac{T_{11} - T_{22} + \left(ikT_{12} - \frac{T_{21}}{ik} \right)}{T_{11} + T_{22} + \left(ikT_{12} + \frac{T_{21}}{ik} \right)}, \\ S_{22} &= \frac{T_{22} - T_{11} + \left(ikT_{12} - \frac{T_{21}}{ik} \right)}{T_{11} + T_{22} + \left(ikT_{12} + \frac{T_{21}}{ik} \right)}, \\ S_{12} &= \frac{2 \det(T)}{T_{11} + T_{22} + \left(ikT_{12} + \frac{T_{21}}{ik} \right)} \end{aligned} \quad \dots (3.2)$$

For a homogeneous slab from equation (3.1),

$$T_{11} = T_{22} = T_s \text{ and } \det(T) = 1$$

And the S matrix is symmetric. Using the information in equation (3.1) we can derive

$$S_{21} = S_{12} = \frac{1}{\cos(nkd) - \frac{i}{2} \left(z + \frac{1}{z} \right) \sin(nkd)} \quad \dots (3.3)$$

$$S_{11} = S_{22} = \frac{i}{2} \left(\frac{1}{z} - z \right) \sin(nkd) \quad \dots (3.4)$$

Solving equation 3.3 and 3.4 for n and z yields [9]:

$$n = \frac{1}{kd} \cos^{-1} \left[\frac{1}{2S_{21}} (1 - S_{11}^2 + S_{21}^2) \right] \quad \dots (3.5)$$

$$z = \sqrt{\frac{(1 + S_{11})^2 - S_{21}^2}{(1 - S_{11})^2 - S_{21}^2}} \quad \dots (3.6)$$

The design principle of the antenna revolves mainly around equation (3.5) which gives the expression for the refractive index as a function of the reflection and transmission S parameters

and the slab length d . The application of equation (3.5) is first performed over a single unit cell of the arc shaped parasitics (ASP) as shown in Figure 3.12. The unit cell is excited by waveguide ports excited on the two faces of the dielectric slab on which the ASP is printed. On running the simulation in a full wave solver for the desired frequency of interest, the S11 and S21 values can be obtained. The length of the arc of the ASP is 1.7 mm about 1/10 of the wavelength at 14 GHz.

Of the total 10 ASPs selected to enhance the endfire gain, five are on the left side of the endfire axis and the other five are symmetrically on to the other side. Equation (3.5) is used to calculate the refractive index as illustrated in Figure 3.13 which depicts the way the refractive indices were calculated starting from the end fire central axis, towards the extreme left. Since the structure is symmetrical across the endfire axis, the same calculation of the refractive index holds for the right side as well.

From Figure 3.13, starting from the extreme right, i.e. the central ASP, setting up the S parameter extraction and retrieval of the refractive index on the full wave solver returns values specific to the band of interest and length of the slab d equal to 1mm. This procedure is repeated for other 4 cases of $d=1.5, 2, 2.5$ and 3 mm. The distance along the x axis in Figure 3.13 is not to scale, it is a pictorial representation for clarity purposes of describing the setup. This methodology extracts the real part of the refractive index for this kind of unit cells in a sequential way. Their values as a function of frequency are plotted in Figure 3.14, where the real part of the refractive index variation on the structure is shown, with different curves signifying the distance between the arc shaped parasitic element and the square resonator (d) – 1mm being the closest one near to the central axis and 3 mm for the one on the extreme flaring edges. The imaginary part of the refractive index in these cases is near zero signifying minimum loss in radiating energies.

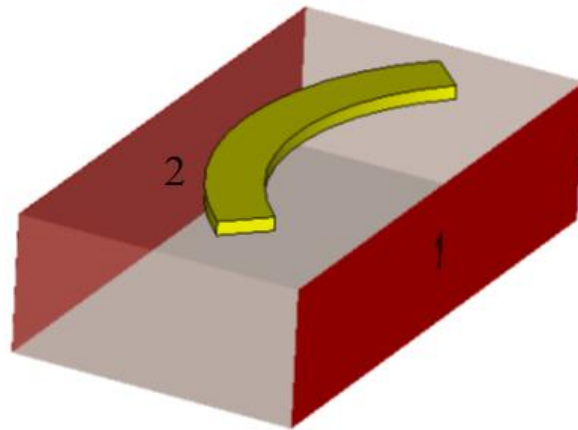


Figure 3.12 A single unit cell of the arc shaped parasitic

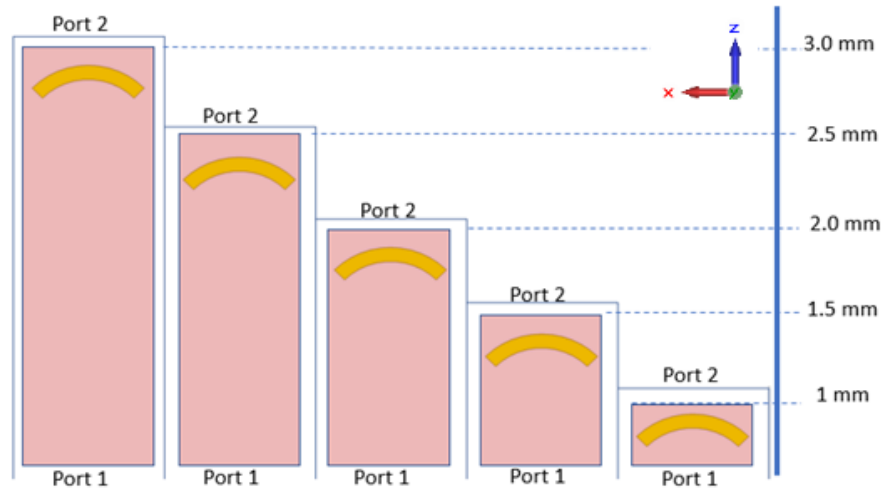


Figure 3.13 Illustration depicting the way of refractive index retrieval

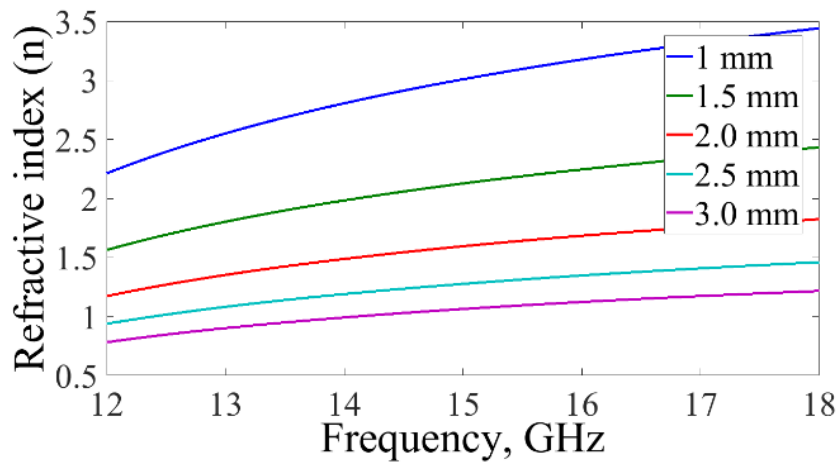


Figure 3.14 Real part of the refractive index of the unit cell parasitic arc shaped resonators from centre towards edges.

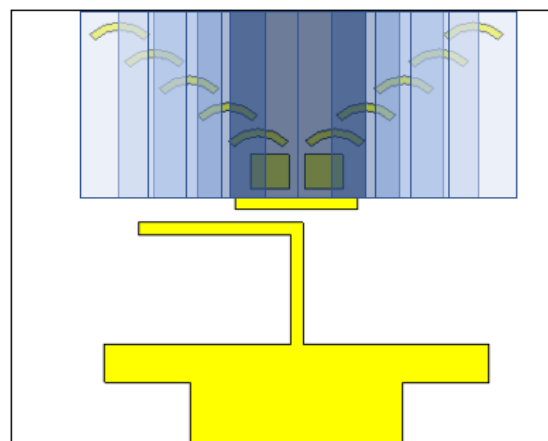


Figure 3.15 Gradient depiction of the gradient variation of the refractive index

Figure 3.15 shows gradient depiction of the variation of the refractive index from the centre towards the edges with dark blue representing the highest real part of refractive index and

lighter shade depicting a decreased value. This distribution of the real part of the refractive index makes the antenna behave analogous to a graded index optical fibre that focuses energy towards the centre increasing the gain of the antenna. The simulation results of the antenna have been presented in [11].

3.2.4 Effect of antenna back plate

The antenna design described above in sections 3.2.1-3.2.3 is fed with a suitably designed 50-ohm coaxial SMA connector (see Figure 3.16(a)). As the goal is to use the antenna in an array, a common mechanical support plate to connect and support multiple antenna elements is needed. The supporting plate is designed with a square hole in the center as shown in Figure 3.16(b). The presence of the supporting plate with a hole has two functions: 1) It sufficiently isolates the ground of the designed antenna and maintains a purity in the tuning of the resonant frequency. 2) It enhances the obtained gain pattern by providing for improved cross polar levels. The 3D Co-polar gain radiation pattern obtained out of the antenna without the back plate and with the holed back plate is shown in Figure 3.17. The 3D Cross-Polar gain pattern for the same two cases is shown in Figure 3.18.

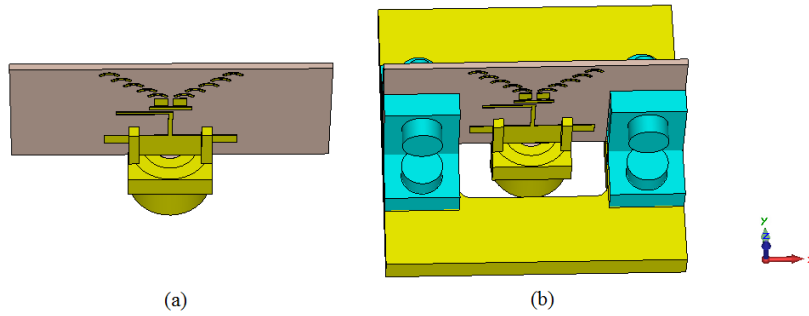


Figure 3.16 (a) Antenna without back plate (b) with holed back plate

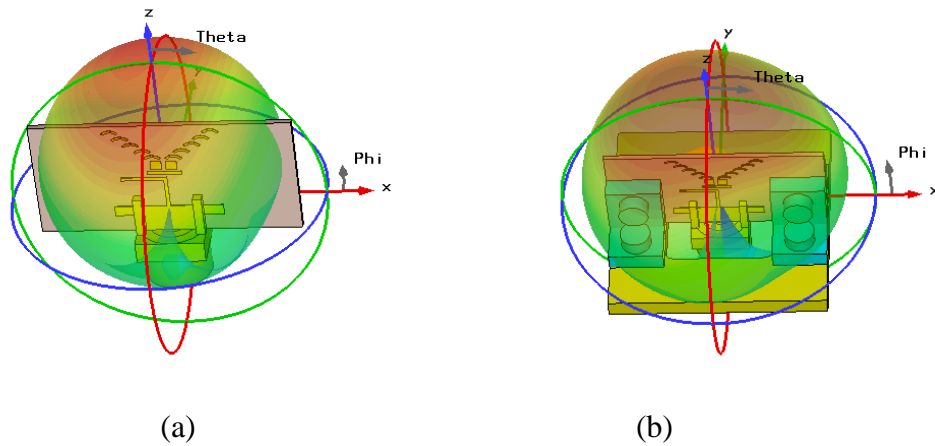


Figure 3.17 3D Co-Polar radiation pattern of the antenna (a) Without back plate (b) With back plate

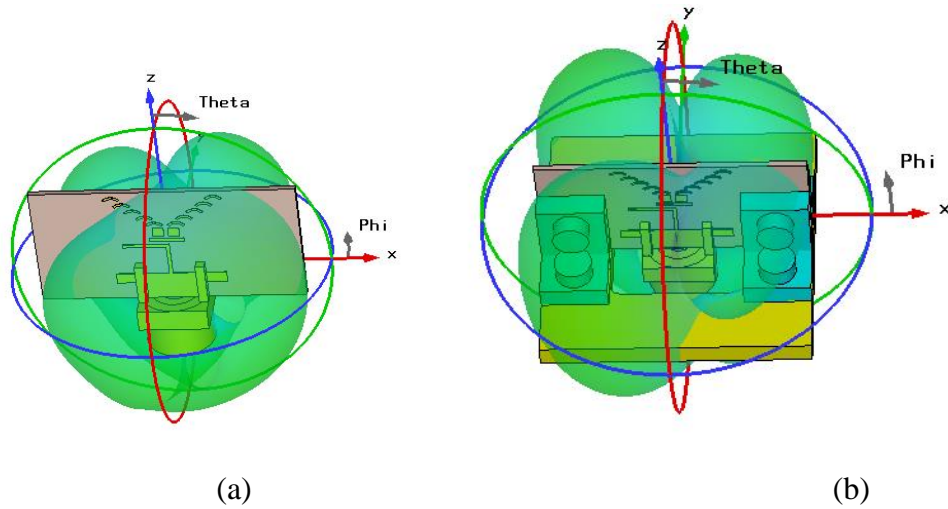


Figure 3.18 3D Cross-Polar radiation pattern of the antenna (a) Without back plate (b) With back plate

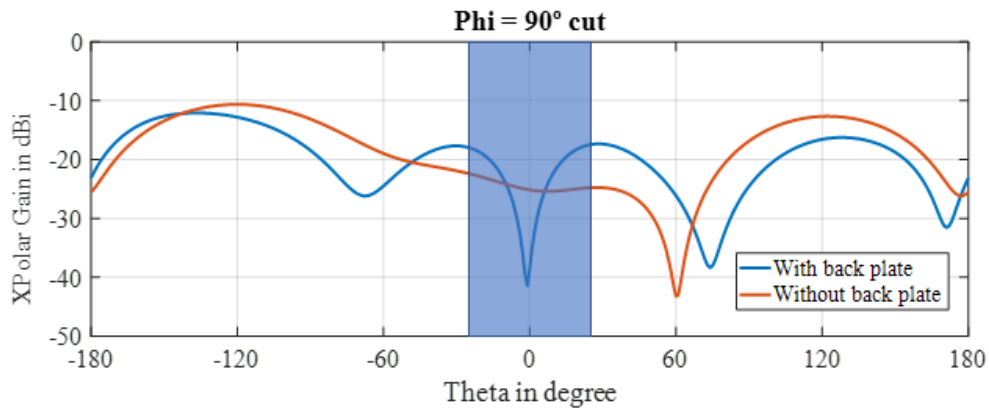


Figure 3.19 Cross polar discrimination (XPD) comparison for cases of without and with back plate

The cross polar discrimination (XPD) improvement for the case with the back plate is compared with the case without and is shown in the cartesian plot in Figure 3.19. It can be clearly seen that the XPD is improved considerably with the use of a holed back plate by 15 dB along the boresight direction for a beamwidth of 20°.

3.3 Antenna characteristics

The complete antenna, as shown in Figure 3.20, consists of a dipole driver element with arms printed on opposite sides of the substrate and a printed reflector to improve the forward radiation. A parasitic rectangular director couples the E-field into the two square parasitic elements that act as driving sources to the arrangement of the arc shaped parasitic unit cell. These are flared in a V shape and spaced 0.2 mm from each other. The dimensions of the proposed quasi-Yagi antenna are shown in Figure 3.20. The simulations were carried out in Ansoft HFSS.

The antenna has an operational band from 13.5 to 15 GHz, with a fractional bandwidth of 10.52 %. The simulated return losses of the antenna are shown in blue dashed line in Figure 3.21: a

10 dB return loss bandwidth of approximately 1.5 GHz around 14 GHz is obtained. The energy channelling behaviour of the arc shaped transitions is illustrated by the simulated current densities shown in Figure 3.22 at 14 GHz. A slight asymmetry of the current distributions can be observed that explains the approximately 20 degrees deviation of the maximum on the elevation cut shown for both theoretical and measurement results on Figure 3.23(a). An almost symmetric response is obtained in the azimuth cut shown in Figure 3.24(a).

To check the validity of the proposed structure the prototype shown in Figure 3.24 was fabricated and measured in an anechoic chamber, with the printed antenna backed by an aluminium supporting structure, with a square gap in the middle to allow for the SMA feeding and to enhance the XPD.

The return losses measurement results are compared in Figure 3.21 with the simulated ones with good agreement between them. Besides, both principal pattern cuts as well as boresight direction (0°) gain were measured in a far field anechoic chamber, directly attaching the prototype to the support plate of the roll over azimuth positioner, whose dimensions are much larger than the base of the fabricated prototype of Figure 3.25.

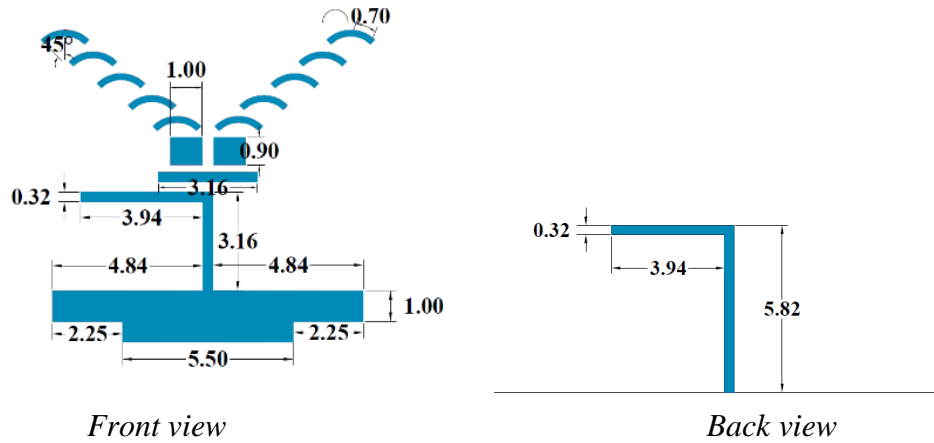


Figure 3.20 Low profile, high gain Quasi-Yagi antenna element dimensions.

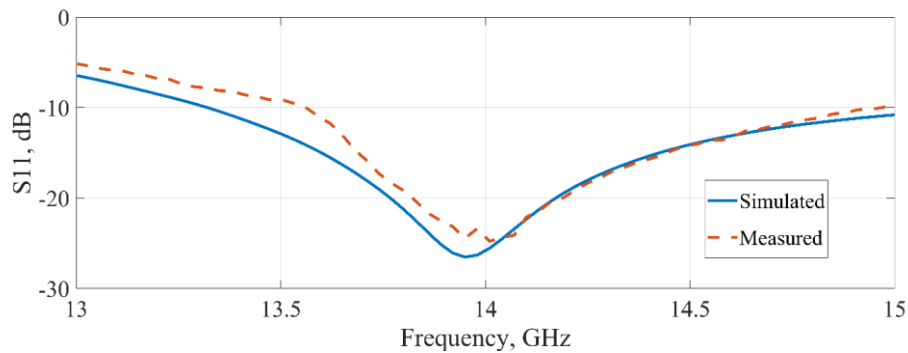


Figure 3.21 Simulated and measured return loss behaviour of the antenna element operating from 13.5 GHz to 15 GHz for 10 dB return loss.

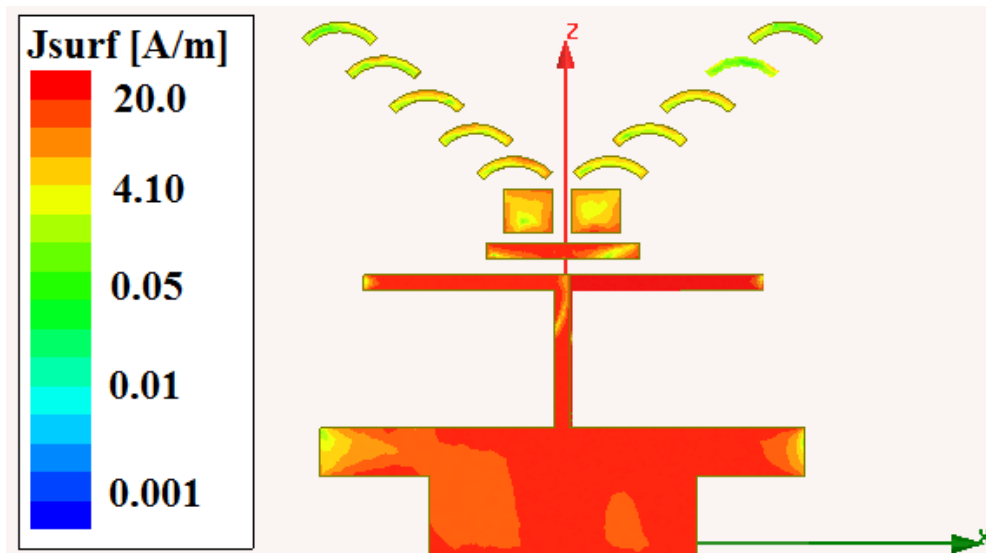


Figure 3.22 Surface current distribution at 14 GHz.

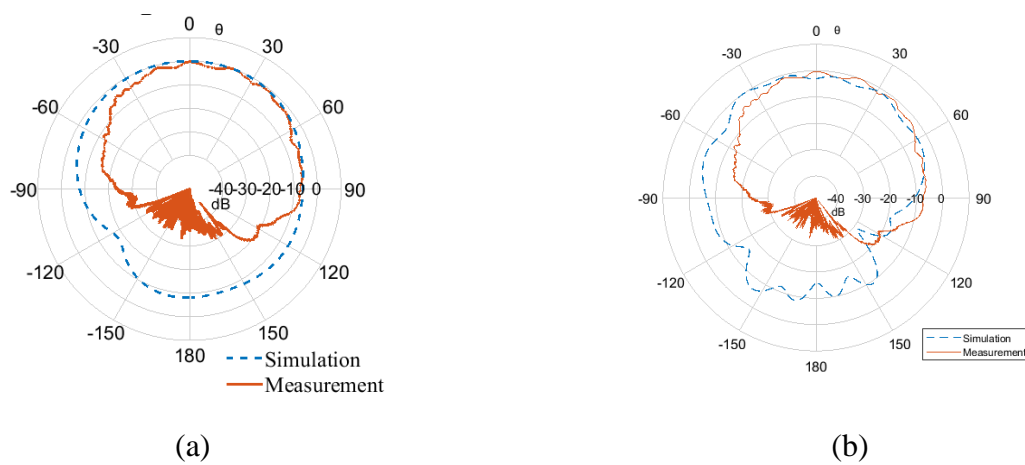
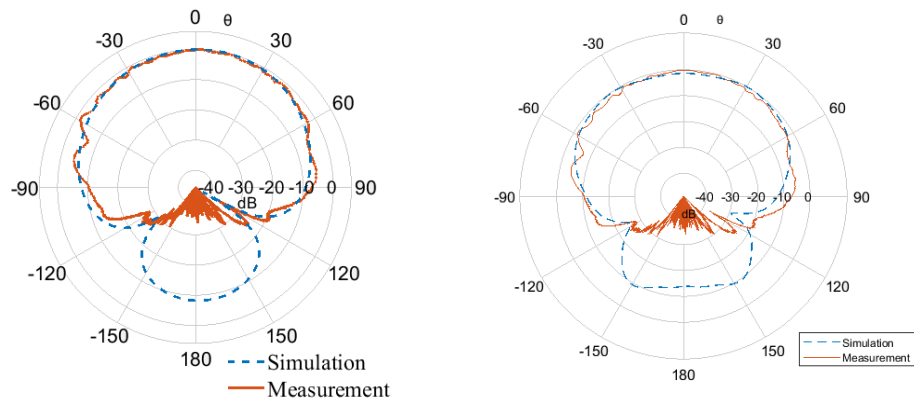


Figure 3.23 Comparison of simulated and measured elevation cut (a) simulation curve is without anechoic chamber backplate (b) Simulation curve is with anechoic chamber backplate.

Quasi-optics endfire antenna element



(a)

(b)

Figure 3.24 Comparison of simulated and measured azimuth cut (a) simulation curve is without anechoic chamber backplate (b) Simulation curve is with anechoic chamber backplate.

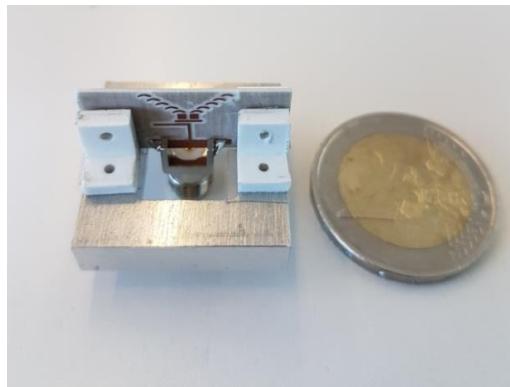


Figure 3.25 Fabricated prototype with size of a square cm and the supporting structure.

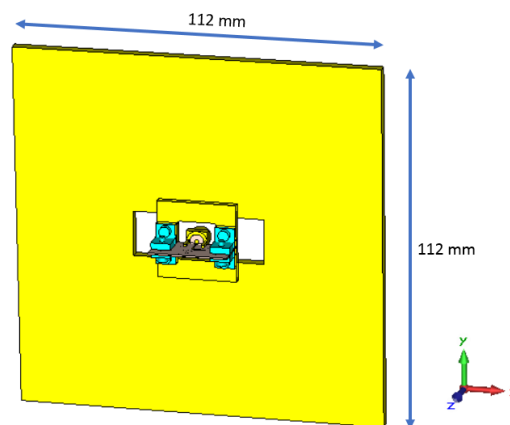


Figure 3.26 Anechoic chamber support

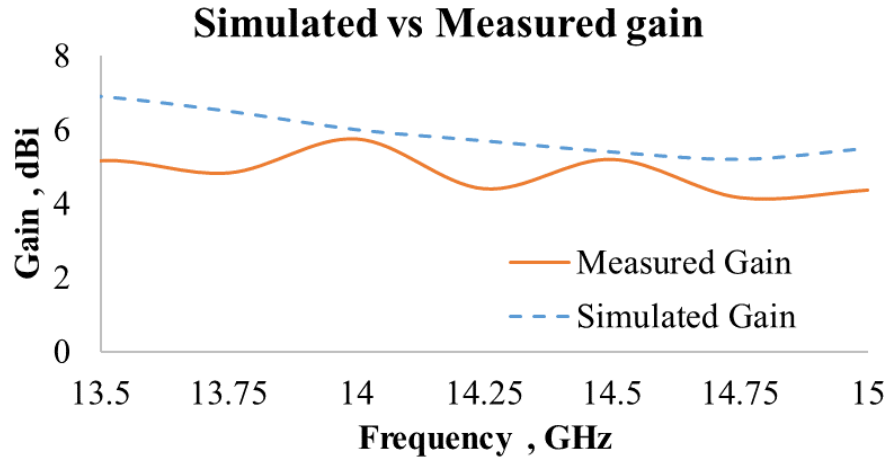


Figure 3.27 Simulated and measured gain plot vs frequency

The model of the support plate is shown in Figure 3.26 to give a comparison of the size. The simulated (blue dashed lines) and measured (red lines) radiation patterns for the co-polar component are compared in Figures 3.23 and 3.24 for both principal planes, elevation and azimuth cuts, respectively. On these Figures the measurements are compared with both the simulations without the support plate (a) and with the support plate (b) included in the model. Taking into account that the large size of the supporting plate generates a reflected signal that adds to the prototype radiation causing an increased degradation of the measured patterns when departing from boresight (0°), that both the roll positioner and mast covered by absorbers block the measured signal in the back side, and that a deviation of approximately 20° from boresight of the maximum results from the asymmetry of the radiating structure, reasonable agreement between measurements and simulations is obtained.

Moreover, the gain of the antenna was measured using the two-antenna method for its variation over frequency. The simulated (blue dashed line) and measured (red line) gains in the boresight direction are compared in Figure 3.27. A gain variation of 1 dB is seen in the band of interest that can be attributed to the ripple associated to the variations of the direct and reflected signal with frequency. The measured gain at 14 GHz was around 6.0 dBi and keeps around 0.5 dB below the theoretical one in the 10 dB return loss bandwidth. Based on these results and preliminary theoretical checks of some modifications of the structure, oriented to symmetrize the current distributions on it, the optics inspired design methodology for low profile endfire antenna proposed can be considered experimentally validated. The antenna element has been used as basic element for the array designs in next two chapters.

3.3.1 Possible alternate realization of the antenna

The antenna design discussed in the previous section has the arc shaped parasitics distributed on the same side of the driver dipole. Further symmetry in the surface current flow and thus symmetry in the radiation pattern can be introduced by displacing an arm of the V shaped arc resonators onto the back side of the substrate. The E field coupling is achieved by splitting the rectangular parasitic into two and moving the corresponding square parasitic to the back as shown in Figure 3.28(a) front view and Figure 3.28(b) back view.

Quasi-optics endfire antenna element

The simulation results of the antenna showing the surface current distribution on the antenna arms is shown in Figure 3.29 for the vector currents and Figure 3.30 for the surface plot at 14 GHz.

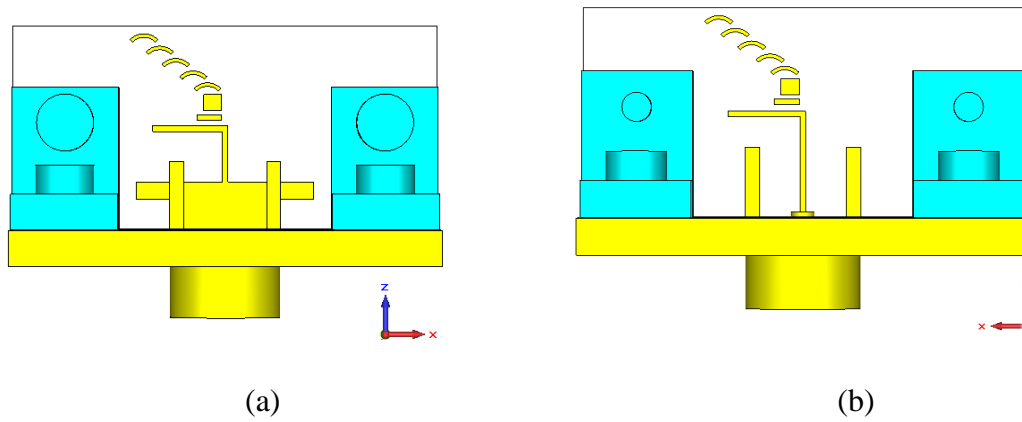


Figure 3.28 (a). Front view (b). Back view

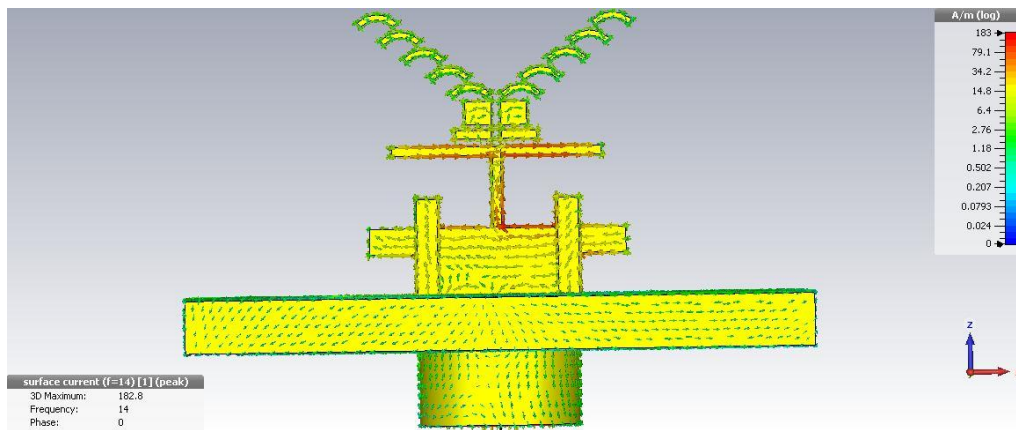


Figure 3.29 Vector surface currents at 14 GHz

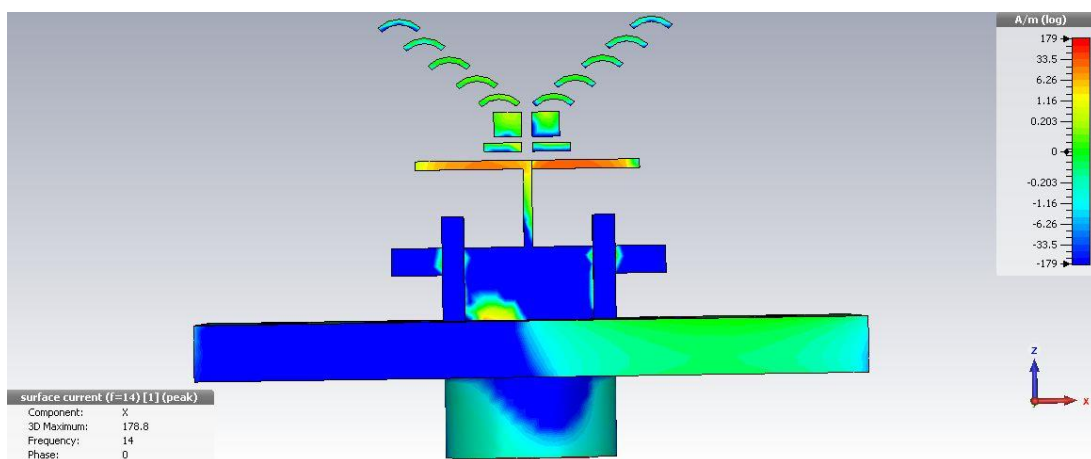


Figure 3.30 Surface currents at 14 GHz

From Figures 3.29 and 3.30 a slight improvement in the symmetry of the current distribution is seen in comparison to Figure 3.22. The radiation pattern plots at 14 GHz are shown in Figure 3.31. The radiation pattern retains its symmetry as in the original design with a good symmetry

in the Phi 90 plane and Phi 0 plane. The premise of this alternate design was to show that the radiation pattern symmetry can be further improved by symmetrically directing the surface currents over the antenna arms.

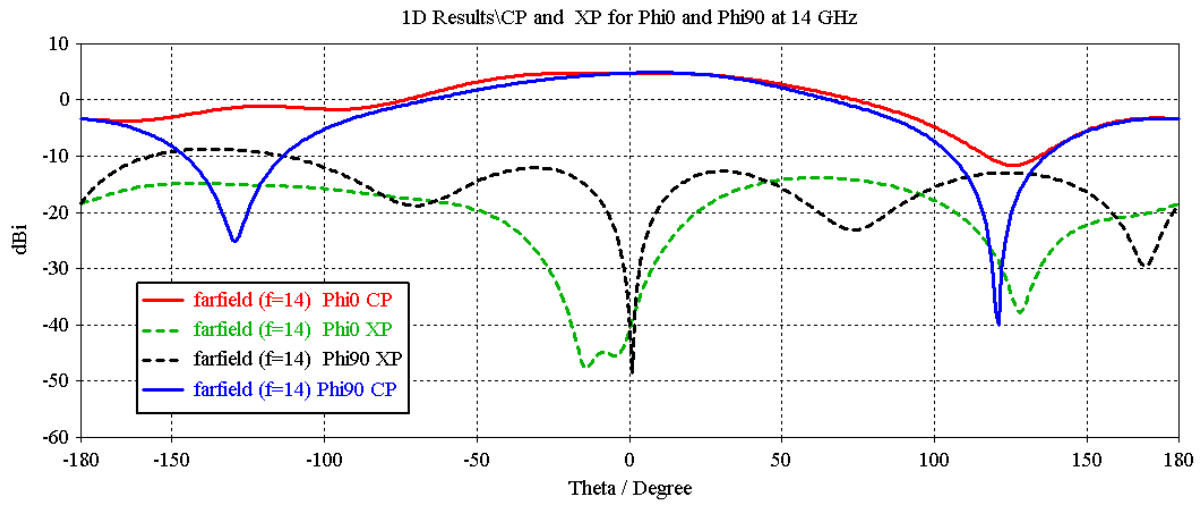


Figure 3.31 Radiation pattern plot at Phi 0 and Phi 90 plane

3.4 Conclusion

A low-profile end fire antenna element inspired on optical principles is presented along with its validation based on measurements from a prototype. The antenna element can find potential use in Multi-user Massive MIMO antenna arrays as well as in multibeam switching antenna arrays for 5G. This is discussed in detail chapter 4.

3.5 References

- [1] “Ericsson 5G delivers 5 Gbps speeds”, Ericsson press release July 2014
- [2] A Harada et al. “5G trials with major Global vendors”, NTT Docomo Technical Journal , Special articles on 5G Technologies towards 2020 deployment, Volume 17, No. 4, April 2016
- [3] P. Fleming, “5G research at Nokia networks”, 5G day at MIT wireless center, May 2015
- [4] N. Kaneda, Y. Qian, and T. Itoh, “A novel Yagi–Uda dipole array fed by a microstrip-to-CPS transition,” in Asia–Pacific Microwave Conf. Dig., Yokohama, Japan, pp. 1413–1416, Dec. 1998.
- [5] W. R. Deal, N. Kaneda, J. Sor, Y. Qian and T. Itoh, "A new quasi-Yagi antenna for planar active antenna arrays," in IEEE Transactions on Microwave Theory and Techniques, vol. 48, no. 6, pp. 910-918, Jun 2000.
- [6] G. R. DeJean and M. M. Tentzeris, "A New High-Gain Microstrip Yagi Array Antenna With a High Front-to-Back (F/B) Ratio for WLAN and Millimeter-Wave Applications," in IEEE Transactions on Antennas and Propagation, vol. 55, no. 2, pp. 298-304, Feb. 2007.
- [7] G. R. DeJean, T. T. Thai, S. Nikolaou and M. M. Tentzeris, "Design and Analysis of Microstrip Bi-Yagi and Quad-Yagi Antenna Arrays for WLAN Applications," in IEEE Antennas and Wireless Propagation Letters, vol. 6, pp. 244-248, 2007.
- [8] J. Floc'h and A. Ahmad, "Broadband Quasi-Yagi Antenna for WiFi and WiMax Applications," Wireless Engineering and Technology, vol. 4, no. 2, pp. 87-91, 2013.
- [9] D. Smith, D. Vier, T. Koschny, and C. Soukoulis, "Electromagnetic parameter retrieval from inhomogeneous metamaterials," Phys. Rev. E, vol. 71, pp. 036617(1-11), Mar. 2005.
- [10] D. M. Pozar, “Microwave Engineering”, 4th Edition, John Wiley and Sons Inc., 2011.
- [11] V. Basavarajappa, B.B. Exposito, L.Cabria and J. Basterrechea, "Millimeter Wave Multi-Beam-Switching Antenna", in Proc. IEEE International Symposium on Wireless Communication Systems (ISWCS), Bologna, Italy, 29-31 Aug. 2017.

Chapter 4

Massive MIMO antenna array

4.1 Introduction

In the quest for antennas that can support high data rates demanded by 5G communications, an interdependent string of requirements that characterize these antennas have recently been developed. Most prominent among these are the requirements of low profile and high radiation efficiencies [1] for the operation of the antennas in millimeter wave. In addition, there is a need for wideband, multi-frequency antennas with simpler fabrication and ease of deployment. At millimeter wave it is well known that the antennas require high gain to combat the high path loss at those frequencies. End fire antennas with directors and aided parasitics help in achieving these high gains. The next plausible step in the design of these antennas is the incorporation of high gain multi-beam capabilities. These techniques are generally based on reflectors, lenses or beamforming circuits [2]. Additional ways to realize multibeam operation, recently have centered around reconfigurable techniques, finite large arrays, beam tilting and beamswitching.

A brief survey of the prevalent antenna array design techniques to realize multibeam is discussed next. Paper [3] introduces a way to beam-switch along the azimuthal plane along 360° without the use of conventional butler matrices, phase feeding networks, or ESPAR based strategies. It uses Quasi-lumped couplers (QLCs) which are a pair of parallel transmission lines separated by two tunable varactors giving rise to a four-port network. The ratio of the power between the input port and the output port of each QLC can be controlled by varying the capacitance of the varactor. A circular cascaded network of the QLCs are used to attain a round-robin way to circulate power to attain operations in both single and multi-mode over Yagi antennas. However, to switch between multiple elements along the circle would mean the design of multiple, multi layered reconfigurable rat race couplers which is a limitation of this proposal. The scalability of the design to higher frequencies would necessitate the consideration of appropriate substrate material considerations and tangent losses, which in turn would limit the radiation efficiencies. [4] presents a way to attain multi-beam radiation using a 3×3 antenna array of probe fed patch antennas without a beamforming network. The probe fed patch antennas are coupled to each other using four microstrip lines that acts as substitute for feeding network. Up to nine beams can be obtained with a gain around 10 dBi. Paper [5] investigates the impact of mutual coupling and edge effects on the gain variation along large arrays. Two arrays made of dipoles and patch elements are compared. It is proposed that due to the omnidirectional pattern of the dipoles the gain variation is more due to the increased mutual coupling between the elements and an increased observed deviation is seen in the embedded element gain. On the contrary in the directional patch elements the coupling is much lower. The arrays are composed of 32 elements each and their performance is evaluated for edge effects in a finite configuration. Paper [6] proposes a way to switch between five beams and tilt each of the beams in the plane perpendicular to the comb line feed. Five parallel comb line feed networks consisting of 3 lines each are fed by a 3-way power divider using RF switch. There are five such RF switches each connecting a triplet of comb lines. The phasing provided to the comb

lines is controlled by changing the length of the transmission lines between the feeding point and the radiating element. The antenna provides tilt in the elevation plane.

A comparison of the proposed antenna array and its operation to the above related works is presented next. In comparison to paper [3], the proposed beamswitching scheme operates in the radiating half-plane rather than in the azimuth 360° plane. It also operates at a frequency of 14 GHz as compared to 1 GHz in the QLC design and does not employ multi-layered rat race couplers for multi-mode beam switching operation. In contrast to the paper [4], which uses beam steering without a feeding network, the proposed antenna array uses a beamswitching scheme with a two-vector state phase feeding network. Multiple simultaneous beams of up to four at a time can be obtained using the proposed feeding scheme. The operational frequency is of the same order. Paper [5] states that in case of the directional patch array there is a lower gain variation between elements at angles closer to the direction normal to array; similar observations have been made and verified experimentally in the proposed 4x4 antenna array. The gain along the boresight is similar with no much variation. Although, along other directions which are oblique to the normal direction there is a slight drop in the gain. The paper [5] also concludes that more directive patch elements are a better choice for Massive MIMO. In comparison to the paper [6], the proposed 4x4 antenna array provides multi beams using a two-vector state beam switching scheme and operates at 14 GHz. The required phasing is provided by the transmission line phasing network.

After this introductory section, that presents a survey of the state-of-art in multibeam antennas and attempts to relate the proposed antenna in the contextual arena with a discussion on the compared features of the different methodologies, the rest of the chapter is organized as follows: Section 4.2 provides the beam switching characteristics of the antenna array and presents the novel two vector beam switching method to generate simultaneous high gain multiple beams. Section 4.3 details the measurements and provides a discussion on the multibeam-pattern and the gain measured. Section 4.4 concludes.

4.2 Antenna Array Design and Beamswitching Concept

4.2.1 Fundamental beam unit

To realize beamsteering or beamswitching, the general procedure followed over an antenna array is to primarily control the way the amplitude and phases are fed into the elements of the antenna array [7]-[9]. Other factors such as the antenna array inter-element spacing, and the individual element radiation pattern also play a crucial role. In course of achieving the desired radiation pattern, which may at times be a single lobe that is steered to oblique angles or multibeam generation, a method called as the antenna pattern synthesis is followed [10]-[12]. This often involves weighting the amplitudes and phases in predefined ways such as the Dolph-Chebyshev or the Binomial distribution where the chosen amplitudes and phases affect the main lobe direction and the SLL. These and other such beamsteering methods are promising owing to the freedom of beam steerability they introduce into the structure. An additional requirement of these methods is that, the distinct phases and amplitude must be actively fed into each element of the antenna array which can often be expensive owing to the use of wideband/multi-band phase shifters and their corresponding active dynamic control. To realize almost a similar functionality using a passive phasing network, it is necessary to have a beamswitching scheme that minimizes the required phase states, so that multi-beam operation can be attained with simpler networks. Such a scheme is proposed in this chapter, that can generate multiple patterns

in certain directions using minimal phase reconfiguration of the feeding network. It uses a unique way to control the direction of the patterns using two phases or binary phase control. This binary phase control of 0° and 180° when applied in conjunction with variation of the interelement spacing can produce unique multi-beam patterns along certain directions. The feeding network can be passive or active, the key point is that the feeding network needs to produce only two phases to generate multi directional beams. A switching between several of such beam configurations emulates the effect of beam steering with minimal loss of spatial and angular resolution. The proposed fundamental beamswitching scheme that is responsible for the multi directional beam operation is discussed next:

The building block for the proposed beamswitching scheme rests on physical principle and observation that the direction of the formed beam aligns along the vector connecting the points where 0° and 180° phases are fed on a two-element array. An additional degree of freedom is offered by the inter element spacing. By controlling the vector alignment using the two phases a corresponding directional beam can be attained. This primary building block based primarily over two antennas can be systematically mapped and extended to larger arrays to attain multi-beam capabilities. The two-element building block requires that the antennas individually are directional and suitably spaced to avoid grating lobes. Owing to the differential way of excitation, a cancellation null is seen along the boresight and the pattern lobes are placed symmetrically around it. The symmetric property arises owing to the symmetrical excitation of the phases. The validation of the building block scheme with depiction of the corresponding vector alignment and beam directions is shown in Figure 4.1.

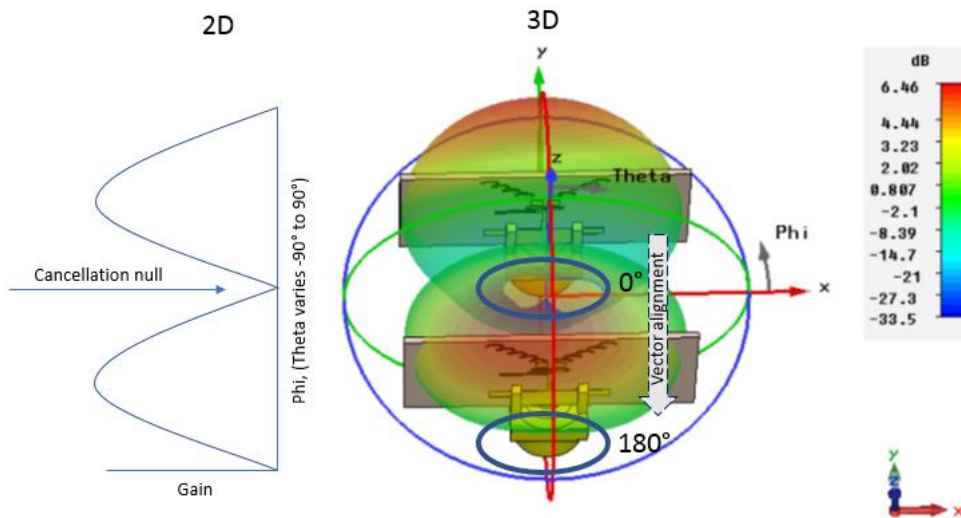


Figure 4.1 Building block of the multi-beam scheme

Consider Figure 4.1, where two directive antenna elements are placed suitably spaced apart to avoid grating lobes. The individual directive antenna element consists of a printed end fire configuration with additional parasitic elements to enhance the directivity along the end fire direction [13] and was presented on previous Chapter. For the sake of completeness, a brief description of the antenna element is as follows: The antenna has an operational band from 13.5 to 15 GHz, with a fractional bandwidth of 10.5 %. It has one arm of the $\lambda/2$ dipole printed on one side of the substrate with $\epsilon_r = 3.55$, loss tangent ($\tan \delta$) = 0.0027 and a thickness of 0.508

mm. The other arm is printed on the back side. A printed reflector is added at the point of connection of the SMA to the substrate to improve the (Front to Back) F/B ratio. The radiation from the dipole being omni-directional is made directional by the reflector and by the parasitic elements, that couple the dipole electric field along the substrate plane. It has a return loss < 10 dB in the band 13.5 GHz to 15 GHz. The endfire antenna element is inspired by the energy focusing graded index fiber optics principle.

Each antenna element is fed by a phase of 0° and 180° respectively with the same unity amplitude. Such an excitation results in the formation of a two-directional pattern along the cut normal to the two dielectric planes ($\Phi 90$). The 3D antenna pattern and its 2D projection are shown in the Figure 4.1. A cancellation beam resulting in the formation of a null divides the pattern into two symmetrical halves. The orientation of the pattern is aligned along the vector connecting the two-phase feeding points. This gives scope to develop a multibeam antenna array, that utilizes a visual representation of the vectors and their correspondingly mapped 3D patterns. The orientation of the beams can be symmetrically controlled for varied interelement distances. A study of the inter element spacings and the dependence of the formation of nulls and the pattern beams on it is shown in Figure 4.2 which, represents the two-element antenna pattern in Figure 4.1 for varied spacings of 0.25λ to 1.5λ . As can be seen in the Figure 4.2, the symmetrical phase excitation results in a well pronounced deep null along the boresight independent of the spacing. This shows that the antenna using this methodology is a suitable candidate for applications, mainly in NLOS and in applications requiring oblique incidence of beams with no beams along boresight. A direct observation from the parametric variation in Figure 4.2 is that the pointing angles of the first beams located symmetrically across the boresight nulls, moves away from the boresight as the interelement spacing decreases. Also, the beamwidth increases with decrease in interelement spacing. For spacings, larger than λ multibeam appear which, when used in larger arrays, can lead to constructive use as multiple lobes of similar magnitude.

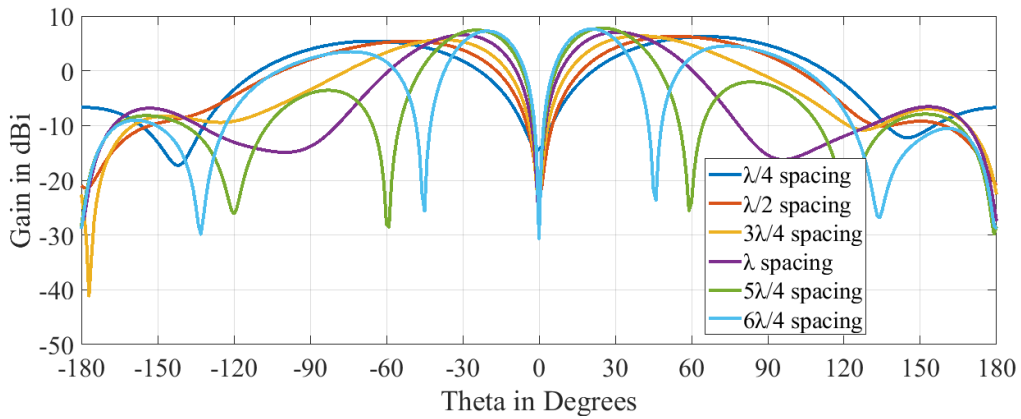


Figure 4.2 Inter element spacing dependent phasing-enforced, beam pointing for two element array.

4.2.2 Antenna Array design

The antenna element described in [13] and analysed on previous Chapter, was used in the 4×4 sub-array design as shown in Figure 4.3. 4×4 subarray validation is chosen as a pre-cursor for the 8×8 array operation. As the proposed beamswitching scheme has an additive symmetry, the 4×4 subarray deductions can be extended onto the 8×8 without loss of generality. The

antenna array interelement spacing was set to 0.8λ lying within the 0.5λ to λ regime to avoid the onset of grating lobes for boresight pattern.

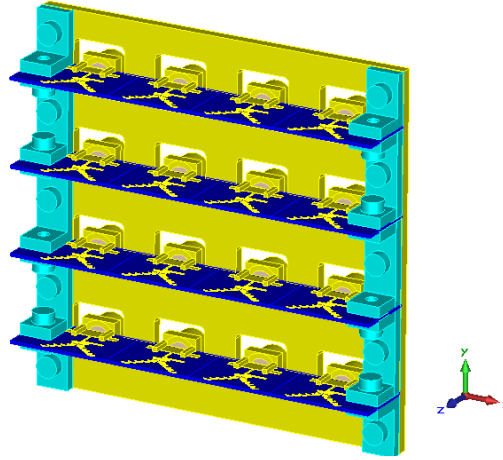


Figure 4.3 Simulation model of the 4x4 array with supporting structure.

The antenna array was simulated using full wave simulations for S parameters and the individual antenna patterns computed were subjected to pattern post processing to test the beam switching scheme. The port to port isolation throughout the array was better than 25 dB. The simulated return loss at the 16 ports is shown in Figure 4.4 and the port-to-port isolation with respect to a selected port (port1) is shown in Figure 4.5.

From Figure 4.4, a similar return loss characteristic for the 16 antennas is seen which is essential in realizing the near identical pattern multiplication with the 4x4 array factor to obtain the switched beams. Figure 4.5 represents a good port-to-port isolation ($< -25\text{dB}$) which helps in isolating the individual patterns and reduces mutual coupling that may influence the current distribution on the neighbouring antenna elements. The simulated radiation efficiency along the embedded ports is shown in Figure 4.6. Around the band 13.5 GHz to 15 GHz the percentage radiation efficiency varies from 96.5 to 98.

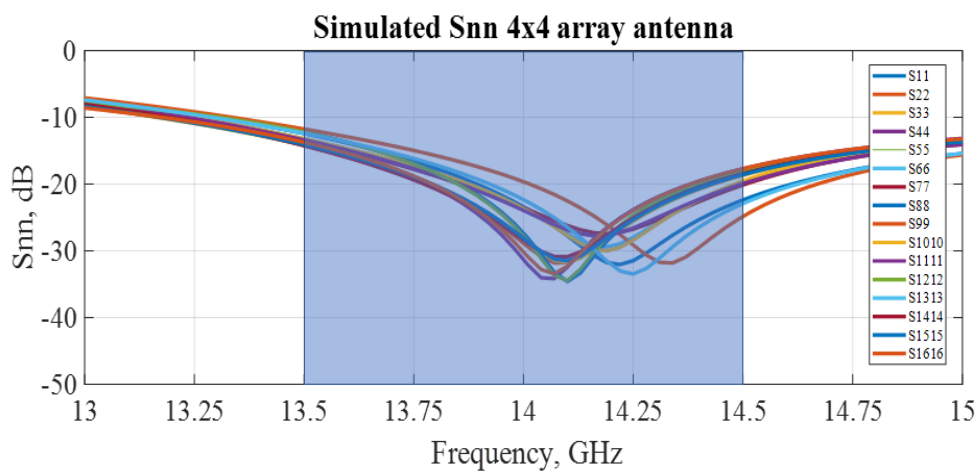


Figure 4.4 Simulated return loss (S_{nn}) of the 4x4 array antenna.

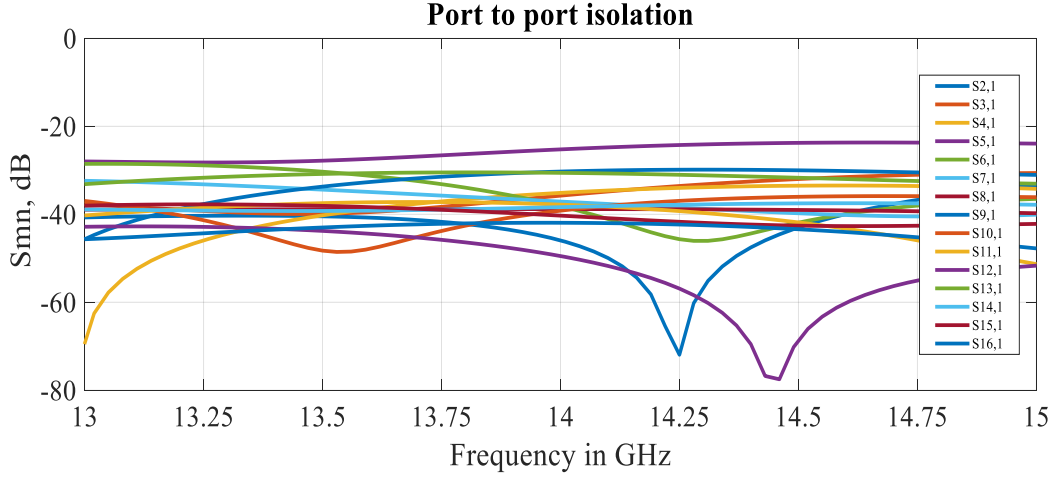


Figure 4.5 Port to port isolation with respect to port 1.

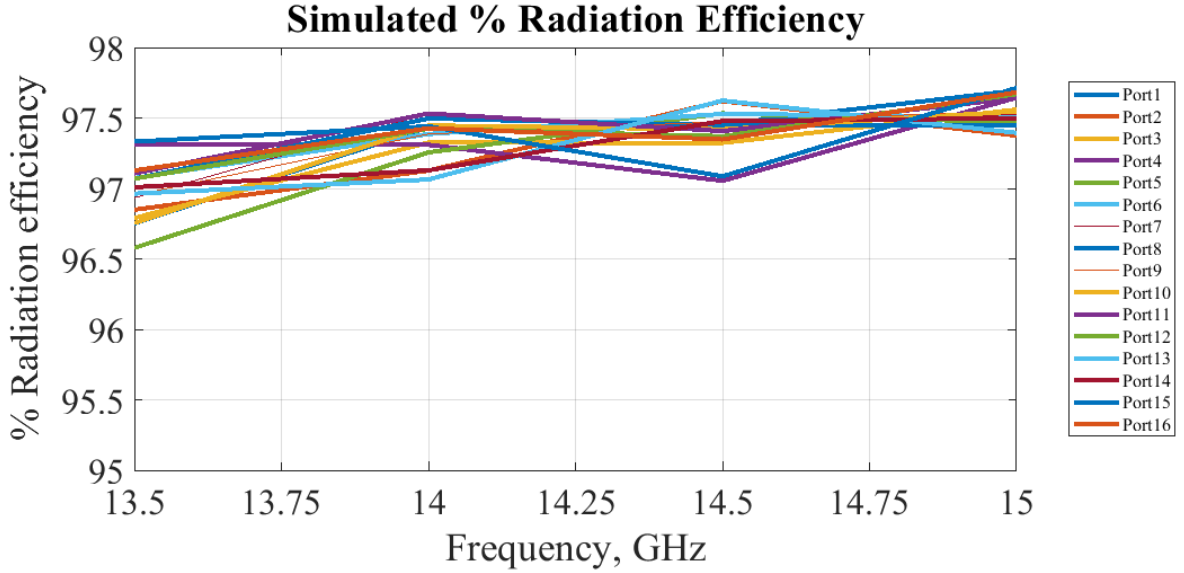


Figure 4.6 Simulated radiation efficiency over the 16 ports.

4.2.3 Phase shifting feed network design

Due to the nature of the proposed beam switching scheme in section 4.2.1, a two-state phase feeding network is necessary to feed into the elements of the antenna array. Since the proposed scheme is phase only, the amplitudes are set to be uniformly distributed over the array. This equal amplitude distribution can be realized by a tree-based corporate feeding network extended to a 4x4 array as shown in Figure 4.8. As the designed beamswitching scheme requires only two-phase states, such a phase feeding network was deemed both simple and cost-effective from the experimental validation point of view.

The phase shifting network in Figure 4.8(a) consists of tailored transmission lines printed on a $\epsilon_r = 3.55$ substrate of thickness 0.508 mm. The methodology adapted for the realization of the feeding network involved identifying the positions of 16 antenna elements in the antenna array and working the feedline backwards to the source. The source port impedance of 50 ohms is transitioned over 100 ohms branching lines along with the use of quarter wave transformer

at 14GHz to realize the network. The 4x4 array was symmetrically divided into 4 sections of 2x2 each and the designed feeding line for a 2x2 network was mirrored symmetrically across the other three sections so that the phase component retains its consistency along the line.

A similar approach was followed in realizing the phase network of Figure 4.8(b) with the difference being that across a half of the network an additional phase delay of 180° was introduced using a U-bend amounting to an additional 180° phase shift. The impedance distribution along the network for the $0^\circ/180^\circ$ phasing network is shown in Figure 4.7. The designed network therefore had 8 output ports at 0° and other 8 output ports at 180° as in the phase response shown in Figure 4.9.

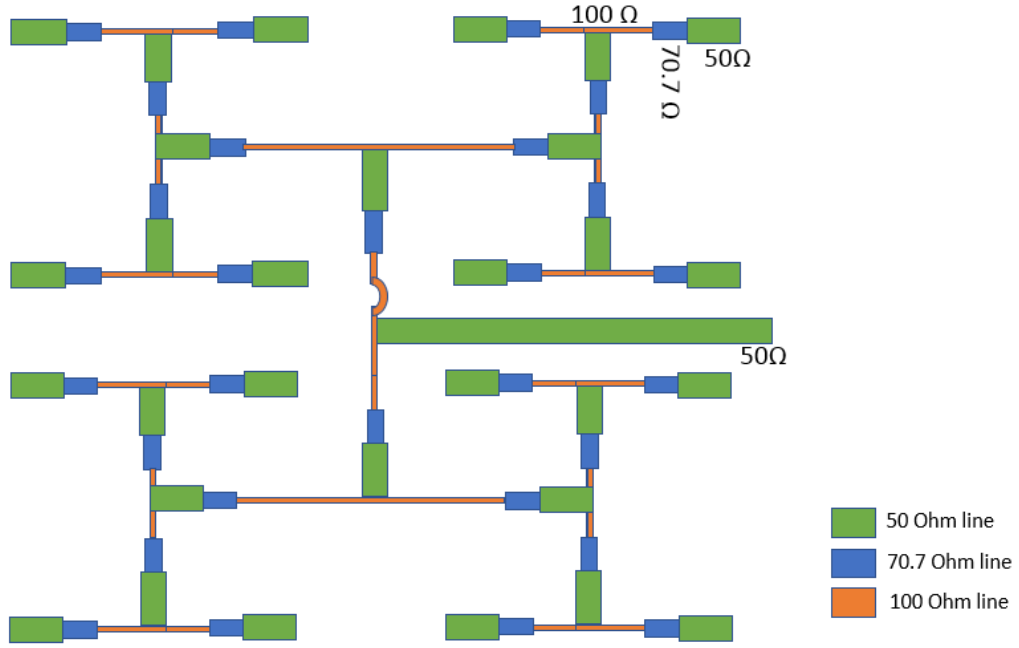
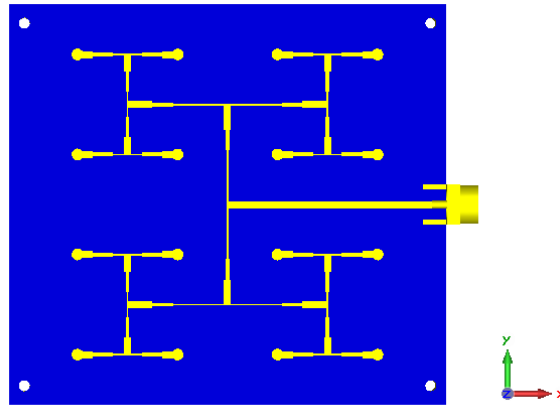


Figure 4.7 Line impedance distribution along the $0^\circ/180^\circ$ phasing network.

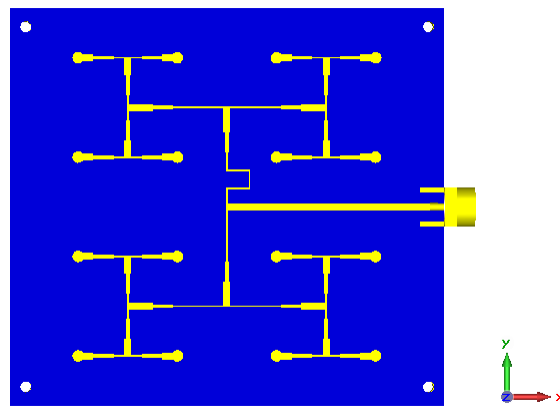
Figure 4.8(c) depicts the back view of the phase feeding network which consists of SMA connectors feeding onto the ports of the phasing network. An edge fed SMA connector was used as the primary source to feed into the phasing network.

4.2.4 An alternate 180-degree hybrid-based feed network

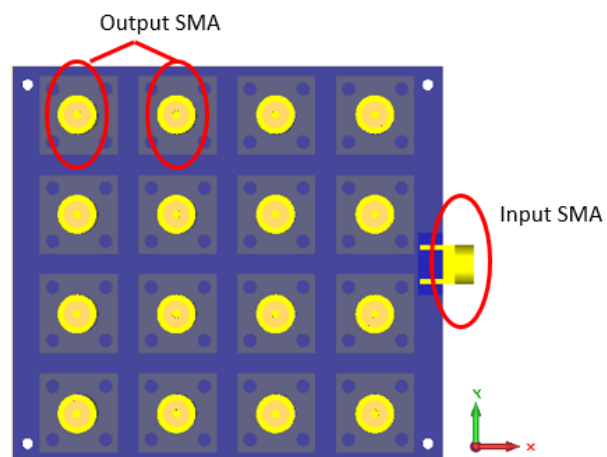
The proposed beamswitching scheme requires two phase states namely the 0° and 180° to realize the different beamstates A to E introduced in next Section. A 180-degree hybrid coupler with the sum and difference ports fed to produce in-phase and out-of-phase signals will fit into the phasing network requirements. A schematic realization of the scheme is shown in Figure 4.10(a), where the input signal is first divided using a 1:8 power divider and each output is fed into the difference port of the 180-degree hybrid with the sum port matched. This results in two output signals of equal amplitude with phases of 0° and 180° . These signals can then be connected to the 16-port antenna as required.



(a) Top view of the all 0° phase network



(b) Top view of the 0° and 180° phase network



(c) Back view of the 0° and 180° phase network

Figure 4.8 (a) Top view of the all 0° phase network (b) Top view of the 0° and 180° phase network (c) Back view of the 0° and 180° phase network.

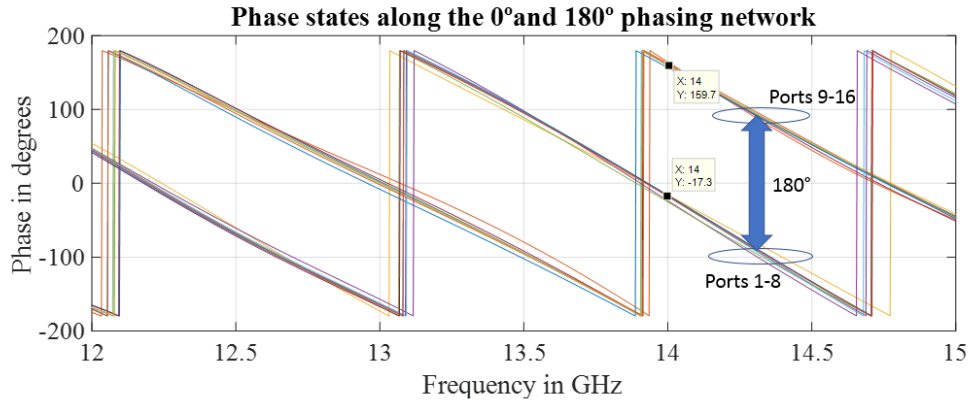


Figure 4.9 Phase response of the dual phasing network of 0° and 180° .

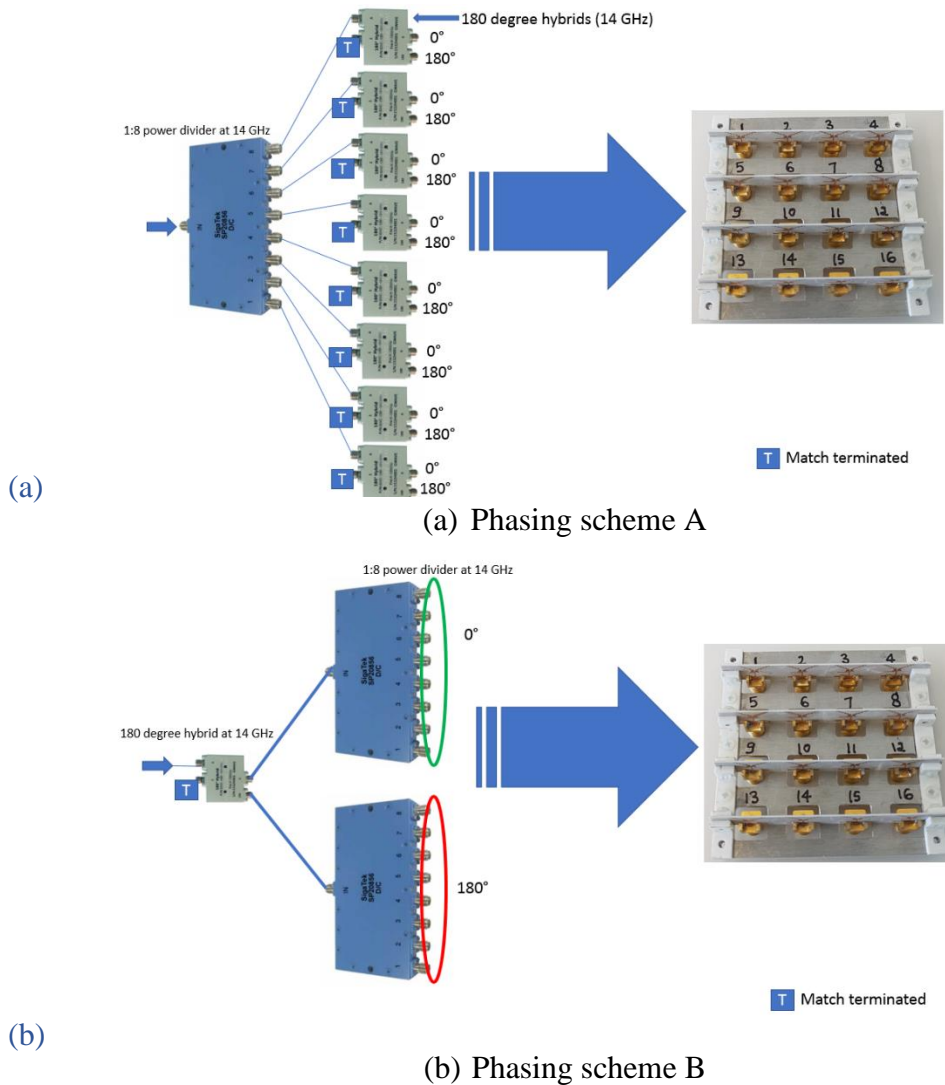


Figure 4.10 180-degree hybrid-based phasing network

Another cost effective-alternative as in Figure 4.10(b) is to feed the input signal to the difference port of the 180-degree hybrid first, with the sum port match terminated. The two

output ports can then be fed to two 1:8 power dividers to obtain eight ports each of 0° and 180° phases respectively along the output. These can then be fed into the antenna as required by the beamswitching scheme. These schemes are valid only for testing the non-boresight cases of B to E and for the boresight case a 1:16 power divider operating at 16 GHz can directly be used. This scheme can be used as a method to validate the different beam states formed, however just as the feeding network designed in section 4.2.3 requires re-connecting cables.

4.2.5 Excitation matrices of the beamswitching scheme

The two-element array building block can be used to construct the multi-beam operation by considering the constructive and destructive sequential addition of the two-element pattern. The table 4.1 explains the way of deriving patterns A to E by their component patterns.

Pattern A is the classical boresight beam which uses a uniform amplitude and phase excitation to obtain the directional beam along the boresight. The mechanism of beam formation is depicted in the second column as an addition of 3 individual beams formed respectively from (array row 1 and 2), (array row 2 and 3) and (array row 3 and 4). Each of these rows have uniform amplitude excitation and equal phase of zero. Row 1 and row 2 add up constructively so does 2,3 and 3,4. The resultant beam is a main beam in the boresight with an increased amplitude.

Pattern B depicts an excitation where (row 1 and row 2) are fed with a phase 0° and (row 3 and row 4) are fed with a phase of 180° . Going by the previous analogy of splitting the 4 rows into 3 groups of 2, Row 1 and row 2 excitation produces a single main lobe. As in the discussion in section 4.2.1, row 2 and row 3 being fed by opposite vectors, produces a split beam with reduced amplitude. Row 3 and row 4 excitation produces the same main lobe as row 1 and row 2. The resultant of the three beams can be viewed as the split central beam whose magnitude is being enhanced by the end beams due to row 1,2 and row 3,4 as depicted in column 3.

Pattern C depicts an alternating opposite vector excitation along the rows 1,2,3 and 4. Thus rows 1,2 and 3,4 give rise to a split beam. The row 2 and 3 also gives rise to a split beam but the vector alignment is in the opposite direction thus effectively acting as a cancellation to the boresight pointing beam of the split beams of row 1,2 and 3,4. The resultant is a beam cancelled over wider angle along the boresight and symmetrically obliquely oriented as in column C4.

Pattern D is used to illustrate that owing to the selection of phases and combined use of thinning of the array, an extra dimension of control, exploiting the interelement spacing can be used to attain multiple lobes when a opposite vector excitation is used. In the pattern, the row 1 is phase tethered with row 4; with row 2 and row 3 match terminated. This emulates a thinned planar array scenario and leads to a four-beam multiple pattern. As a theoretical rule, the number of multiple lobes formed increases with the number of thinned rows.

Pattern E is used to demonstrate that the proposed concept can be used to orient twin symmetric beams along other desired direction using the vector alignment rule discussed in Section 4.2.1. In excitation E the vector alignment is along the $\phi = -45^\circ$ plane through a selected 2×2 sub array feeding, combined with 2×2 sub array and a thinning over the other 2×2 sub arrays along the other diagonal. This leads to a beam oriented along the -45° direction as in column 4 of pattern E.

With the above five states that have been demonstrated and experimentally validated in the following discussion, other multibeam states using the proposed scheme can be realized by one

or more combinations of pattern A to E which in turn are obtained from the fundamental two element split beam block.

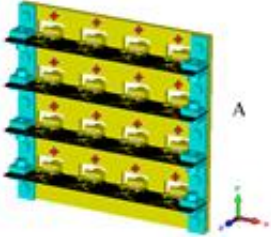
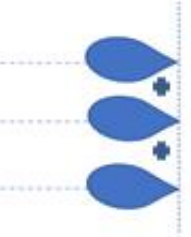

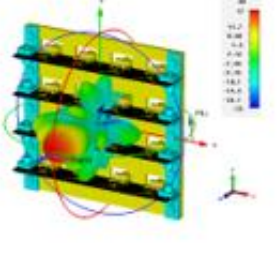
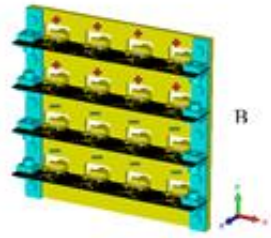
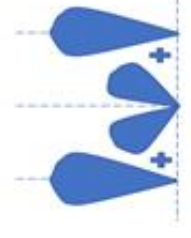

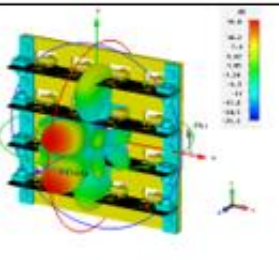
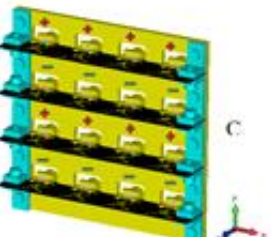


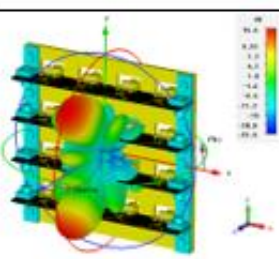
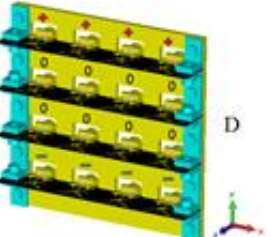


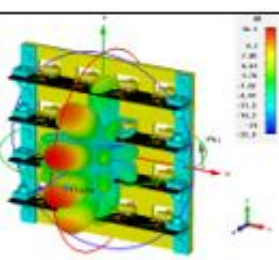
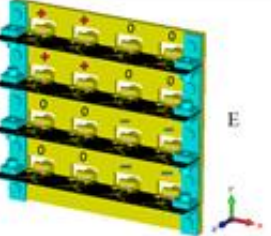


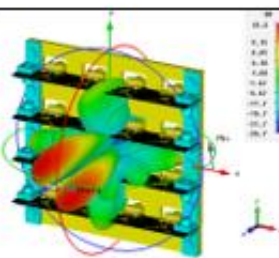
Excitation	Pattern configuration		Full wave solved pattern
	Component patterns	Resultant pattern	
 A			
 B			
 C			
 D	Spacing $> \lambda$ emulates multilobes 		
 E	Phi = -45 plane cut 		

Table 4.1 Demonstration of the two-phase vector alignment Beamswitching scheme.

The different matrices with the antenna excitations as individual elements can be expressed in the matrix form as shown below. These matrices are related to each other by simple matrix operations.

$$\begin{aligned}
 A &= \begin{bmatrix} k & k & k & k \\ k & k & k & k \\ k & k & k & k \\ k & k & k & k \end{bmatrix} \\
 B &= \begin{bmatrix} k & k & k & k \\ k & k & k & k \\ -k & -k & -k & -k \\ -k & -k & -k & -k \end{bmatrix} & C &= \begin{bmatrix} k & k & k & k \\ -k & -k & -k & -k \\ k & k & k & k \\ -k & -k & -k & -k \end{bmatrix} \\
 D &= \begin{bmatrix} k & k & k & k \\ 0 & 0 & 0 & 0 \\ 0 & 0 & 0 & 0 \\ -k & -k & -k & -k \end{bmatrix} & E &= \begin{bmatrix} k & k & 0 & 0 \\ k & k & 0 & 0 \\ 0 & 0 & -k & -k \\ 0 & 0 & -k & -k \end{bmatrix}
 \end{aligned} \quad \dots (4.1)$$

Table 4.2 depicts the antenna state and gives a variation of the excitation vector over the 16 ports. It can be clearly seen that it is a two-vector variation.

PORT NUMBERS	ANTENNA STATE				
	A	B	C	D	E
1	K	K	K	K	K
2	K	K	K	K	K
3	K	K	K	K	0
4	K	K	K	K	0
5	K	K	-K	0	K
6	K	K	-K	0	K
7	K	K	-K	0	0
8	K	K	-K	0	0
9	K	-K	K	0	0
10	K	-K	K	0	0
11	K	-K	K	0	-K
12	K	-K	K	0	-K
13	K	-K	-K	-K	0
14	K	-K	-K	-K	0
15	K	-K	-K	-K	-K
16	K	-K	-K	-K	-K

Table 4.2 Pattern steering excitation. $K = \text{amp}1$, phase 0 ; $-K = \text{amp}1$, phase 180 ; 0 implies no port excitation

4.3 Antenna Array Measurements and Discussion

The antenna array and phasing network that was discussed in Section 4.2.2 and Section 4.2.3 was fabricated. The fabrication process involved the preparation of the CAD files and the PCB printing was performed through LPKF protomat on a dielectric sheet of thickness 0.508mm and $\epsilon_r = 3.55$. The back plate of the individual element made of aluminium was extended to span the area of 4x4 array footprint. Each of the group of four antenna elements that lie along the XZ plane were printed onto a common dielectric substrate with L holder PVC supports at the edges. The common dielectric support for a group of four equally spaced elements eliminates the need to introduce L holders periodically five times over the YZ plane thereby minimizing dielectric (PVC) influence. The SMA connectors are edge fed. They are supported by the L holders and the dielectric, that rest on the aluminium back plate encompassing the 4x4 array footprint as shown in Figure 4.11. Figure 4.11 (a) shows the front view and Figure 4.11 (b) shows the back view of the fabricated 4x4 antenna array.

The antenna array in Figure 4.11 was measured for its S parameters and this is depicted in Figure 4.12. The active reflection coefficient with respect to port 6 for the boresight case derived from individual ports Snn parameters is compared with them in Figure 4.12. For boresight beam conditions, from [14], the active reflection coefficient at a port is the summation of the individual Snn values added onto the port of interest. For other angles of incidence the active reflection coefficient changes. In Figure 4.12 the case considered is for a direct boresight incidence. It can be seen that the return loss at each of the ports is well below 10 dB over the band of 13.5 GHz to 14.5 GHz.

Table 4.3 depicts the measured mutual coupling between the ports at 14 GHz that demonstrates that the values are always below -23dB even for worst cases of (S1,5), (S1,2), (S1,6), (S2,6), (S6,10), (S6,11) and that in general (S6,3), (S6,5), (S6,7), (S6,9), (S6,11), they are well below -30dB. The measurement Figure 4.13 and Figure 4.14 shows the two selected worst and best cases on grounds of brevity.

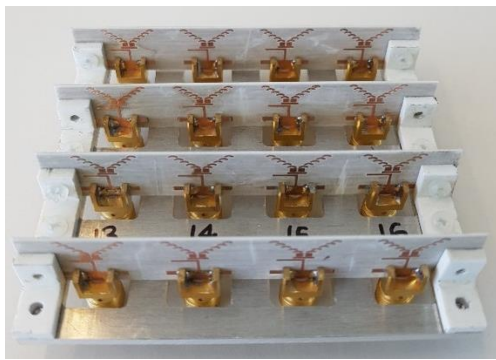


Figure 4.11 (a)



Figure 4.11 (b)

Figure 4.11 Fabricated 4x4 array (a) Front view (b) Back view.

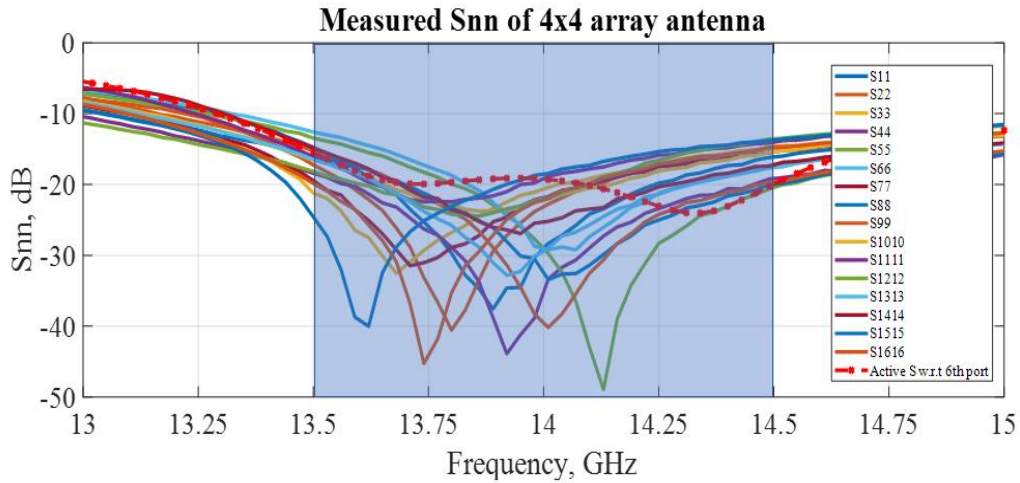


Figure 4.12 Measured S parameters compared with active S parameter with respect to port 6.

Ports	Mutual coupling at 14 GHz in dB
$S(1,2)$	-34.16
$S(1,5)$	-25.06
$S(1,6)$	-35.01
$S(2,6)$	-25.11
$S(6,10)$	-24.02
$S(6,11)$	-31.39
$S(6,3)$	-36.07
$S(6,5)$	-31.33
$S(6,7)$	-34.10
$S(6,9)$	-37.02
$S(6,11)$	-31.39

Table 4.3 Measured mutual coupling between ports of the antenna array at 14 GHz.

Though, the mutual coupling values are depicted in Table 4.3 at 14 GHz, the measured values are retained uniformly close to that at 14 GHz over the band 13.5 GHz to 14.5 GHz. This facilitates the wideband operation of the array in terms of its pattern dependency on frequency.

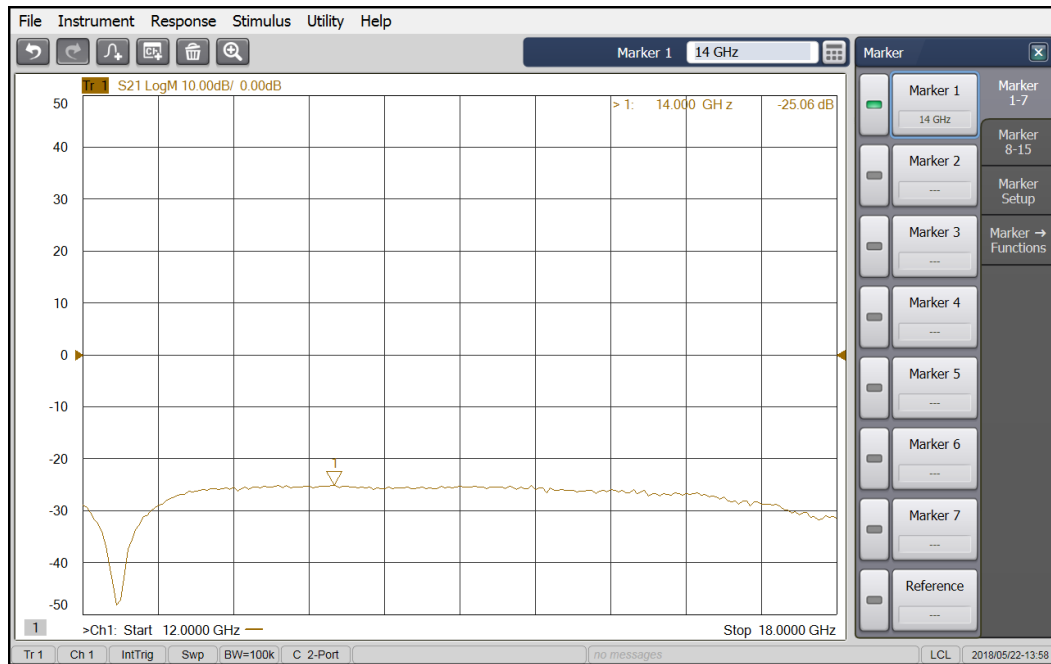


Figure 4.13 Measured Mutual coupling between ports 1 and 5 which is shown to represent the worst case.

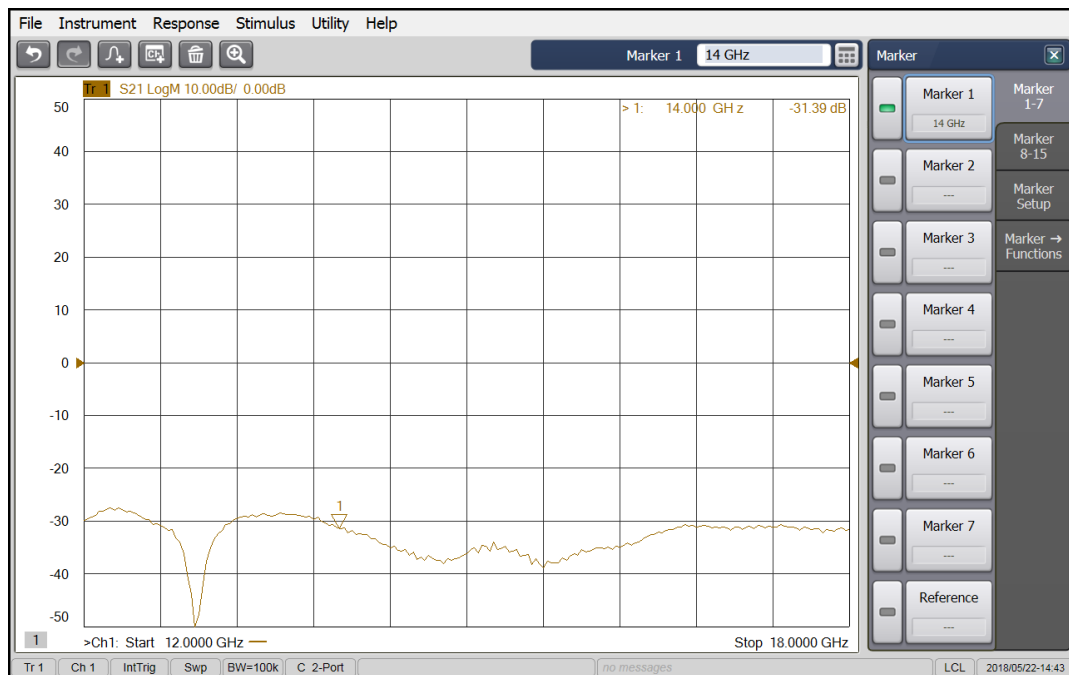


Figure 4.14 Measured Mutual coupling between ports 6 and 11 which is shown to represent the best case.

The phase feeding network discussed in Section 4.2.3 was fabricated and characterized individually before feeding on to the antenna array. The fabricated feed networks for the all 0° phase and $0^\circ/180^\circ$ phase are shown in Figure 4.15. The simulated frequency response for the

phase feeding network for input and output ports is shown in Figure 4.16. The measured phase response was close to the simulated one in Figure 4.9 and an almost balanced amplitude and phase operation between ports was seen.

From Figure 4.16 (a) there is a 2dB imbalance seen over the 16 ports in the 0° phasing network and from Figure 4.16(c) there is a 4dB imbalance seen over the 16 ports. This difference can be primarily attributed to the impedance variation along the U-shaped bend to introduce the delay in the $0^\circ/180^\circ$ phasing network. And, the fact that the parallel U-shaped arms can also couple significantly to each other at these frequencies. This proposed phasing feed network was a cost-effective way of realizing the two states of phasing. The use of 180-degree hybrids and programmable phase shifters as discussed later in the chapter are additional ways to realize the beamswitching scheme. Also, the imbalance of 2-4 dB calculates to amplitude variation between 0.16 to 0.21 in the linear magnitude scale, which under the beamswitching scheme requirement can still be within tolerance limits of being considered uniform. Much of the control in the proposed beamswitching scheme rests on the phases.

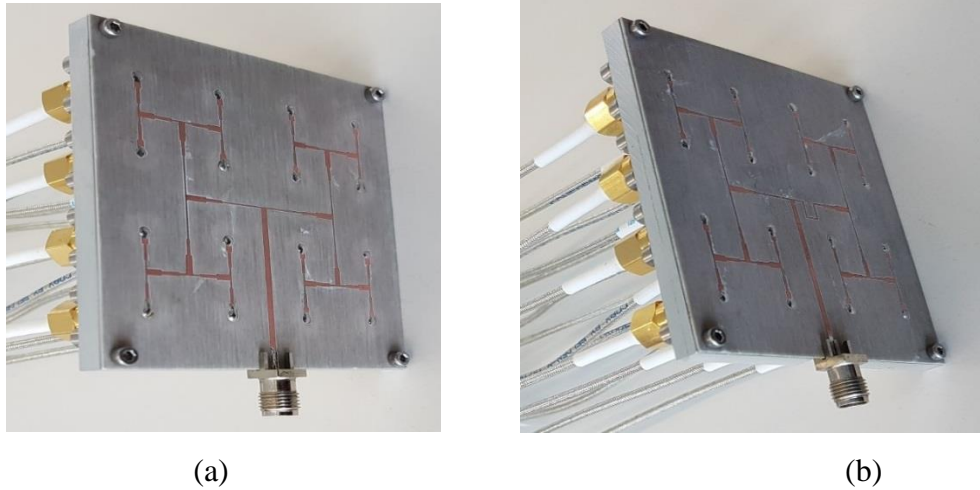
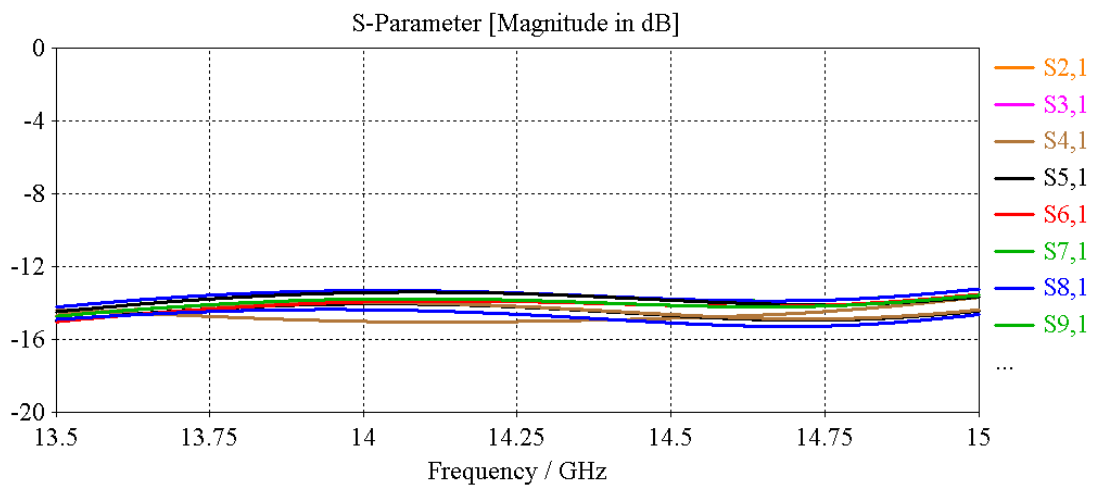
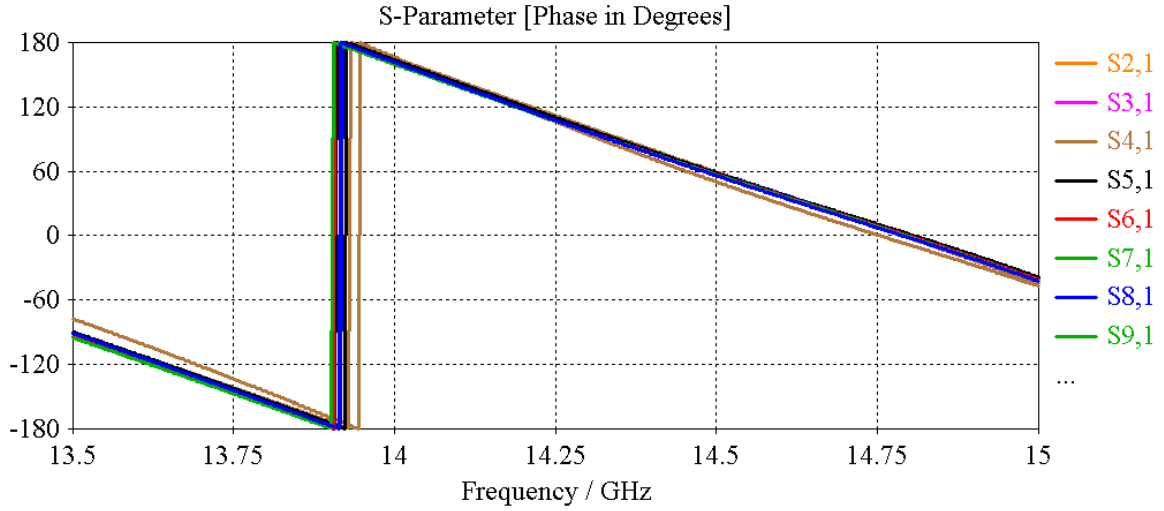


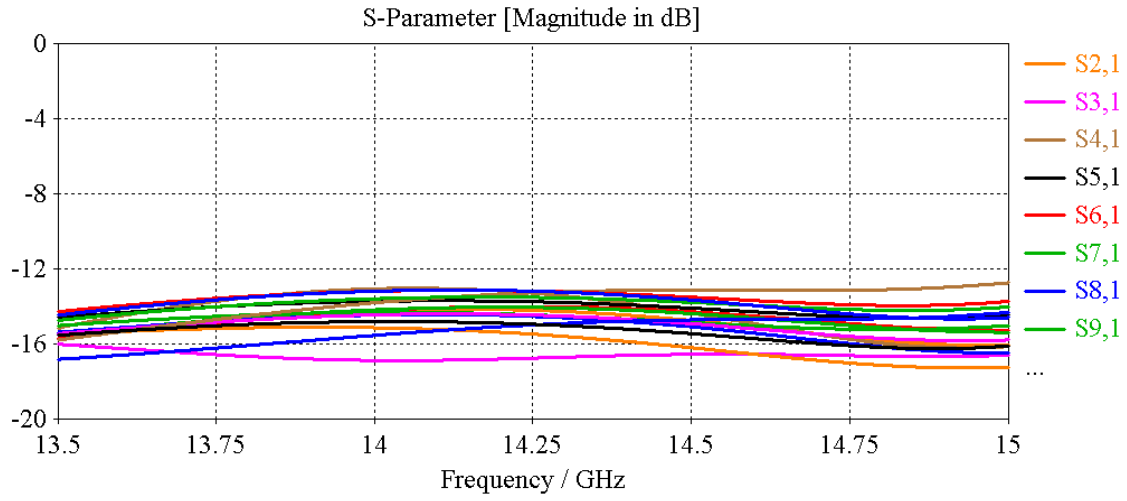
Figure 4.15. Fabricated phasing network (a) Equal phase (b) $0^\circ/180^\circ$ phase



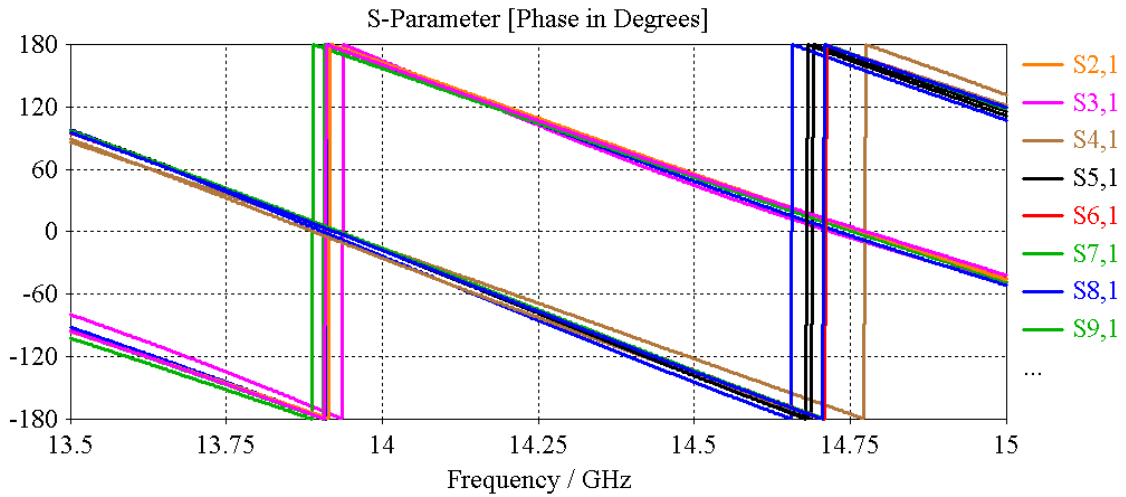
(a)



(b)



(c)



(d)

Figure 4.16 Simulated (a) Frequency response of the magnitude of S_{ij} of the 0° phasing network (b) Phase of S_{ij} of the 0° phasing network (c) Frequency response of the magnitude of S_{ij} of the $0^\circ/180^\circ$ phasing network (d) Phase for the $0^\circ/180^\circ$ phasing network

Massive MIMO antenna array

The antenna array and the phase feeding network were aligned and assembled with help of a supporting structure, and semi-rigid cables (whose losses were characterized in the post processing) were used to connect the feed network to the antenna array. A manual replacement and reconfiguring of the cable was performed to switch between the patterns. All open ports realized from such a reconfiguration were terminated with matched 50 ohm loads to emulate real working conditions. The complete assembled antenna is shown in Figure 4.17.



Figure 4.17 Fabricated antenna array with phasing network.



Figure 4.18 Pattern measurement of the 4x4 antenna array in anechoic chamber.

Figure 4.18 depicts the antenna setup for pattern measurement in the anechoic chamber. Since most of the beams to be measured were designed to have a cancellation beam at boresight, the beam pointing angle of boresight case was used as reference in calibration with an alignment of the roll axis for the measurement of other patterns. The measured antenna pattern is compared with simulation for the case A-E and is presented in Figures 4.19, 4.21, 4.23, 4.25 and 4.27. A good cross polar discrimination (XPD) is obtained for beamwidths around 40° for the case A-E. The dependency of the Co-polar gain, Cross polar gain (XP) and XPD on frequency were also measured for the different antenna states of A-D using two-antenna method. These measurements are depicted in Figures 4.20, 4.22, 4.24, 4.26. For case E, only the gain as a function of frequency was measured and is shown in Figure 4.28. It is important to note that the antenna beam patterns were stable throughout the operating bandwidth of the antenna for the phase excitations. The following discussion details the observations made in the above measurement of the antenna pattern and gain characteristics.

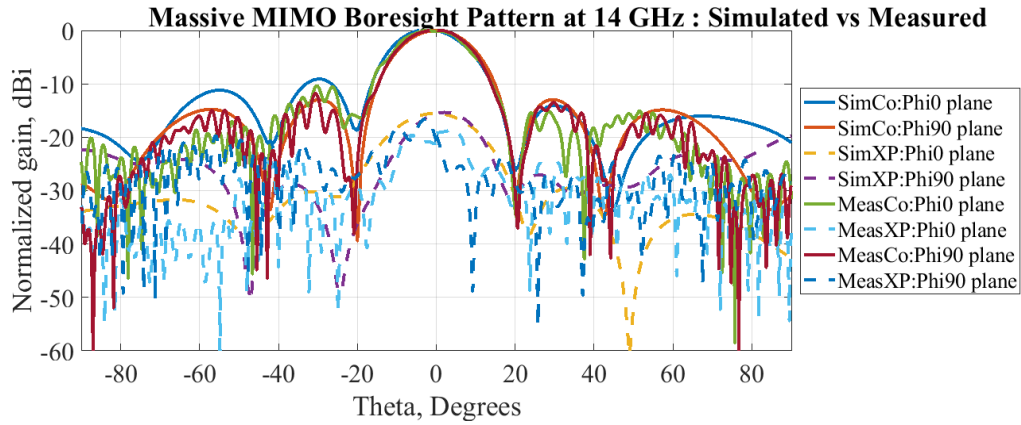


Figure 4.19 Simulated vs measured pattern state A.

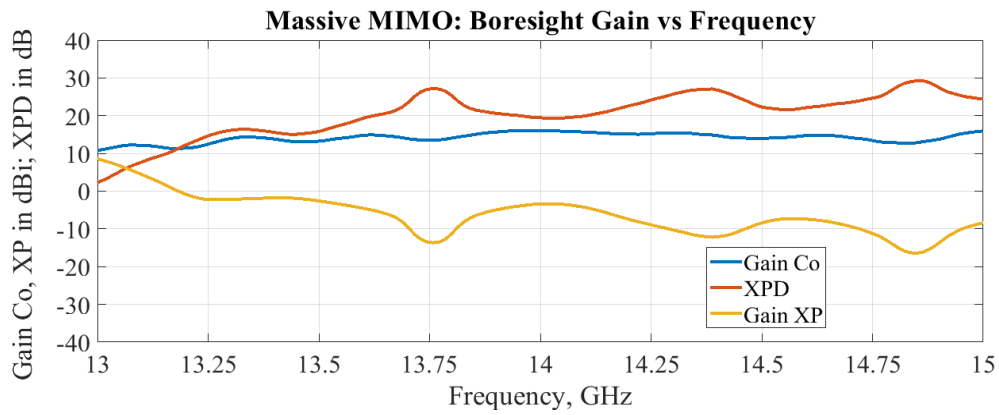


Figure 4.20 Measured gain vs frequency pattern state A.

Figure 4.19 depicts the boresight or the classical case A. This pattern is obtained by feeding all the 16 elements of the planar antenna array with an equal amplitude and phase to obtain the classical boresight beam of the planar array. Figure 4.19 compares the normalized gain patterns obtained by full wave simulation of the antenna array model with the actual measured pattern in the anechoic chamber. This comparison is done over two principal cut planes namely Phi0 and Phi90. The measurements are made for the co-polar plane wave incidence and cross polar plane wave incidence to obtain the (SimCo, MeasCo) Co-polar plots and (SimXP, MeasXP) Cross-polar plots respectively. As can be seen from the Figure 4.19 there is a good agreement between the simulated and measured Co-polar patterns both in the Phi0 and Phi90 plane for an angular range of 40 degrees centred around the boresight. The measured pattern for angles beyond the $+20^\circ$ and -20° (for angles $|Theta| > 20^\circ$) compares well with the simulated profile pattern shape but exhibits pronounced ripples. This behaviour can be attributed to the dominance of the reflections in the chamber at these oblique angles in comparison to the lower power levels inherent in the pattern for angles $|Theta| > 20^\circ$. With regards to the Cross-polar patterns there is a good agreement seen between the measurements and simulations with the Cross-polar levels maintaining well below -18 dB throughout the angular range. To qualify the normalized pattern with the actual gain seen, Figure 4.20 depicts the behaviour of measured gain vs frequency. This measurement was carried out by the two-antenna method and when the antenna under test (AUT) and the probe were aligned in boresight. A processed sweep of the transmission parameter over the frequency range 13 GHz to 15 GHz was used to obtain the

Gain values. The figure depicts a Co-polar gain varying around 18 dBi centred around 14 GHz. The Cross-polar discrimination is around 20 dB around 14 GHz.

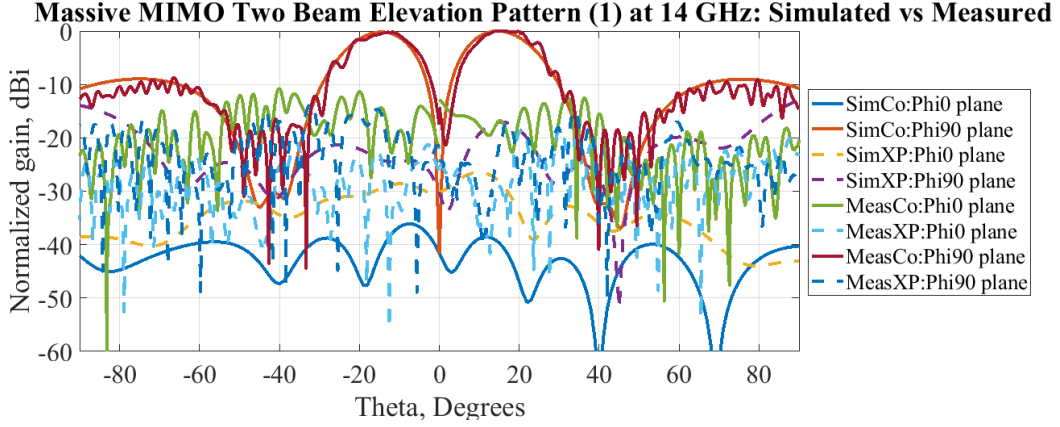


Figure 4.21 Simulated vs measured pattern state B.

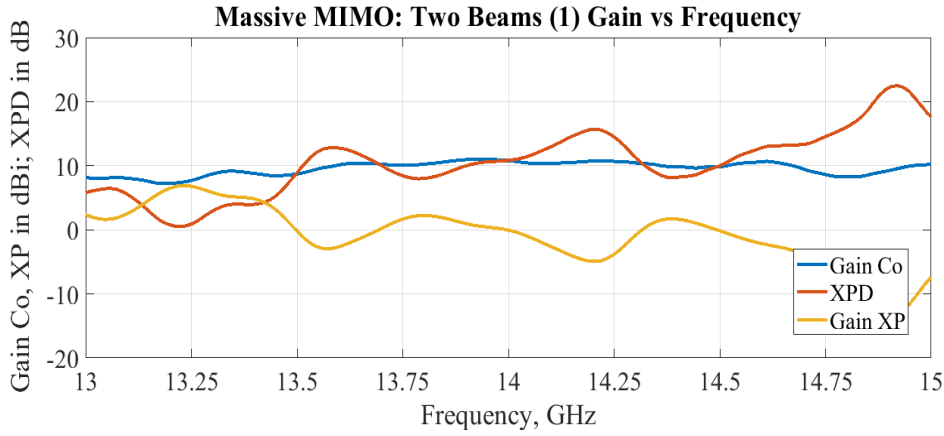


Figure 4.22 Measured gain vs frequency pattern state B.

Figure 4.21 shows the two-beam state B. The pattern behaviour of most importance that was focused upon during the measurement was the appearance of the twin lobe or two beams due to the excitation scheme. This two-beam pattern asserted by full wave simulations has been clearly validated by pattern measurements as shown in Figure 4.21. This proves the split beam building block concept of the proposed beam switching scheme when applied on an array. As can be seen from the Figure 4.21, there is a good agreement between the simulated and measured Co-polar pattern. Clearly, distinct two beams are measured spread up to 35° on either side of the $\theta=0^\circ$ axis. Though moderately high side lobe levels of 12 dB were measured, as mentioned earlier the side lobe levels were not the primary target in this case. As explained for Figure 4.21, the ripple effect is seen in this case as well, for measured angles $|\theta| > 20^\circ$.

Another notable feature of the measurement is the equal peak amplitudes of the two lobes making the case B suitable for simultaneous multiple beam projections for multiple users requiring the same Quality of Service (QoS). The Cross-polar levels are well below -12 dB throughout the angular range for both the simulations and measurement. In Figure 4.22, a measurement of the gain vs frequency is shown. It is to be noted that as there is no boresight (0°) pattern in this case, the positioner in the chamber was calibrated to the boresight case of Figure 4.19 for LOS alignment and the state B antenna replaced the state A antenna in this setup

to carry out the gain measurement, with the AUT turned to 18° - the direction of peak gain. As the two lobes are similar (symmetric), measurement was made on one lobe. The measurement in Figure 4.22 shows that a Co-polar gain of 10 dBi was seen centred around 14 GHz with a cross-polar discrimination (XPD) of 10 dB.

Massive MIMO Two Beam Elevation Pattern (2) at 14 GHz: Simulated vs Measured

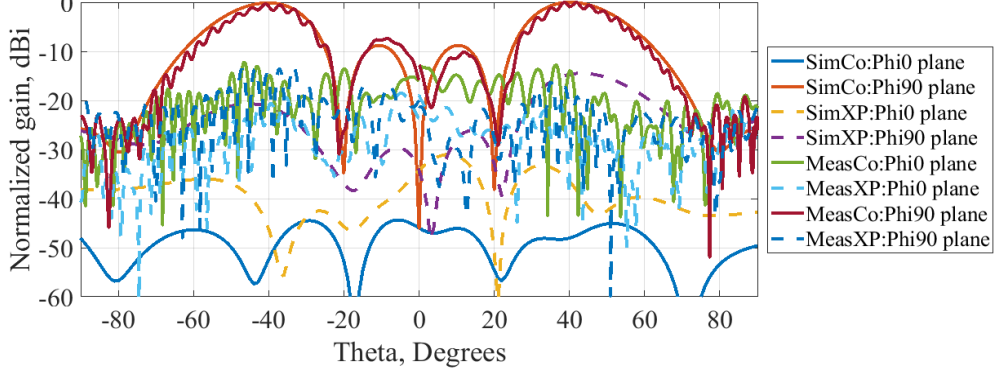


Figure 4.23 Simulated vs measured pattern state C.

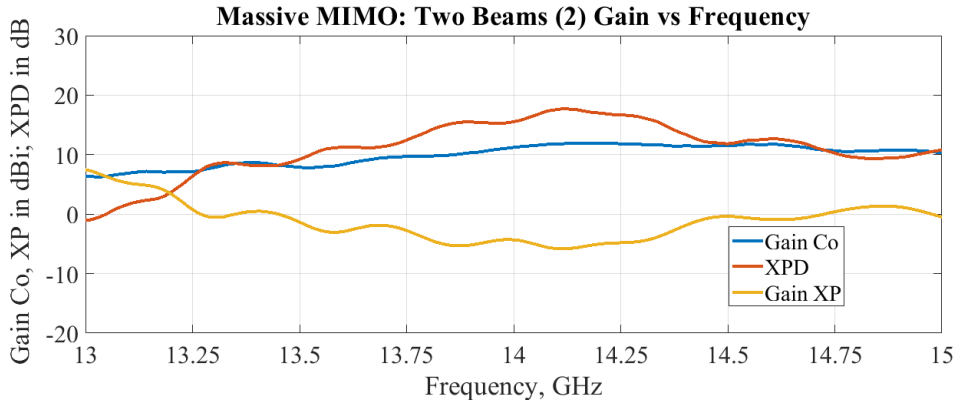


Figure 4.24 Measured gain vs frequency pattern state C.

Figure 4.23 depicts the two-beam antenna pattern. In this case, the focus was to assert by pattern validation that the beams can be steered to other angles by using the beamswitching scheme of state C. As can be inferred from Figure 4.23, in contrast to Figure 4.21, the two beams now have their peaks around 40° symmetrically around the central $\theta=0^\circ$ axis. Though the pattern profile shape matches well those in full wave simulations two interesting observations can be made here: The ripples as detailed in Figure 4.21 and 4.22 were attributed to angles $|\theta| > 20^\circ$. However, in this case, even for $|\theta| < 20^\circ$, a few ripples are seen in the central minor lobes. This asserts the earlier explanation of the low power levels, and the dominance of the reflections in the chamber as the reason for the ripples. In this case, the central minor lobes have low power levels of -12 dB and in measuring the pattern at those angles and power, reflections take precedence. Also, the ripple effect is also seen slightly over the two-high power main lobes as well. In this case, this can be attributed mainly to those introduced due to the twists in feeding the semi-rigid cables to the antenna. A look at the excitation scheme C shows that this state requires an alternating feeding of 0° and 180° lines which, while being realized physically by twisted (crossed-over) cables adds to the ripple effects. The simulated and measured Co-polar

patterns agree well in the Phi 90 plane. The Cross-polar pattern is well below -12 dB at the peak lobes. The gain vs frequency as shown in Figure 4.24 was measured using the same setup as in Figure 4.21 with the exception that the beam alignment of AUT and probe was now set to 40° in the peak lobe direction. A gain of 10 dBi around 14 GHz with improved Cross-polar discrimination (XPD) around 18 dB was measured. This improvement in XPD can be attributed to the cancellation beam concept proposed in Table 4.1 where an inverted split beam due to row 2,3 cancels out the main beams due to row 1,2 and row 3,4.

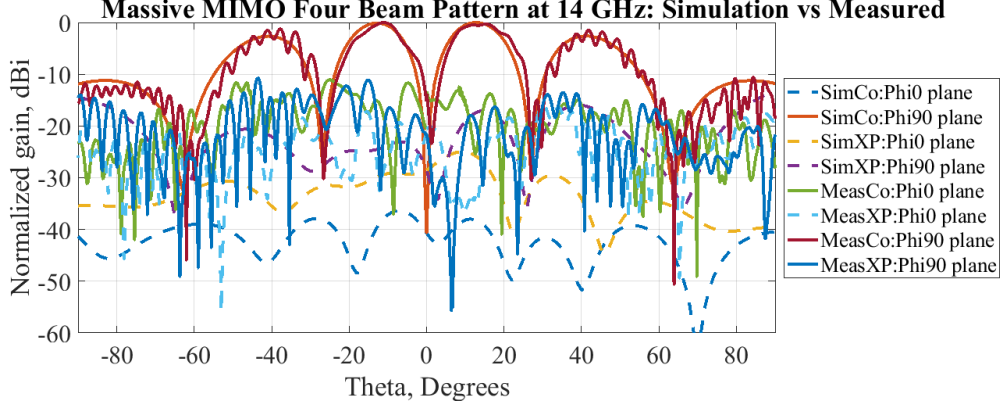


Figure 4.25 Simulated vs measured pattern state D.

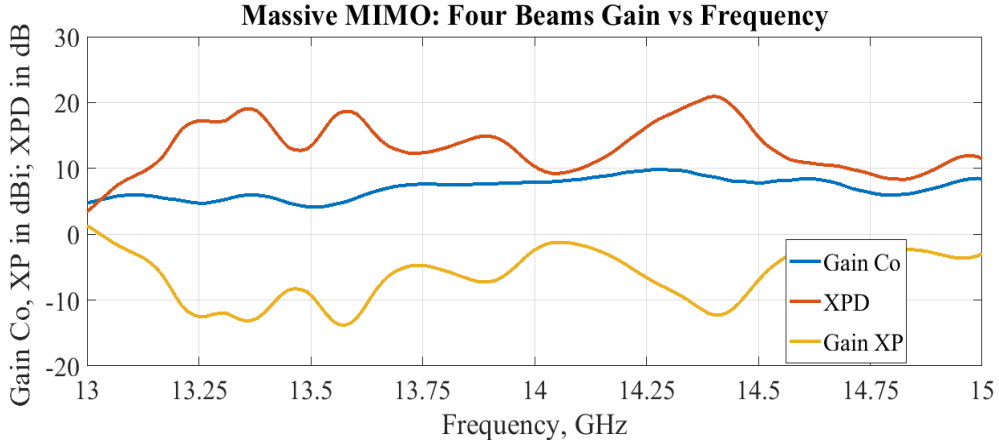


Figure 4.26 Measured gain vs frequency pattern state D.

Figure 4.25 shows the four-beam state D. This Figure validates the multibeam operability of the proposed beamswitching scheme. As can be seen, there is a good agreement between the simulated and measured Co-polar patterns along the Phi90 plane. Also, the four beams are of similar amplitudes and therefore clearly distinguished from being misinterpreted as side lobes. The beamwidth obtained at extreme lobe angles (beams at $+40^\circ$ and -40°) is not smeared or spread as is usually the case in scanned arrays operating at towards the horizon angles. This provides an increased control over the area of illumination or coverage area on the cell site in terms of serving multiple group of users at the cell edge resulting in decreased dropped services during handovers. Of notable importance is the observation that the cross polar pattern is well below -12 dB over all the four beams upholding the use of each beam individually to exploit polarization diversity corresponding to the individual direction of the beam. Figure 4.26 shows the measured gain vs frequency, for the four-beam case. The setup to measure the gain the

chamber was same as in Figure 4.23 with the calibration done with respect to one of the beam peaks. The gain seen at each beam can therefore be deduced to be around 8 dBi with a small correction of 2 dBi for the extreme lobes. This slight drop in gain in comparison to the previous cases is due to two reasons: The only row 1 and row 4 are excited, thinning row 3,4 which results in drop in the array gain. The other is that the fixed total power fed to the array is to be distributed over four beams which results in a drop in the gain seen at each beam. A solution to this can be obtained when this 4x4 sub-array is extended to the 8x8 antenna array with more elements to emulate a similar state as D. A Cross-polar discrimination varying from 10 to 20 dB is seen over the frequency band 13 to 15 GHz as shown in Figure 4.26. It is to be noted that though the antenna XPD is of paramount importance, the realized value of XPD also further depends on propagation medium [15].

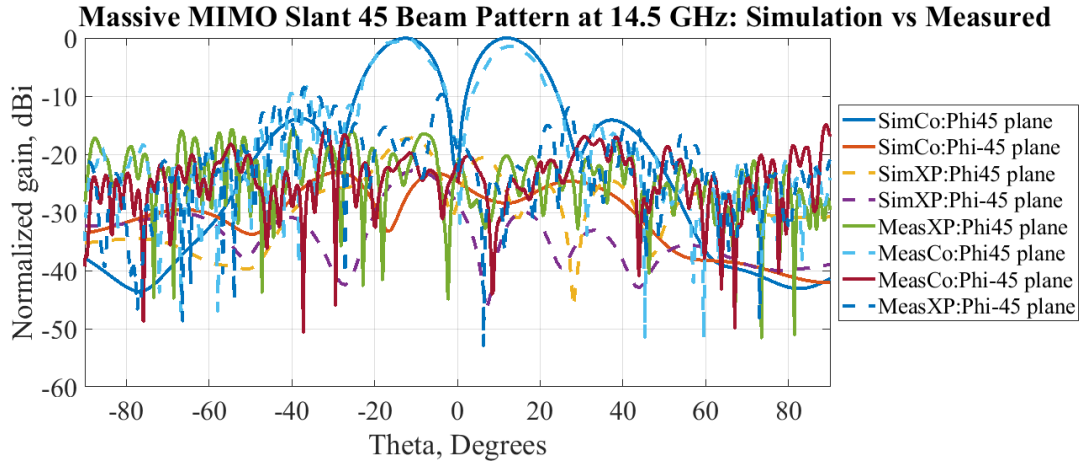


Figure 4.27 Simulated vs measured pattern state E.

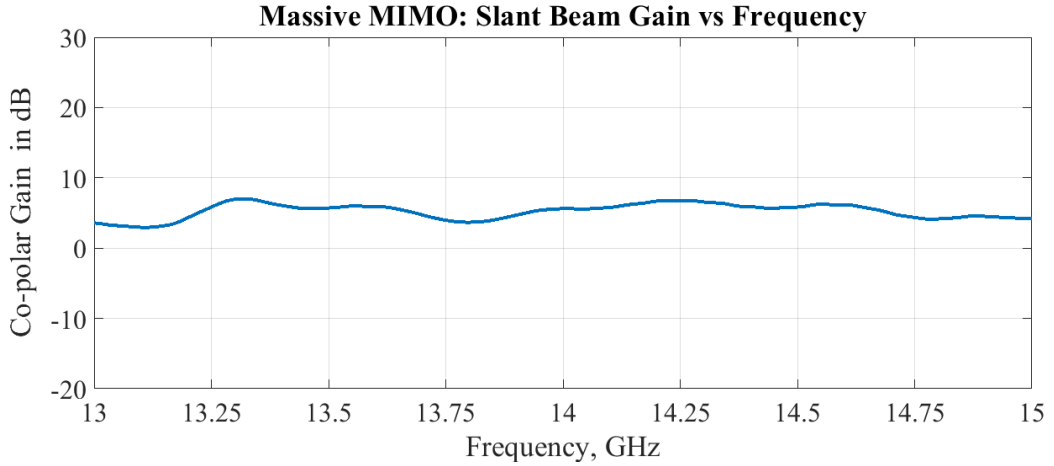


Figure 4.28 Measured gain vs frequency pattern state E.

Figure 4.27 depicts the slant beam state E. The main purpose of this excitation scheme is to demonstrate that the proposed beamswitching scheme can be used to orient beams along directions other than horizontal and vertical. This means the state E can project the horizontal polarized wave solely along the slant 45 or slant -45 direction without loss of its horizontal polarization property, in applications requiring the corresponding diagonal coverage. Figure 4.27 depicts cuts made at Phi+45 and Phi-45 planes. The simulated and measured co-polar

patterns have a good agreement and the cross polar patterns are well below -18 dB over the angular range. Figure 4.28 shows the measured gain vs frequency. For the gain measurement the positioner and the roll setup in the chamber was made to align the AUT beam (slanted at 45°) to the probe beam. This was performed retaining the boresight case position coordinates turned by an angle 45°. The state E antenna was then replaced into this setup to make the two-antenna method gain measurement targeted at one of the two slant lobe peaks. The gain measured was 8 dBi around the frequency of interest. This gain realized through state E will increase when this scheme is mapped onto 64 antenna arrays.

4.4 Conclusion

A method to realize multiple beam operation using two-phase configuration was demonstrated. The beamswitching scheme facilitates the control of the geometric planes onto which the beams are projected. A complete characterization of the fabricated 4x4 antenna sub-array in terms of its active S parameters and antenna pattern was presented. The antenna array has a gain of 16 dBi for a 4x4 configuration in the case A (boresight). The proposed beamswitching scheme and the antenna array can find potential application in scenarios where enhanced multi user perception is required such as in densely crowded stadiums or in custom designed 5G small cell scenarios. Another capability of this beamswitching scheme is to cast beams along NLOS which can be of potential use given the recent interest in NLOS communications in Millimeter wave Massive MIMO. A programmable 3-state (0°, 180°, open) phase shifter connected to each of these sixteen ports or 180-degree hybrid couplers using switches to select between hybrid coupler ports are sufficient to realize the demonstrated five beam states or other designed beam states - without switching between antennas. The latency of the beamswitching network then translates to a direct consequence of the state switching time of the phase shifter and the synchronicity between these phase shifters. This considerably reduces the latency in comparison to use of switches. Finally, the method proposed introduced a building block and a methodology for using it to construct directional multiple beams. The antenna array that has been experimentally validated will be tested on models of heterogeneous ultra-dense cellular networks for their performance.

4.5 References

- [1] D. Liu, W. Hong, T. S. Rappaport, C. Luxey and W. Hong, "What will 5G Antennas and Propagation Be?," in *IEEE Transactions on Antennas and Propagation*, vol. 65, no. 12, pp. 6205-6212, Dec. 2017.
- [2] W. Hong et al., "Multibeam Antenna Technologies for 5G Wireless Communications," in *IEEE Transactions on Antennas and Propagation*, vol. 65, no. 12, pp. 6231-6249, Dec. 2017.
- [3] P. Y. Wang et al., "Beam Switching Antenna Based on a Reconfigurable Cascaded Feeding Network," in *IEEE Transactions on Antennas and Propagation*, vol. 66, no. 2, pp. 627-635, Feb. 2018.
- [4] D. Guan, Y. Zhang, Z. Qian, Y. Li, M. Asaadi and C. Ding, "A Novel 2-D Multibeam Antenna Without Beamforming Network," in *IEEE Transactions on Antennas and Propagation*, vol. 64, no. 7, pp. 3177-3180, July 2016.
- [5] C. M. Chen, V. Volski, L. Van der Perre, G. A. E. Vandenbosch and S. Pollin, "Finite Large Antenna Arrays for Massive MIMO: Characterization and System Impact," in *IEEE Transactions on Antennas and Propagation*, vol. 65, no. 12, pp. 6712-6720, Dec. 2017.
- [6] H. Tanabe, K. Sakakibara and N. Kikuma, "Multibeam-switching millimeter-wave antenna using beam-tilting design in perpendicular plane to feeding line of microstrip comb-line antenna," 2017 IEEE MTT-S International Conference on Microwaves for Intelligent Mobility (ICMIM), Nagoya, 2017, pp. 139-142.
- [7] A. F. Morabito and P. Rocca, "Optimal Synthesis of Sum and Difference Patterns With Arbitrary Sidelobes Subject to Common Excitations Constraints," in *IEEE Antennas and Wireless Propagation Letters*, vol. 9, pp. 623-626, 2010.
- [8] S. T. Smith, "Optimum phase-only adaptive nulling," in *IEEE Transactions on Signal Processing*, vol. 47, no. 7, pp. 1835-1843, July 1999.
- [9] A. F. Morabito, A. Massa, P. Rocca and T. Isernia, "An Effective Approach to the Synthesis of Phase-Only Reconfigurable Linear Arrays," in *IEEE Transactions on Antennas and Propagation*, vol. 60, no. 8, pp. 3622-3631, Aug. 2012.
- [10] G. Byun, H. Choo and S. Kim, "Improvement of Pattern Null Depth and Width Using a Curved Array With Two Subarrays for CRPA Systems," in *IEEE Transactions on Antennas and Propagation*, vol. 63, no. 6, pp. 2824-2827, June 2015.
- [11] H. Steyskal, R. Shore and R. Haupt, "Methods for null control and their effects on the radiation pattern," in *IEEE Transactions on Antennas and Propagation*, vol. 34, no. 3, pp. 404-409, March 1986.
- [12] S. A. Schelkunoff, "A mathematical theory of linear arrays," in *The Bell System Technical Journal*, vol. 22, no. 1, pp. 80-107, Jan. 1943.
- [13] V. Basavarajappa, B.B. Exposito, L. Cabria and J. Basterrechea, "Millimeter wave multibeam switching antenna," in *Proc. IEEE ISWCS 2017*, Bologna, Italy, 2017.
- [14] D. M. Pozar, "A relation between the active input impedance and the active element pattern of a phased array," in *IEEE Transactions on Antennas and Propagation*, vol. 51, no. 9, pp. 2486-2489, Sept. 2003.
- [15] Recommendation ITU-R p.310-9* "Definitions of terms relating to propagation in non-ionized media", [Weblink](#)

Chapter 5

Spatial modulation aided Single-RF MIMO

5.1 Introduction

Towards achieving Massive MIMO operation, Chapter 3 introduced an antenna element and chapter 4 introduced an antenna array to form multiple beams. This chapter introduces a reconfigurable antenna array suitable for implementation onto a medium-throughput modulation called Spatial Modulation. Spatial modulation introduces an additional spatial location information of the antennas to encode message bits implicitly. The premise of Single RF MIMO and Spatial Modulation mainly revolves around reduction of power fed by using a Single RF chain or reduced number of RF chains while still retaining the same throughput. In this context Single RF MIMO has been referred to in literature as few-RF, reduced-RF and Single RF. Large Scale MIMO antenna arrays, that are introduced in chapter 4 can embed the Single RF MIMO technology inside them to reduce the amount of power consumption in the array. In conventional Large-Scale arrays having more than 50 antennas, an equal number of RF chains are required. This results in a power-hungry solution, which can be overcome by using a single or a reduced number of RF chains to feed the elements in place of multiple ones. This can mainly be achieved by dividing the Large Scale MIMO array into sub-arrays fed by Single RF chains, thereby reducing the power consumption by a factor equal to the number of antennas in each sub-array. With regards to Spatial Modulation, the pattern reconfigurability can be obtained by twin beam switching as discussed in this chapter. As can be seen these techniques are very closely related despite of subtle differences. To make the distinction clear the following tree chart highlights the notable features:

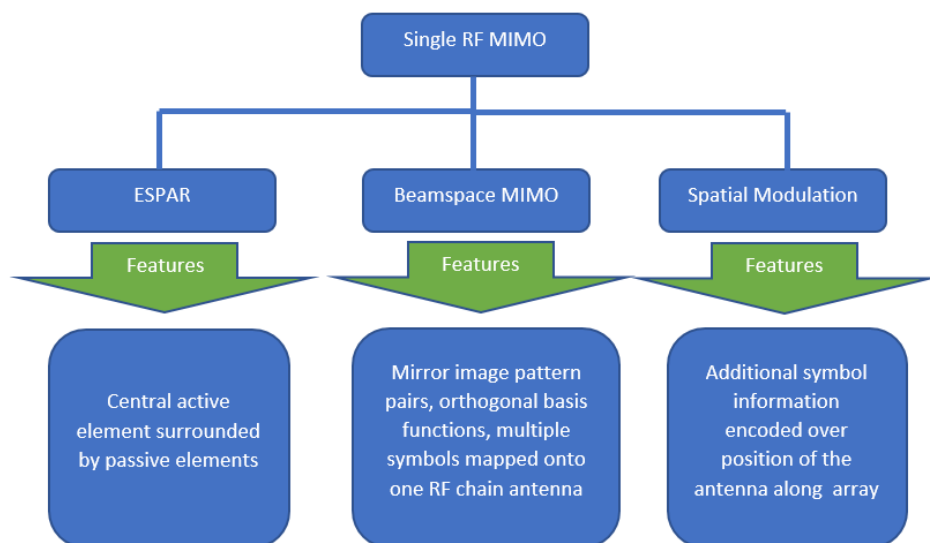


Figure 5.1 Technologies to realize Single/few/reduced-RF MIMO

Each of the above three technologies to realize Single RF MIMO are explained in Section 5.2. In this chapter the antenna array proposed is designed for operation as a reconfigurable antenna for spatial modulation. The antenna array generates twin-beams that can be switched/rotated over the azimuth in a circular fashion. The choice of the design of a twin beam pattern has been made considering potential applications in scenarios where the beams are to be oriented obliquely with no radiation along boresight. The possible scenarios include a crowded open-air theatre or stadium, indoor 5G small cell scenarios such as conference rooms as in Figure 5.1, and other such scenarios that require NLOS propagation.



Figure 5.2 Indoor twin beam antenna for non-boresight multi-user azimuthal coverage

Related works in relation to Single RF MIMO are discussed next and the features of the proposed reconfigurable antenna array design are compared to them.

Paper [1], discusses a compact and frequency tunable single RF MIMO. It is among one of the earliest designs to realize Single RF MIMO. Mirrored image pattern pairs (MIPP) are obtained using a PIN diode controlled Single RF switching to realize orthogonal basis functions onto which complex vector radiation patterns containing the symbols are mapped. The scheme proposes a single integrated radiator with a way to switch between the radiation patterns. The antenna operates in the 1.9 to 2.2 GHz frequency range and its design is for application in mobile device. In comparison, the proposed Single RF MIMO antenna array operates around 14 GHz and is intended for integration on the base station side alongside Large-Scale arrays. The switching in the proposed design is attained using a switchable feeding network. Simultaneous twin-beam mirrored image pattern pairs are obtained using a 2-vector phase excitation scheme.

Paper [2], proposes a reconfigurable antenna for spatial modulation purposes with radiation pattern diversity. The antenna design consists of a source meander line radiating element which is surrounded by two L shaped resonators connected to PIN diode switches. By controlling the way in which the switches are toggled, several radiation patterns are generated to aid in spatial modulation. The antenna operates around 2-3 GHz. In comparison, the proposed Single RF MIMO antenna array uses phase aided switching and does not harness the use of reflectors along specified switching directions as in [2] where the L shaped resonators alternately act as director and reflector by suitable switching. On the contrary the directionality of the beam is

fixed by the phasing used in the beamswitching scheme. Also, the proposed reconfigurable antenna provides eight different beam patterns that can be exploited in Spatial Modulation.

Paper [3] proposes a design for single RF chain MIMO using low power CMOS switches. The important implementation in this design is the use of discrete switch which simplifies the design and implementation of DC bias circuitries and reconfigurable loads. It provides a compact antenna structure optimized for multiplexing multiple signals. In comparison, the proposed 3x3 Single RF MIMO array offers beam control and switching along the azimuth 360° whereas the design in [3] is validated for operation as a single arm of ESPAR (Electronically scanned parasitic antenna array).

Paper [4], details spatial multiplexing using single radio switched parasitic array with proof of concept and demonstrated experiments. The concept of transmitting multiple signals using one RF chain and a compact switched parasitic array is validated. The experiments were conducted at 2.6 GHz in an indoor environment using a prototype made of printed dipole of which the centre one is active and coupled to two other passive ones. In comparison, in the proposed antenna the multiple patterns are generated by phasing control.

Single RF antenna array concepts and designs have lately found large application in Spatial modulation [5], [6]. The additional dimension of antenna index coding required by spatial modulation is attained by selective use of the multi-pattern operation offered by single RF MIMO antennas.

The rest of the chapter is organized as follows: Section 5.2 introduces three key technologies to realize Single RF. Section 5.3 presents the proposed reconfigurable antenna concept using a 3x3 antenna array. Section 5.4 extends the 3x3 array concept and maps it onto 4x4 array allowing for integration into the 64-antenna array and presents a novel beamswitching scheme that results in an azimuthal paired beam rotation. Section 5.5 also presents the experimental validation of the concept with the measurement of pattern and gain in the anechoic chamber. Section 5.5 concludes the chapter.

5.2. Single RF MIMO Technologies

5.2.1 ESPAR (Electronically scanned parasitic antenna array)

Towards the quest of reducing the number of RF chains, a widely investigated area since the 1970s [7], is the ESPAR or the Electronically Scanned Parasitic Antenna Array. The main concept of ESPAR is the use of a central actively fed antenna element, that is parasitically coupled onto the peripheral elements, that are reactively loaded to steer the beam in different directions as shown in Figure 5.3 depiction of ESPAR on an infinite ground plane.

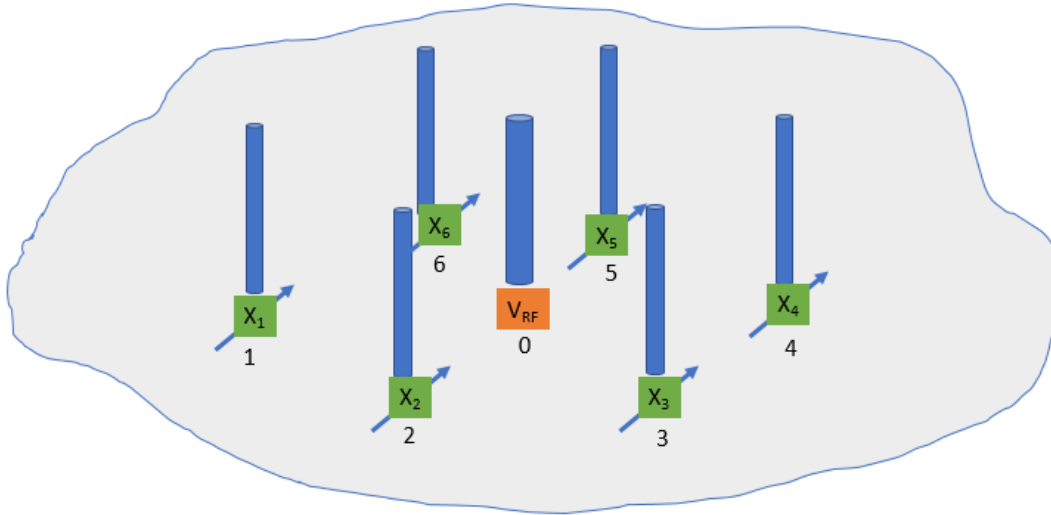


Figure 5.3 Illustration of ESPAR antenna with 7 elements on an infinite ground plane

The reactive loads alter the antenna currents and, as a consequence, the radiation characteristics. The control of the reactive load thereby gives control over the beam characteristics. Since [7], several different approaches towards realizing pattern control by reactive loads have been proposed. In the following discussion a brief survey of ESPAR antennas proposed is detailed highlighting the uniqueness of each design.

[8] presents an ESPAR antenna operating at 2.484 GHz with six monopole elements of length $\lambda/4$ placed along a circle with radius $\lambda/4$ as shown in Figure 5.4. The central element is actively fed. Unlike Digital beamforming arrays where the weights of the array element are controlled by an adaptive beamforming algorithm, in this proposed ESPAR antenna, the non-linear relationship between the control voltage and the beam patterns obtained is used to tune the reactive loads which in turn adapt the weights accordingly. The weights are optimized in this way iteratively by an adaptive beamforming algorithm as in a non-linear filtering problem to cast beams along different directions along the azimuth.

Utilizing a Fractal Koch monopole-based antenna element, paper [9], proposes an ESPAR antenna for mobile computing devices using three elements: with a driven central Koch monopole flanked by two other parasitic monopoles to control the beam as shown in Figure 5.5. The antenna operates in the 2.4 GHz ISM band.

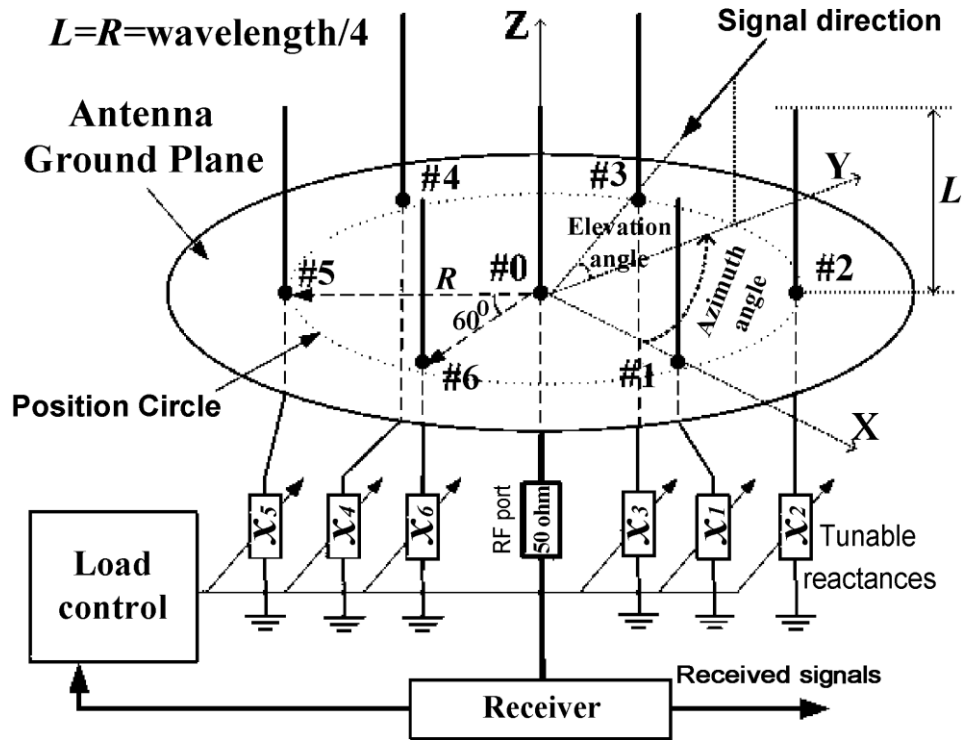


Figure 5.4 Seven element ESPAR antenna equipped with adaptive beamforming algorithm [8]

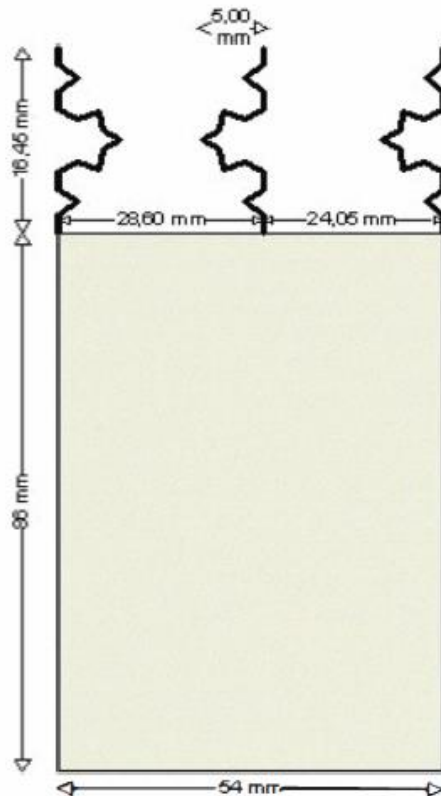


Figure 5.5 The ESPAR setup depicted for mobile computing application [9]

Paper [10] introduces beamswitching using parasitic antenna array using the yagi antenna concept but with a closer spacing than the usual yagi antenna spacing to facilitate coupling. A

central printed fed element is coupled onto parasitics flanked on its either side. The first parasitic element facing the driven element at the center has provision for 2 pin diodes that can be switched to act as a director in one state or a reflector in other state alternatively, to switch the beam along two directions. When all the pin diodes are off, a third omnidirectional pattern is obtained. The antenna shown in Figure 5.6 was designed and verified experimentally to operate at 2.4 GHz.

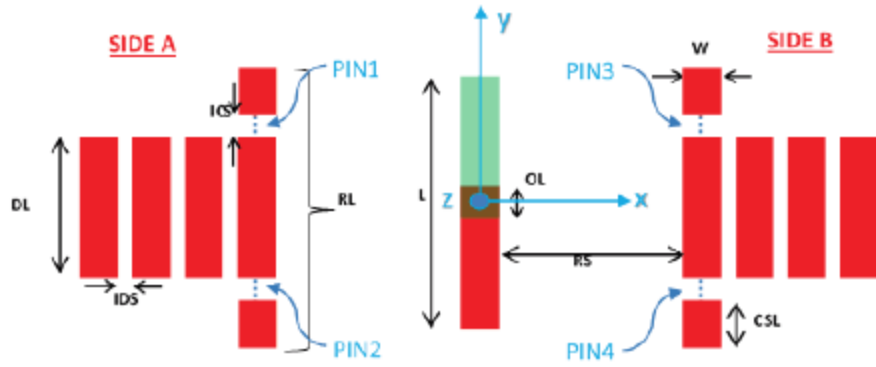


Figure 5.6 The beam-switched planar parasitic antenna array [10]

[8], [9] and [10] present the diverse ways of implementation of the ESPAR antenna concept. Though other works using other antenna elements and switching concepts have been proposed they have not been presented here on brevity grounds. Largely, the principle of operation of these are built on the main concept in Figure 5.3. Interested readers can refer to [11] for a detailed treatment of ESPAR antennas.

5.2.2 Beamspace MIMO

In classical MIMO, the number of RF chains is equal to the number of antennas used to attain MIMO operation. Beam space MIMO deviates from this mainstream concept in the proposition that - a single RF chain, employed in a switched parasitic antenna array (SPA) can be used to transmit two symbols simultaneously using a Single RF chain as in Figure 5.8, whereas classical MIMO would require two antennas or two RF chains to transmit two symbols as in Figure 5.7. The antenna that is centrally fed is coupled onto the two other parasitic antennas using a mapping of the transmitted symbols onto the orthogonal basis functions that form the core of the mechanism of Beamspace MIMO. The derived basis functions can be proved to be orthogonal if the individual antenna patterns are mirror image of each other. Later, by weighting the basis functions linearly by the symbols (2 symbols), the antenna can transmit two symbols simultaneously over a single pattern. At the receiver side, knowing the orthogonal basis functions the symbols can be decoded back as linear combination with the symbols. To reemphasize, the requirement for the functioning of this concept is that the antenna patterns used are mirror images of each other. A fast switching between the two Basis functions (in case of a 3 element SPA) is needed. To facilitate this, the decomposition of the combined pattern onto the individual basis functions 1 and 2, and the corresponding mapping of the symbols is performed first. The technique is to have one RF chain for the first symbol, while use a simple electronic circuitry incorporating an XOR gate to map the other symbol exclusively to the first one. This operation is attained by the actual feeding of the first symbol to the central RF chain,

while the XOR output between the two symbols is fed as control signal to the two parasitic antennas as in Figure 5.8. This XOR gate introduced mutual exclusiveness introduces mapping of symbol 1 onto basis function 1 and the symbol 2 is mapped onto the basis function 2. This translates to the effective realization, that just a single RF chain is used to transmit two symbols paving way for reduced power consumption. After the above introduction to the concept of BeamSpace MIMO, the following section introduces the theory [12] of realizing the basis functions from Mirror Image Pattern Pairs (MIPP).

Consider an antenna system that generates two mirror image pattern pairs $G_1(\theta, \phi), G_2(\theta, \phi)$, then the set of angular functions $B_\Sigma(\theta, \phi), B_\Delta(\theta, \phi)$ are defined as [12]:

$$B_\Sigma(\theta, \phi) = \frac{1}{\sqrt{2}}(G_1(\theta, \phi) + G_2(\theta, \phi)) \quad \dots (5.1)$$

$$B_\Delta(\theta, \phi) = \frac{1}{\sqrt{2}}(G_1(\theta, \phi) - G_2(\theta, \phi)) \quad \dots (5.2)$$

(5.1) and (5.2) form orthogonal basis functions. The mapping of the symbols onto orthogonal basis functions ensures an almost independent fading between the two signals when BPSK is used and therefore resulting in a more accurate constellation reconstruction at the receiver.

The combined antenna pattern (G_T) with the symbols mapped can be expressed as:

$$G_T = s_1 B_\Sigma(\theta, \phi) + s_2 B_\Delta(\theta, \phi) \quad \dots (5.3)$$

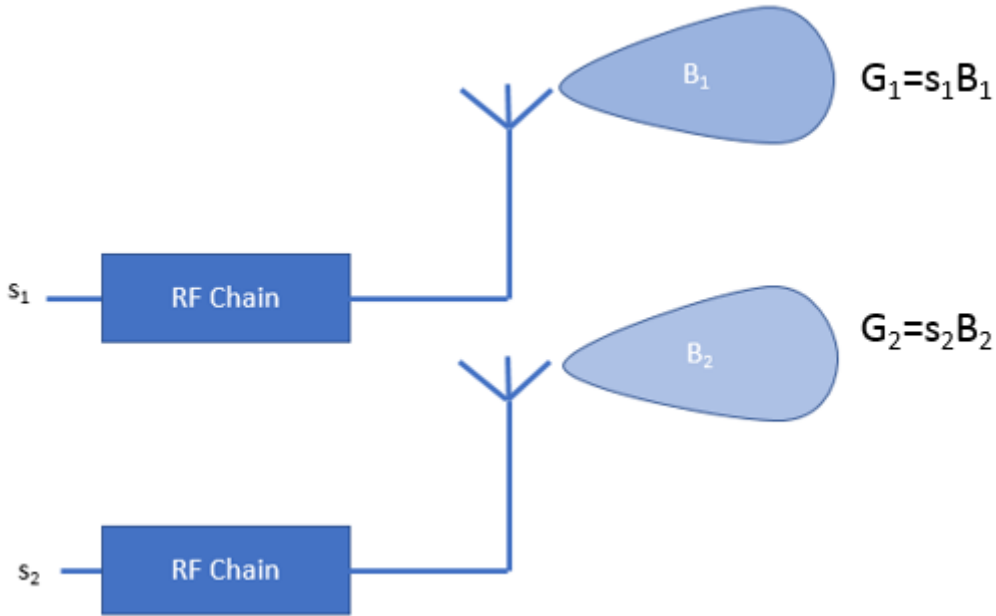


Figure 5.7 Classical MIMO

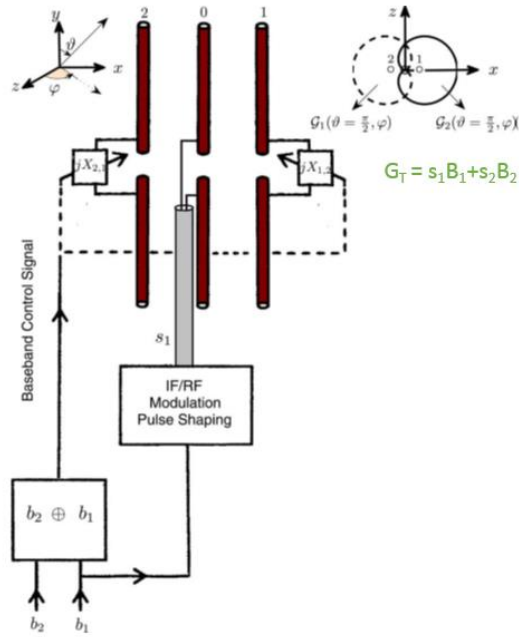


Figure 5.8 Beamspace MIMO [12]

The practical realization and implementation of the above concept has been detailed in [12], [13] and [1]. The fabricated antennas and the realization is shown in Figure 5.9 -5.11.

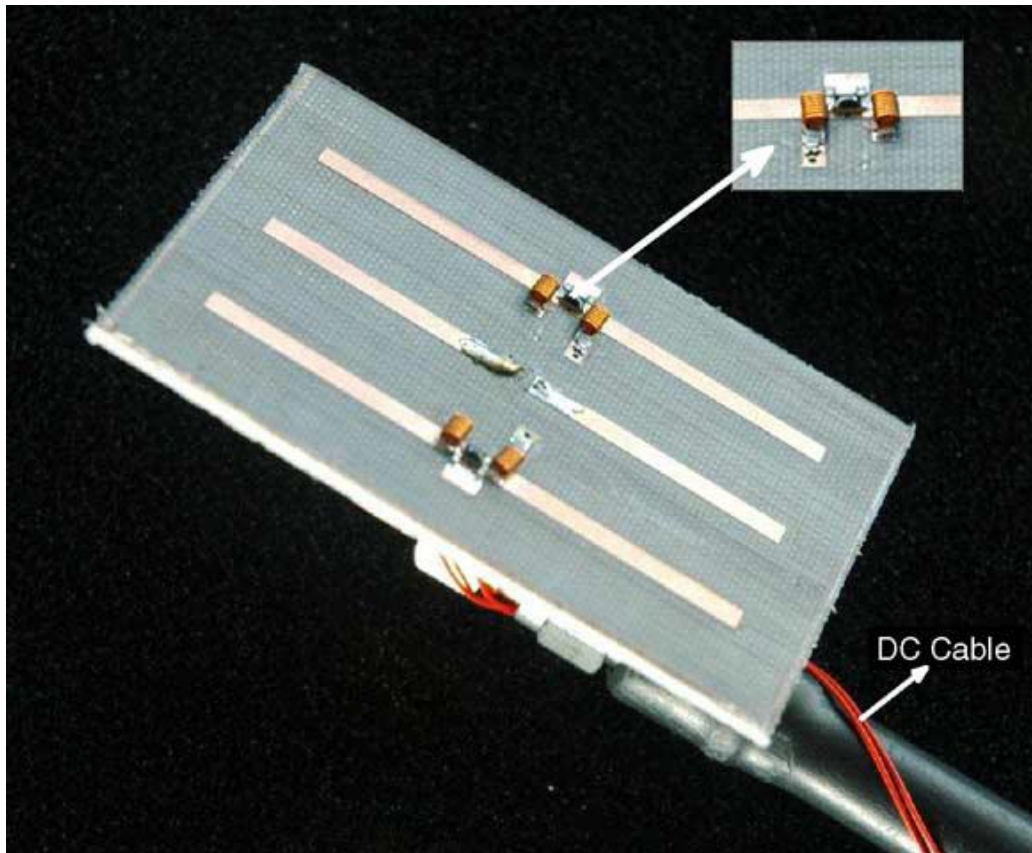


Figure 5.9 Switched parasitic antenna array [12]

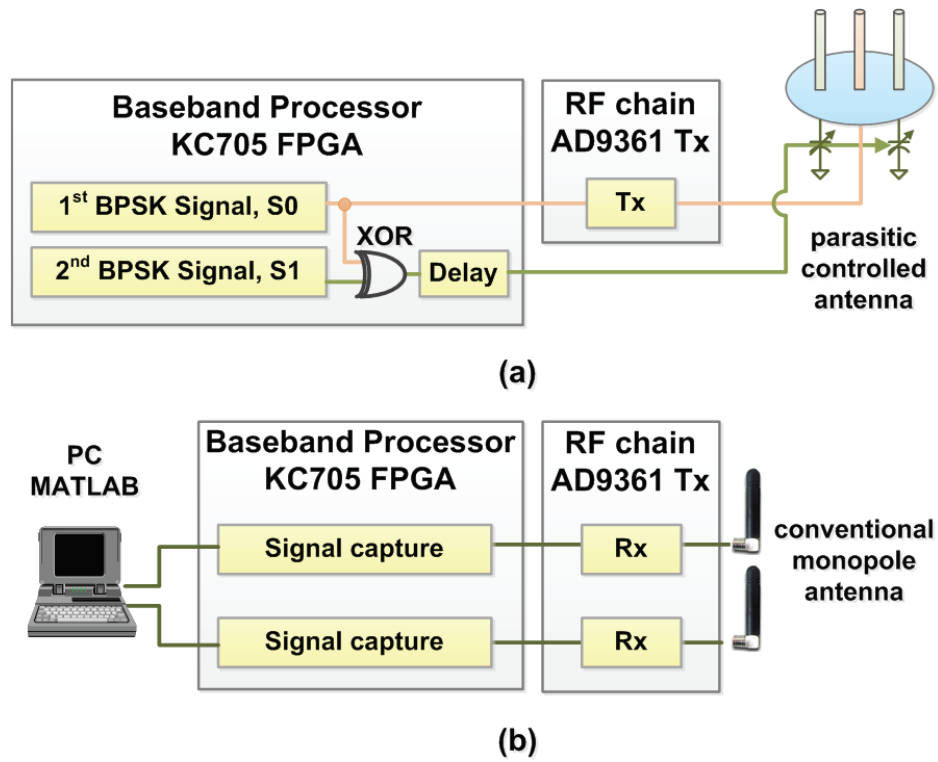


Figure 5.10 Switched parasitic antenna array and the control circuitry setup [13]

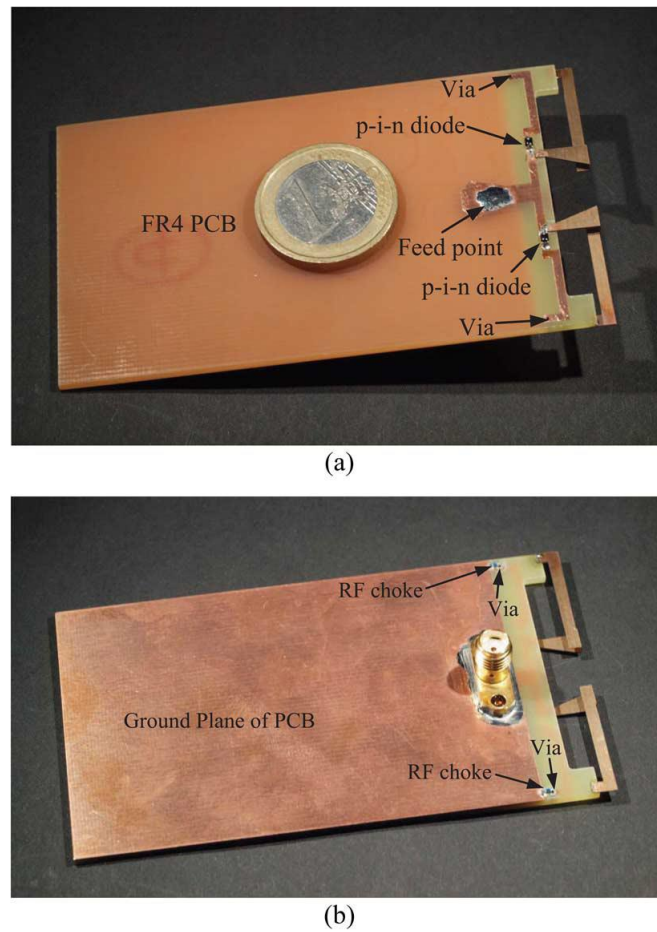


Figure 5.11 Planar printed three element SPA for mobile applications [1]

The author wishes to clarify that the proposed antenna in this chapter does not operate on the Beamspace MIMO or wavevector domain. An introduction and details of the Beamspace MIMO domain was provided since Beamspace MIMO antennas form an integral part of single RF MIMO solutions. The proposed antenna in this chapter has a mirror image pattern pair just as in the Beamspace concept, but it is to be made clear that the patterns are mirror beams simultaneously (twin beam) unlike the two independently used mirror beam patterns in Beamspace MIMO. Also, the proposed antenna can be used in broadcast or point to multi-point casting where a single data stream is used unlike Beamspace where two streams can be used. The antenna proposed in this chapter was designed to aid in reconfigurable Spatial Modulation which harnesses pattern diversity and channel signatures as the mechanism to enhance bandwidth. This is discussed in the next section on spatial modulation.

5.2.3 Spatial Modulation

Three common MIMO concepts are Spatial multiplexing, Transmit Diversity (Orthogonal space time block codes) and Spatial Modulation. Spatial modulation is applied for devices with low power consumption, high energy efficiency and medium throughput. It turns out that the upcoming blend between the 5G and the IoT (Internet of Things) requires seamless connectivity between devices requiring a moderate throughput rate [14]. A pattern reconfigurable antenna can be used to provide for the 3rd dimensionality offered by Spatial modulation, namely the space (antenna location/index) information. Figure 5.12 depicts the three closely related transmit MIMO concepts and highlights the difference between them.

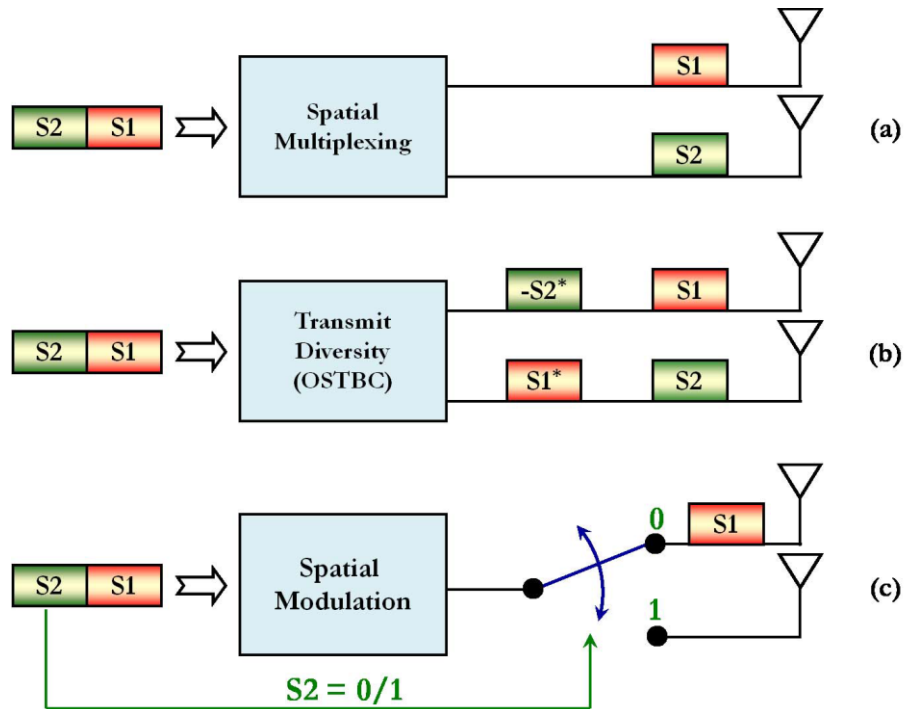


Figure 5. 12 Transmit MIMO techniques [14]

Spatial multiplexing involves transmitting the two symbols over two separate antennas in one channel use as shown in Figure 5.11 (a). This brings in the requirement to have as many RF chains or antennas as the number of symbols intended to be transmitted. In OSTBC the symbols are encoded (using a suitable coding technique that provides implicit orthogonality) and then transmitted in two channel uses, as shown in Figure 5.12 (b). On the other hand, in

Spatial modulation one subset of transmitted bits is used to select the transmit antenna through which the first symbol is to be transmitted. This implicit information results in a reduction of the required number of RF chains. In the following the three-dimensional encoding method of spatial modulation is described.

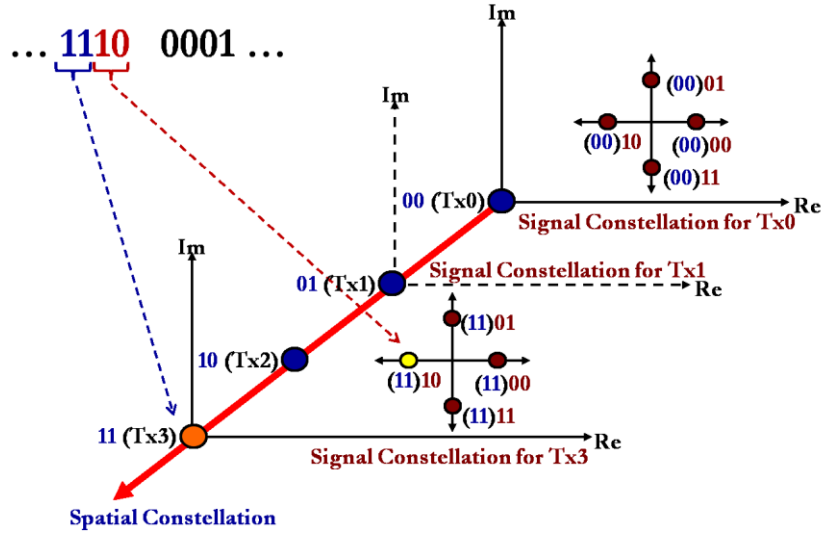


Figure 5.13 Spatial modulation three-dimensional encoding 3D constellation [14]

Consider Figure 5.13, where the two-dimensional constellation diagram is tessellated onto the Z axis which is an additional space axis to depict the selection of antenna index or location information. Considering the transmission of a 4-bit block code, the 2D constellation diagram has an Imaginary and Real part to represent the transmitted two bits, and the remaining two bits are used to designate the antenna on the array. For example, if the transmitted bit sequence is 1110 then the first two bits '11' are used to select the Fourth transmitter antenna (Tx3) and the next two bits are the message transmitted. The transmitted symbol location in the 3D constellation diagram in Figure 5.13 is represented in yellow. Thus, spatial modulation rests on using the implicit information transmitted by selecting the transmit antenna on which to transmit the symbols. This additional spatial dimension of spatial modulation can be exploited in the corresponding design of Pattern Reconfigurable antennas that can generate multiple patterns that are tagged onto specific transmit antennas. This property of each radiation pattern containing the information on the antenna location in the array is harnessed in spatial modulation in terms of "unique channel signatures" during decoding at the receiver. As the radiation pattern is generated at each location of the antenna along the antenna array, the path that the ray takes is characterized differently due to the interaction with scatterers in the environment. This introduces richness of the received information especially when the same symbol is transmitted along the entire array. This gives scope for efficient and accurate decoding at the receiver. The individual channel impulse responses themselves can be viewed as the message transmitted in this case. The above theoretical framework of Spatial modulation has been validated experimentally in [15]. The author refers interested readers to this paper where a real time implementation of spatial modulation on the testbed is provided. The details of this are omitted here on brevity grounds.

To realize the requirements of the devices being deployed in IoT (Internet of Things), a reconfigurable antenna is proposed with pattern reconfigurability that can be employed for

transmission using spatial modulation in indoor 5G small cell scenarios or point to multipoint casting. The rest of the chapter discusses the reconfigurable antenna.

5.3 Single RF MIMO Antenna array concept

5.3.1 Antenna description

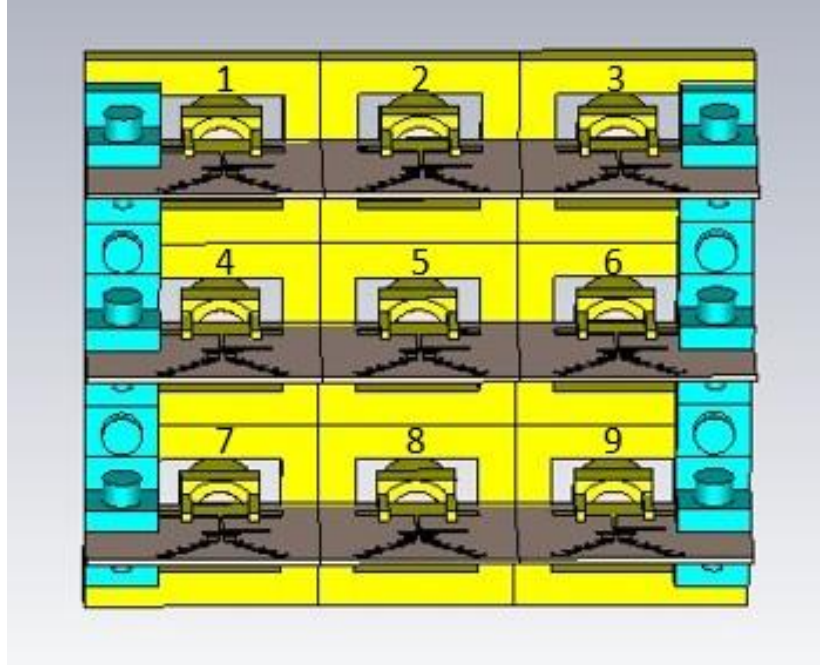


Figure 5.14 Reconfigurable antenna geometry

The proposed reconfigurable antenna for spatial modulation is shown in Figure 5.14. It consists of 9 antenna elements placed in a 3x3 square matrix form operating in the band 13.5 to 14.5 GHz centred at 14 GHz. The orientation of the antenna as shown in the Figure 5.15 is such that the antenna array ground plane (yellow) lies perpendicular to the quasi-endfire antenna elements. The antenna beam projects out perpendicular to the ground plane. The antenna elements are numbered as shown in Figure 5.15.

5.3.2 Antenna scheme of excitation

To realize Single RF, the central antenna number 5 is 'phase tethered' electronically to the neighbouring antennas using a phase excitation technique. The motive behind this is to obtain a twin-beam configuration that can be rotated over the azimuth. The antenna pattern labelled as rotate1 in Figure 5.17 is obtained by exciting the antenna 5 with amplitude 1 and phase 0, and simultaneously feeding the antenna 2 with amplitude 1 and phase 180 as in Figure 5.15, while the rest of the antenna elements are open. This scheme results in the generation of a simultaneous twin-beam MIPP (Mirrored image pattern pair) oriented along antenna element 5 and 2. So, at any given time a single port excitation spread over two antennas differentially generates the twin beam patterns.

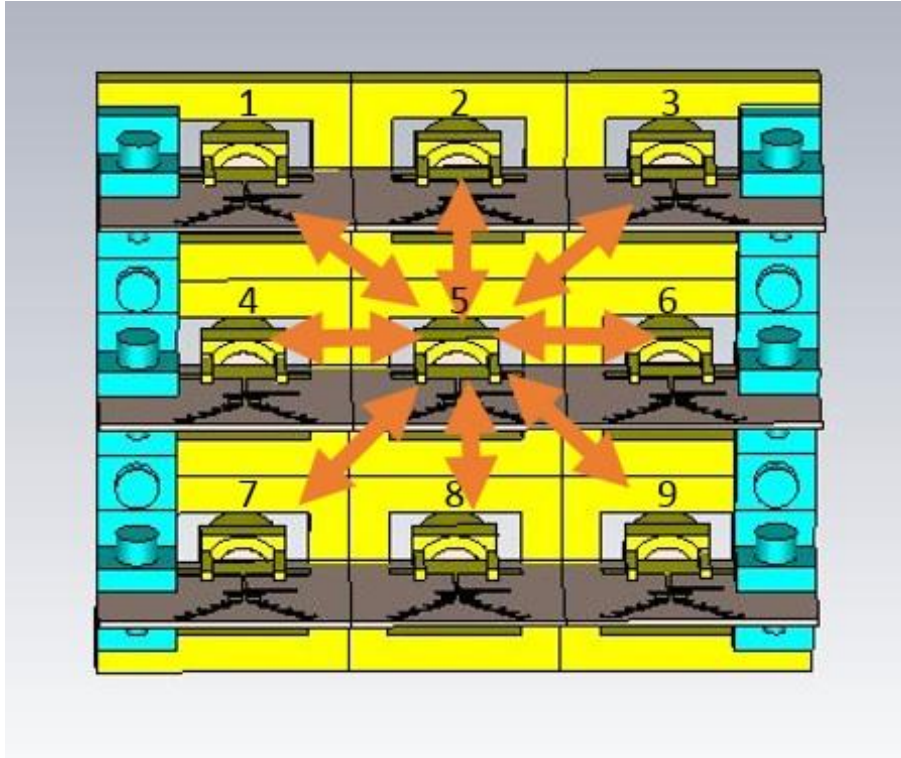


Figure 5.15 Antenna pairs for the orientation of the sequential rotational far field

The above scheme when repeated with antenna element 5 sequentially alongside elements 3,6,9,8,7,4,1 generates beams rotate2 to rotate8 as in Figure 5.15, oriented along those directions. At a single instant of time, there is a mirrored beam pattern oriented along the excitation vector plane, coming out of the array plane perpendicularly. The following switching scheme performed sequentially in time generates an azimuthal rotational Single RF antenna. The reduction ratio in the number of RF chains is 9:2 - almost 4 times decrease in the input power consumption.

5.3.3 Switching scheme, excitation matrices and rotational beams

Table 5.1 describes the different amplitude and phase states to attain the rotatable twin beam, with associated excitation matrices shown in Figure 5.16.

Results for the simulation of the eight rotational beam states for this configuration are shown on Figure 5.17 using the name convention of Table 5.1.

Index of 1 st Antenna element, amplitude, phase	Index of 2 nd Antenna element, amplitude, phase	Name of the pattern figure
5,1,0	2,1,180	Rotate1
5,1,0	3,1,180	Rotate2
5,1,0	6,1,180	Rotate3
5,1,0	9,1,180	Rotate4
5,1,0	8,1,180	Rotate5
5,1,0	7,1,180	Rotate6
5,1,0	4,1,180	Rotate7
5,1,0	1,1,180	Rotate8

Table 5.1 Phasing scheme of the 3x3 antenna

$$\begin{array}{ll}
 \text{Rotate 1} & \text{Rotate 2} \\
 \begin{bmatrix} 0 & \text{Amp1}, \text{Ph180} & 0 \\ 0 & \text{Amp1}, \text{Ph0} & 0 \\ 0 & 0 & 0 \end{bmatrix} & \begin{bmatrix} 0 & 0 & \text{Amp1}, \text{Ph180} \\ 0 & \text{Amp1}, \text{Ph0} & 0 \\ 0 & 0 & 0 \end{bmatrix} \\
 \text{Rotate 3} & \text{Rotate 4} \\
 \begin{bmatrix} 0 & 0 & 0 \\ 0 & \text{Amp1}, \text{Ph0} & \text{Amp1}, \text{Ph180} \\ 0 & 0 & 0 \end{bmatrix} & \begin{bmatrix} 0 & 0 & 0 \\ 0 & \text{Amp1}, \text{Ph0} & 0 \\ 0 & 0 & \text{Amp1}, \text{Ph180} \end{bmatrix} \\
 \text{Rotate 5} & \text{Rotate 6} \\
 \begin{bmatrix} 0 & 0 & 0 \\ 0 & \text{Amp1}, \text{Ph0} & 0 \\ 0 & \text{Amp1}, \text{Ph180} & 0 \end{bmatrix} & \begin{bmatrix} 0 & 0 & 0 \\ 0 & \text{Amp1}, \text{Ph0} & 0 \\ \text{Amp1}, \text{Ph180} & 0 & 0 \end{bmatrix} \\
 \text{Rotate 7} & \text{Rotate 8} \\
 \begin{bmatrix} 0 & 0 & 0 \\ \text{Amp1}, \text{Ph180} & \text{Amp1}, \text{Ph0} & 0 \\ 0 & 0 & 0 \end{bmatrix} & \begin{bmatrix} \text{Amp1}, \text{Ph180} & 0 & 0 \\ 0 & \text{Amp1}, \text{Ph0} & 0 \\ 0 & 0 & 0 \end{bmatrix}
 \end{array}$$

Figure 5.16 Antenna array excitation matrices (Amp: Amplitude; Ph: Phase; 0: Port not excited)

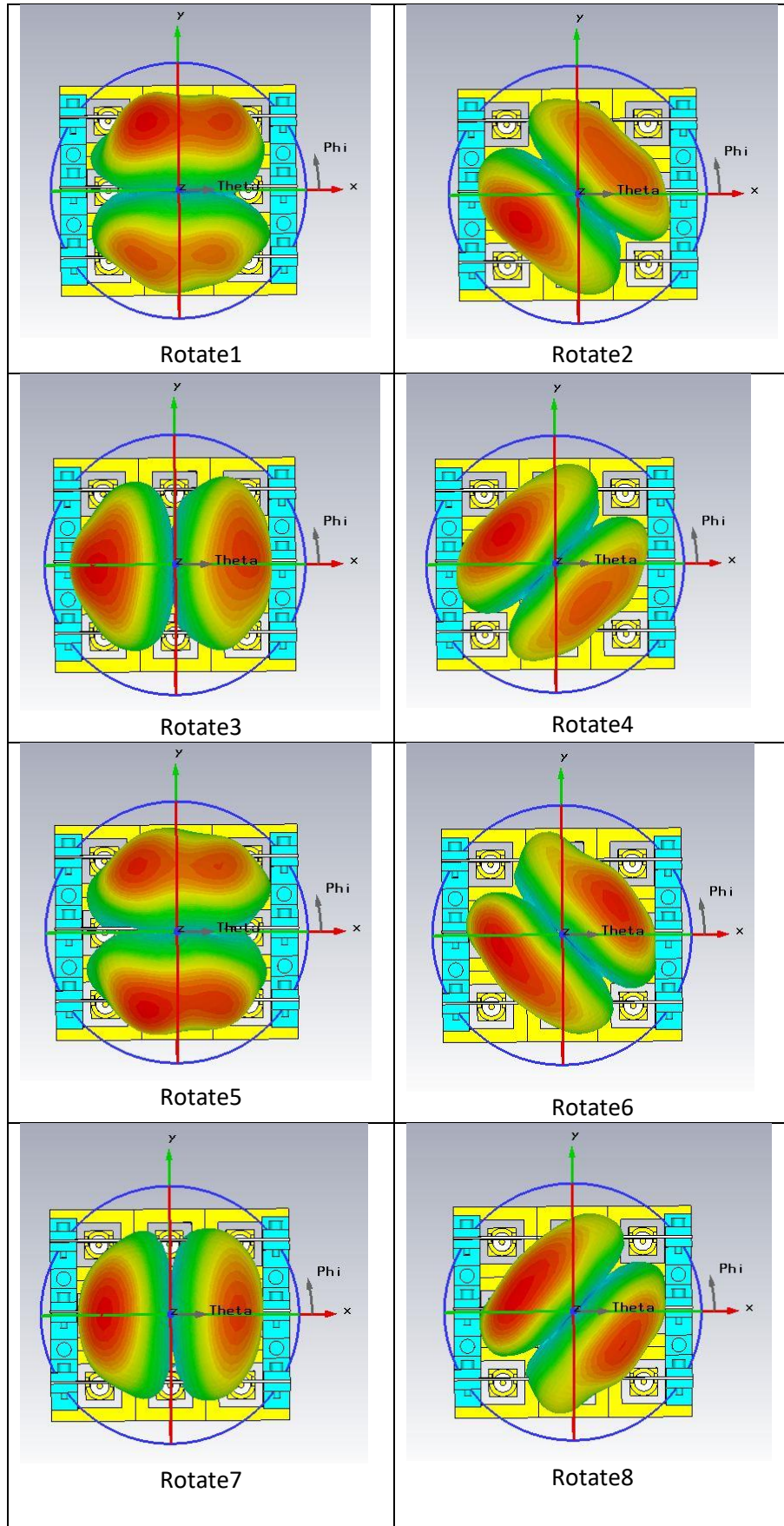


Figure 5.17 Rotational pattern beams

5.3.4 Full wave simulator calculated 3D Correlation Coefficient

Under Gaussian power distribution function for Elevation and Azimuth, the Full wave simulator calculated 3D Correlation Coefficient of the rotate1 pattern with the rest of the patterns is given below:

	Rotate1	Rotate2	Rotate3	Rotate4	Rotate5	Rotate6	Rotate7	Rotate8
Rotate1	1.0	0.08	0.47	0.21	0.29	0.2	0.43	0.10

For the above calculation, the correlation formula equation 5.4 was used,

$$\rho_e = \frac{\left| \int_{4\pi} \int_{4\pi} [\vec{F}_1(\theta, \phi) \cdot \vec{F}_2(\theta, \phi)] d\Omega \right|^2}{\int_{4\pi} \int_{4\pi} |\vec{F}_1(\theta, \phi)|^2 d\Omega \int_{4\pi} \int_{4\pi} |\vec{F}_2(\theta, \phi)|^2 d\Omega} \quad \dots (5.4)$$

where, F_1 and F_2 represent the **complex** vector radiation pattern of the two patterns to be correlated, ρ_e represents the correlation coefficient. The formula can be intuitively interpreted as the measure of geometrical overlap between the individual patterns as against the total steradian sphere. This also gives a measure of orthogonality between the beams to an extent.

A low correlation coefficient implies the beams differ from each other remarkably. A pictorial depiction of the adaption of the above 3x3 beamswitching scheme onto a 9x9 array is shown in Figure 5.18. The antenna array of 9x9 can be divided into 9 sub-arrays of 3x3 each with each 3x3 sub array providing the eight beam states individually. With regards to the power budget there is a reduction in power of the ratio 1:9 using this scheme. Also due to the individual use of the sub arrays there is no overlap between the eight beam states of each sub array. In fact, the spatially separated location of each of these sub-arrays adds to the channel richness arising from impulse responses due to varied locations in space. In addition to antenna index as transmitted by spatial modulation an additional sub-array index can also be transmitted which increases the data throughput substantially giving rise to a possible 4th dimensional (4th dimension of sub-array index location) increase of throughput. Though this may seem far-fetched, the exploitation of sub-array index of reconfigurable antenna patterns as an additional arm of the 3D constellation diagram leads to increased data rates, in case of Spatial Modulation.

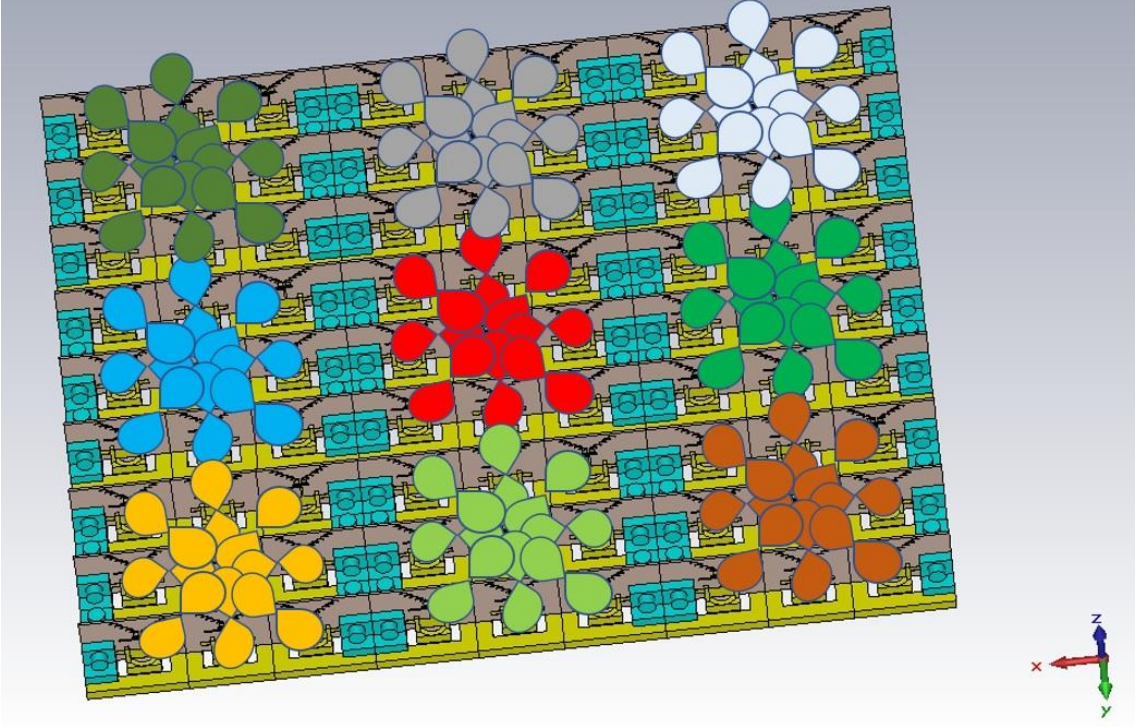


Figure 5.18 9x9 array with single RF MIMO scheme built on 3x3 subarray

5.4 Single RF MIMO antenna array measurement and discussion

In general, as massive MIMO antenna arrays have 64 or 128 antennas, it would be better to design and test the beamswitching proposed in section 5.3 over a 4x4 sub-array yielding into a symmetric division of the Massive MIMO array into sub arrays from operational point of view. All the conclusions drawn over the 3x3 array can be extended onto the 4x4 case.

Spatial modulation in Large Scale MIMO antenna arrays used in cellular base stations for high data rate applications can benefit by the periodic application of sub arrays employing Single RF MIMO. A prototype of the fabricated 4x4 sub array is shown in Figure 5.19. The antenna element of the array operates at 14 GHz and is discussed in chapter 3. The interelement spacing over the planar array along the x and y direction is 0.8λ . A phasing network as shown in Figure 4.7 (b) with two phase states feeds the antenna array to realize Single RF operation.

A total of 8 usable antenna radiation patterns are generated over the 4x4 sub array. To extend the use of this scheme in a generalized Massive MIMO antenna array that incorporates Single RF operation inside it, the following number of usable antenna patterns is deduced based on the number of elements in the antenna array: Owing to the dependence of the 4x4 Single RF antenna array pattern on the physical distance of separation between the two excited antenna elements (leading to undesirable grating lobes), all the combinations arising out of $C(16,8)$ cannot be used physically. Hence 8 usable patterns can be obtained. This scheme of the sub array can be extended to a larger array antenna whose elements are expressed as a square matrix whose dimension is an integral multiple of 4. As an example, a Massive MIMO array of 64 elements can produce a total of $8 \times N$ reconfigurable usable antenna radiation patterns, where N is number of 4x4 sub-arrays used in the larger array. In the case of 8x8 Massive MIMO it calculates to a total of $8 \times 4 = 32$ usable index coded antenna patterns.

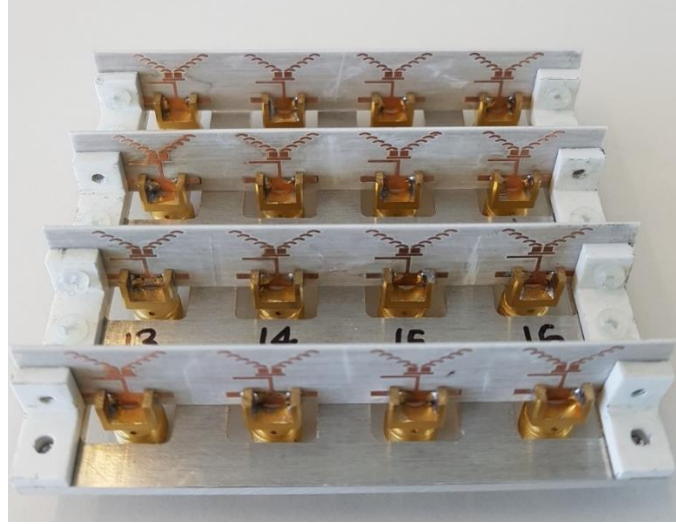


Figure 5.19 Fabricated antenna array

5.4.1 Mirror image pattern pair generating scheme

In the proposed single RF scheme, the single RF mirror pattern pairs are based on the excitation matrices shown in Figure 5.20. Each element of the 4x4 matrix represents the excitation fed to the corresponding antenna of the 4x4 antenna array. The excitations are of uniform amplitude of 1 and can have phases of 0° and 180° represented by '+' and '-' respectively. A not fed antenna element is represented by '0'. Following the excitation matrix, a mirrored pattern pair can be used to switch the beam clockwise thereby obtaining 8 patterns. Only 5 patterns are simulated and compared with measurements in the anechoic chamber for concept validation owing to the symmetrical nature of the antenna array.

$$\begin{array}{cc}
 \begin{bmatrix} 0 & + & + & 0 \\ 0 & + & + & 0 \\ 0 & - & - & 0 \\ 0 & - & - & 0 \end{bmatrix} & \begin{bmatrix} 0 & 0 & + & + \\ 0 & 0 & + & + \\ - & - & 0 & 0 \\ - & - & 0 & 0 \end{bmatrix} \\
 A & B \\
 \begin{bmatrix} 0 & 0 & 0 & 0 \\ - & - & + & + \\ - & - & + & + \\ 0 & 0 & 0 & 0 \end{bmatrix} & \begin{bmatrix} - & - & 0 & 0 \\ - & - & 0 & 0 \\ 0 & 0 & + & + \\ 0 & 0 & + & + \end{bmatrix} \\
 C & D \\
 \begin{bmatrix} 0 & - & - & 0 \\ 0 & - & - & 0 \\ 0 & + & + & 0 \\ 0 & + & + & 0 \end{bmatrix} \\
 E
 \end{array}$$

Figure 5.20 Excitation matrices of the five states

The five twin beam patterns are named 'Rotate 1' to 'Rotate 5' as shown in the pictorial depiction in Figure 5.21. As can be seen from Figure 5.21, The 'Rotate 1' and 'Rotate 5' states overlap, they are different only in terms of the excitation vector orientation. The matrices corresponding to each of these states are named A to E respectively.

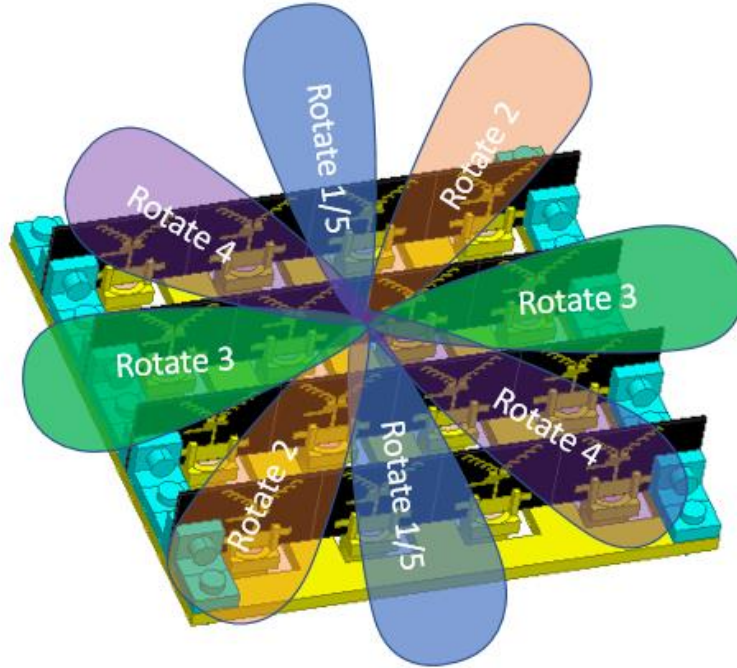


Figure 5.21 Pictorial depiction of the attainable rotate beam patterns

The 4x4 antenna array was simulated using the full wave solver Ansys HFSS. The fabricated antenna was measured for its pattern and gain characteristics in the anechoic chamber setup as shown in Figure 5.22. The simulated and measured patterns are compared in Figure 5.22-5.27 for the different electronically rotated pattern states. A beam pattern pair is realized with cross polar levels better than 20 dB. The beam cuts are identical in shape but are measured at differently oriented angles in space. The gain vs frequency behaviour of the antenna array was also measured using the two-antenna method and this is shown for the different pattern states in Figure 5.28-5.32. A co-polar gain of 8 dBi is seen over the band 13.5 GHz to 14.5 GHz.

5.4.2 Pattern and gain measurements



Figure 5.22 Antenna measurement setup in anechoic chamber

Pertaining to the pattern measurements as discussed in chapter 4, there is a pronounced ripple effect seen at certain angles of incidence due to the reflections. An interesting observation was made to support this claim when the 3x3 array antenna was setup to measure the rotate1 to rotate8 pattern in the chamber. For the 3x3 array antenna, two antennas are excited at a time and the emitted power levels at 14 GHz are not high enough to combat the reflections that arise due to the absorbers. Therefore, the phase information had to be distributed over more number of antennas, in this case, it was increased from 1 to 4. This resulted in the emitted power taking dominance over the reflections to an appreciable extent and therefore facilitated the pattern measurements. The setup shown in Figure 5.22 uses the same antenna and phasing network discussed in chapter 4, the difference lies in the way the pattern reconfigurability is introduced. In the 4x4 antenna array, for each rotate pattern state a group of 4 antennas were selected to feed phase 0° and a group of another 4 antennas were selected to feed phase 180° . The remaining 8 antennas were match terminated to avoid port reflections. A suitably designed absorber was used to back the ground plane of the antenna. As this measurement emphasizes on retaining the same phase center for multiple patterns, a proper alignment of the antenna array aperture with respect to the positioner axis was performed beforehand to eliminate misalignment errors.

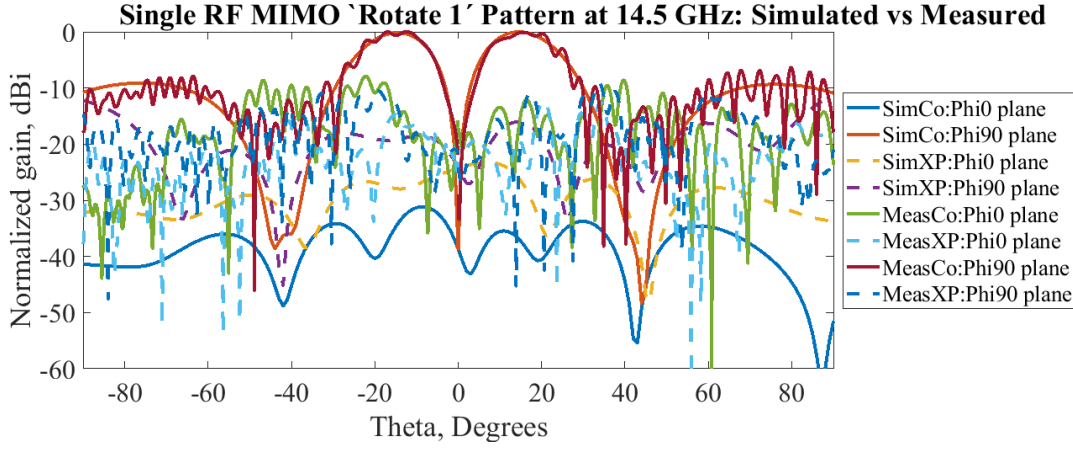


Figure 5.23 Rotate 1 pattern

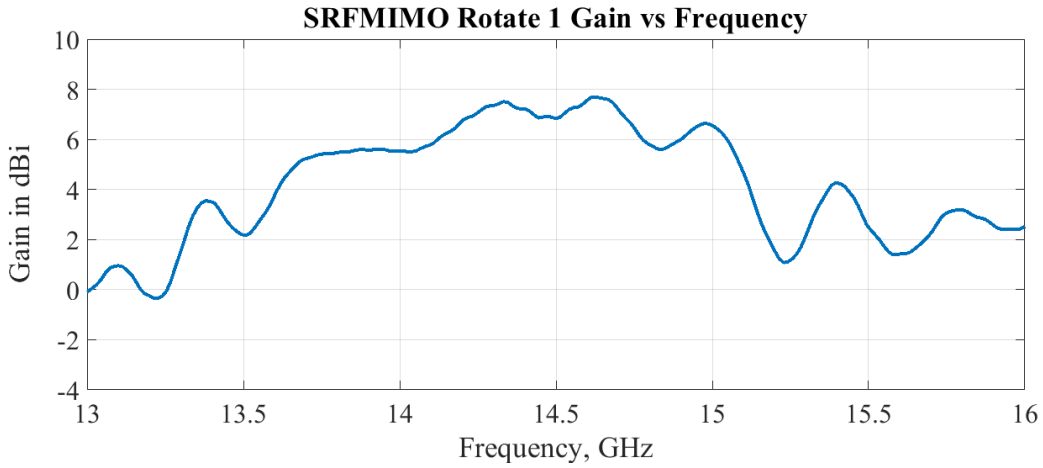


Figure 5.24 Measured Gain vs frequency for rotate 1

Figure 5.23 depicts the comparison between the simulated and measured Rotate1 pattern state. Along the Phi90 plane there is a good agreement between the simulations and measurements for $|Theta| < 20^\circ$ with no ripples seen. When employed to spatial modulation, the antenna index symbol can be sent implicitly over this unique pattern cut characteristic generated over the Phi90 plane. The additional information namely the actual message symbols or bits obtain their unique channel signature based on the pattern shape depicted in Figure 5.23. The dual beams formed help in reinforcing the overall pattern orientation along an axis, in this case the Phi90 plane. Therefore, the measurements by confirming the pattern shape and orientation uphold the use of the pattern for spatial modulation applications. As seen in previous discussion in chapter 4 ripples are seen for angles $|Theta| > 20^\circ$ for similar reasons expressed earlier in chapter 4. The cross polar levels are well below -12 dB throughout the angular range. Figure 5.24 depicts the measured gain vs frequency graph using the two- antenna method. The beam alignment was carried out keeping the boresight beam generated by 4x4 antenna array as reference to make the gain measurements. A gain around 8 dBi was measured in the band (which is acceptable as spatial modulation is a low power application as detailed in the section 5.2.3).

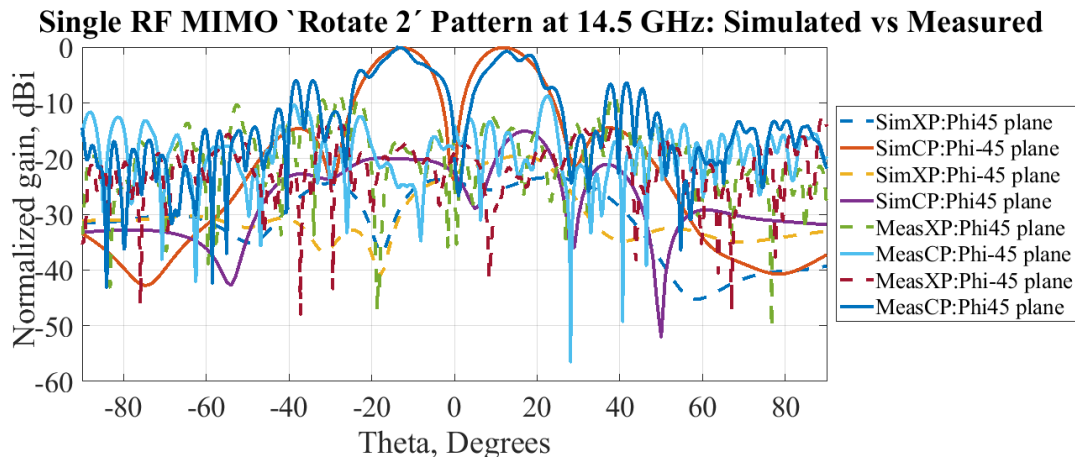


Figure 5.25 Rotate 2 pattern

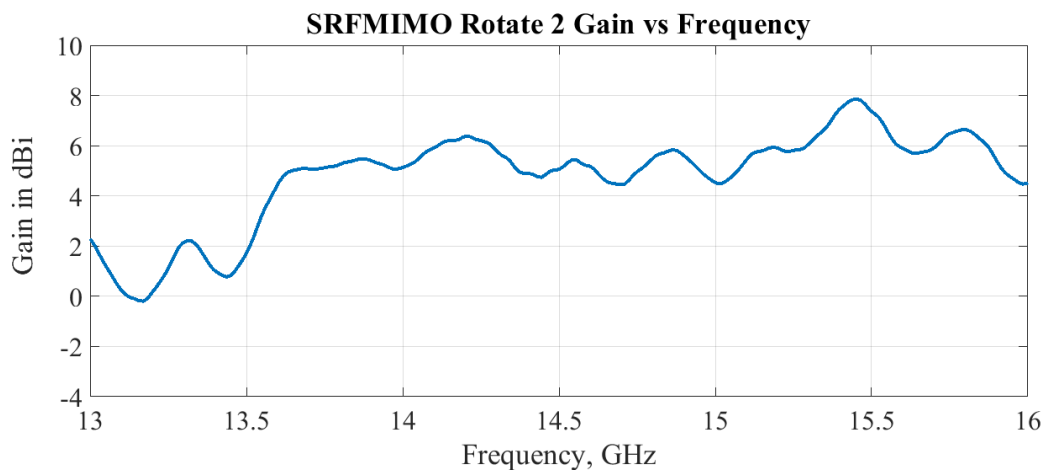


Figure 5.26 Measured Gain vs frequency for rotate 2

Figure 5.25 presents the comparison between simulation and measurement of the Rotate2 beamstate pattern which essentially is the slant 45 oriented beam pattern. The importance of this beamstate stems from the fact that the orientation is neither vertical nor horizontal in this configuration. The slant 45 beam has been validated by pattern measurements by making cuts along the Phi +45 and Phi-45 plane. The two-beam pattern is measured along the Phi45 plane with a good agreement between the simulated and measured results. In terms of application to spatial modulation, this pattern has a unique signature of the pattern being slant 45 oriented which can be used to represent yet another antenna state/index implicitly. The message symbols are mapped directly onto the two-beam pattern. Figure 5.26 shows the measured gain vs frequency graph. A gain of around 8 dBi is measured in the band. The gain measurement was performed by setting the roll positioner to slant 45 and the probe to align with the slant 45 AUT for maximum illumination. The two-antenna method was used to measure the transmission parameters which were then processed to obtain the gain.

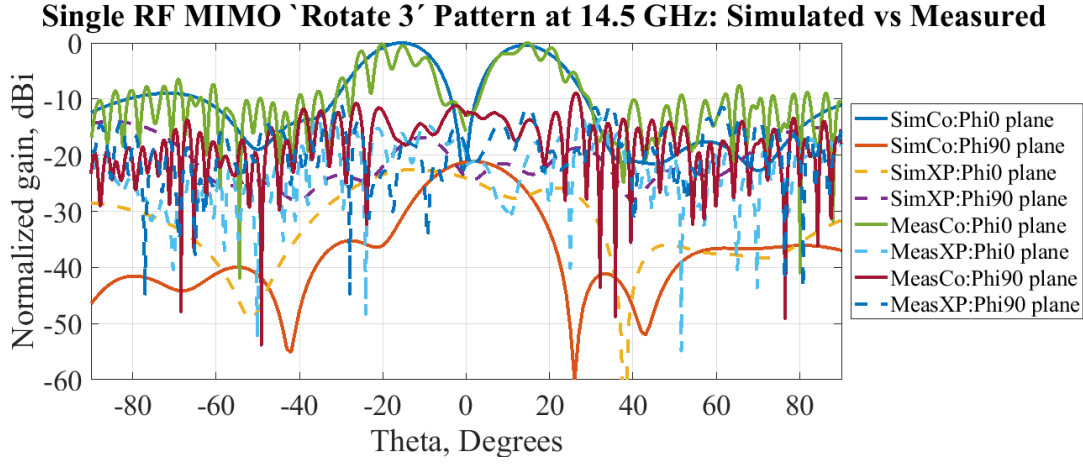


Figure 5.27 Rotate 3 pattern

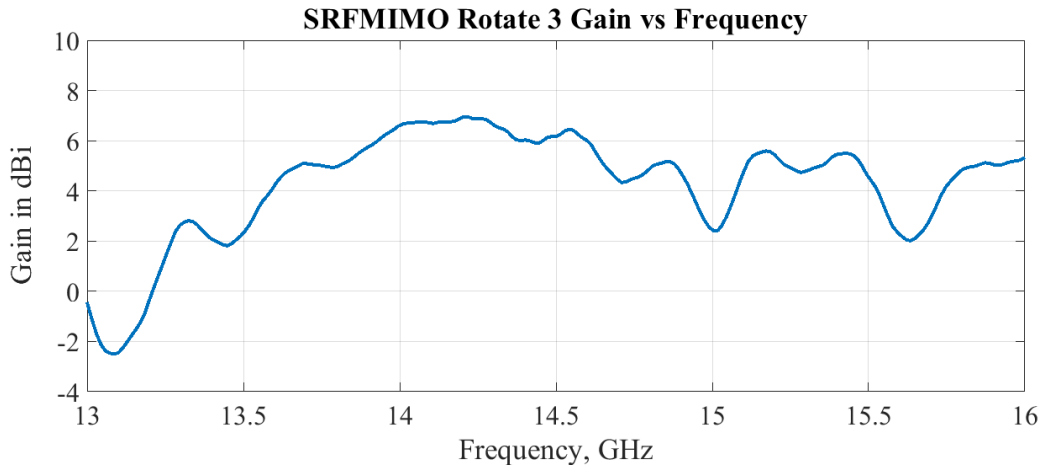


Figure 5.28 Measured Gain vs frequency for rotate 3

Figure 5.27 depicts the comparison between simulation and measurement for the Rotate3 beam state case. An interesting deviation from the earlier two Rotate1 and Rotate2 states is seen. From Figure 5.27, though the measured pattern profile shape is retained in comparison to the simulation, the ripples are uniformly present throughout the angular range. This can be explained by considering the orientation of the antenna elements for this special case on the antenna array. For this phase feeding the antenna elements are not facing each other but are edge coupled over the dielectric surface. This results in decreased strength of the phasing, and the resulting power generated, which gives rise to a uniform ripple throughout the angular range. To be precise, in this beam state case, considering the Figure 5.19, antenna elements 5,6,13,14 are phase coupled to antenna elements 7,8,15,16 which are not placed laterally in front of each other but through their edges which results in decreased conductive area of exposure for the phase coupling. Nevertheless, the pattern still retains its shape, making it still suitable for spatial modulation applications. The measured cross polar levels are less than -12 dB throughout the angular range. From Figure 5.28 a gain of about 7 dBi was measured over the desired band.

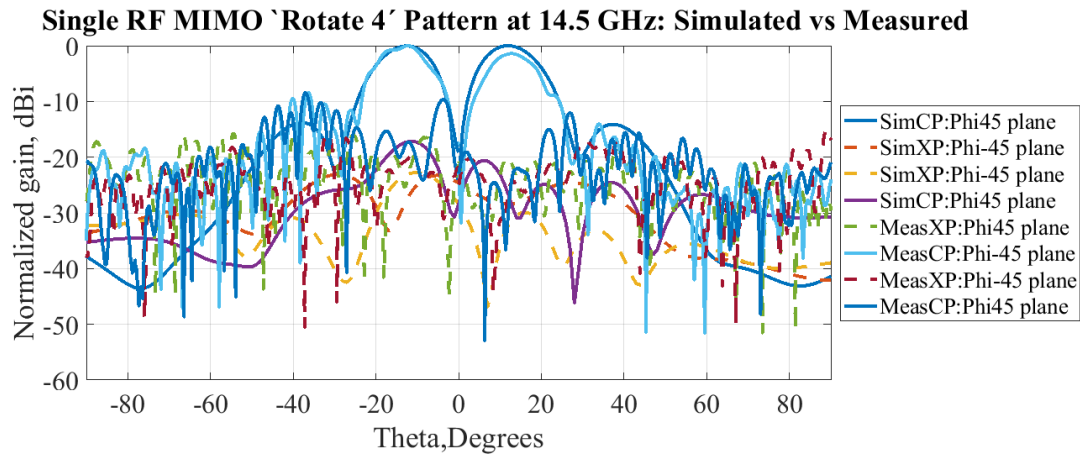


Figure 5.29 Rotate 4 pattern

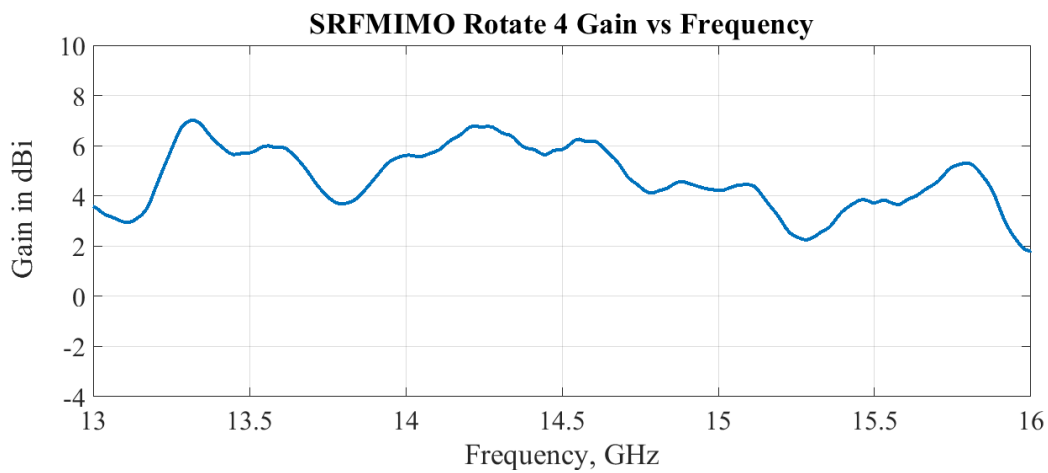


Figure 5.30 Measured Gain vs frequency for rotate 4

Figure 5.29 presents the comparison between simulation and measurement of the Rotate4 beamstate pattern which essentially is the slant -45 oriented beam pattern. The importance of this beamstate stems from the fact that the orientation is neither vertical nor horizontal in this configuration. The slant -45 beam has been validated by pattern measurements by making cuts along the Phi -45 and Phi+45 plane. The two-beam pattern is measured along the Phi -45 plane with a good agreement between the simulated and measured results. In terms of application to spatial modulation, this pattern has a unique signature of the pattern being slant -45 oriented in contrast to the slant +45 oriented beam in Figure 5.25, which can be used to represent uniquely yet another antenna state/index implicitly. The message symbols are mapped directly onto the two-beam pattern. Figure 5.30 shows the measured gain vs frequency graph. A gain of around 7 dBi is measured in the band. The gain measurement was performed by setting the roll positioner to slant -45 and the probe to align with the slant -45 AUT for maximum illumination. The two-antenna method was used to measure the transmission parameters which were then processed to obtain the gain.

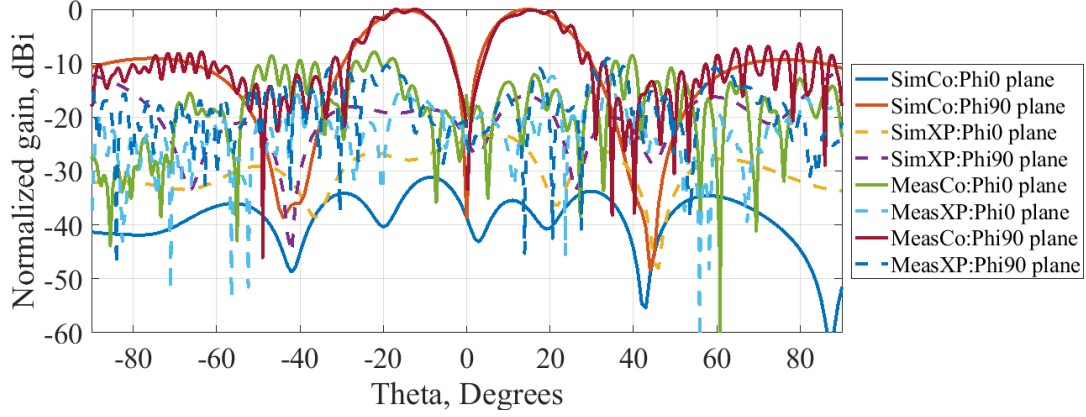
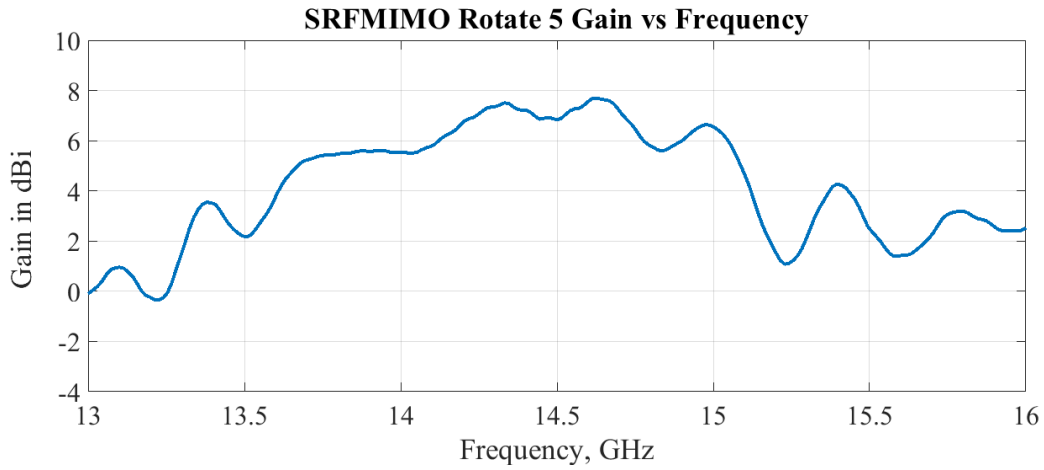
Single RF MIMO 'Rotate 5' Pattern at 14.5 GHz: Simulated vs Measured*Figure 5.31 Rotate 5 pattern**Figure 5.32 Measured Gain vs frequency for rotate 5*

Figure 5.31 depicts the comparison between the simulated and measured Rotate5 pattern state. Along the Phi90 plane there is a good agreement between the simulations and measurements for $|Theta| < 20^\circ$ with no ripples seen. When employed to spatial modulation, the antenna index symbol can be sent implicitly over this unique pattern cut characteristic generated over the Phi90 plane. This pattern though similar to pattern in Rotate1 beamstate differs in the fact that the received vector orientation is reversed owing to the reversed polarity of excitation in comparison to Rotate1 pattern beamstate. The additional information namely the actual message symbols or bits obtain their unique channel signature based on the pattern shape depicted in Figure 5.31. The dual beams formed help in reinforcing the overall pattern orientation along an axis, in this case the Phi90 plane. Therefore, the measurements by confirming the pattern shape and orientation uphold the use of the pattern for spatial modulation applications. As seen in previous discussion in chapter 4 ripples are seen for angles $|Theta| > 20^\circ$ for similar reasons expressed earlier in chapter 4. The cross polar levels are well below -12 dB throughout the angular range. Figure 5.32 depicts the measured gain vs frequency graph using the two- antenna method. The beam alignment was carried out keeping the boresight beam generated by 4x4 antenna array as reference to make the gain measurements. A gain around 8 dBi was measured in the band.

Rotate beamstates Rotate6, Rotate7, Rotate8 were not measured and are not discussed as these are exactly similar to their mirrored counterparts which have been measured. In total therefore, 8 pattern beamstates are confirmed by measurements for the proposed reconfigurable antenna array.

5.5 Conclusion

The chapter introduced a reconfigurable antenna design for Spatial Modulation implemented on a 4x4 antenna subarray. The twin beam mirrored pattern pairs were validated experimentally for their pattern and gain.

Such a beamswitching scheme when applied in a Massive MIMO array can lead to significant reduction of RF chains and power consumption. The limitation of Single RF MIMO, namely that it can be used in low data traffic situations can be alleviated to an appreciable extent if the proposed single RF scheme, works with integration onto a Massive MIMO array by selective use of the constituent sub-arrays of the Massive MIMO.

Moreover, instead of using different antenna patterns switched over different phase centres over the antenna array, the proposed single RF scheme owing to the symmetrical excitation of the ports maintains the same phase center for multiple radiation patterns over the sub-array, which is an advantage in spatial modulation where the same antenna index can be reused in time domain. The patterns can be switched over the same sub-array rather than moving along the planar array to switch patterns.

The use of sub-array indexing as an additional dimension to the 3D constellation diagram of Spatial Modulation was proposed. This would multiply the total information bits that can be mapped onto the collocated time-spread different patterns. The resultant is added spatial and pattern diversity as seen at each element of the array resulting in improved decoding at the receiver end.

Such a reconfigurable antenna would be well suited for application in transmit techniques involving time-based duplexing schemes such as Time Division Duplexing (TDD) where Channel State Information (CSI) would not be needed in the downlink.

5.6 References

- [1] M. Yousefbeiki and J. Perruisseau-Carrier, "Towards Compact and Frequency-Tunable Antenna Solutions for MIMO Transmission with a Single RF Chain," in *IEEE Transactions on Antennas and Propagation*, vol. 62, no. 3, pp. 1065-1073, March 2014.
- [2] A. Ourir, K. Rachedi, D. T. Phan-Huy, C. Leray and J. de Rosny, "Compact reconfigurable antenna with radiation pattern diversity for spatial modulation," 2017 11th European Conference on Antennas and Propagation (EUCAP), Paris, 2017, pp. 3038-3043.
- [3] Y. K. Cho, J. N. Lee, Y. H. Lee, G. Jo, J. Oh, and B. H. Park, " $\lambda/16$ spaced single RF chain MIMO antenna using low-power CMOS switches," in *Microwave Conference (EuMC)*, 2015 European, Sept 2015, pp. 726-729.
- [4] O. N. Alrabadi, C. Divarathne, P. Tragas, A. Kalis, N. Marchetti, C. B. Papadias, and R. Prasad, "Spatial multiplexing with a single radio: Proof-of-concept experiments in an indoor environment with a 2.6-GHz prototype," *IEEE Communications Letters*, vol. 15, no. 2, pp. 178-180, February 2011.
- [5] L. Xiao, Y. Xiao, L. You, P. Yang, S. Li and L. Hanzo, "Single-RF and Twin-RF Spatial Modulation for an Arbitrary Number of Transmit Antennas," in *IEEE Transactions on Vehicular Technology*, vol. 67, no. 7, pp. 6311-6324, July 2018.
- [6] D. Phan-Huy et al., "First Visual Demonstration of Transmit and Receive Spatial Modulations Using the "Radio Wave Display"," WSA 2017; 21th International ITG Workshop on Smart Antennas, Berlin, Germany, 2017, pp. 1-7.
- [7] R. Harrington, "Reactively controlled antenna arrays," 1976 Antennas and Propagation Society International Symposium, Amherst, MA, USA, 1976, pp. 62-65.
- [8] Chen Sun, A. Hirata, T. Ohira and N. C. Karmakar, "Fast beamforming of electronically steerable parasitic array radiator antennas: theory and experiment," in *IEEE Transactions on Antennas and Propagation*, vol. 52, no. 7, pp. 1819-1832, July 2004.
- [9] P. Tragas and A. Kalis, "A Printed ESPAR Antenna for Mobile Computing Applications," 12th European Wireless Conference 2006 - Enabling Technologies for Wireless Multimedia Communications, Athens, Greece, 2006, pp. 1-4.
- [10] Z. Imran and C. Panagamuwa, "Beam-switching planar parasitic antenna array," 2014 Loughborough Antennas and Propagation Conference (LAPC), Loughborough, 2014, pp. 160-164.
- [11] A. Kalis, A. Kanatas and C. Papadias, Eds., "Parasitic Antenna Arrays for Wireless MIMO Systems," Springer Science+Business Media, 2014.
- [12] O. N. Alrabadi, J. Perruisseau-Carrier and A. Kalis, "MIMO Transmission Using a Single RF Source: Theory and Antenna Design," in *IEEE Transactions on Antennas and Propagation*, vol. 60, no. 2, pp. 654-664, Feb. 2012.
- [13] Y. Cho, J. Lee, Y. Lee, G. Jo, J. Oh and B. H. Park, " $\lambda/16$ spaced single RF chain MIMO antenna using low-power CMOS switches," 2015 European Microwave Conference (EuMC), Paris, 2015, pp. 726-729.
- [14] M. Di Renzo, "Spatial modulation based on reconfigurable antennas-A new air interface for the IoT," MILCOM 2017 - 2017 IEEE Military Communications Conference (MILCOM), Baltimore, MD, 2017, pp. 495-500.
- [15] N. Serafimovski et al., "Practical Implementation of Spatial Modulation," in *IEEE Transactions on Vehicular Technology*, vol. 62, no. 9, pp. 4511-4523, Nov. 2013.

Chapter 6

Millimeter wave antenna

6.1 Introduction

A constellation-based satellite system or Local Multipoint Distribution System (LMDS) requires the deployment of antennas in a 5G millimeter wave small cell scenario. Millimeter Wave propagation requires high gain beams to combat the high path loss: this high gain can either be beamformed using an array of antennas or beam focused using a lens that enhances the gain [1]. The key requirements on the antenna in such an environment would be wide-angle scanning, wide band or dual-band coverage, multiple beam casting and highly directive gain. The lens approach to beam focusing is appealing owing to the simplicity of its design and the ease with which the beam can be steered to different angles using the same lens with minimal reconfiguration.

The latter lens approach has been considered in this Thesis to develop a proposal of antenna for the Millimeter Wave range which is presented in this chapter. The lens operates by launching 3 beams along directions of -60° , 0° and $+60^\circ$ acting simultaneously as transmitter and receiver. The central beam can be used to transmit, and the outer beams can be used to receive primarily, though, any combination of the transmit receive antennas is possible to attain, giving the possibility of a full duplex operation to enhance the spectral efficiency while simultaneously achieving self-interference cancellation (SIC) through antenna separation isolation [2]. Owing to the beam focusing high gain that is mainly attained through the lens with use of less number of antennas, the number of Analog to Digital Converters (ADCs), Amplitude Detectors (ADs) and Low Noise Amplifiers (LNAs) would be reduced, adding to the reduction of the power consumption when using algorithms in hybrid precoding. The antenna at its transmit and receive mode can be used in a 5G small cell scenario for Outdoor to Indoor (O2I) signal transition of the narrowband/wideband signal or in situations wherein 120° sector beams are required that, when combined, greatly reduce the coverage gap areas. Ultra-Dense cells, increasing the available spectrum and increasing the spectral efficiency are the three main dimensions that are focused upon to increase the cellular network capacity [3]. Among these, denser cells are more appealing owing to its cost effectiveness. Denser cell deployment brings up the need for multibeam antennas. It is reported that Tri-beam deployments of antennas on sectors rotated by 10° significantly reduces the coverage gaps [3]. This transmit receive antenna system in addition upholds the principle of having fewer RF chains as required in receive spatial modulation for Millimeter Wave Massive MIMO systems. In the following a state-of-art survey on current lens technologies is presented and compared to the present approach.

A lens antenna is generally made of dielectric or transmission line delays. In [1] a metallic delay lens is introduced in which the focusing action is obtained by reduction of the phase velocity of the radio waves passing through the lens. In comparison to [1] a method of increasing the phase velocity of the radio waves is proposed in metal plate lens such as the Ruze lens [4] and the Rotman lens [5]. An approach to distribute the radiating source elements along a focal

surface of a planar EM lens is discussed in [6], which is termed as the lens antenna array. The angle dependent energy focusing property of lens antenna array is harnessed in improving the channel capacity of mmWave channel. Another approach in realizing delay lens is using a transmission line delay that emulates the various phases as along a lens [7]. Here the profile of the transmission line is chosen in a such a way that a line source placed inside the lens radiates a plane wave on the outside before being launched. A multi-layer leaky wave-based solution based on the substrate integrated waveguide (SIW) technology is proposed in [8]. The method consists of launching the source waves through a SIW and coupling it to the radiating leaky wave slots, with a quasi-optical system of EM coupling. [9] introduces a parallel plate waveguide-based (PPW) solution to the multi-beam casting problem. A continuous delay lens based quasi optical beamformer was designed, manufactured and tested for operation in the Ku band. [10] provides the analysis of the design in [9] using a ray tracing technique. A detailed numerical analysis tool is provided in [11] to predict the performance of the beamformer. [12] proposes a 4-port parallel plate lens antenna using a uniform cylindrical dielectric as the lens. The lens is excited by coaxial probes which reduces the size and increases the bandwidth. The main advantage of the structure is that a single slab dielectric is used with no layering. However, for higher power requirement applications including those at high frequencies, as the authors in [12] state, beyond 14 GHz dielectric losses dominate and the radiation efficiency starts decreasing. In [13], a concept to realize a Luneburg lens antenna using a bed of nails is proposed. The lens operation is achieved by the modulation of the refractive index simultaneously by the continuous variation of metal post thickness and parallel plate waveguide spacing. The concept presents a way to discretize the lens operation by approximation using a bed of nails. It achieves a bandwidth of 40% in the Ku band.

In this chapter, a millimeter wave multi-beam antenna operating dual band with a 1 GHz bandwidth each around the 28 GHz and 31 GHz frequencies is presented. The antenna is designed on the principle of transformation of the cylindrical wavefront to planar wavefront to enhance the gain. A metal ridge lens is used for the wavefront transformation by a phase extraction and compensation method. The dual band operation of the antenna aids in transmitting and receiving at two independent frequencies. The main advantage of the antenna is the high-power handling capability due to the non-usage of breakdown dependent dielectrics. Another advantage is in the reduction of the number of RF chains significantly due to the use of the shared lens to enhance the obtained gain. The antenna has been experimentally validated for casting the beam in three primary target directions of -60° , 0° and 60° , however other beam directions can be suitably designed. The spatial footprint of the antenna is 170 mm x 150 mm and has a gain of 15 dBi at each of the three ports. The fabrication has been done using Computer Numerical Control (CNC) machining and the antenna is an all-metal prototype. The theoretical simulated results have a good agreement with the measurements. The antenna can find potential use in 5G small cell deployments of millimeter wave LMDS.

The approach adapted in the design of the antenna in this chapter relates and differs from the prior works as detailed next. The papers [4-10] introduce diverse ways of realizing the energy focusing property with SIW, transmission line and lens technology. [9-11] propose a way to design a beamformer- all in the sub-20 GHz frequency range using a ridge-based lens. The approach however in these methods is to use ray optics to arrive at the position of the feeding horns and to decide on the contour of the lens. In this paper, a proposition is made to design the feeding horn and ridge-based lens using a phase extraction and compensation method, building solely upon full wave simulations. The use of an initial simpler full wave simulation to extract information on the phases of the wavefront helps in the easier refining of the design model to attain beam focusing. In the approach in [11] an analytical formulation is made based on ray optics to predesign the beamformer, which is subject to local and global optimization procedures to fine tune the beamformer. In the proposed design the final optimization is minimized owing to the individual considerations and co-design of the parts that make up the beamformer. Another

key difference is to use E plane sectoral horns that aid in the ease of integration to the parallel plate waveguide. The antenna has also been designed for dual band operation in the Ka band as opposed to [9-11] which gives it scope to act as transceiver for Tx and Rx at two different frequencies. Also, the designed uniform height of the ridge lens makes the 3D fabrication much simpler as compared to [9] since there is no tapering of the ridge towards the edges. The parallel plate waveguide beamformer is designed and performance validated by full-wave simulation for operation in the dual band of 28 GHz and 31 GHz, with a bandwidth of 1 GHz each. A systematic design approach encompassing the co-design of the sectoral E-plane feed horns, the parallel plate waveguide, the ridge lens and the flared horn aperture is presented. The multi-beam angular directions have been validated with directional gains around 15 dBi targeted in the directions of -60° , 0° and 60° .

After introducing the prior and related works and highlighting the features of the presented work in comparison to them in this Section, the rest of the chapter is organized as follows: Section 6.2 deals with the design principle of the antenna and explains the mechanism of the antenna operation. Section 6.3 focuses on the detailed antenna design. Section 6.4 presents the measurement and discussion of the three port antenna characteristics that include the S parameter measurement, Port-to-Port isolation measurement, pattern and gain measurement. Section 6.5 concludes, summarizing the results achieved and the potential applications of the antenna. The validation and presentation of the design by full wave simulation was presented in [15] and the content of this chapter also includes the framework for theoretical principle of operation of the antenna, fabrication of the prototype, the design and fabrication of custom made-transitions and the measurement of S parameters, radiation pattern, Gain and XPD.

6.2 Design principle

The millimeter wave antenna presented has three ports of excitation illuminating a common ridge-based lens through E plane sectoral horns before radiating out into free space through flared horn apertures. The purpose of using the ridge-based lens is to enhance the gain seen at each of the ports of the antenna. This is obtained by transformation of wavefronts from cylindrical to quasi-planar. The wavefront transformation guides the design of the ridge-based lens using the following theoretical approach:

The geometry of the structure is described in Figure 6.1 which depicts the various parts of the antenna, with three E plane sectoral horns feeding a ridge-based lens through a parallel plate waveguide before radiating out as a flared aperture. The antenna is placed along the XZ plane with radiation in the z direction when the central port is excited. The other two outer ports are oriented obliquely at angles of $+60^\circ$ and -60° . The three ports are all facing inward convergingly towards a central focus, which utilizes a smaller spatial footprint as compared to the case when the outer horns face outwards. The three horns in the converging case share a small footprint of the shared aperture.

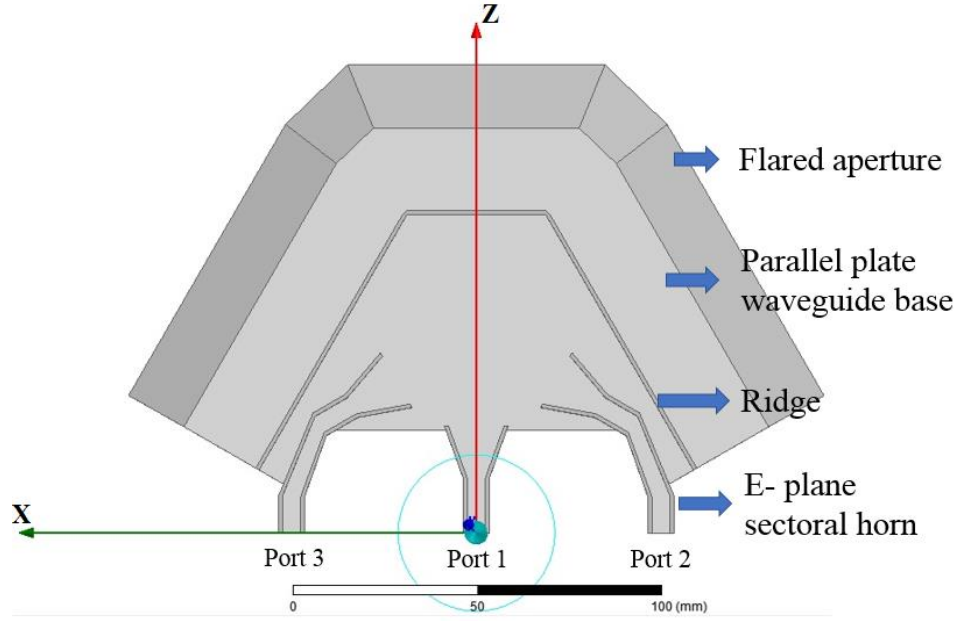


Figure 6. 1 Transversal section of the waveguide lens antenna

The initial distance from the E-plane sectoral horn aperture to the ridge is set using the azimuthal beamwidth of the E-plane horn at -12 dB and by calculating the corresponding arc length and radius ratio, using the trigonometric rule:

$$\theta = \frac{l}{r} \quad \dots (6.1)$$

where, θ is the subtended beamwidth angle in radians and l is the subtended arc length and r is the radius. Using the above rule, the distance ' r ' between the E-plane horn aperture and the ridge was set to 50 mm, which is in the Far-field region of the E-plane sectoral horn. The Far-field distance is 47.8 mm calculated for the horn aperture of 15 mm x 7.5 mm at 28 GHz. This further for a -12 dB beamwidth of 66° (1.15 radians) of the E-plane sectoral horn, necessitates a ridge length of 57 mm for optimal illumination.

The design of the parallel plate waveguide which discussed in section 6.3.1 ensures that higher order modes are cut-off and the excited mode is the lowest order TE mode. For the following discussion the dominant TE mode is considered along the x direction.

Figure 6.2 depicts the wavefront transformation of the waves along the millimeter wave antenna. The central port has cylindrical wavefronts, clearly seen in Figure 6.3 when no ridge is present in the structure, emanating towards the ridge placed at the far field distance (D_{Fraun}) and planar wavefronts emanating out after transformation through ridge-based lens. A methodological control over this transformation can be obtained by analysing the phases of the wavefront as it propagates through the millimeter wave antenna.

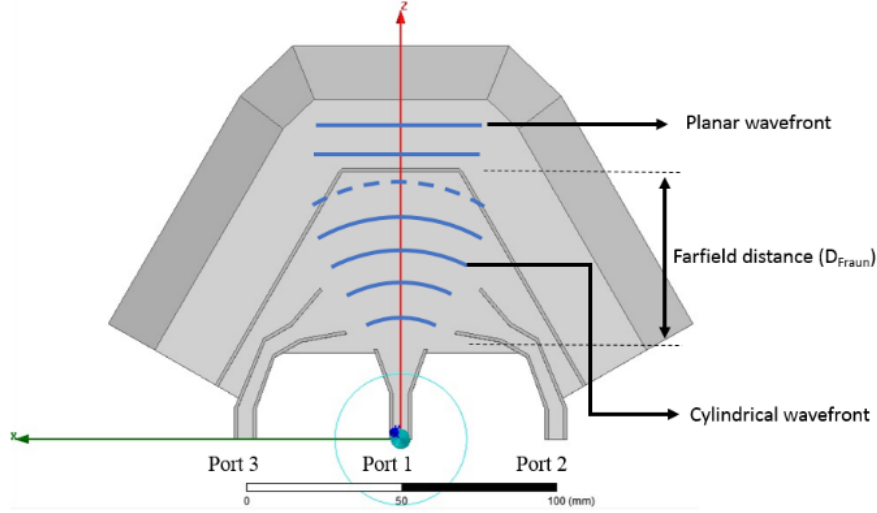


Figure 6.2 Depiction of the wavefront transformation

Let the phase of the incident cylindrical wavefront be denoted by ϕ_{inc} . Then considering the variation of the wavefront as a function along x and the far field distance (D_{Fraun}), the radius of the wavefront is given by $\sqrt{x^2 + D_{Fraun}^2}$, κ denoting the wavenumber, the phase of the incident cylindrical wavefront (ϕ_{inc}) is then given by :

$$\phi_{inc} = \kappa(\sqrt{x^2 + D_{Fraun}^2}) \quad \dots (6.2)$$

The phase at the base of the ridge plate (ϕ_{Fraun}) is given by:

$$\phi_{Fraun} = \kappa.D_{Fraun} \quad \dots (6.3)$$

The phase of the wavefront seen in (6.2) is cylindrical and the phase of the wavefront seen in (6.3) planar, so the transformation or the phase correction required as a function of x is the difference between (6.3) and (6.2):

$$\phi_{correction}(x) = \phi_{Fraun} - \phi_{inc} \quad \dots (6.4)$$

$$\phi_{correction}(x) = \kappa.D_{Fraun} - \kappa(\sqrt{x^2 + D_{Fraun}^2}) \quad \dots (6.5)$$

Since the amount of phase correction depicted in (6.4) must travel up the first face of the ridge and then down the back face, this phase correction is to be distributed over two equal length faces thus giving the height of the ridge as a function of (x):

$$Heightridge(x) = \frac{\phi_{correction}(x)}{2.\kappa} \quad \dots (6.6)$$

Equation (6.6) depicts the design equation for the ridge-based lens. This would mean a varying ridge height as a function of x . For the present design a uniform height is assumed considering an averaging to ease the fabrication process while retaining most of the pattern and gain characteristics. In the following discussion, an applied electromagnetics analysis approach based on the theory developed above is described to arrive at the design of the millimeter wave antenna.

A phase extraction and compensation method using full wave simulations is used in the design of the ridge-based lens. The phase distribution on the transversal section of the antenna is depicted in Figure 6.4 after the incorporation of the designed lens.

Before the incorporation of the lens, a horn antenna radiating into the parallel plate waveguide is used to arrive at the height of the ridge lens. The phase gradient whose variation is linear for small distances is calculated by dividing the amount of phase change by the length over which the change occurs to obtain the phase gradient. The calculated phase gradient from this is $4^\circ/\text{mm}$. In this case, the change in phase from the center towards the edges is 160° as in Figure 6.4, which translates to a length of 40mm ($160/4$) resulting in the ridge height equal to $(40/2) = 20\text{mm}$. This difference between the extremes results in an overall averaging over the ridge height. The phase distribution for the case when the ridge lens was removed from the model keeping all the other parameters is shown in Figure 6.3. Due to the non-influence of the lens the cylindrical phase distribution emitted by the horn propagates as is, cylindrically along the parallel plate waveguide. The phase shown is for a transversal cut.

As can be seen on Figure 6.4, after the incorporation of the ridge the output phase translates to a quasi-planar phase behaviour achieved by radiation through phase compensation of symmetrically distributed phases for port 1. For each of the figures from 6.3 to 6.12 a similar phase distribution is seen for 31 GHz, therefore the 31 GHz plots are not presented here on grounds of brevity.

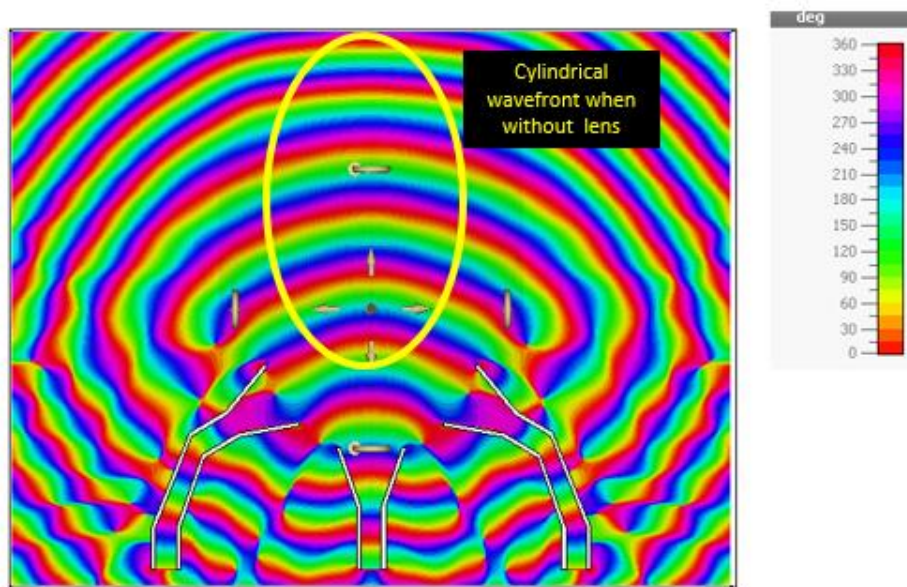


Figure 6.3 Cylindrical phase distribution without the ridge lens at 28 GHz

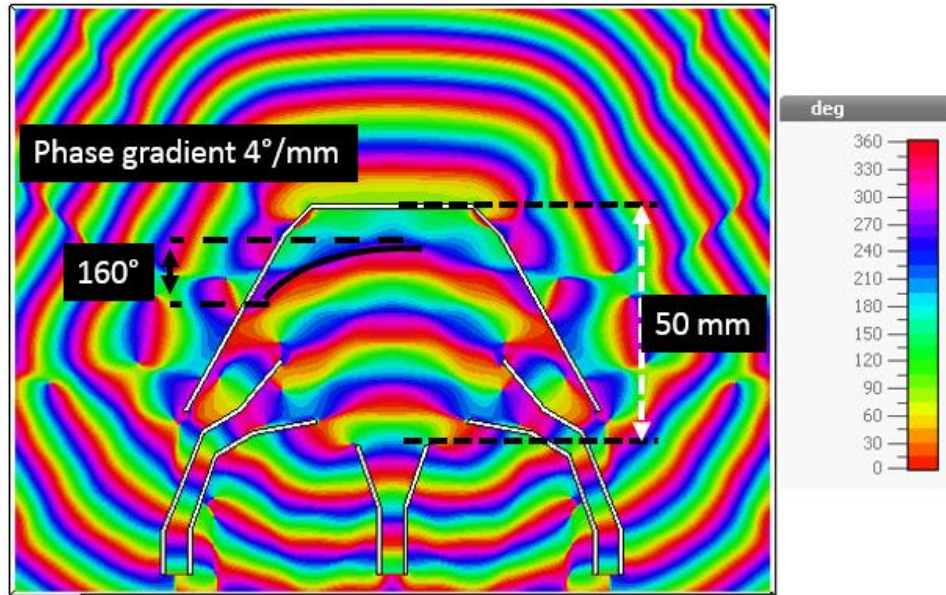


Figure 6.4 Cylindrical to planar phase distribution due to the ridge lens at 28 GHz

On the other hand, Figure 6.5 shows how the phase patterns dealt in figures 6.3 and 6.4 transformed onto their far-field components. For the case without the ridge lens as in Figure 6.5 (a) the beam is widespread in angle with less focusing towards the boresight. For the case with ridge lens, Figure 6.5(b), there is a narrower beam with lower sidelobes in comparison to Figure 6.5(a). This comparison has been made to explicitly demonstrate the effect of the lens on the antenna beam.

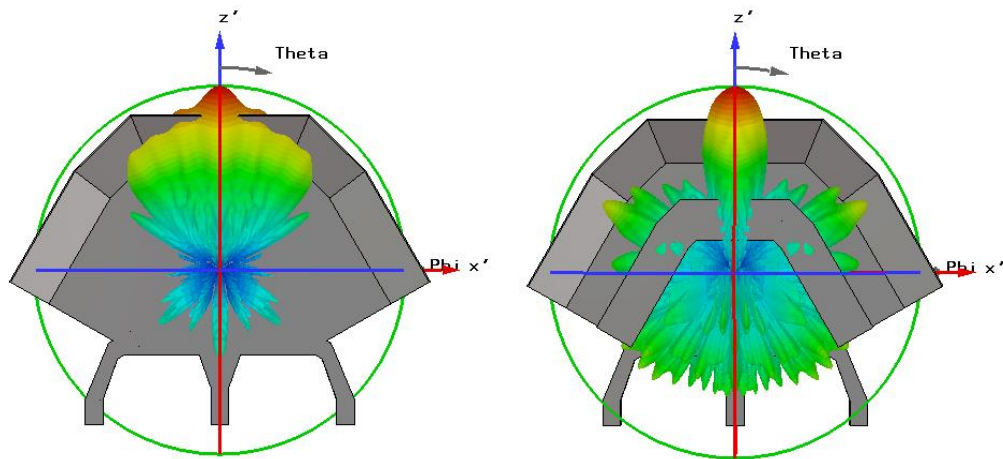


Figure 6.5 Comparison of the obtained pattern directionality and beamwidth for the case

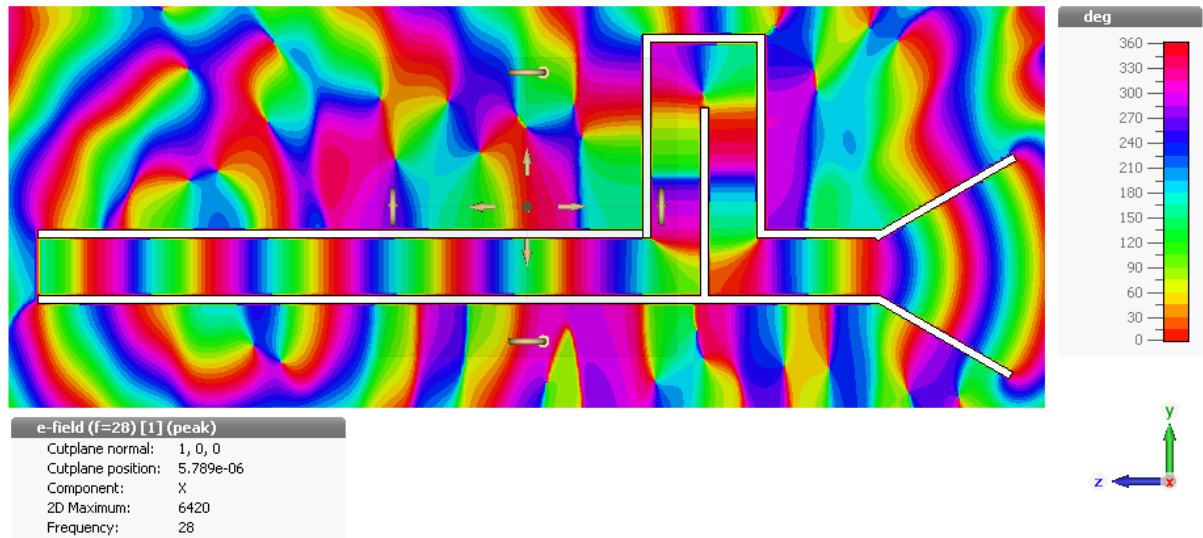
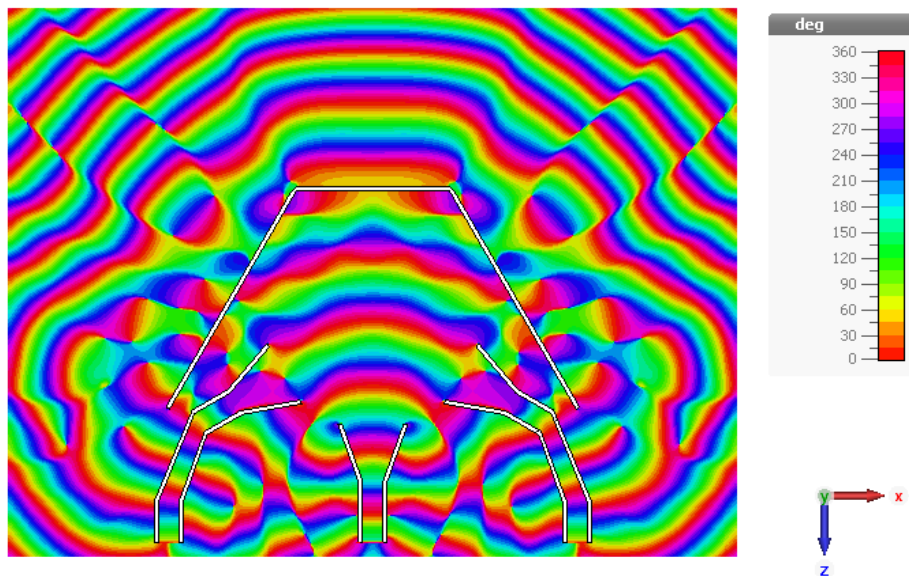


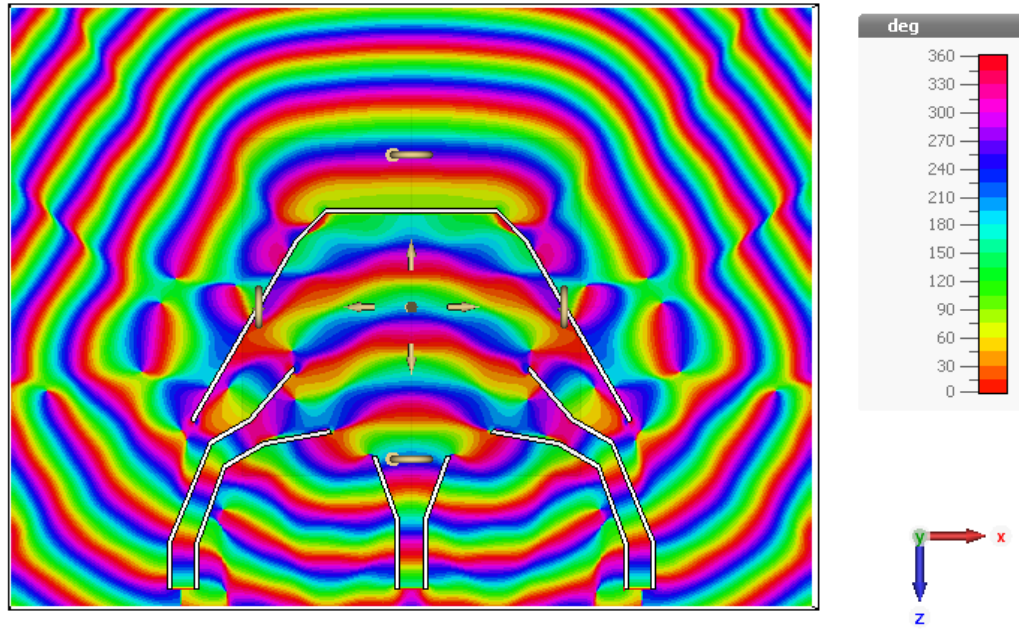
Figure 6.6 Phase distribution along the central YZ plane at 28 GHz

To illustrate the behaviour of the phase across the antenna, Figure 6.6 shows the phase distribution for a central plane cut along the YZ plane when port 1 is fed. As seen from the figure, the phase distribution projected along the YZ plane is largely uniform at the aperture, leading to constructive gains. As is discussed later, this phase distribution is used to decide on the optimal flare angle.

As the design of the lens antenna involves integration of three ports, and the minimal Fraunhofer distance to be maintained is fixed over a band, the ridge lens facing the three ports was conceived as an inverted truncated V as in Figure 6.7(a) to accommodate the three horns with minimal phase disturbance. Though in the simulation model the corners were sharp at the truncation, for fabrication purposes and to smoothen the phase abruptness on their proximity, chamfers were introduced as in Figure 6.7(b). As can be seen when comparing phase distribution on both cases, chamfers reduce the abrupt phase changes at the corners that can be observed on Figures 6.7(a) increasing the angular region where quasi-planar phase fronts are obtained.

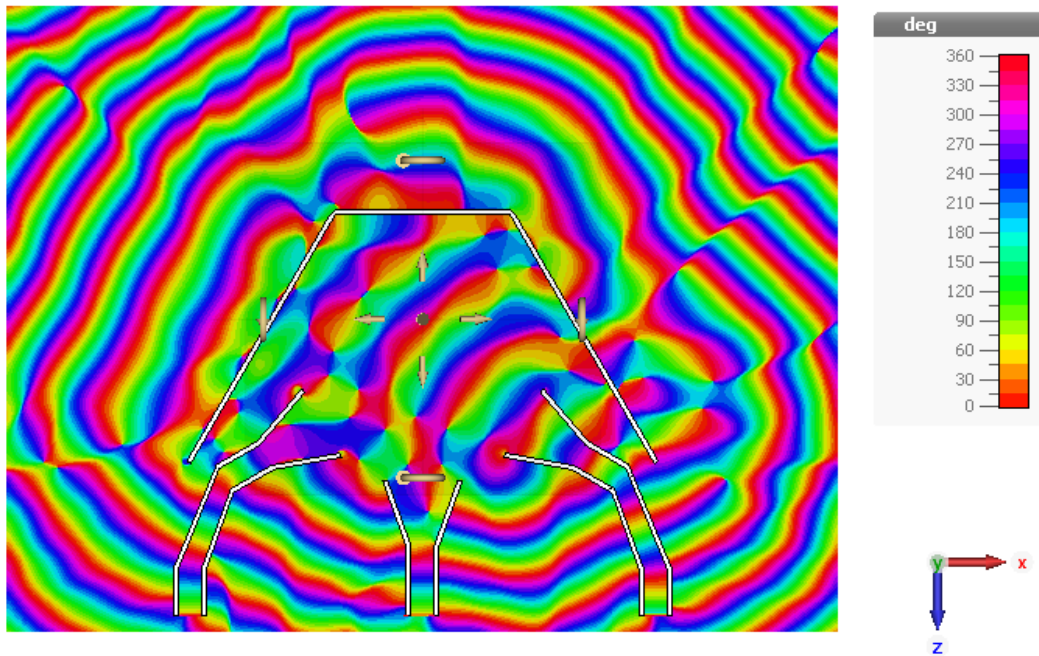


(a)



(b)

Figure 6.7 (a) Initial design with sharp corners on the lens and (b) final design with chamfered corners showing the phase distribution on the central plane when port 1 is excited at 28 GHz



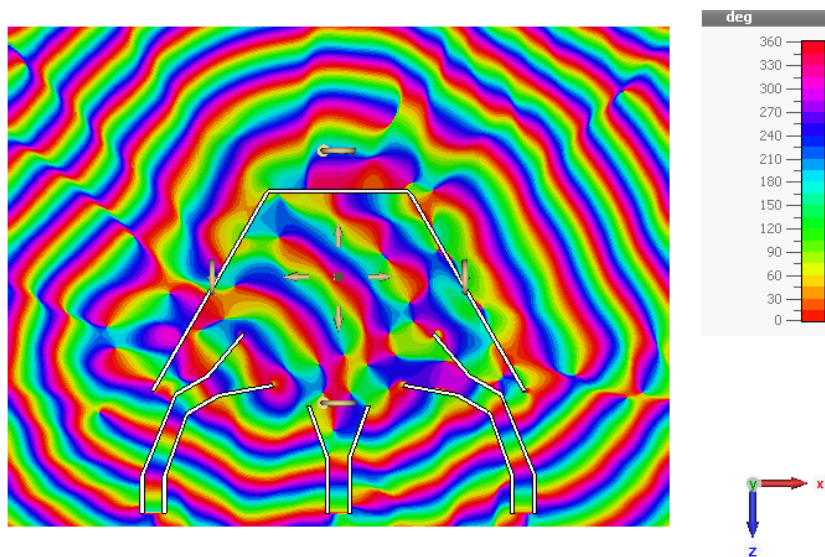
(a)



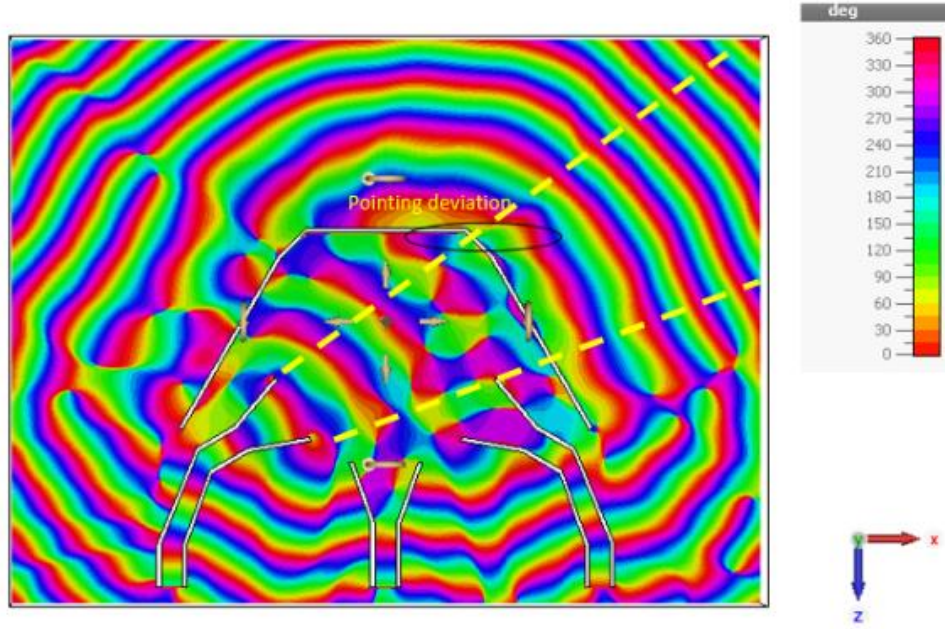
(b)

Figure 6.8 (a) Initial design with sharp corners on the lens and (b) final design with chamfered corners showing the phase distribution on the central plane when port 2 is excited at 28 GHz.

Though, the chamfering, betters the performance as compared to the sharp truncated corners. This can be noticed in the Figure 6.8(a) for port 2, where the phase changes are more abrupt than the ones seen with chamfer as in Figure 6.8(b). Similarly Figure 6.9(a) and 6.9(b) illustrate the case for port 3. At ports 2 and 3, due to the asymmetric configuration of the lenses, the phase compensation dampens and results in a progressive phase that deviates the main lobe influenced also by the presence of feeding horns 1 and 3 or 2, respectively. Due to this, as can be seen from Figure 6.8 and 6.9, the constant phase lines are not parallel to the lens but present a slight tilt that translates into a small deviation of 3° of the beam and in phase aberration as well as a more irregular response as compared to port 1 excitation case.



(a)



(b)

Figure 6.9 (a) Initial design with sharp corners on the lens and (b) final design with chamfered corners showing the phase distribution on the central plane when port 3 is excited at 28 GHz.

The averaging of the ridge height has been performed to meet three essential requirements: to keep the ridge lens design simple, to offer similar input matching at the three ports and to have a stable radiation pattern over the three ports. The average height cannot produce the same effects as the tapering of the ridge height but simplifies the fabrication process. The deviation seen is a pointing error and an increase of phase aberrations, that manifest as the asymmetric increase of sidelobes, but to a smaller extent.

The parallel plate waveguide lens-based antenna working principle was discussed in this section. The gain of a E plane sectoral horn antenna designed around the frequency of 28 GHz and 31 GHz is about 10.5 dBi. The lens-like operation performed on the E_x field vector of the feeding horns along with the flared aperture results in a gain increase of about 6 dBi. There is a transformation of the phase distribution from cylindrical to planar wavefront for the E_x field within the waveguide. A gradual change of the wavefronts along the periphery of the ridge is seen. The planar wavefront thus generated is responsible for projecting the high gain beams aided by the flared aperture.

6.3 Antenna Design

The antenna design consists of the co-design of a conglomeration of four interdependent design parts - namely the parallel plate waveguide, the feeding horns, the ridge-based lens and the flared radiating aperture. The following section describes the design procedure of each of these parts in separate and in unison. A 3D perspective view of the geometry of the antenna is shown in Figure 6.10. A summary of the information provided on previous section concerning the design of the ridge-based lens is also included for the sake of completeness.

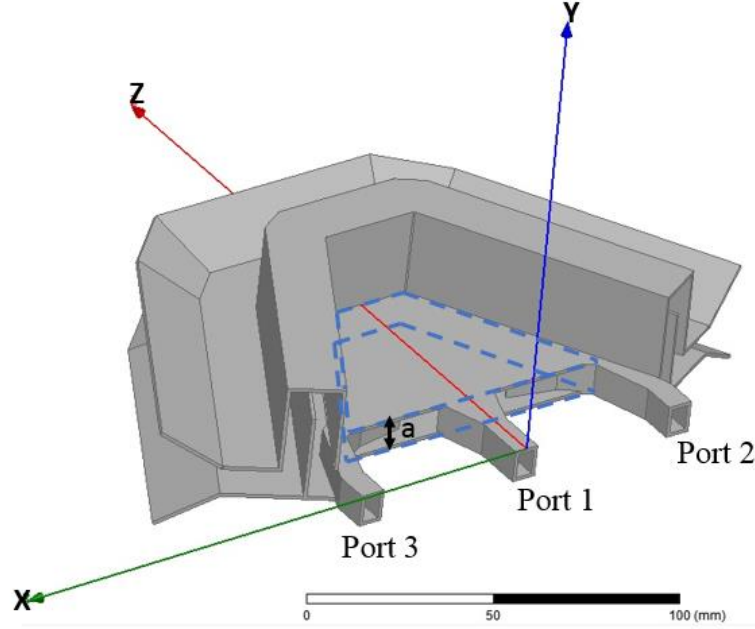


Figure 6.10 3D perspective view of the dual band multi-beam antenna

6.3.1 Design of the parallel plate waveguide

The parallel plate waveguide (PPW) structure is chosen to act as the shared guiding interface between the three launching ports and their corresponding wave propagation. Following the axis notation in Fig. 6.10, for the excitation of port 1, the parallel plate extension along the x direction can be theoretically considered to be infinite, which in the proposed scenario depicts resulting radiation to free space along the z direction. The separation between the plates ‘a’ is a critical factor in ensuring the propagation of the guided wave along the direction z. This is derived using the following steps to ensure propagation for frequencies above 20 GHz. The antenna, as shown in Figure 6.10, is placed with the parallel plate waveguide plates placed parallel to the xz plane, with the plate separation distance ‘a’ along the y axis. In the above scenario, considering excitation along port 1, the Maxwell’s wave equation becomes:

$$\nabla^2 \mathbf{E} + \omega^2 \mu \epsilon \mathbf{E} = 0 \quad \dots (6.7)$$

As stated earlier, the plates can be considered to be infinite in the x direction and it is necessary to consider the propagation in the z direction. Therefore, component E_x only is assumed along with the additional conditions that the partial derivative along x is zero and along y and z is non-zero. These imposed assumptions define the TE modes and the differential wave equation is used to obtain the classical dispersion relation [14]:

$$\beta_z^2 + \beta_y^2 = \omega^2 \mu \epsilon = \beta^2, \text{ where } \beta_y = \frac{m\pi}{a} \quad \dots (6.8)$$

where index $m=1, 2, \dots$ which on solving for β_z yields

$$\beta_z = \sqrt{\omega^2 \mu \epsilon - \left(\frac{m\pi}{a}\right)^2} \quad \dots (6.9)$$

The first TE mode is the TE₁ mode. Since the wave must propagate in the positive z direction, for the propagation to physically occur $\beta_z^2 > 0$; following this the guidance condition was deducted as:

$$f > \frac{m}{2a\sqrt{\mu\epsilon}} \quad \dots (6.10)$$

that gives the limit for the cut-off frequency. From this the separation between the parallel plates of the antenna 'a' was derived and set. The separation 'a' calculated for frequencies above 20 GHz is 7.5 mm, which is very much suitable for tapping in the frequencies of interest namely 28 GHz and 31 GHz. The same calculated parallel plate separation 'a' is retained for the other two outer ports, given, their desired cut-off frequencies are above the designed 20 GHz. This helps in attaining a shared aperture configuration for the three ports with multiple frequency operation.

6.3.2 Design of the feeding horns

The parallel plate waveguide with a derived separation of 7.5 mm between the plates acts as the driving factor in deciding the aperture dimensions of the horns that feed into the structure. An E-plane sectoral horn whose opening is flared in the direction of the E field, while keeping the other constant was chosen. The front aperture dimensions of the E-Plane sectoral horn were chosen as 15 mm x 7.5 mm and the back- wall dimensions were chosen as 5 mm x 7.5 mm with a flaring between the two faces provided over a length of 14 mm. The selection of these dimensions, that are dependent on the parallel plate waveguide dimension ensures co-design of the horn and the parallel plate waveguide interface; and the input matching of the sectoral horn at 28 GHz and 31 GHz. The feeding horns are further extended from their back walls by means of a propagating waveguide section at the designed frequency. The length of this waveguide section is chosen to have all the three port planes originating at the same plane. This provides for the ease and uniformity of feeding the ports, especially in an array.

The horns at the outer ends are spaced from the center horn so that a minimal spatial footprint is obtained while retaining the obtainable beamwidth. The outer horns are tilted towards the center to target the design angle of 60° and a waveguide section, suitably chamfered to reduce losses, connects these outer end horns to their feeding port plane.

6.3.3 Design of the ridge-based lens

The wavefront of the E_x component of the field emitted by the E-plane sectoral horn is cylindrical and this is converted to planar wavefront by means of a metal ridge-based lens. Phase correction is performed over the path lengths of the rays traced over the parallel plate waveguide, from the sectoral horn towards the lens. The variable that introduces the required delay for the correction is the height of the ridge. The initial distance from the E-plane sectoral horn aperture to the ridge is set using the azimuthal beamwidth of the E-plane horn at -12 dB and by calculating the corresponding arc length and radius ratio, using the trigonometric rule:

$$\theta = \frac{l}{r} \quad \dots (6.11)$$

where, θ is the subtended beamwidth angle in radians and l is the arc length subtended and r is the radius. Using the above rule, the distance 'r' between the E-plane horn aperture and the ridge was set to 50 mm, which is in the Far-field region of the E-plane sectoral horn. The Far-field distance is 47.8 mm calculated for the horn aperture of 15 mm x 7.5 mm at 28 GHz. This

further for a -12 dB beamwidth of 66° (1.15 radians) of the E-plane sectoral horn, necessitates a ridge length of 57 mm for optimal illumination.

The position and the length of the ridge being set, the height of the ridge can be calculated by considering the path length correction required to convert the cylindrical wavefront to planar wavefront at the interface of the ridge. The phase plot for the E_x field component over the parallel plate waveguide floor is extracted using full wave solver and the maximum difference in phase between the phase of the emitted cylindrical wavefront at its center and that at the edge is calculated. This difference is then divided by the calculated phase gradient (constant over small distances) to attain the height of the ridge. It must be noted that intuitively, this suggests a varying ridge height along the section. However, here an average height derived from the maximum phase differences is considered. This has been performed to meet three essential requirements: to keep the ridge lens design simple, to offer similar input matching at the three ports and to have a stable radiation pattern over the three ports. The average height cannot produce the same effects as the tapering of the ridge height but simplifies the fabrication process. The deviation seen is a pointing error and an increase of phase aberrations more evident for the asymmetric cases of lateral feeding ports, that manifest as the asymmetric increase of sidelobes as seen in Figs. 6.23-24 and 6.26-27. The correction of these effects was clearly out of the scope of this early stage investigation on this kind of structure and methodologies like the one proposed in [16] can be adapted towards dielectric-based design.

6.3.4 Design of the flared radiating aperture

The antenna designed through the above steps has a pointing fan beam in the elevation plane. The gain of the antenna can be improved by 1-2 dBi by providing a guiding section that flares out at an optimal flaring angle to further enhance the gain. The flaring is provided at the aperture of the waveguide section that follows the ridge lens. The change in the flaring angle causes a change in the path lengths between the waveguide and the aperture axially along the yz plane. The path difference is smallest for the case of flaring angles near 0° measured outward along yz plane and experiments a growing quadratic deviation from center as the flaring angle increases. This flare angle cannot be increased beyond a limit as the phase distribution becomes predominantly quadratic and the fields do not add up constructively to enhance the gain and directivity. The optimal flaring angle in this design was chosen as 30° considering the phase distribution at the aperture. The flaring angle was set in such a way to keep the phase fronts of the radiated field as close to planar as possible for all three feeding ports while keeping the antenna directivity related to each port high, which reinforces the importance of the flaring angle as a parameter to enhance gain.

6.4 Measurement and Discussion

The antenna design principle described in section 6.2 for a single port was extended to a three-port model and the antenna was simulated in Ansys HFSS, a full wave EM solver. The material of the antenna was chosen as aluminium. It is designed for dual band operation in the frequency bands 28 GHz and 31 GHz with a bandwidth of 1 GHz each. The antenna due to its operation at the high millimeter wave frequencies requires a finer dense mesh with around 16 million mesh cells for better accuracy of the results. The simulation model of the antenna shown in Figure 6.10 was further refined with mechanical considerations as shown in the exploded view of Figures 6.11 and 6.12. The design procedure primarily retained the internal dimensions of the waveguide intact which is critical for the operation of the parallel plate operation. The antenna was prepared for fabrication considering mechanical tolerances. The mechanical design of the antenna was made in CAD software CATIA v 5.2. The design file was divided into 8

separate designs encompassing five brass pieces for the lens and three designs for parallel plate beamformer. The tolerances between holes for pins were 0.02 mm and for screws was 0.2mm. The dimension tolerances for the path inside was 0.02 mm. All tolerances are according to ISO 2768.

Fabrication of the parallel plate beamformer was made using Computer Numerical Control (CNC) machining and the brass lens was made using standard thickness plate of brass of 1mm machined accordingly into five pieces. The individual parts depicted in Figures 6.11 and 6.12, were later assembled with aid of precise alignment pins to form the whole structure. The three distinct parts that go into the assembly were the base plate with the profile of the feeding horns machined into it, the upper plate with lens cover profile and the lens plate. The three parts provide in unison, provision for a track of 1mm width for the insertion of the five brass metal plates that act as the parts of the whole lens. The model of the complete assembly is shown in Figure 6.13.

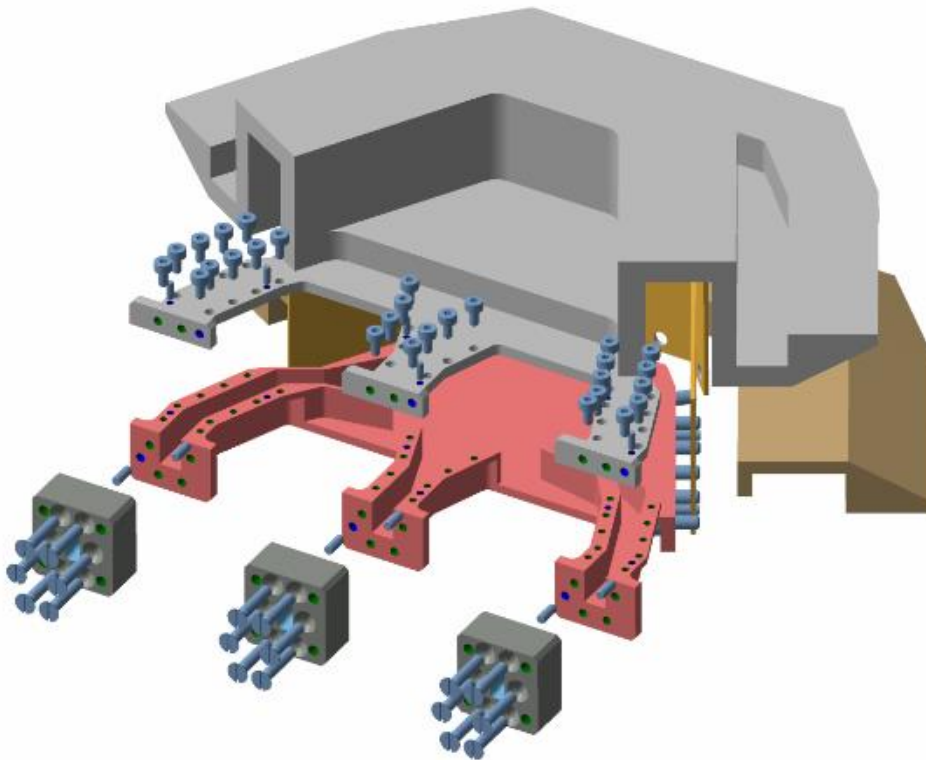


Figure 6.11 Top exploded view of the antenna

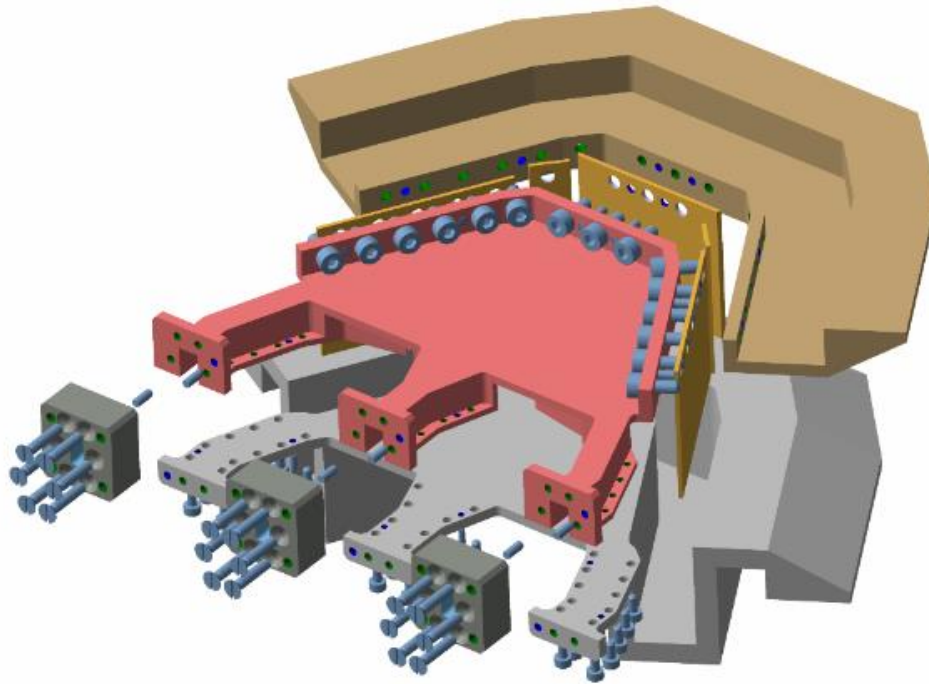


Figure 6.12 Bottom exploded view of the antenna

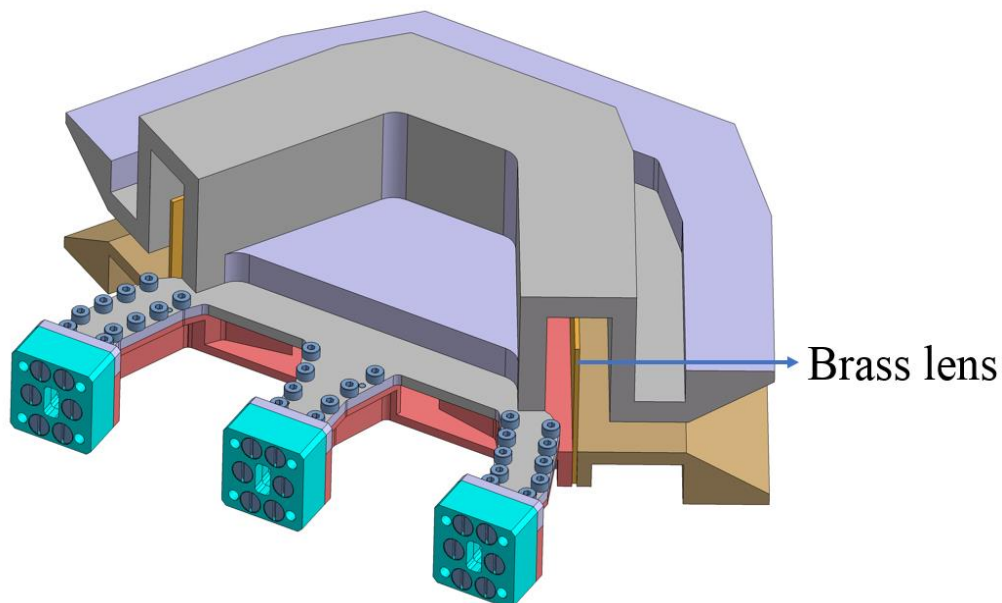


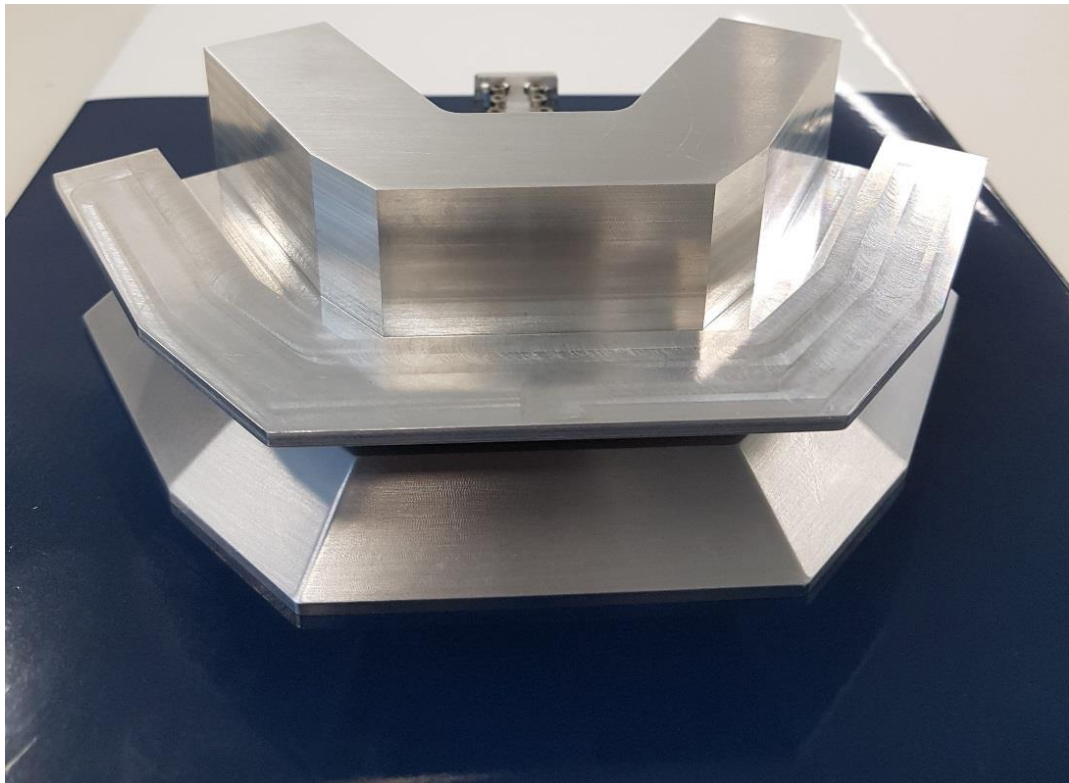
Figure 6.13 Model of the assembled antenna

Since the feeding port of the E plane sectoral horn has non-standard dimensions, a waveguide to waveguide transition was designed to operate at 28 GHz and 31 GHz. This transition interfaces the waveguide face of the standard WR28 coax-to-waveguide transition to the waveguide face of the feeding E plane sectoral horn. The fabricated waveguide-waveguide

transitions are shown in Figure 6.14. The fabricated and assembled prototype is shown in Figures 6.15(a)–(c). The final prototype has a footprint of 170mm by 150mm. The final assembly includes all the parts shown above along with the coax to waveguide transitions that go into each of the three ports.

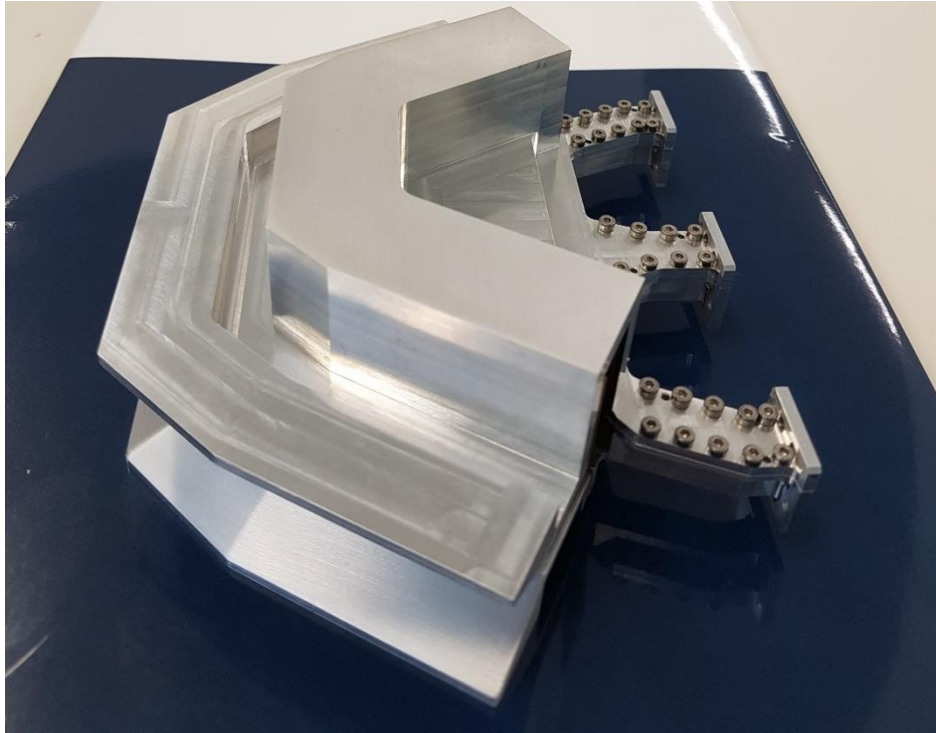


Figure 6.14 WR28 to custom horn aperture transitions for the three ports

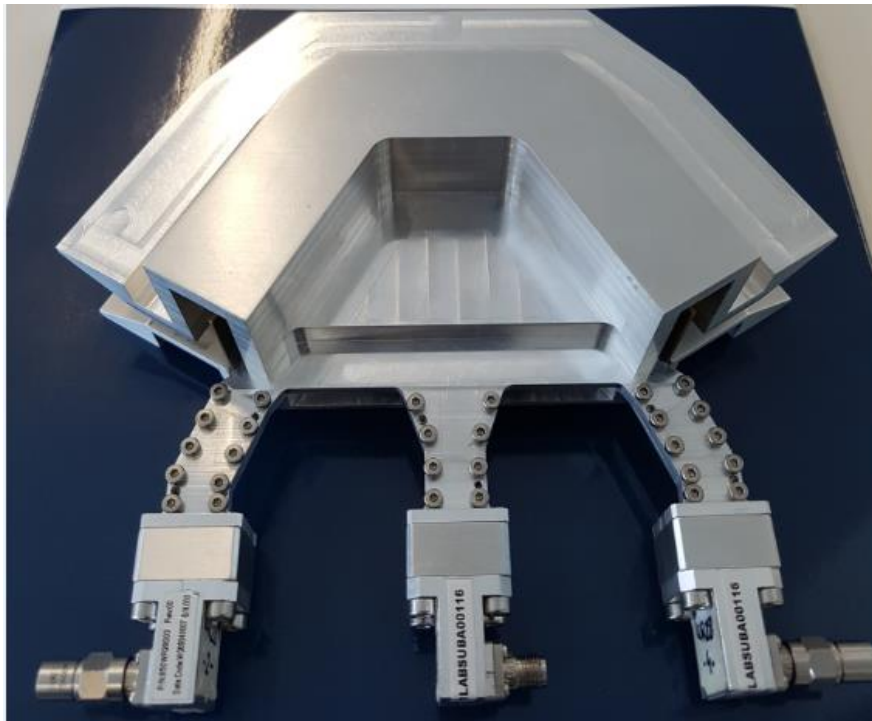


(a)

Millimeter wave antenna



(b)



(c)

Figure 6.15 (a) Front view of the fabricated prototype (b) Side view of the fabricated prototype (c) Top view of the millimeter wave antenna prototype

6.4.1 S parameter measurement

The fabricated antenna was measured for its return loss and isolation at the high frequencies of Ka band namely 28 GHz and 31 GHz using the Keysight Vector Network Analyzer (VNA) N5245B. Prior to the measurement the VNA was calibrated using an E-CAL for 2 port configurations for the frequency range 26 GHz to 32 GHz. The three-port antenna has the S_{11} , S_{22} and $S_{33} < -10$ dB around the 28 GHz and 31 GHz band. The band of operation is designed between 27.5 GHz to 28.5 GHz for the first band and between 30.5 GHz and 31.5 GHz for the second band at each of the three ports. The return losses due to the ports 2 and 3 have similar characteristics as compared to the central port 1. When one port was being measured for return loss the other two ports were matched with a 50-ohm termination. Figure 6.16 shows the simulated vs measured return loss at the central port. There is a good agreement between the simulated and measured results with a slight discrepancy that can be attributed to the use of 90° elbow connector at port 1 for measurement. The simulated vs measured return loss for port 2 and port 3 as shown in Figures 6.17 and 6.18 have a good agreement over the band of interest.

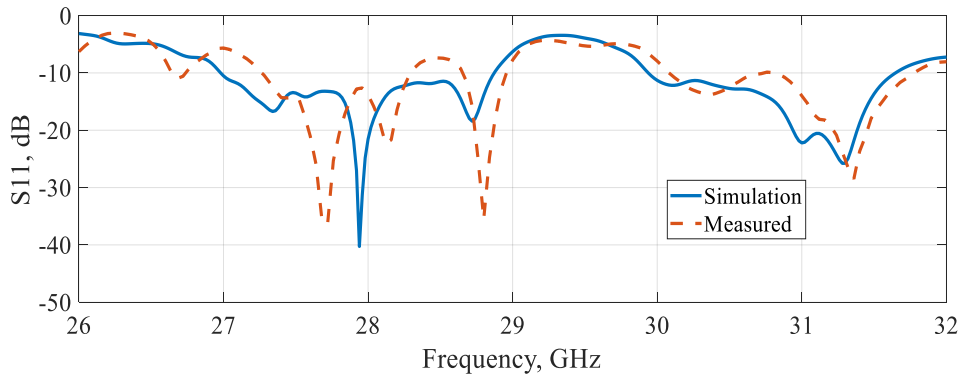


Figure 6.16 Simulated vs measured return loss at port 1

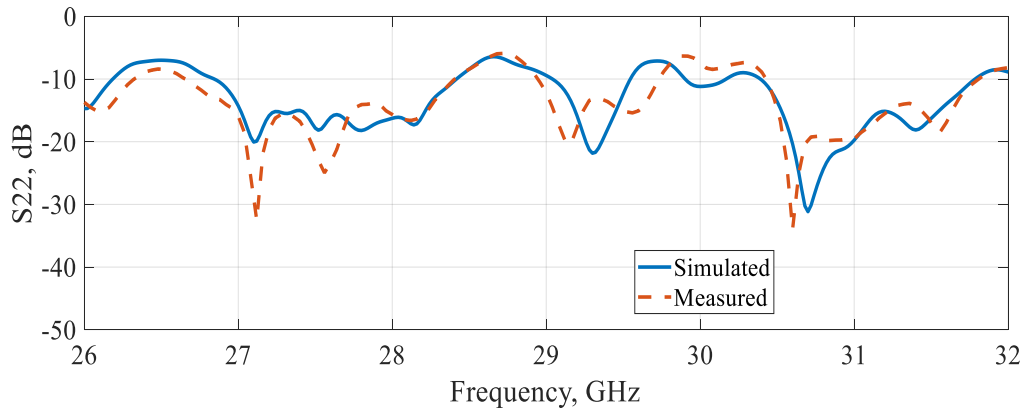


Figure 6.17 Simulated vs measured return loss at port 2

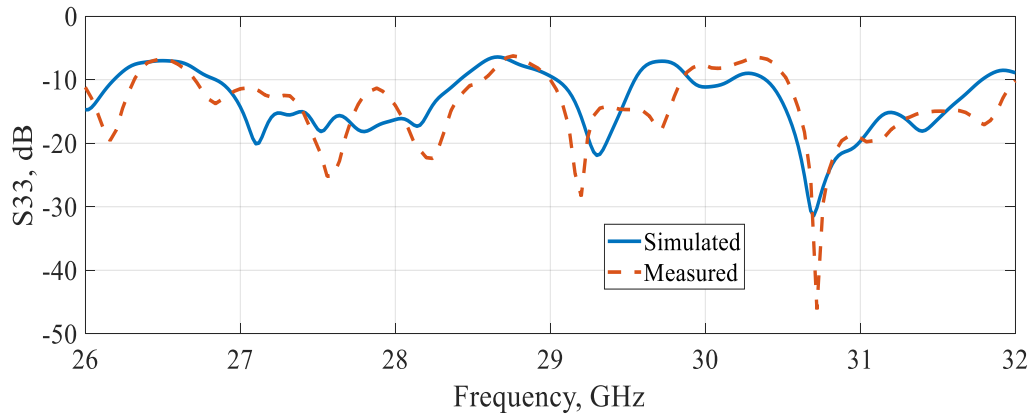


Figure 6.18 Simulated vs measured return loss at port 3

6.4.2 Port -to- Port isolation measurement

The Port-to-Port isolation is calculated by simulations and validated by measurements in this section. The isolation between ports 1 and 2 and ports 1 and 3 are considered, not including the case of port 2 and 3 as the antenna is not intended to use port 2 as transmitter and port 3 as receiver or vice versa. Moreover, this case will have a higher coupling and therefore lower isolation owing to the two horns looking into each other. The proposed antenna is designed to act as a transceiver at two different independent frequencies. It can transmit at 28 GHz through the central port and receive at 31 GHz at the other two ports. To make this possible, the antenna has been designed with a Port-to-Port isolation less than -25 dB between the transmitter and the receiver. The transmitter and the receiver of the antenna have the same polarization; therefore, the isolation has been improved by arranging the two outer ports to face each other through their horns in a cross fashion. The simulated and measured Port-to-Port isolation characteristics are depicted in Figure 6.19.

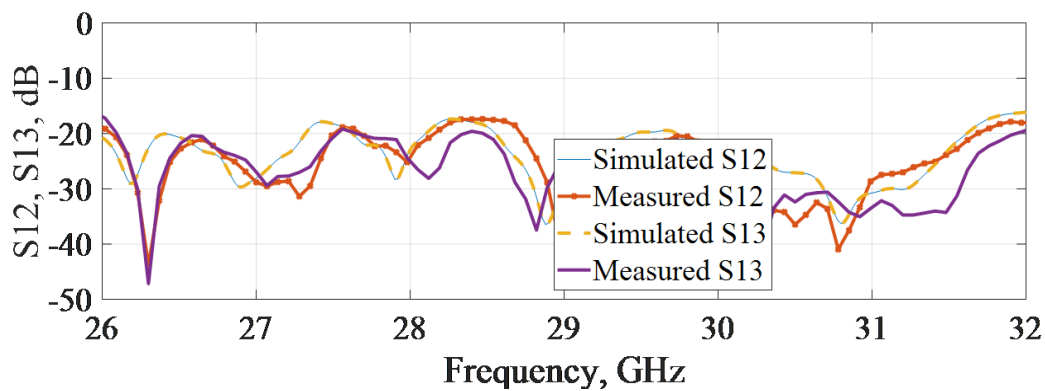


Figure 6.19 Port-to-Port isolation

6.4.3 Radiation Pattern stability over the designed dual wideband validated by simulations

The antenna was designed for operation over two bands centered around 28 GHz and 31 GHz, each with a bandwidth of 1 GHz. To demonstrate the pattern behavior over the 1 GHz band, six frequency points of 27.5, 28, 28.5 GHz centered around 28 GHz and 30.5, 31 and 31.5 GHz centered around 31 GHz were chosen. The normalized directivity plots at these frequencies are compared for the principal plane cuts in Figures 6.20-6.31.

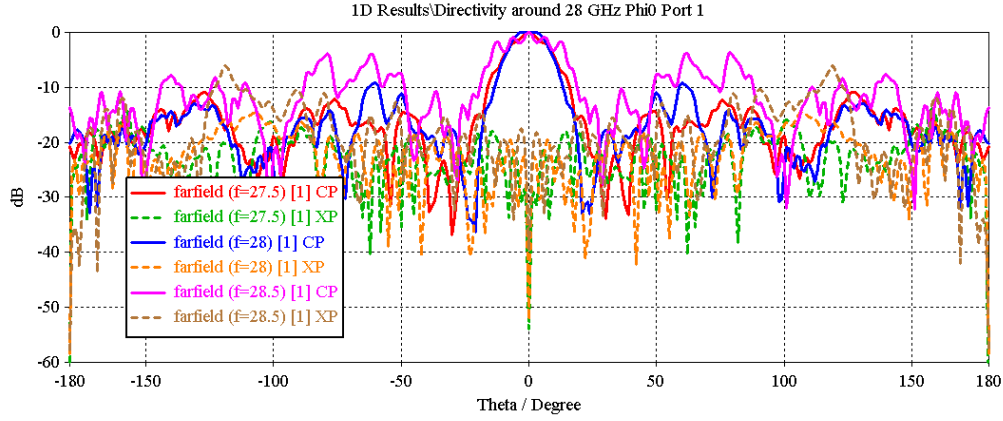


Figure 6.20 Normalized directivity pattern vs frequency around 28 GHz for Phi0 plane at port1

As seen in Figure 6.20, for port 1 excitation and frequencies below 28 GHz the 3 dB beamwidth and the SLL retains its stability. Towards the upper end of the 28 GHz band, nearing 28.5 GHz, there is a significant increase in the SLL, mainly around $\pm 63^\circ$, and significant degradation of the main lobe shape and beamwidth. However, it is to be noted that throughout the 1 GHz band the cross-polarization values remain similar around the central boresight 3dB beamwidth of 20° along Phi0 plane. Overall, in the band from 27.5 GHz to 28.5 GHz a 3dB beamwidth of 20° along Phi0 plane and a XPD of 20 dB can be obtained for linear polarization.

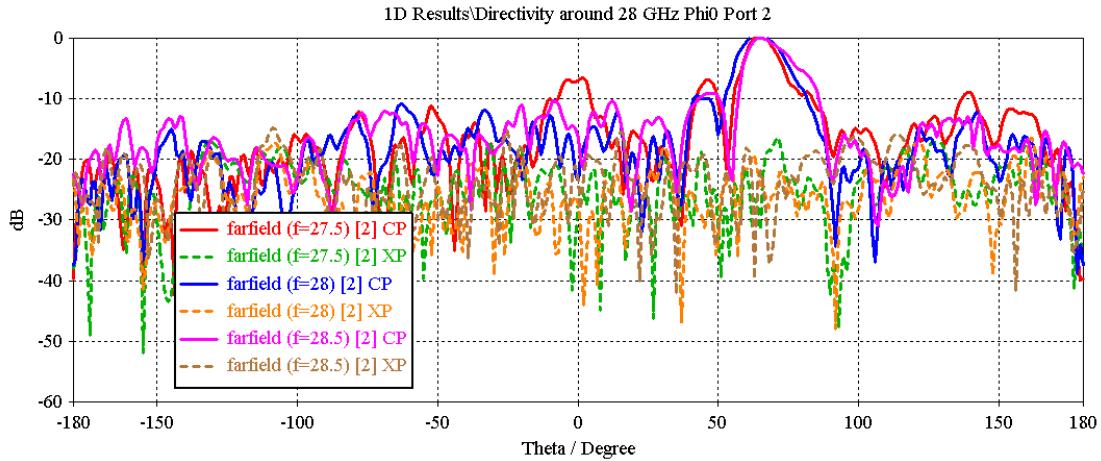


Figure 6.21 Normalized directivity pattern vs frequency around 28 GHz for Phi0 plane at port2

From Figure 6.21, the 3dB beamwidth of port 2 beam projecting towards an angle of $+63^\circ$ is 10° with an XPD of 20 dB at $+63^\circ$ direction for all the three frequency points. The SLL is a bit higher for the lower end case of 27.5 GHz. The adjacent lobe level degrades for the lower end of the band and an increased level of radiation is observed also around $\theta = 0^\circ$.

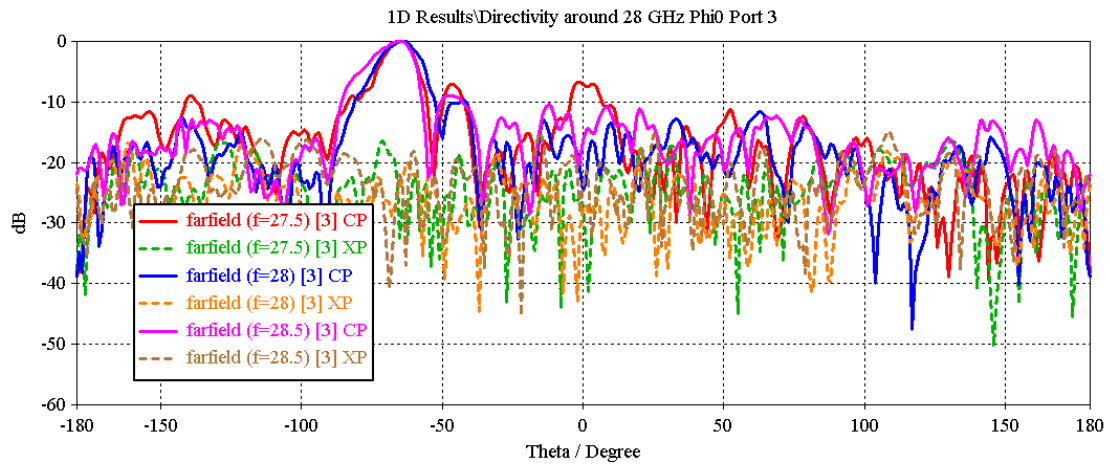


Figure 6.22 Normalized directivity pattern vs frequency around 28 GHz for Phi0 plane at port3

From Figure 6.22, the port 3 pattern is almost symmetrical to port 2 with the beam projected at -63° , the 3dB beamwidth of 10° for port 3 beam projecting towards an angle of -63° . It has an XPD of 20 dB at -63° direction for all the three frequency points. The SLL is a bit higher for the lower end case of 27.5 GHz. Same behaviour than in previous case is observed for the adjacent lobe and at $\theta = 0^\circ$. On these last two cases, phase aberrations, that may not be corrected with the proposed design method, manifest on the asymmetric distribution of adjacent lobes around the main lobe.

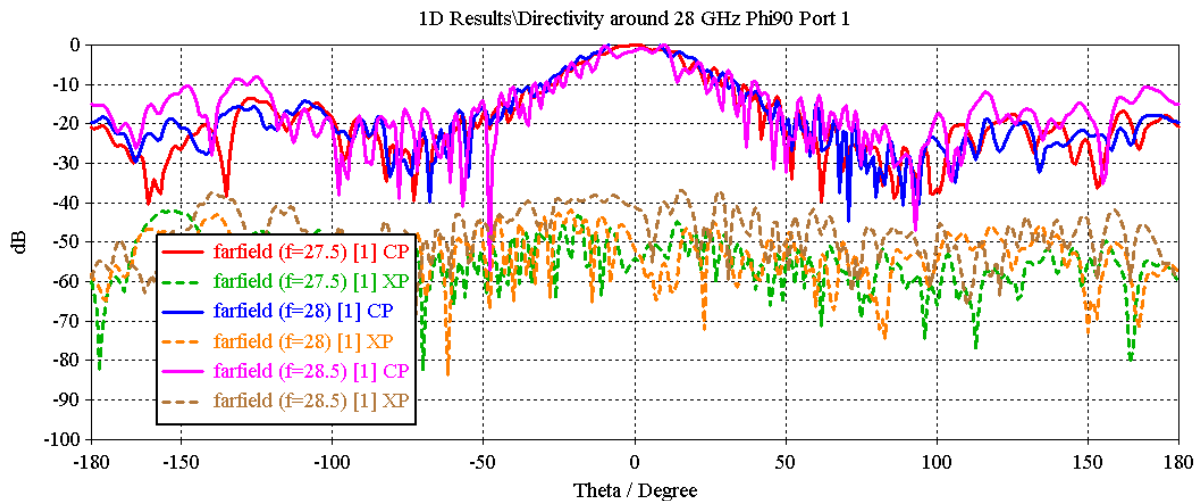


Figure 6.23 Normalized directivity pattern vs frequency around 28 GHz for Phi90 plane at port1

From Figure 6.23, for the cut along the Phi90 plane at port 1, the most striking factor is the XPD around boresight, which is about 40 dB. The beam along Phi90 is a fan-shaped beam with similar SLL and 3 dB beamwidth along the band 27.5 GHz to 28.5 GHz. A higher degradation of the response can be observed for the upper frequency for this cut.

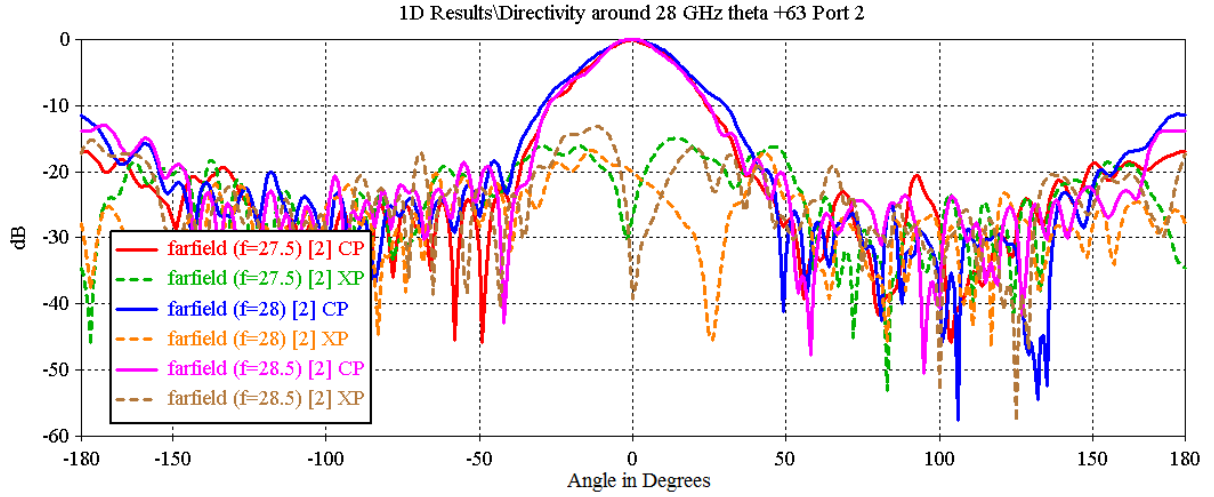


Figure 6.24 Normalized directivity pattern vs frequency around 28 GHz for $\theta = +63^\circ$ plane at port2

From Figure 6.24, the 3dB beamwidth seen by port 2 at $+63^\circ$ direction is 20° , for the cut along $\theta = +63^\circ$ plane and this remains stable over the entire frequency band. The SLL also retains similar values throughout the band. The XPD stays at 20 dB for up to 10° beamwidth. Frequency response keeps stable along the band for this cut.

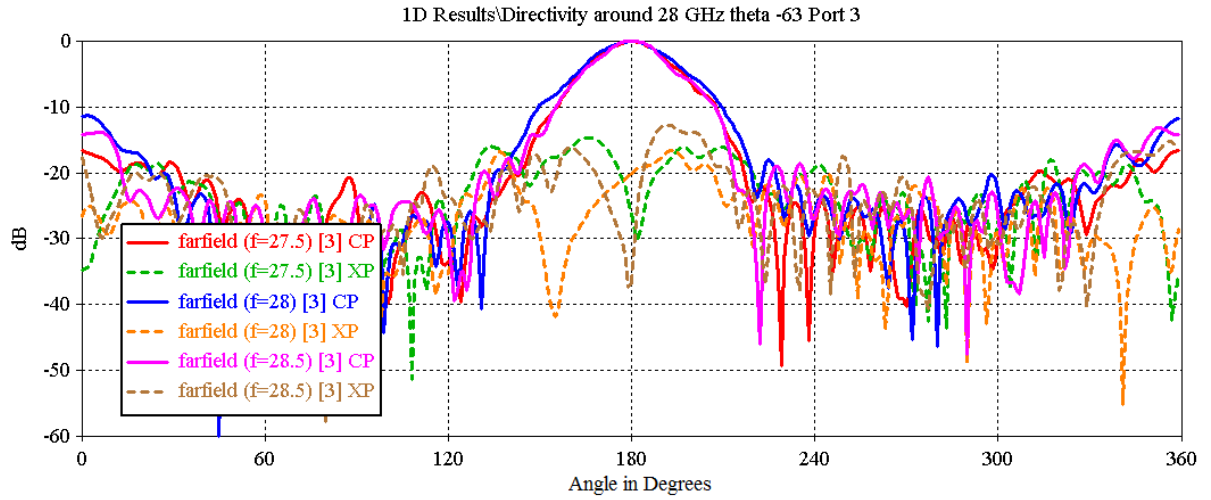


Figure 6.25 Normalized directivity pattern vs frequency around 28 GHz for $\theta = -63^\circ$ plane at port3

From Figure 6.25, the 3dB beamwidth seen by port 3 at -63° direction is 20° , for the cut along $\theta = -63^\circ$ plane and this remains stable over the entire frequency band. This pattern is symmetrical w.r.t port 2 pattern of Figure 6.24 as expected. The SLL also retains similar values throughout the band. The XPD stays at 20 dB for up to 10° beamwidth. Again, frequency response remains stable.

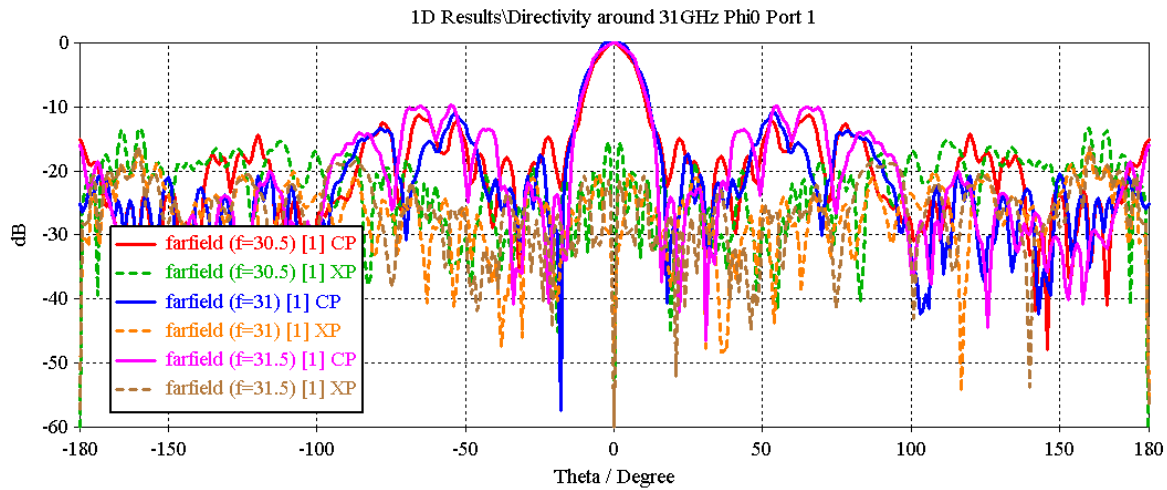


Figure 6.26 Normalized directivity pattern vs frequency around 31 GHz for Phi0 plane at port1

As seen in Figure 6.26, for frequencies around 31 GHz the 3 dB beamwidth and the SLL retains its stability. It is also to be noted that throughout the 1 GHz band the cross-polarization values remain similar around the central boresight 3dB beamwidth of 14° along Phi0 plane. Overall, in the band from 30.5 GHz to 31.5 GHz a 3dB beamwidth of 14° along Phi0 plane and a XPD of 20 dB can be obtained for linear polarization. As in Figure 6.20, increased radiation levels around $\pm 63^\circ$ are observed.

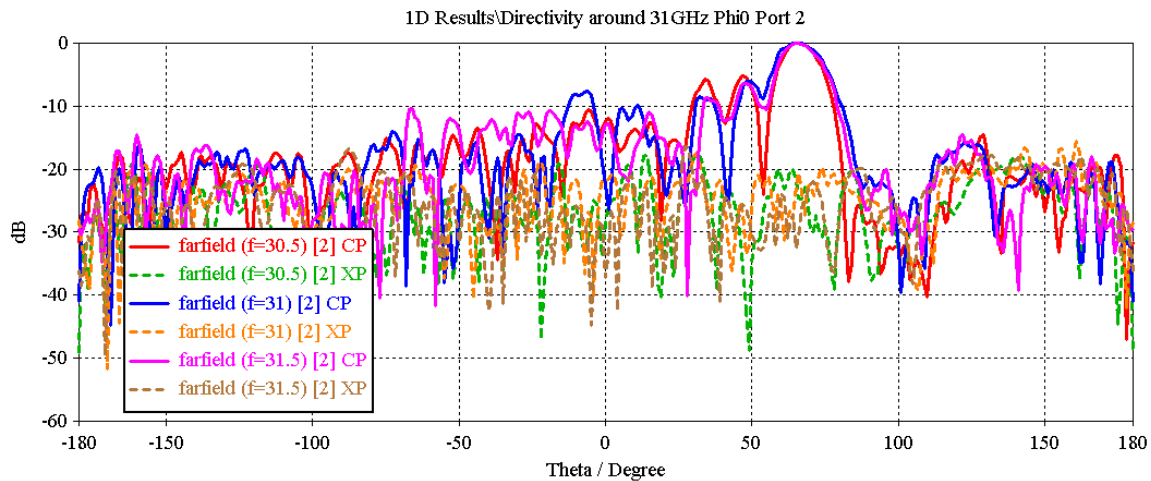


Figure 6.27 Normalized directivity pattern vs frequency around 31 GHz for Phi0 plane at port2

From Figure 6.27, the 3dB beamwidth of port 2 beam projecting towards an angle of $+63^\circ$ is 10° with an XPD of 20 dB at $+63^\circ$ direction for all the three frequency points. The SLL is a bit higher for the lower end case of 30.5 GHz.

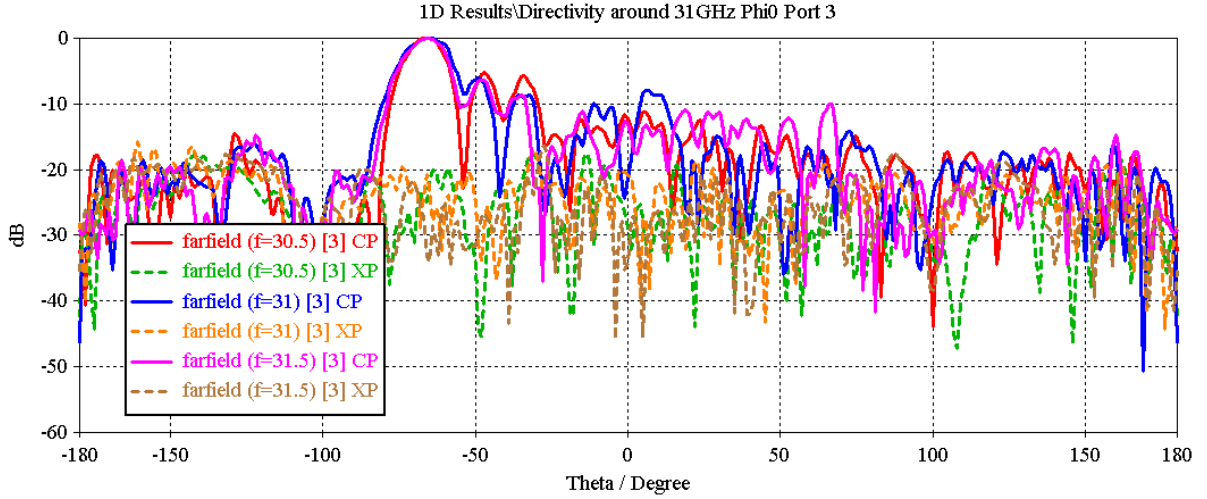


Figure 6.28 Normalized directivity pattern vs frequency around 31 GHz for Phi0 plane at port3

From Figure 6.28, the port 3 pattern is almost symmetrical to port 2 with the beam projected at -63° , the 3dB beamwidth of 10° for port 3 beam projecting towards an angle of -63° . It has an XPD of 20 dB at -63° direction for all the three frequency points. The SLL is a bit higher for the lower end case of 30.5 GHz. Phase aberrations are most evident in the last two cases.

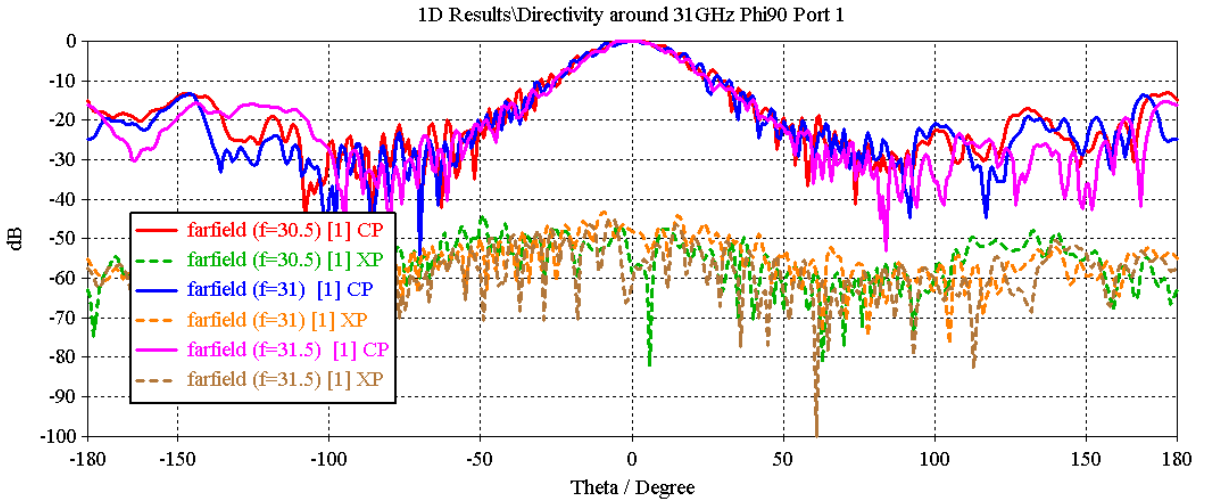


Figure 6.29 Normalized directivity pattern vs frequency around 31 GHz for Phi90 plane at port1

From Figure 6.29, for the cut along the Phi90 plane at port 1, the most striking factor is the XPD around boresight, which is about 40 dB. The beam along Phi90 is a fan-shaped beam with similar SLL and 3 dB beamwidth along the band 30.5 GHz to 31.5 GHz. Frequency response keeps more stable than in previous band in this case.

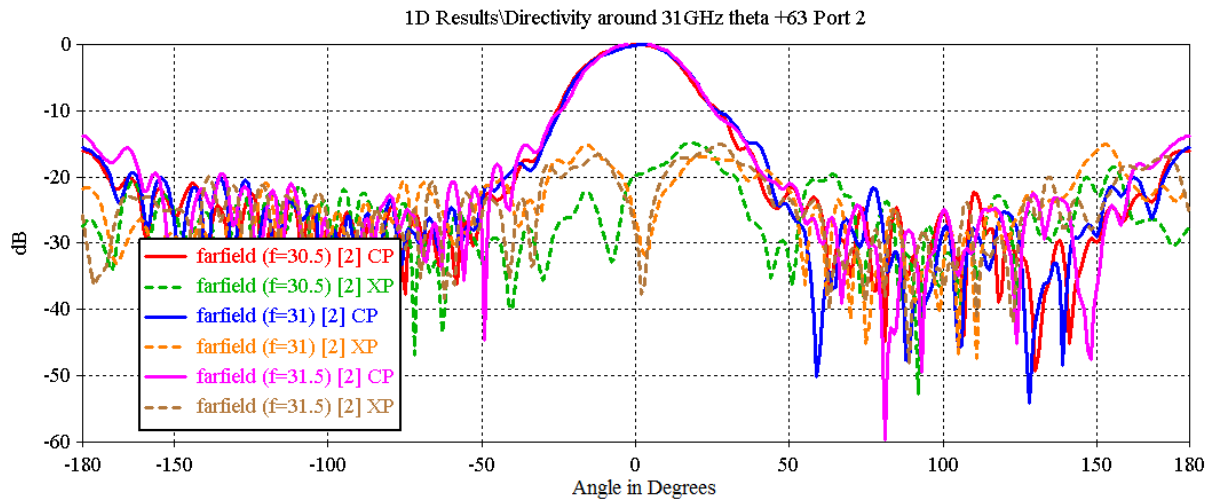


Figure 6.30 Normalized directivity pattern vs frequency around 31 GHz for $\theta = +63^\circ$ plane at port 2

From Figure 6.30, the 3dB beamwidth seen by port 2 at $+63^\circ$ direction is 30° , for the cut along $\theta = +63^\circ$ plane and this remains stable over the entire frequency band. The SLL also retains similar values throughout the band. The XPD stays at 20 dB for up to 10° beamwidth. Frequency response keeps stable with frequency.

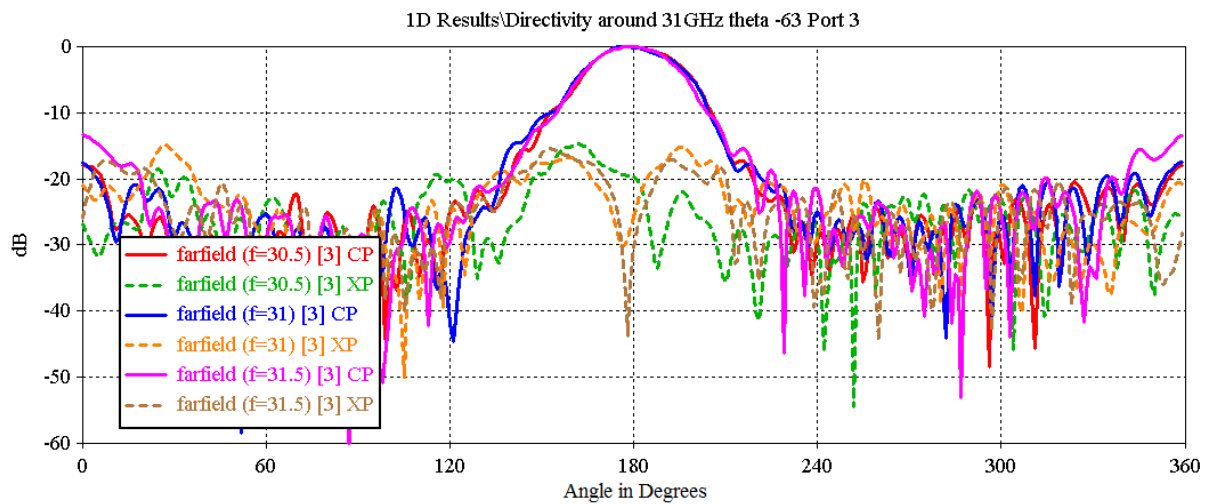


Figure 6.31 Normalized directivity pattern vs frequency around 31 GHz for $\theta = -63^\circ$ plane at port 3

From Figure 6.31, the 3dB beamwidth seen by port 3 at -63° direction is 30° , for the cut along $\theta = -63^\circ$ plane and this remains stable over the entire frequency band. This pattern is symmetrical w.r.t port 2 pattern of Figure 6.30 as expected. The SLL also retains similar values throughout the band. The XPD stays at 20 dB for up to 10° beamwidth. Again, as in previous case, frequency response is stable with frequency.

To summarize, the antenna behaviour at the upper band (31 GHz) is expected to provide a better pattern response than in the lower band with improved pattern stability with frequency. In both bands, residual radiation will be expected from the lateral sides flanking the central ridge when

port 1 is excited. When port 2 or 3 are excited, phase aberrations, which cannot be accounted for with the design method proposed, will be unavoidably present and will manifest as a shift on the main lobe pointing direction and as an asymmetric distribution of side lobes around it. Concerning the ripple present on the pattern cuts at the lower band (except at the design frequency, which presents a clearly much more smooth behaviour), a possible explanation for this behaviour has to be found on the scattering due to the high number of symmetric wedge structures present for port 1: the edge corners inside the flare, the edges of the flare, and the top and bottom structures.

Considering this, a validation of the proposed antenna radiation characteristics has been carried out exclusively at the centre frequencies of the lower and upper design bands, as described in next subsection.

6.4.4 Pattern and gain measurement

The antenna was measured for its directional characteristics in the anechoic chamber. The measurement setup is shown in Figure 6.32. A suitable support to adhere the millimeter wave antenna to the anechoic chamber positioner was designed and fabricated. The chamber support was mainly designed considering minimal intrusion into the way the parallel plate waveguide radiates. It consists of a L shaped structure fixed on to the top of the free area encompassing the parallel plate waveguide. The other end of the L shaped structure was designed to mount onto the chamber positioner plate. A simulation model considering the designed chamber support was designed and solved for the radiation patterns including the chamber support effects. The pattern measurements of the millimeter wave antenna with the chamber support is compared with simulations that account for the presence of the chamber support as well.

The Multi-beam antenna casts beams along directions of $+63^\circ$, 0° and -63° , which are within the tolerance limit of 5° for use within a sector cell with minimal sector-sector and inter-cell interference. Though the direction of the beams is so chosen as to cover the sector of a typical base station cell, they can be reconfigured to other desired angles. The simulated gain obtained along the three beams for the two frequencies of operation are compared with the corresponding measured gains as shown in the Table 6.1. It is seen that there is a good agreement between the simulated and measured gains. For all the cases the gain is calculated with alignment along the main beams.

The azimuthal beam pattern at 28 GHz for port 1 is shown in Figure 6.33. The simulated and measured patterns agree closely with low comparable cross polar level. The elevation beam pattern at 28 GHz for port 1 is also shown in Figure 6.33 compared with simulations. As can be seen, the elevation beam is a fan shaped broad beamwidth beam along the yz plane and the azimuth beam is a narrow beamwidth beam. The measurement was performed for beam pointing along 0° due to port 1. The measurement was carried out at ports 2 and 3 for both the elevation and azimuth at frequency of 28 GHz. The Figures 6.34 and 6.35 depict the beams pointing in $+63^\circ$ and -63° for ports 2 and 3 respectively. There is a good agreement between simulation and measurement both with regards to the co-polar and cross polar levels. It is to be noted that these beams are formed on the same shared aperture. Similar description and analysis apply to the case of 31 GHz the only difference being in the slightly increased SLL near the -63° and $+63^\circ$ angles. The simulated vs measured antenna pattern at 31 GHz for the three ports are shown in Figures 6.36, 6.37 and 6.38. The antenna at each of the three ports is horizontally polarized.

Finally, the antenna was measured for its gain vs frequency dependence along the three ports. The Co-polar gain, the Cross polar gain and the Cross polar discrimination (XPD) was calculated from the measured S parameters by two-antenna method. The gain was calculated vs frequency with the main beam of the AUT facing the probe in all the three cases. These measured parameters are depicted for the three ports in Figures 6.39, 6.40 and 6.41. A co-polar

Millimeter wave antenna

gain close to 15 dBi was measured for all the three ports with XPD values better than 30 dB on the lowest band and better than 20 dB in the upper band.

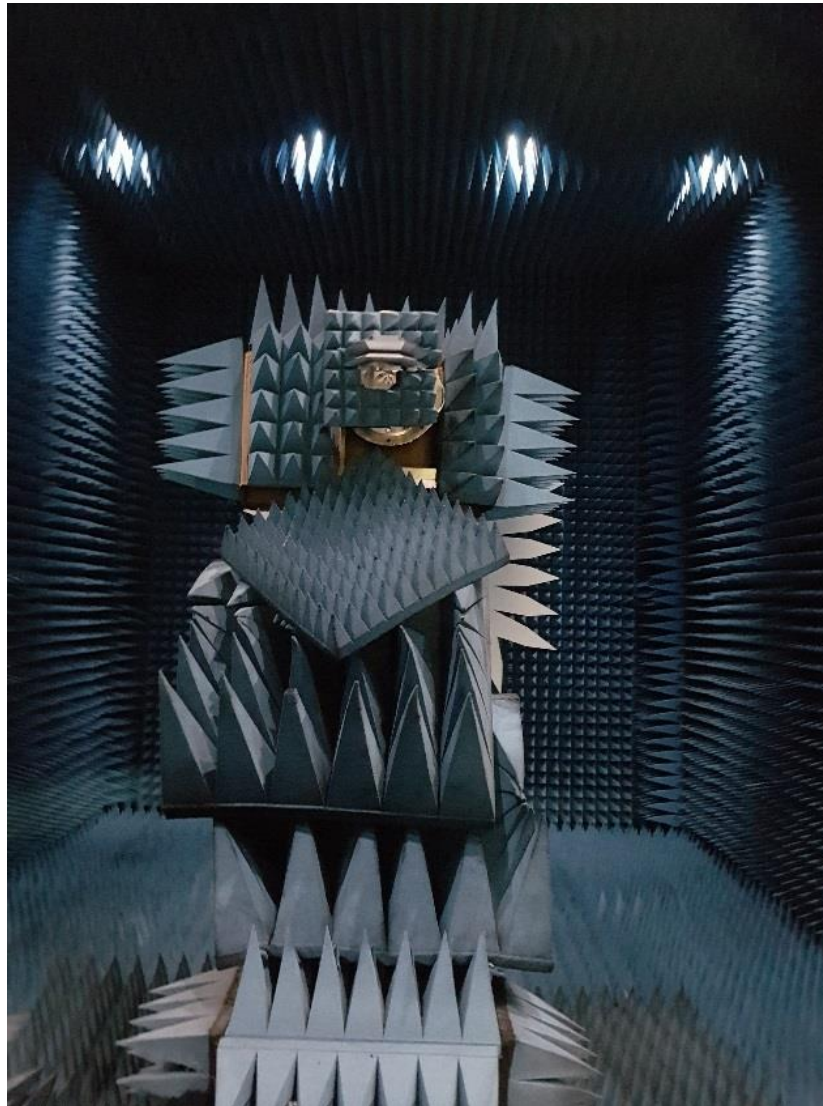


Figure 6.32 Antenna measurement setup in the anechoic chamber

Frequency in GHz	Beam gain in dBi		
	Port 1 (Sim.,Meas.)	Port 2 (Sim.,Meas.)	Port 3 (Sim., Meas.)
28	13.8, 14.08	15.5, 14.95	15.5, 15.89
31	15.8, 14.72	14.4, 13.78	14.4, 13.82

Table 6.1 Simulated vs measured beam gains at the three ports over the dual band

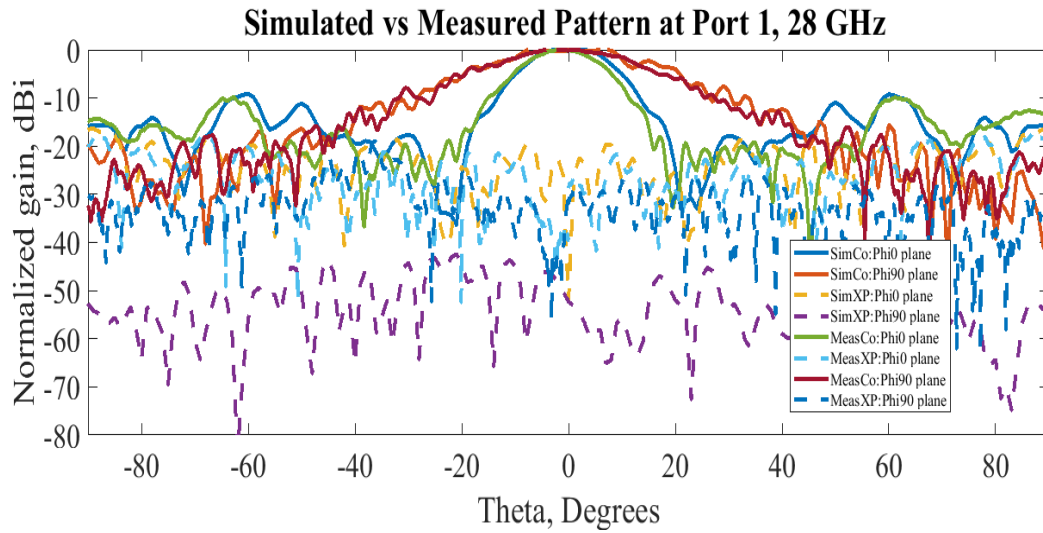


Figure 6.33 Simulated vs measured pattern at port 1 for 28 GHz

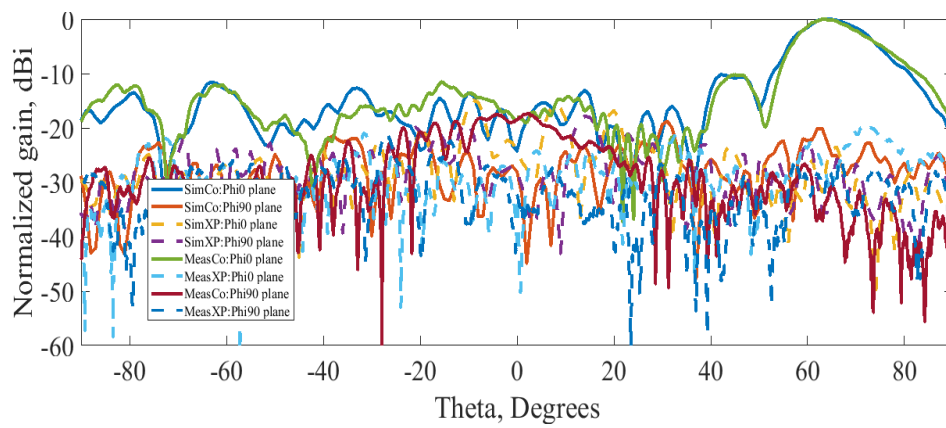


Figure 6.34 Simulated vs measured pattern at port 2 for 28 GHz

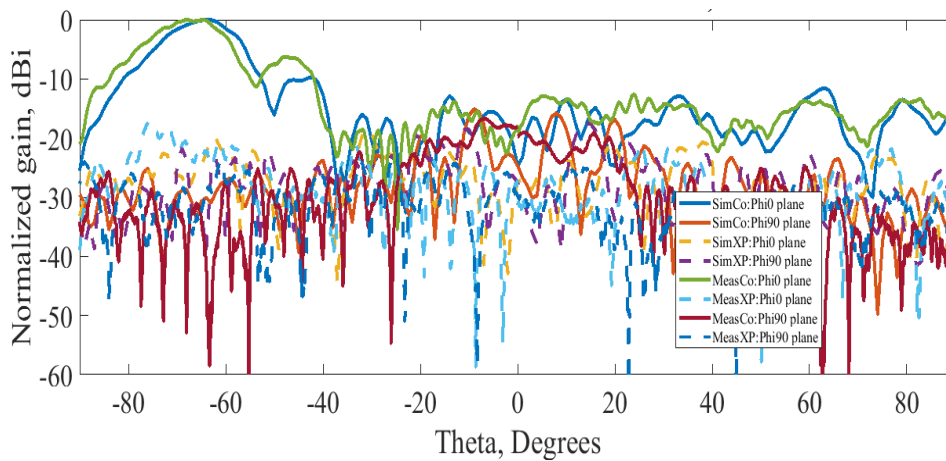


Figure 6.35 Simulated vs measured pattern at port 3 for 28 GHz

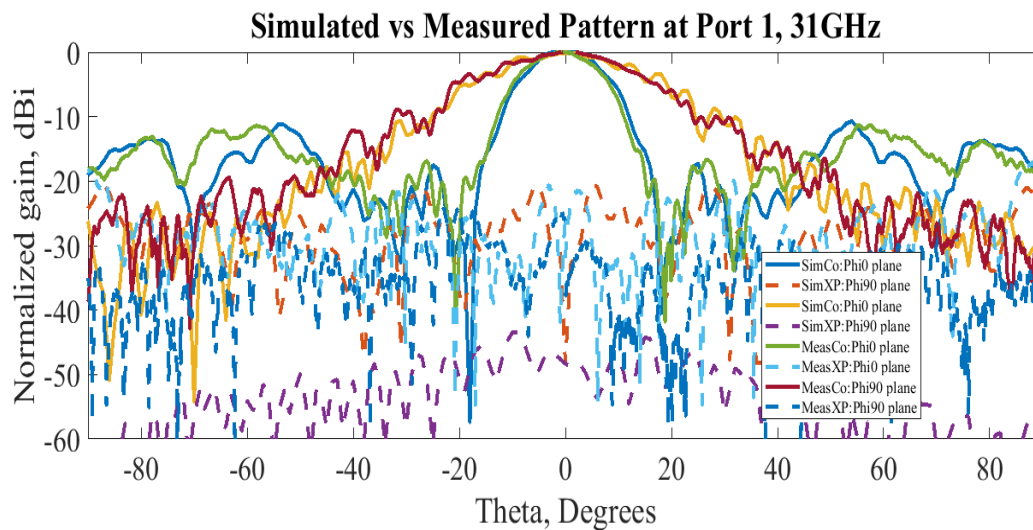


Figure 6.36 Simulated vs measured pattern at port 1 for 31 GHz

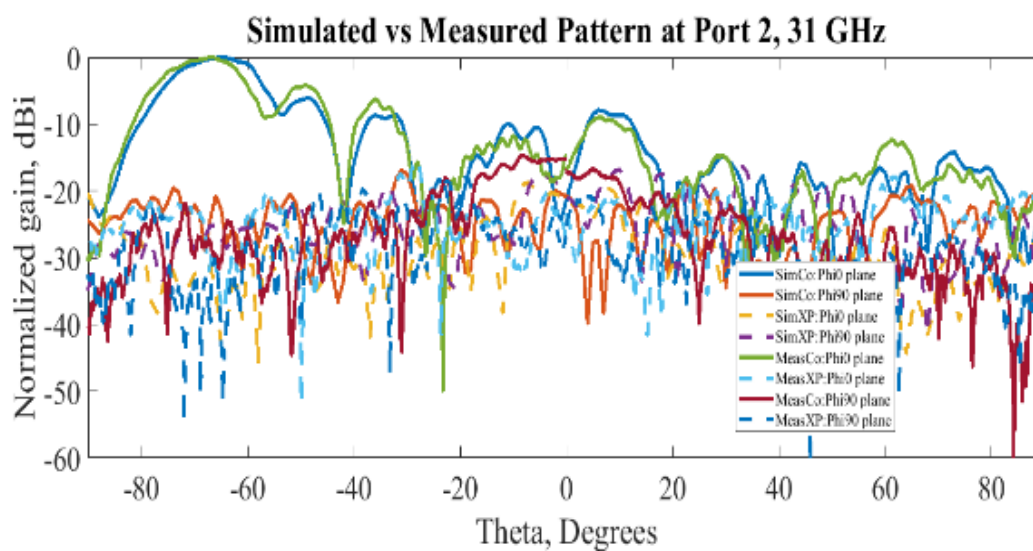


Figure 6.37 Simulated vs measured pattern at port 2 for 31 GHz

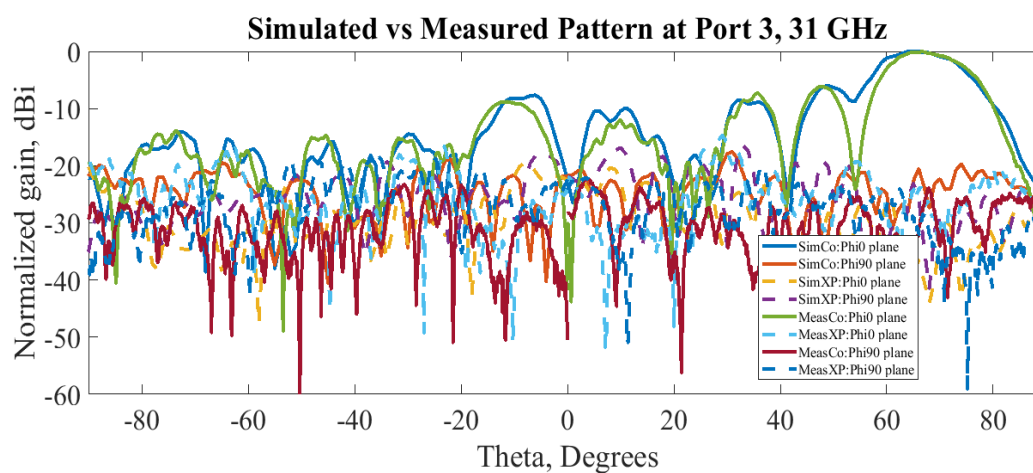


Figure 6.38 Simulated vs measured pattern at port 3 for 31 GHz

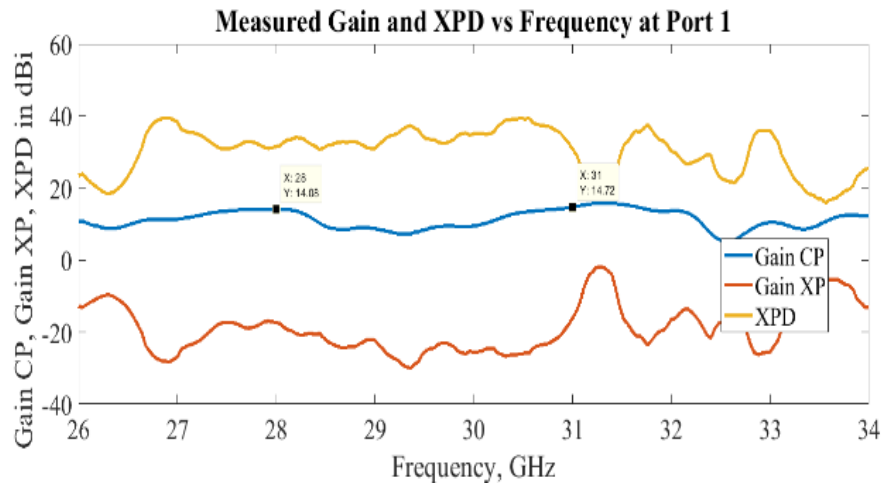


Figure 6.39 Measured Gain and XPD vs frequency at port 1

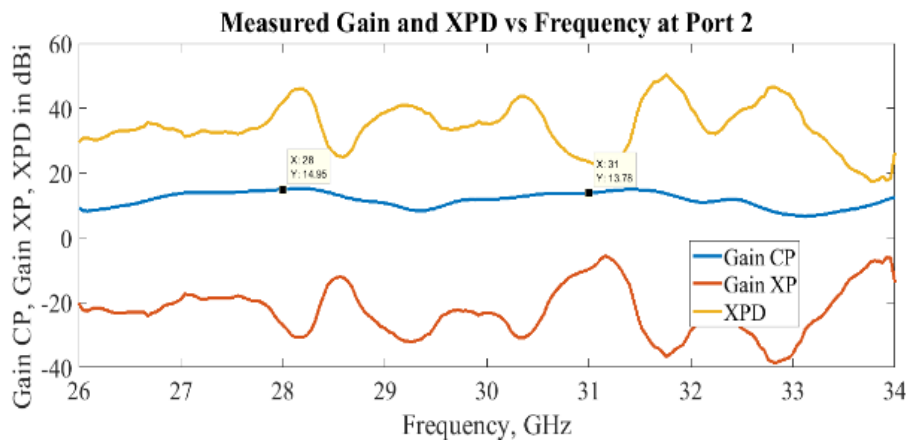


Figure 6.40 Measured Gain and XPD vs frequency at port 2

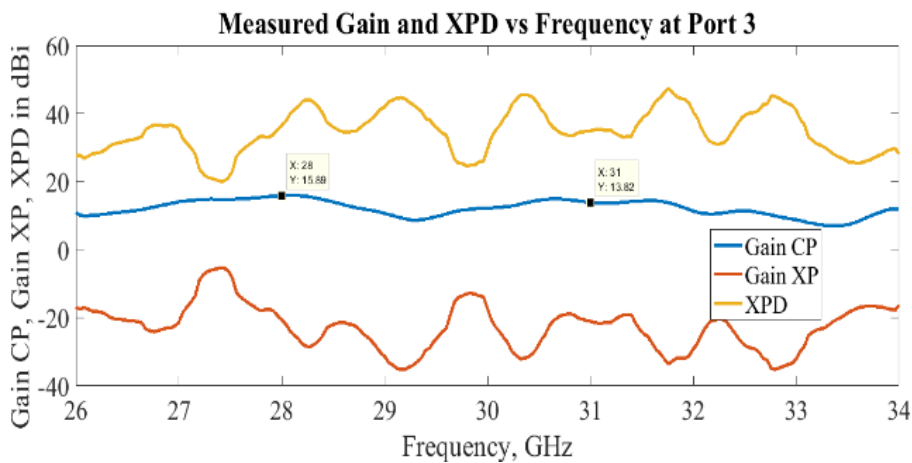


Figure 6.41 Measured Gain and XPD vs frequency at port 3

6.5 Conclusions

The design and experimental validation of a multi-beam dual band parallel plate beamformer has been presented. The antenna design has been shown to be a co-design process of four interdependent designs integrated to operate in unison. The antenna has an operational band in the 27.5 GHz to 28.5 GHz and the 30.5 to 31.5 GHz band. This dual band operation makes the antenna a potential candidate for use in the Local Multipoint Distribution System (LMDS) using millimeter wave for 5G. The three-port gain within the frequency band has been calculated by full wave simulations as being around 15 dBi and these values have been validated experimentally. The antenna beams are directed at $+63^\circ$, 0° and -63° , however using the proposed design methodology other beam directions can be obtained. The current design beam angles can be used in millimeter wave based 5G LMDS small cell scenarios which require an angular projection of 120° in each sector of the cell. Other potential use of the antenna is in the rotational surveillance radars, when used as a circular array of three 120° sectors. The general design methodology presented here allows to custom design this antenna for suitable high gain multi-beam applications. The prototype of the antenna has been fabricated and experimentally validated for its pattern and gain characteristics in situ with the S parameters and there is a good agreement between simulation and measurements.

6.6 References

- [1] W. E. Kock, "Metallic delay lenses," in *The Bell System Technical Journal*, vol. 27, no. 1, pp. 58-82, Jan. 1948
- [2] F. Luo and C. Zhang, "Full-duplex Radios in 5G: Fundamentals, Design and Prototyping," in *Signal Processing for 5G: Algorithms and Implementations*, 1, Wiley-IEEE Press, 2016, pp.541-544.
- [3] M. N. Hamdy, "Application Notes on Multi Beam. Antennas Planning - Limitations & Solutions," *Wireless Network Engineering*, August 2015.
- [4] J. Ruze, "Wide-Angle Metal-Plate Optics," in *Proceedings of the IRE*, vol. 38, no. 1, pp. 53-59, Jan. 1950.
- [5] W. Rotman and R. Turner, "Wide-angle microwave lens for line source applications," in *IEEE Transactions on Antennas and Propagation*, vol. 11, no. 6, pp. 623-632, November 1963.
- [6] Y. Zeng and R. Zhang, "Cost-Effective Millimeter-Wave Communications with Lens Antenna Array," in *IEEE Wireless Communications*, vol. 24, no. 4, pp. 81-87, 2017.
- [7] P. Alitalo, F. Bongard, J. Mosig and S. Tretyakov, "Transmission-line lens antenna with embedded source," 2009 3rd European Conference on Antennas and Propagation, Berlin, 2009, pp. 625-629.
- [8] M. Ettorre, R. Sauleau and L. Le Coq, "Multi-Beam Multi-Layer Leaky-Wave SIW Pillbox Antenna for Millimeter-Wave Applications," in *IEEE Transactions on Antennas and Propagation*, vol. 59, no. 4, pp. 1093-1100, April 2011.
- [9] H. Legay et al., "Multiple beam antenna based on a parallel plate waveguide continuous delay lens beamformer," 2016 International Symposium on Antennas and Propagation (ISAP), Okinawa, 2016, pp. 118-119.
- [10] F. Doucet, N. J. G. Fonseca, E. Girard, H. Legay and R. Sauleau, "Analysis and design of a continuous parallel plate waveguide multiple beam lens antenna at Ku-band," 2017 11th European Conference on Antennas and Propagation (EUCAP), Paris, 2017, pp. 3631-3635.
- [11] F. Doucet, S. Tubau, E. Girard, N. Fonseca, H. Legay and R. Sauleau "Design of continuous parallel plate waveguide lens-like beamformers for future low-cost and high performances multiple beam antennas", 38th ESA Antenna Workshop on Innovative Antenna Systems and Technologies for Future Space Missions, October 2017, ESTEC, Noordwijk, The Netherlands .
- [12] O. Manoochehri, A. Darvazehban, M. A. Salari, A. Emadeddin and D. Erricolo, "A Parallel Plate Ultra-Wideband Multibeam Microwave Lens Antenna," in *Early Access IEEE Transactions on Antennas and Propagation*, June 2018
- [13] C. D. Diallo, E. Girard, H. Legay and R. Sauleau, "All-metal Ku-band Luneburg lens antenna based on variable parallel plate spacing Fakir bed of nails," 2017 11th European Conference on Antennas and Propagation (EUCAP), Paris, 2017, pp. 1401-1404.
- [14] D. M. Pozar, *Microwave Engineering*, 4th Edition, Wiley, 2011.
- [15] V. Basavarajappa, A. Pellon, A. Ruiz, B. B. Exposito, L. Cabria and J. Basterrechea, "Millimeter Wave Dual-Band Multi-Beam Waveguide Lens-Based Antenna," *WSA 2018; 22nd International ITG Workshop on Smart Antennas*, Bochum, Germany, 2018, pp. 1-6
- [16] F. Doucet, N. J. G. Fonseca, E. Girard, H. Legay and R. Sauleau, "Analytical Model and Study of Continuous Parallel Plate Waveguide Lens-like Multiple-Beam Antennas," in *IEEE Transactions on Antennas and Propagation*, vol. 66, no. 9, pp. 4426-4436, Sept. 2018.

Chapter 7

Conclusion

As was discussed along the thesis, the work began with the state-of-the-art survey on the three technologies-Massive MIMO, Single RF MIMO and Millimeter wave antenna. This was followed by introduction of the concept, design and experimental validation of the antennas- custom designed for each of these scenarios. In the following a brief description of each chapter and the conclusions that can be drawn are presented with the potential future work highlighted along the chapters:

Chapter 2. The state-of-the-art survey on Massive MIMO provided the key areas on which the design of Massive MIMO antennas can be based upon: Interference, Energy efficiency, Area Spectral efficiency, Area Energy efficiency and most importantly the number of antennas. Several Massive MIMO demonstrators by ARGOS, Lund and Samsung were discussed along with their key features. Single RF MIMO antenna using techniques of time division multiplexing, code division multiplexing, antenna selection and techniques pertaining to the ESPAR (Electronically scanned parasitic antenna array) were surveyed. Pertaining to Millimeter Wave antenna implementations some of the key aspects and challenges in realizing this were considered. Several antennas that operate in the millimeter wave were surveyed with a focus on the attainable gain and impedance bandwidth.

For Massive MIMO antennas the survey hinted at the use of a directional antenna element as basic element of the array (discussed in chapter 3) which on implementation, as discussed in chapter 4, showed that a good multibeam performance for Massive MIMO could be obtained.

The Single RF MIMO survey that also included survey of ESPAR antennas resulted in the formation of ideas towards a pattern reconfigurable antenna array presented in chapter 5 using an electronic phase tethered excitation of antenna elements.

The millimeter wave antenna survey helped in assessing the features of the state-of-art towards realizing high gain and resulted in the idea of using a ridge-based lens, over parallel plate waveguide for gain enhancement.

To conclude the survey of the state-of-art contributed in a significant way in the formulation, refining and adaptation towards 5G, of ideas proposed in later chapters.

Chapter 3. The design of a low-profile end fire antenna element inspired on fiber-optic principles is presented. A gradient refractive index based theoretical framework of the design, supported by parametric variation is discussed. The antenna prototype has been fabricated and experimentally validated. It has an operation over 1.5 GHz of bandwidth centred around 14 GHz with a directional gain radiation pattern. The inherent layered structure when incorporated in an array aids to the better cooling of the antenna front end.

Conclusion

The prototype has been adopted in a Massive MIMO array and its performance has been validated. It can be concluded that the antenna element can find potential use in Multi-user Massive MIMO antenna arrays as well as in multibeam switching antenna arrays for 5G. The design and implementation of the Massive MIMO array and its Multi-Beam characteristics were discussed in detail chapter 4.

The antenna element can be further improved by correcting the beam squint of 20° . One of the methods to achieve this was presented in chapter 3 by use of symmetric arms. Also, work towards further enhancing the gain due to the parasitics is of interest which can consider other novel unique arrangements of parasitics following the refractive index-based mechanism proposed.

Additionally, further investigations on the radiating element trending to reduce its profile, increase its bandwidth or generating dual polarization are open research points for the future.

Chapter 4. Towards realizing the Massive MIMO antenna array, a 4×4 sub-array was considered for experimental purposes. A methodology to realize multiple beam operation using two-phase configuration was demonstrated. The beamswitching scheme facilitates the control of the geometric planes onto which the beams are projected.

A complete characterization of the fabricated 4×4 antenna sub-array in terms of its active S parameters and antenna pattern was presented. The antenna array has a gain of 16 dBi for a 4×4 configuration in the case A (boresight).

The proposed beamswitching scheme and the antenna array can find potential application in scenarios where enhanced multi user perception is required such as in densely crowded stadiums or in custom designed 5G small cell scenarios. Another capability of this beamswitching scheme is to cast beams along NLOS which can be of potential use given the recent interest in NLOS communications in Millimeter wave Massive MIMO.

As a future extension, a programmable 3-state (0° , 180° , open) phase shifter connected to each of these sixteen ports or 180-degree hybrid couplers using switches to select between hybrid coupler ports are sufficient to realize the demonstrated five beam states or other designed beam states - without switching between antennas. The latency of the beamswitching network then translates to a direct consequence of the state switching time of the phase shifter and the synchronicity between these phase shifters. This considerably reduces the latency in comparison to use of switches.

It can be concluded that the method proposed introduced a building block and a methodology for using it to construct directional multiple beams. The antenna array that has been experimentally validated will be tested on models of heterogenous ultra-dense cellular networks for their performance in the near future.

Chapter 5. The chapter introduced a reconfigurable antenna design for Spatial Modulation implemented on a 4×4 antenna subarray. The twin beam mirrored pattern pairs were validated experimentally for their pattern and gain.

Such a beamswitching scheme when applied in a Massive MIMO array can lead to significant reduction of RF chains and power consumption. It can be concluded that the limitation of Single RF MIMO, namely that it can be used in low data traffic situations

can be alleviated to an appreciable extent if the proposed single RF scheme, works with integration onto a Massive MIMO array by selective use of the constituent sub-arrays of the Massive MIMO.

Moreover, owing to the symmetrical excitation of the ports, the proposed single RF scheme maintains the same phase centre for multiple radiation patterns over the sub-array instead of using different antenna patterns switched over different phase centres over the antenna array. This implies an advantage in spatial modulation where the same antenna index can be reused in time domain. The patterns can be switched over the same sub-array rather than moving along the planar array to switch patterns.

The use of sub-array indexing as an additional dimension to the 3D constellation diagram of Spatial Modulation was also proposed. This would multiply the total information bits that can be mapped onto the collocated time-spread different patterns. The resultant is added spatial and pattern diversity as seen at each element of the array resulting in improved decoding at the receiver end.

Such a reconfigurable antenna would be well suited for application in transmit techniques involving time-based duplexing schemes such as Time Division Duplexing (TDD) where Channel State Information (CSI) would not be needed in the downlink. As a future extension, the proposed antenna concept can be evaluated in large Massive MIMO arrays.

Chapter 6. The design and experimental validation of a multi-beam dual band parallel plate beamformer was presented. The antenna design has been shown to be a co-design process of four interdependent designs integrated to operate in unison. The antenna has an operational band in the 27.5 GHz to 28.5 GHz and the 30.5 to 31.5 GHz band. This dual band operation makes the antenna a potential candidate for use in the Local Multipoint Distribution System (LMDS) using millimeter wave for 5G. The antenna beams are directed at $+60^\circ$, 0° and -60° , however using the proposed design methodology other beam directions can be obtained, with the limitations imposed by size of the feeding E-plane horns and their couplings.

The current design beam angles can be used in millimeter wave based 5G LMDS small cell scenarios which require an angular projection of 120° in each sector of the cell. Other potential use of the antenna can be found in the field of rotational surveillance radars, when used as a circular array of three 120° sectors. The general design methodology presented here allows to custom design this antenna for suitable high gain multi-beam applications.

The prototype of the antenna has been fabricated and experimentally validated for its pattern and gain characteristics in situ with the S parameters and there is a good agreement between simulation and measurements.

As a future extension of the proposed antenna, the fundamental PPW TEM mode is being harnessed along with TE₁ to obtain a dual polarized antenna that can significantly enhance the polarization diversity at these frequencies.

It has to be considered that the proposed antenna design is based on assumptions oriented to simplify the fabrication of the prototype. Control of phase aberrations and the influence of feeders over the field distribution inside the parallel plate waveguide has some limitations, especially when extreme ports are intended to generate beams with high angular deviations with respect to the central port, as is the case.

Further investigations can be driven towards further improving the currently employed path tracing inside the structure in such a way that it allows for a structured design and optimization methodology for both the ridge height and its geometry in order to minimize

Conclusion

these adverse effects. The methodology proposed in chapter 6 reduces the high level of computer resources required by the full wave solver, and these resources would only be required to check the accuracy of the path tracing model. Further investigations towards refinement of the proposed path tracing technique can further reduce the computational cost and time.

To conclude, three 5G application oriented, experimentally validated, functional antenna prototypes; backed up with solid design theory were proposed in the thesis with implications that can be extended to several 5G use cases.